UNIVERSITY OF ROCHESTER
LABORATORY FOR LASER ENERGETICS

Volume 152
July–September 2017
DOE/NA/1944-1361

LLE Review

Quarterly Report

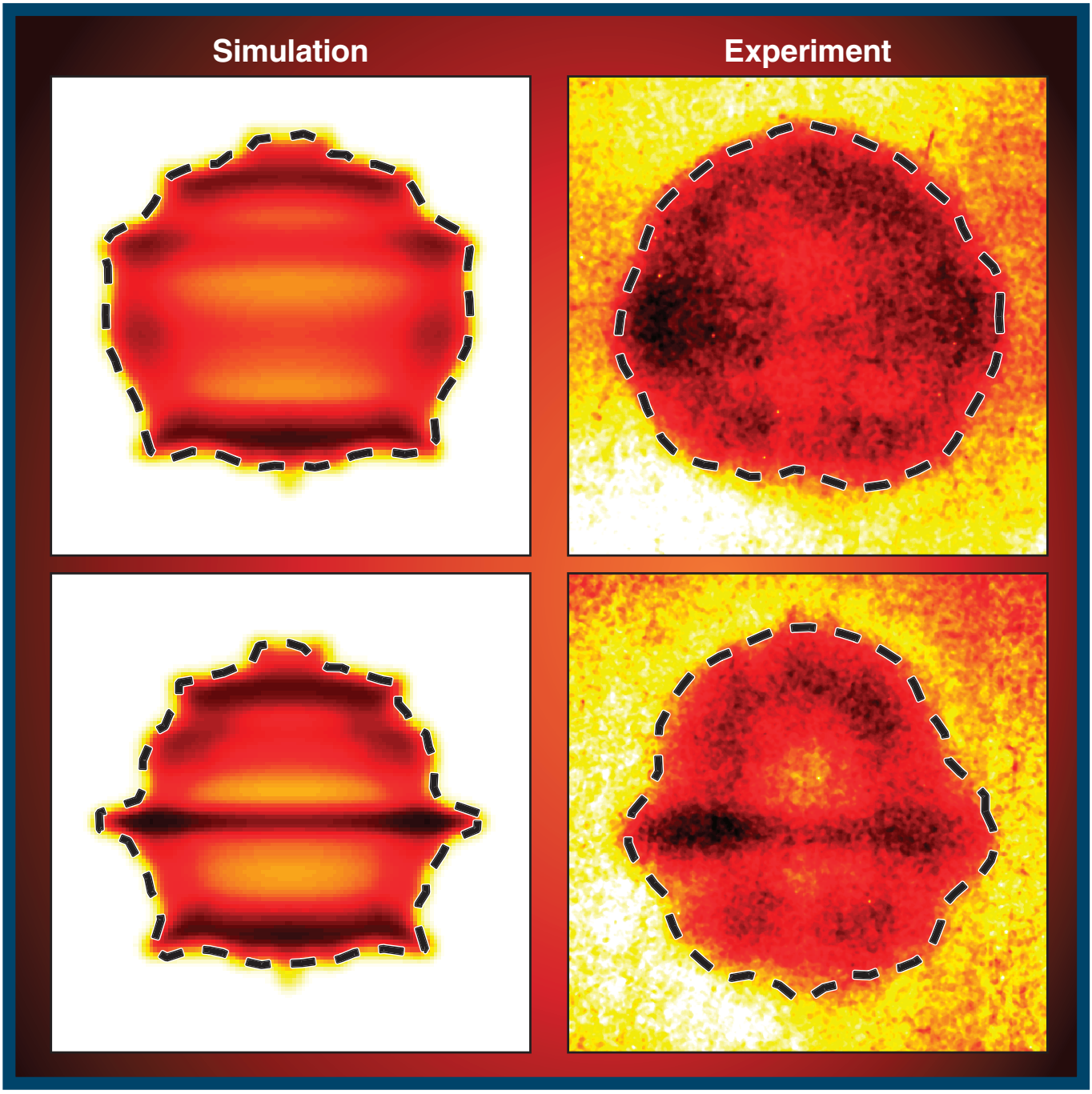

About the Cover:

The backlit radiograph images on the front cover are simulated and experimental results from recent National Ignition Facility (NIF) experiments that demonstrated the proof-of-principle concept using the wavelength-detuning cross-beam energy transfer (CBET) mitigation scheme. A technique called cone-swapping was employed on the southern hemisphere to induce the required wavelength difference from each hemisphere about the equatorial region (where the majority of CBET occurs in polar direct drive) using the current NIF configuration. Shown in the top row are the results from this configuration when zero wavelength detuning was used; this sets the baseline measurement for reference. The images in the bottom row result when wavelength detuning was enabled with a ±2.3-Å UV detuning. An observable change in the morphology and shell trajectory of the equatorial region was not only predicted but observed experimentally, validating the *DRACO* simulations and demonstrating the wavelength-detuning CBET mitigation scheme. The small amount of detuning currently available on the NIF (±2.3 Å UV) represents only the beginning of foreseeable CBET mitigation benefits since it is predicted that NIF laser amplification can achieve full power at ±6 Å UV with changes only to the front and back ends of the entire chain.

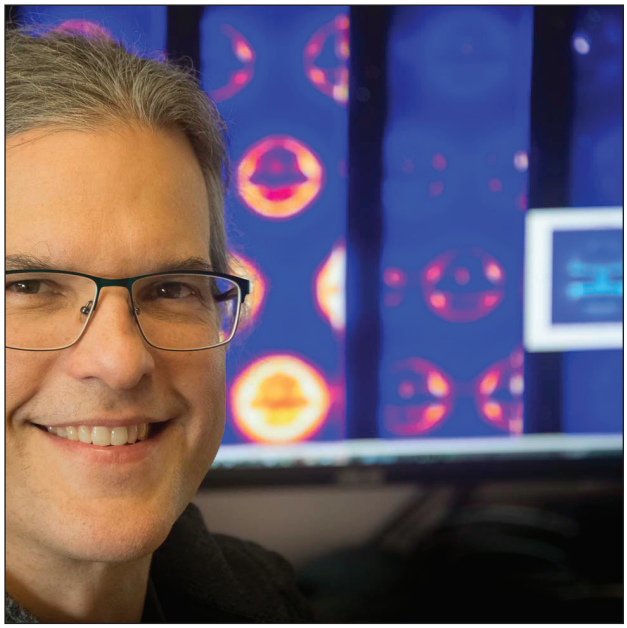

The photo to the right shows J. A. Marozas and another set of simulated and experimental self-emission images showing good agreement in the background. Those self-emission images show the predicted and measured shell morphology as well as the self-emitting core that is consistently observed only when wavelength detuning is enabled.

The work described in this volume includes current research at the Laboratory for Laser Energetics, which is supported by New York State Energy Research and Development Authority, the University of Rochester, the U.S. Department of Energy Office of Inertial Confinement Fusion under Cooperative Agreement No. DE-NA0001944, and other agencies.

For questions or comments, contact Richard W. Kidder, Editor, Laboratory for Laser Energetics, 250 East River Road, Rochester, NY 14623-1299, (585) 275-7730.

Worldwide-Web Home Page: http://www.lle.rochester.edu/

Printed in the United States of America
Available from
National Technical Information Services
U.S. Department of Commerce
5285 Port Royal Road
Springfield, VA 22161
www.ntis.gov

UNIVERSITY OF ROCHESTER
LABORATORY FOR LASER ENERGETICS

Volume 152
July–September 2017
DOE/NA/1944-1361

LLE Review

Quarterly Report

UR LLE

Contents

In Brief

This volume of the LLE Review, covering July–September 2017, features "First Observation of Cross-Beam Energy Transfer Mitigation for Direct-Drive Inertial Confinement Fusion Implosions Using Wavelength Detuning at the National Ignition Facility," by J. A. Marozas, M. J. Rosenberg, D. Turnbull, T. J. B. Collins, P. B. Radha, P. W. McKenty, J. D. Zuegel, F. J. Marshall, S. P. Regan, T. C. Sangster, W. Seka, E. M. Campbell, and V. N. Goncharov (LLE); and M. Hohenberger, M. W. Bowers, J.-M. G. DiNicola, G. Erbert, B. J. MacGowan, L. J. Pelz, and S. T. Yang (LLE). This article (p. 169) reports on the cross-beam energy transfer (CBET) results from two-beam energy exchange via seeded stimulated Brillouin scattering, which detrimentally reduces ablation pressure and implosion velocity in direct-drive inertial confinement fusion. Direct-drive implosions at the National Ignition Facility were conducted to reduce CBET by detuning the laser-source wavelengths (±2.3 Å UV) of the interacting beams over the equatorial region of the target. For the first time, wavelength detuning was shown experimentally to increase the equatorial region velocity by 16% and to alter the in-flight shell morphology. These experimental observations are consistent with design predictions of radiation–hydrodynamic simulations that indicate a 10% increase in the average ablation pressure.

Additional highlights of research presented in this issue include the following:

- T. J. B. Collins and J. A. Marozas present two novel target designs for using direct laser ablation (direct drive) at the National Ignition Facility to assemble and ignite cryogenic fuel using the existing indirect-drive beam configuration (p. 176). These are the first ignition-relevant "polar" direct-drive target designs to include the physical effects of CBET between laser beams and nonlocal electron heat transport. A wavelength-detuning strategy is used to reduce scattered-light losses caused by CBET, allowing for ignition-relevant implosion velocities. Two designs are described: a moderate-adiabat alpha-burning design with a D–T neutron fusion yield of 1.2×10^{17} and a lower-adiabat ignition design with a gain of 27. Both designs have low in-flight aspect ratios, indicating acceptable hydrodynamic stability levels of perturbation growth during the implosion.

- M. Stoeckl and A. Solodov report on the linearity of the photostimulated luminescence process to make repeated image-plate scanning a viable technique to extract more-dynamic range (p. 184). In order to obtain a response estimate for second and subsequent scans with a BAS-MS image plate and the Typhoon FLA 7000 scanner, a new model for the readout fading of the image plate is introduced; it relates the depth distribution of activated photostimulated luminescence centers within the image plate to the recorded signal. Model parameters are estimated from an image-plate scan series for the hard x-ray image-plate diagnostic over a collection of experiments providing x-ray energy spectra whose approximate shape is a double exponential.

- B. W. Plansinis, W. R. Donaldson, and G. P. Agrawal report on a time-to-frequency converter that was constructed using an electro-optic phase modulator as a time lens, allowing the pulse shape in time to be transferred to the frequency domain (p. 192). The device was used to record the temporal shape of infrared pulses at a wavelength of 1053 nm (width about 7 ps) and compared these measurements to those made by using both a streak camera and an autocorrelator. Numerical simulations were used to establish that the time-lens–based system can accurately measure the shape of infrared pulses between 3 and 12 ps. The numerical model was also used to determine how such a system can be modified to measure pulses whose width lies in the range of 1 to 30 ps, a range of interest for the OMEGA EP laser.

- R. Mancini reports on the Ninth Omega Laser Facility Users Group Workshop (p. 198).

- This volume concludes with a summary of LLE's Summer School Research Program (p. 204), the FY17 Laser Facility Report (p. 206), and the National Laser Users' Facility and External Users' Programs (p. 209).

Richard W. Kidder
Editor

First Observation of Cross-Beam Energy Transfer Mitigation for Direct-Drive Inertial Confinement Fusion Implosions Using Wavelength Detuning at the National Ignition Facility

In direct-drive inertial confinement fusion (ICF), laser beams irradiate a plastic shell containing a thick layer of frozen deuterium–tritium (DT) and ablatively drive an implosion. The ultimate goal of ICF is ignition and energy gain; the minimum shell kinetic energy required for ignition (defined as when the energy from DT fusion reactions exceed the laser energy incident on the target) is given by $E_{\min} \sim \alpha^{1.88} P_{\text{abl}}^{-0.77} v_{\text{imp}}^{-5.89}$ (Ref. 1), where the three parameters of the implosion—α, v_{imp}, and P_{abl} [adiabat (the ratio of the fuel pressure to the Fermi-degenerate pressure at peak implosion velocity), implosion velocity, and ablation pressure, respectively]—are determined primarily by the deposition of the laser energy into the coronal plasma of the target, the subsequent heat conduction to the ablation surface, and the resulting equation of state (EOS) of the shell material. Cross-beam energy transfer (CBET)[2] has been identified in direct-drive experiments on the OMEGA[3] and National Ignition Facility (NIF)[4] lasers to significantly reduce absorption, ablation pressure, and implosion velocity.

The role of CBET in direct drive was identified in early research[5,6] but only recently identified as the leading cause of decreased energy coupling. When attempts were made to match multiple calculated observables (shell morphology, trajectory, scattered-light spectra and distribution, and shock timing) with experiments, the critical role of CBET became apparent:[7,8] lowering laser absorption by 20% to 30%. Good agreement with the multiple experimental observables was obtained[7,8] when both the CBET and nonlocal electron transport[9] models were included in 1-D *LILAC*[10] and 2-D *DRACO*[11] simulations. Historically, the role of CBET[5,6] was masked by using a flux-limited electron transport model that matched laser absorption.

CBET laser–plasma interaction results from two-beam energy exchange via stimulated Brillouin scattering (SBS),[2] which reduces absorbed light and consequently reduces ablation pressure and implosion velocity. The dominant CBET loss mechanism in direct drive occurs when rays counter-propagate (backscatter mode), thereby increasing scattered light, as illustrated in Fig. 152.1(a). For the ignition-relevant overlapped beam intensities of $\sim 8 \times 10^{14}$ W/cm^2 for these NIF experiments, CBET is calculated to reduce laser absorption by 22%, the average implosion speed by ~9%, and the average ablation pressure by 35% via simulations of the experimental

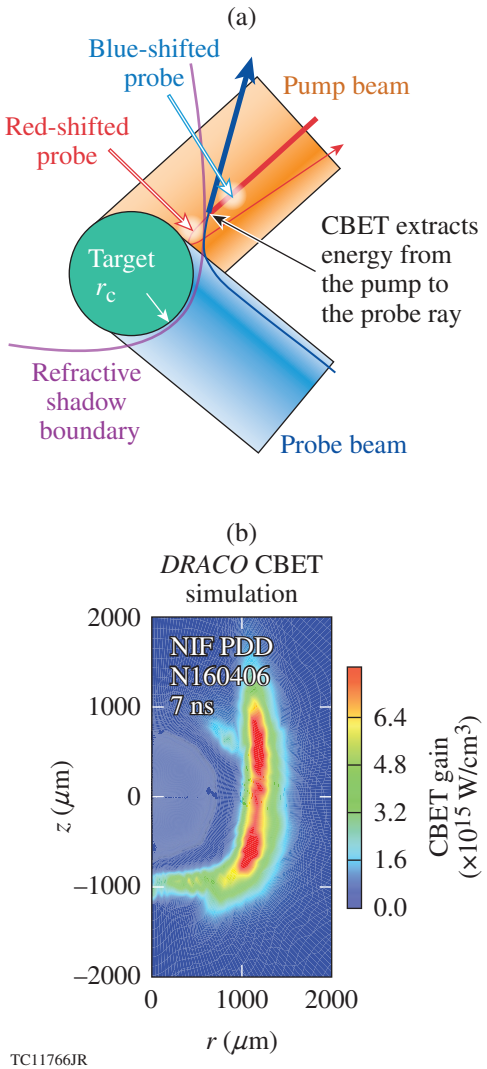

Figure 152.1
(a) The effect of cross-beam energy transfer (CBET) in polar direct drive (PDD) predominantly affects the equatorial region; (b) successful CBET mitigation benefits the same region.

conditions. These drive-related results are consistent with other ongoing OMEGA-[7] and NIF-scale[8] experiments. Reducing the target mass compensates for CBET losses, but the thinner shells become compromised as a result of instability growth.[12] As shown by the above equation for E_{min}, efficient laser energy coupling and hydrodynamic stability are essential aspects of direct-drive ICF, making CBET mitigation vital. Mitigation strategies of the deleterious CBET effects invoke combinations of spatial, temporal, and wavelength domains. Wavelength detuning, the focus of this article, works by altering the resonance condition between interacting beams.[2] Wavelength detuning was first examined for indirect drive[13] and subsequently for direct drive but was prematurely dismissed as a viable option.[14]

The first direct-drive experiments have been designed for the NIF to study the efficacy of wavelength-detuning CBET mitigation. The target designed for these wavelength-detuning shots on the NIF was adapted from existing 600-kJ designs,[8] where the trajectories and the shape of the imploding shell and scattered light were well described by the CBET model in *DRACO*. The basic target design is shown as the inset in Fig. 152.2, where the laser beam power (shown in red) produces a peak overlapped intensity of ~8×10^{14} W/cm^2 at the initial target radius.

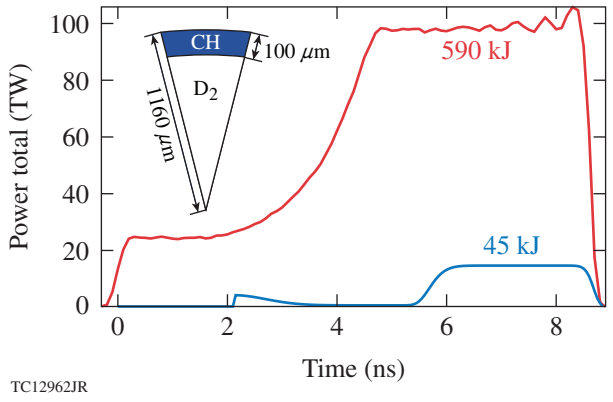

Figure 152.2
The NIF PDD target design for wavelength detuning with cone swapping to induce a wavelength difference across the equator. The total 590-kJ design pulse is shown in red; the 45-kJ backlighter pulse is shown in blue. Inset: the warm plastic (CH), 1160-μm-radius, 100-μm-thick shell with a 20-atm D_2 gas fill.

The indirect-drive NIF beam geometry distributes 192 beam ports [grouped into 48 quads, shown as projected circles in Fig. 152.3(a)] toward the poles of the NIF target chamber, forming cones of quads with a common polar angle.[15] Repointing higher-intensity beams from lower latitudes toward the equator partially compensates for the NIF port geometry and higher incident angles when illuminating direct-drive targets. In this modified configuration, referred to as polar direct drive (PDD).[16,17] CBET predictably dominates in the equatorial region where most of the crossing-beam interactions occur,[18,19] as shown in Fig. 152.1(b). As a result, PDD implosions tend to become oblate because CBET reduces the laser drive preferentially in the equatorial region. With this motivation, a basic wavelength-detuning strategy exploits the PDD configuration, where each hemisphere has a different wavelength or color. However, the nominal symmetric wavelength mapping [see Fig. 152.3(a)] developed for indirect-drive targets precludes achieving hemispheric wavelength detuning using typical PDD repointing configurations.[17]

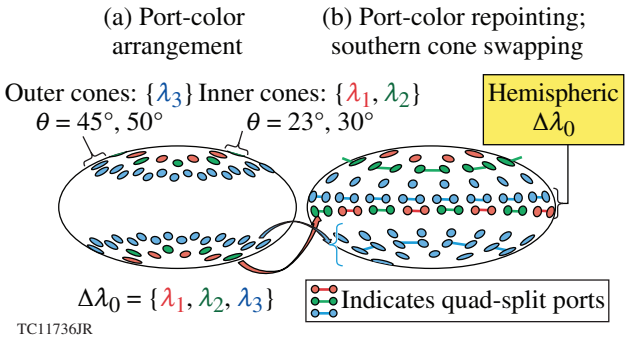

Figure 152.3
NIF Quad-Port Hammer projections for the wavelength-detuning CBET mitigation scheme. (a) Indirect-drive mapping where the colored symbols indicate relative wavelength; (b) PDD repoint mapping that achieves hemispheric detuning, typical northern-hemisphere repointing, and southern-hemisphere cone swapping.

The NIF fiber front end[15] supports three separate initial colors or wavelength shifts $\Delta\lambda_0 = \{\lambda_1,\lambda_2,\lambda_3\}$ detuned from a central wavelength $\lambda_0 \sim 351$ nm. Currently, the three-color $\{\lambda_1,\lambda_2,\lambda_3\}$ mapping onto the NIF indirect-drive ports is symmetric about the equator [see Fig. 152.3(a)]. To induce a wavelength difference about the equatorial region, a dramatic repointing (referred to as "cone swapping") is required in either the northern or southern hemisphere [see Fig. 152.3(b) for the southern case]. For cone swapping, in one hemisphere the higher-latitude ports ("inner cones": $\{\lambda_1, \lambda_2\}$) are repointed to the equator and the lower-latitude ports ("outer cones": $\{\lambda_3\}$) are repointed to the mid- and high latitudes. For the wavelength-detuning experiments described here, only two different colors were specified such that $\lambda_1 = \lambda_2 \neq \lambda_3$, although future enhanced experiments with three colors are planned. The current NIF

configuration, while not optimal, is capable of achieving a modest wavelength-detuning level $\Delta\lambda_0$ = {+2.3,+2.3,–2.3} Å UV, which is adequate for these proof-of-principle experiments. Cone swapping plus wavelength detuning induces the desired partial hemispheric wavelength difference between beams crossing the equatorial region.

The far-field spot envelope [induced from distributed phase plates (DPP's)[20] and small-divergence smoothing] quad-mapping is given by the current indirect-drive configuration on the NIF: the inner cones (λ_1, λ_2; red/green projected circles in Fig. 152.3) use a wide elliptical spot shape not well suited for the equatorial region, while the outer cones (λ_3; blue projected circles in Fig. 152.3) use a narrow elliptical spot shape. The values of the beam energy and repointing were additionally adjusted in the cone-swapping hemisphere to compensate for the swapped spot shapes and the higher incident angles using established PDD design principles.[17] The cone-swapping repointing scheme and the fixed DPP quad-mapping result in nonoptimal implosion symmetry [see Fig. 152.3(b)]. For this reason, fusion yield and areal density are not metrics for these experiments, which concentrate instead on observables directly related to laser energy absorption: implosion trajectory, shell morphology, and scattered light. Future reconfigurations (optimal DPP's for PDD,[17,20] flexible color mapping, and larger wavelength separation) can relieve these constraints, and simulations predict improved overall fusion performance.

In direct drive, many overlapping beams interact with each other in a complicated tangle of intensity, directions, and wavelengths, depending on the beam-port configuration surrounding the imploding target. In addition, each beam strongly refracts and chirps in the expanding, evolving plasma atmosphere during propagation and then scatters energy spectra in a wide spread of exiting paths. The *DRACO* CBET package (*Adaawam*)[21] is an integral part of the 3-D ray-trace package (*Mazinisin*[22]),[17] which models each beam as a set of adaptively chosen rays to minimize noise. An extension to the plane-wave CBET model[2] adapts the steady-state fluid model to 3-D interacting rays in *Adaawam* by generalizing the wave-vector phase-matching condition. The CBET model[2] includes relevant SBS physics and results in gain/loss for a probe ray interacting with the total pump angular spectrum. *Adaawam* calculates the CBET interaction self-consistently in conjunction with the hydrodynamic evolution of the ICF target (via a split-step technique) and captures the necessary coupled interaction of the dynamic electron density profile, temperature, and plasma-flow velocity that dictates the behavior of CBET, and vice versa, since CBET and the hydrodynamics are strongly coupled. *Adaawam* uses advanced iterative feedback control to stabilize the CBET tightly coupled many-beam interactions while maintaining energy conservation. This model has been compared to many observables across a range of implosions on OMEGA[23] and the NIF.[7] An experimentally determined CBET-gain multiplier of 1.5 (from unrelated OMEGA shots[23]) that use the first-principles EOS tables was applied to all pre- and post-shot simulations without attempting to fit the NIF shots having similar intensity but different scale lengths and pulse shapes. The CBET gain multiplier of 1.5 that applies across laser systems indicates a predictive ability on the initial wavelength-detuning shot campaign at the tested $\sim 8 \times 10^{14}$ W/cm^2 intensitity range.

Maximal CBET occurs in the rapidly expanding coronal plasma where two interacting rays satisfy the ion-acoustic-wave–matching conditions[2,13,14] that account for propagation direction, wavelength, and fluid flow; e.g., a CBET resonance occurs at the Mach-1 surface given a radial plasma flow for directly opposed radially propagating rays of equal wavelength. The instantaneous ray wavelength is given by its initial value and the temporal derivative of the electron density (an extension of the common Doppler shift[24]), which dynamically alters the instantaneous refractive index in space, and thereby the wavelength, and is independent of ray direction. Consequently, the CBET resonance features are altered as the coronal plasma evolves, which directly maps onto a chirped scattered-light measurement that can be employed to help analyze the implosions and laser–plasma interaction physics. A future publication will address the complete set of measurements and modeling.

Wavelength detuning between crossing beams responds differently in indirect- versus direct-drive ICF implosions, depending on the dominant CBET mode. In indirect drive, the sign of small wavelength detuning (<2-Å UV) is used to control the direction of energy transfer between interacting beams by leveraging the CBET resonance for the forward-scatter mode.[13] While this mode occurs in direct drive, it does not increase scattered-light loss because the energy exchanged is spatially shifted and deposited in slightly different regions; however, distortions at small wavelength separations can arise.[19] In contrast, an outbound ray in the dominant backscatter mode in direct drive experiences CBET gain regardless of the wavelength-difference sign or magnitude (for nominal levels) because the ion-acoustic wave's contribution dominates the CBET resonance function.[19] Under atypical conditions, the outbound ray may experience a loss resonance but insignificantly impacts scattered light because the outbound rays typically transport little energy. The ensemble CBET exchange is best described as an interaction volume (a weighted volume that determines

the interaction strength, which depends on path length, intensity, wavelength, electron density, coronal temperature, fluid velocity, etc.) because any high-gain region is equally matched by loss and significant CBET occurs only when the ensemble interaction volume is large. For example, there might be high intensity near a turning point over insignificant path lengths that form an ineffective and small interaction volume with minimal resulting CBET.

The resonant CBET gain region of the outbound rays in the backscatter mode never disappears but rather shifts into a smaller interaction volume because the relative instantaneous wavelength difference changes the ion-acoustic-wave–matching conditions of the interacting rays. The resonance region bifurcates and shifts both farther out in the corona (where the outbound rays have lower intensity and experience higher expanding fluid velocity and lower electron density) and closer inside the corona (where the interaction becomes shielded by the refractive shadow-boundary surface and/or outbound rays that have negligible intensity)[19] [see Fig. 152.1(a)]. A sufficiently large wavelength separation (detuning) significantly reduces CBET exchange for direct drive by decreasing the interaction volume. In contrast, an insufficient wavelength separation can lead to deposition and shell distortion via the forward-scatter mode.[19] The efficacy of wavelength-detuning CBET mitigation diminishes as the plasma expands and the target implodes, which causes the CBET resonance regions to gradually drift into larger interaction volumes during the drive pulse.[19] Larger wavelength-detuning values delay the onset of diminished mitigation. Simulations predict that wavelength-detuning CBET mitigation is effective for both symmetric direct drive (OMEGA) and PDD since the same mechanisms occur in both configurations, although the positive impact is more pronounced for PDD.[19]

With this motivation, for the first time in direct-drive ICF, wavelength-detuning CBET mitigation was demonstrated and shown to improve energy coupling. The NIF PDD wavelength-detuning CBET mitigation campaign shots were performed in three pairs; each pair consisted of one implosion backlit with ~6.7-keV x rays produced from a planar Fe foil target energized by two quads of NIF beams with 45 kJ (see the blue curve in Fig. 152.2) of UV laser energy per beam with an equatorial view of the compressing shell and a second implosion for self-emission images of the compressing target from equatorial and polar views. Additional diagnostics measured both hard x rays produced by energetic electrons arising from the stimulated Raman and possible two-plasmon–decay instabilities. The inferred levels contain at most only a few percent of the incident energy and do not affect the analysis of the laser–target coupling and CBET.[7] The first pair of control shots (N160405 and N160406) with the same wavelength for all the beams (zero detuning) were performed to establish the baseline experimental observables. Next, two pairs of experiments with a detuning mapping of $\Delta\lambda_0 = \{+2.3,+2.3,-2.3\}$ Å UV were performed to evaluate the efficacy of wavelength-detuning CBET mitigation. The zero-detuning and first-detuning shots (N160821-001 and N160821-002) employed southern-hemisphere cone swapping, as illustrated in Fig. 152.3(b). The second-detuning shots (N170102 and N170103) employed northern-hemisphere cone swapping, primarily to observe the expected image inversion and to effectively image the self-emission from the antipodal pole. The repointing (accounting for mirror-image cone swapping) and pulse shapes were nominally identical for all shots where the only intended difference was the wavelength configuration.

The simulated and measured backlit gated x-ray radiographs are analyzed to show shell morphology evolution as well as in-flight shell trajectory, which are used to infer energy coupling. The gated images (gate time ~100 ps) shown in Fig. 152.4 compare the shell morphology for the three backlit shots. The experimental framing-camera images are a composite of several images close in time for this slowly moving target that were cross-correlated and adjusted for magnification to enhance the signal-to-noise ratio; the measurements used a 30-μm pinhole. The *DRACO* simulations post-processed with the x-ray imaging code *Spect3D*[25] with matching pinholes and gates. The first two rows are radiographs of matched post-shot simulations and experimental results for the baseline zero-detuning and wavelength-detuning shots with southern-hemisphere cone swapping. The last row shows radiographs for detuning shots with northern-hemisphere cone swapping. All the backlit radiograph data show remarkable agreement between simulation and experiment, especially the expected trend for the detuning shots. A mere ~2% to 3% additional laser energy is absorbed with detuning, but since this energy is localized to the equatorial coronal volume fraction (~25%), and the deposition is redistributed to increase hydrodynamic efficiency, the result is dramatic as observed with the gated x-ray radiographs.

Most notable was the design prediction and measurement of the equatorial mass accumulation near the equator with active wavelength detuning (bottom two rows in Fig. 152.4). As predicted, the mass accumulation flipped orientation when cone swapping was applied to the opposite hemisphere. The wavelength-detuning design attempted to minimize the $\ell = 2$ Legendre mode while accounting for the spot shapes, point-

ing, and energies in conjunction with the expected increased drive in the equatorial region caused by CBET mitigation. The equatorial mass accumulation is a common feature in PDD designs (and not directly related to CBET mitigation), which is caused by lateral mass flow toward the equator (from primarily oblique incidence) when sufficient equatorial drive is available (e.g., from CBET mitigation) and when using non-optimal spot shapes while achieving a small $\ell = 2$.

The shell trajectory is inferred from the simulated and experimental backlit radiographs by first extracting the outer steepest gradient surface or radii [see Figs. 152.4 and 152.5 (inset)]. The majority of the CBET gain occurs in the equatorial region [Fig. 152.1(b)] and consequently the region expected to benefit from wavelength detuning. Both the surface-area–weighted average of the whole extracted surface and a range restricted to the equatorial region (shown here) demonstrate the benefit. When the extracted shell surface is restricted to the equatorial region (±30° region about the equator) and plotted as a function of time (see Fig. 152.5), the inferred implosion speed increases as a result of wavelength-detuning CBET mitigation. The equatorial shell speed increases 9% from 144 to 157 μm/ns based on simulation (experimentally a 16% increase from 133 to 154 μm/ns) because wavelength-detuning CBET mitigation deposits 3% additional energy within the small volume over the equator. The enhanced equatorial velocity is consistently observed when comparing the extracted outer shell contours taken from zero detuning and detuning shots in Fig. 152.5 (inset), where the entire surface-area–weighted average implosion speed increases experimentally by 13%.

In conclusion, the first direct-drive wavelength-detuning CBET mitigation experiments on the NIF with a modest wavelength difference between crossing beams confirmed improved

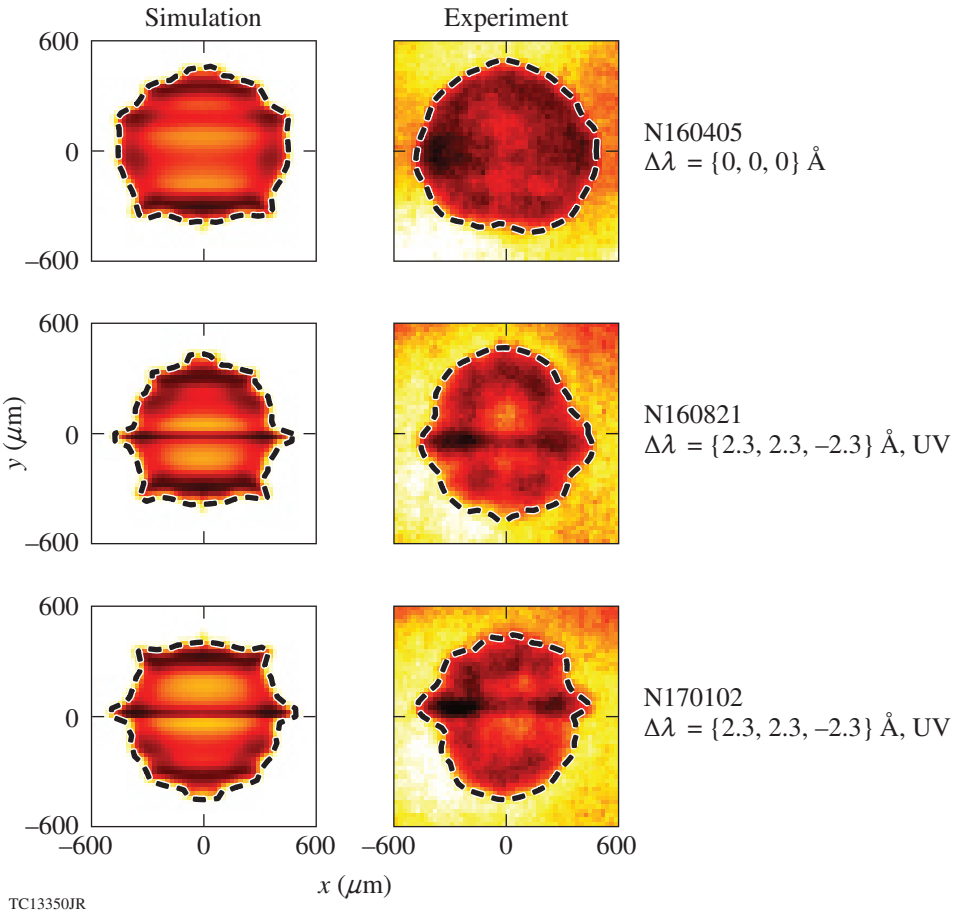

Figure 152.4
Comparison of backlit radiographs from post-shot *DRACO* simulations and NIF experimental results near the end of the laser pulse at $t = 8.5$ ns. The dashed lines indicate the outer shell surface extracted from each image defined by the steepest gradient in the inward radial direction.

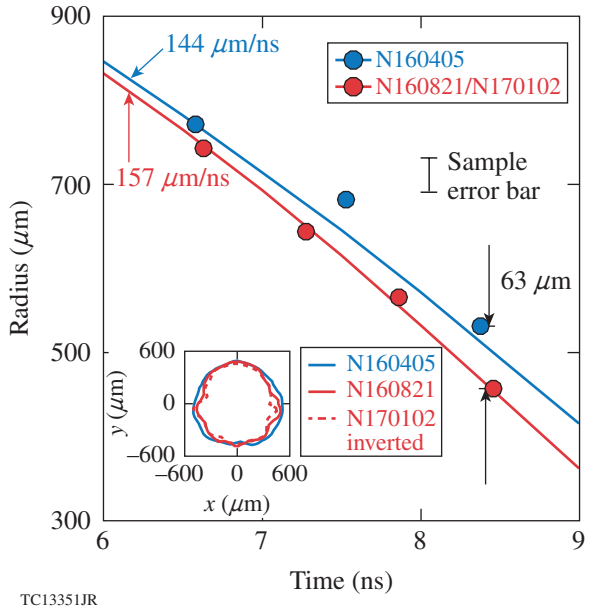

Figure 152.5
Equatorial shell trajectories from post-processed simulated (solid lines) and experimental (symbols) backlit radiographs. The red lines/symbols represent the baseline zero-detuning experiment (N160405). The blue lines/symbols represent the average of the two detuning experiments (N160821 and N170102). The inset shows superimposed extracted surfaces from the experimental radiographs of Fig. 152.4, exemplifying the equatorial mitigation.

coupling predicted by multidimensional hydrodynamic simulations. These direct-drive proof-of-principle experiments are the first such experiments and provide a path forward to recovering the energy loss caused by CBET. Simulations predict that as the wavelength separation increases (e.g., the ±6-Å UV predicted NIF limit), the equatorial drive continues to improve and requires rebalancing to minimize $\ell = 2$. Simulations also indicate that judicious use of all three colors with flexible color-mapping in the fiber front end on the NIF produces better-balanced CBET mitigation designs in PDD. Simulations predict that symmetric direct drive on OMEGA will benefit from wavelength detuning since its three main driver legs already distribute evenly over the target. Additional CBET mitigation domains may be combined with wavelength detuning, e.g., optimized spot shapes that reduce the laser energy refracting over the horizon while maintaining optimal shape [spot-masking apodization (SMA)[20]]. Future experiments are planned to scope out the capabilities of wavelength-detuning CBET mitigation to further improve coupling and to address the asymmetry by proposing system changes to both OMEGA and the NIF: adding multiple wavelength sources to OMEGA, expanding the NIF's wavelength-detuning range, using SMA-DPP's, different wavelengths within NIF's quads, and remapping the NIF fiber front end to obviate cone swapping.

ACKNOWLEDGMENT

This material is based upon work supported by the Department of Energy National Nuclear Security Administration under Award Number DE-NA0001944, the University of Rochester, and the New York State Energy Research and Development Authority.

REFERENCES

1. M. C. Herrmann, M. Tabak, and J. D. Lindl, Nucl. Fusion **41**, 99 (2001).
2. C. J. Randall, J. R. Albritton, and J. J. Thomson, Phys. Fluids **24**, 1474 (1981).
3. T. R. Boehly, D. L. Brown, R. S. Craxton, R. L. Keck, J. P. Knauer, J. H. Kelly, T. J. Kessler, S. A. Kumpan, S. J. Loucks, S. A. Letzring, F. J. Marshall, R. L. McCrory, S. F. B. Morse, W. Seka, J. M. Soures, and C. P. Verdon, Opt. Commun. **133**, 495 (1997).
4. E. M. Campbell and W. J. Hogan, Plasma Phys. Control. Fusion **41**, B39 (1999).
5. C. J. McKinstrie, J. S. Li, R. E. Giacone, and H. X. Vu, Phys. Plasmas **3**, 2686 (1996).
6. C. J. McKinstrie *et al.*, Phys. Plasmas **5**, 1142 (1998).
7. P. B. Radha, M. Hohenberger, D. H. Edgell, J. A. Marozas, F. J. Marshall, D. T. Michel, M. J. Rosenberg, W. Seka, A. Shvydky, T. R. Boehly, T. J. B. Collins, E. M. Campbell, R. S. Craxton, J. A. Delettrez, S. N. Dixit, J. A. Frenje, D. H. Froula, V. N. Goncharov, S. X. Hu, J. P. Knauer, R. L. McCrory, P. W. McKenty, D. D. Meyerhofer, J. Moody, J. F. Myatt, R. D. Petrasso, S. P. Regan, T. C. Sangster, H. Sio, S. Skupsky, and A. Zylstra, Phys. Plasmas **23**, 056305 (2016).
8. M. Hohenberger, P. B. Radha, J. F. Myatt, S. LePape, J. A. Marozas, F. J. Marshall, D. T. Michel, S. P. Regan, W. Seka, A. Shvydky, T. C. Sangster, J. W. Bates, R. Betti, T. R. Boehly, M. J. Bonino, D. T. Casey, T. J. B. Collins, R. S. Craxton, J. A. Delettrez, D. H. Edgell, R. Epstein, G. Fiksel, P. Fitzsimmons, J. A. Frenje, D. H. Froula, V. N. Goncharov, D. R. Harding, D. H. Kalantar, M. Karasik, T. J. Kessler, J. D. Kilkenny, J. P. Knauer, C. Kurz, M. Lafon, K. N. LaFortune, B. J. MacGowan, A. J. Mackinnon, A. G. MacPhee, R. L. McCrory, P. W. McKenty, J. F. Meeker, D. D. Meyerhofer, S. R. Nagel, A. Nikroo, S. Obenschain, R. D. Petrasso, J. E. Ralph, H. G. Rinderknecht, M. J. Rosenberg, A. J. Schmitt, R. J. Wallace, J. Weaver, C. Widmayer, S. Skupsky, A. A. Solodov, C. Stoeckl, B. Yaakobi, and J. D. Zuegel, Phys. Plasmas **22**, 056308 (2015).
9. D. Cao, G. Moses, and J. Delettrez, Phys. Plasmas **22**, 082308 (2015).
10. J. Delettrez, R. Epstein, M. C. Richardson, P. A. Jaanimagi, and B. L. Henke, Phys. Rev. A **36**, 3926 (1987).
11. P. B. Radha, V. N. Goncharov, T. J. B. Collins, J. A. Delettrez, Y. Elbaz, V. Yu. Glebov, R. L. Keck, D. E. Keller, J. P. Knauer, J. A. Marozas, F. J. Marshall, P. W. McKenty, D. D. Meyerhofer, S. P. Regan, T. C. Sangster,

D. Shvarts, S. Skupsky, Y. Srebro, R. P. J. Town, and C. Stoeckl, Phys. Plasmas **12**, 032702 (2005).

12. V. N. Goncharov, T. C. Sangster, R. Betti, T. R. Boehly, M. J. Bonino, T. J. B. Collins, R. S. Craxton, J. A. Delettrez, D. H. Edgell, R. Epstein, R. K. Follet, C. J. Forrest, D. H. Froula, V. Yu. Glebov, D. R. Harding, R. J. Henchen, S. X. Hu, I. V. Igumenshchev, R. Janezic, J. H. Kelly, T. J. Kessler, T. Z. Kosc, S. J. Loucks, J. A. Marozas, F. J. Marshall, A. V. Maximov, R. L. McCrory, P. W. McKenty, D. D. Meyerhofer, D. T. Michel, J. F. Myatt, R. Nora, P. B. Radha, S. P. Regan, W. Seka, W. T. Shmayda, R. W. Short, A. Shvydky, S. Skupsky, C. Stoeckl, B. Yaakobi, J. A. Frenje, M. Gatu-Johnson, R. D. Petrasso, and D. T. Casey, Phys. Plasmas **21**, 056315 (2014).

13. P. Michel *et al*., Phys. Plasmas **16**, 042702 (2009).

14. I. V. Igumenshchev, W. Seka, D. H. Edgell, D. T. Michel, D. H. Froula, V. N. Goncharov, R. S. Craxton, L. Divol, R. Epstein, R. Follett, J. H. Kelly, T. Z. Kosc, A. V. Maximov, R. L. McCrory, D. D. Meyerhofer, P. Michel, J. F. Myatt, T. C. Sangster, A. Shvydky, S. Skupsky, and C. Stoeckl, Phys. Plasmas **19**, 056314 (2012).

15. M. L. Spaeth *et al*., Fusion Sci. Technol. **69**, 25 (2016).

16. S. Skupsky, J. A. Marozas, R. S. Craxton, R. Betti, T. J. B. Collins, J. A. Delettrez, V. N. Goncharov, P. W. McKenty, P. B. Radha, T. R. Boehly, J. P. Knauer, F. J. Marshall, D. R. Harding, J. D. Kilkenny, D. D. Meyerhofer, T. C. Sangster, and R. L. McCrory, Phys. Plasmas **11**, 2763 (2004).

17. J. A. Marozas, F. J. Marshall, R. S. Craxton, I. V. Igumenshchev, S. Skupsky, M. J. Bonino, T. J. B. Collins, R. Epstein, V. Yu. Glebov, D. Jacobs-Perkins, J. P. Knauer, R. L. McCrory, P. W. McKenty, D. D. Meyerhofer, S. G. Noyes, P. B. Radha, T. C. Sangster, W. Seka, and V. A. Smalyuk, Phys. Plasmas **13**, 056311 (2006).

18. J. A. Marozas, T. J. B. Collins, D. H. Edgell, I. V. Igumenshchev, and J. F. Myatt, Bull. Am. Phys. Soc. **56**, 241 (2011).

19. Concept initially presented by J. A. Marozas, T. J. B. Collins, J. D. Zuegel, P. B. Radha, F. J. Marshall, and W. Seka, presented at the 44th Annual Anomalous Absorption Conference, Estes Park, CO, 8–13 June 2014.

20. J. A. Marozas, T. J. B. Collins, J. D. Zuegel, P. W. McKenty, D. Cao, S. Fochs, and P. B. Radha, J. Phys.: Conf. Ser. **717**, 012107 (2016).

21. Inspired by Anishinaabe word *Adaawam*, meaning "to borrow something from someone," to describe the cross-beam energy transfer (CBET), just as energy is borrowed from one beam to another. Resource: J. D. Nichols and E. Nyholm, *A Concise Dictionary of Minnesota Ojibwe* (University of Minnesota, Minneapolis, 1995).

22. Inspired by Anishinaabe word *Mazinisin*, meaning "be imprinted, have a design," to describe laser energy deposition just as the laser imprints on and changes target morphology. Resource: J. D. Nichols and E. Nyholm, *A Concise Dictionary of Minnesota Ojibwe* (University of Minnesota, Minneapolis, 1995).

23. S. X. Hu, D. T. Michel, A. K. Davis, R. Betti, P. B. Radha, E. M. Campbell, D. H. Froula, and C. Stoeckl, Phys. Plasmas **23**, 102701 (2016).

24. T. P. Gill, *The Doppler Effect: An Introduction to the Theory of the Effect* (Logos, London, 1965).

25. J. J. MacFarlane *et al*., High Energy Density Phys. **3**, 181 (2007).

Mitigation of Cross-Beam Energy Transfer in Ignition-Scale Polar-Direct-Drive Target Designs for the National Ignition Facility

In inertial confinement fusion (ICF), a high-powered laser-driven ablation process is used to implode a spherical shell composed largely of fuel [approximately equimolar deuterium (D) and tritium (T)], producing a central volume (the "hot spot") of high density and ion temperature. In the "direct-drive" scheme, the ablation is accomplished by direct illumination of the target using a spherical distribution of short-wavelength ($\lambda \lesssim 351$-nm) UV laser beams. The inertially confined fuel ions rapidly undergo fusion reactions, producing 3.5-MeV alpha particles, some of which are stopped in both the central region and the surrounding dense DT shell. Ignition occurs when these alpha particles deposit enough energy to launch a thermonuclear burn wave, consuming a fraction of the fuel (depending on the imploded fuel's total areal density) before the high pressure generated by the burn wave causes the target to disassemble. Ignition is predicted to occur if the fuel's internal energy exceeds a minimum value,[1]

$$E_{\min} \approx (50.8\ \text{kJ})\,\alpha_{\text{in}}^{1.88}\left(v_{\text{imp}}\big/ 300\ \text{km/s}\right)^{-5.89} \times \left(P/100\ \text{Mbar}\right)^{-0.77}, \quad (1)$$

where α_{in} is the ratio of the pressure to the Fermi-degenerate fuel pressure (the "adiabat") in the dense DT shell, v_{imp} is the peak shell implosion speed, and P is the ablation pressure. The direct-drive approach is of interest because, for the same incident laser energy, it couples ~3 to 5× more energy into the imploding capsule than indirect drive, enabling more fuel mass to be imploded and lowering the threshold on hot-spot energy $E_{\min}$ as well as the pressure and, therefore, convergence. Note that the threshold energy $E_{\min}$ in Eq. (1) depends sensitively on the implosion speed, which in turn is directly related to the energy coupled to the ablating shell.

Ignition and total fusion yield are directly connected to the volume of the hot spot, the central region in which the temperatures and densities are sufficient to initiate fusion reactions. This volume is reduced by perturbations on the inner edge of the shell that are seeded by a number of sources, including laser-drive nonuniformities and target imperfections, and grow as a result of the Rayleigh–Taylor instability as the shell is decelerated by the pressure of the interior gas.[2] As this volume is reduced, so is the energy coupled to the hot spot. Deviations from 1-D implosions can also result in incomplete stagnation, producing residual kinetic energy and reduced hot-spot pressure. In its current configuration, the laser beam ports at the National Ignition Facility (NIF)[3] are preferentially distributed toward the poles of the target chamber, designed primarily for use with x-ray–driven targets enclosed in a hohlraum. Direct-drive implosions using this configuration ["polar direct drive" (PDD)[4,5]] require beam repointing to compensate for the lack of equatorial beams and higher incident angles in the equatorial region.

In order to credibly design PDD targets, it is critical to incorporate the important physics in the simulations. Laser direct-drive experiments on OMEGA[6] and the NIF[7–9] have demonstrated that it is necessary to model both cross-beam energy transfer (CBET) and nonlocal electron heat transport. CBET is seeded stimulated Brillouin scattering (SBS) in which two beams interact by means of an intermediate ion-acoustic wave,[10] increasing the scattered light, reducing the ablation pressure, and decreasing energy coupling and shell velocity (especially in the equatorial region for PDD targets). Nonlocal electrons in the corona, by contrast, increase the conversion efficiency of laser energy to shell kinetic energy by means of their larger mean free paths and more-effective transport. These effects have been observed to be important in the modeling of numerous implosion experiments at comparable laser intensities on OMEGA.[11,12] While nonlocal electron transport can increase the hydrodynamic efficiency of the implosion, CBET scatters a sizable fraction (~20% to 30%) of the incident laser energy, reducing both P and v_{imp} and raising $E_{\min}$. The magnitude of these combined effects is illustrated in Fig. 152.6, where the ablation pressure and shell speed are shown as a function of wavelength-detuning separation, $\Delta\lambda$. The $\Delta\lambda = 0$ limit indicates the effects of unmitigated CBET, compared with the much higher drive pressure and shell speed that can be achieved when CBET is mitigated by means of wavelength detuning, as described below.

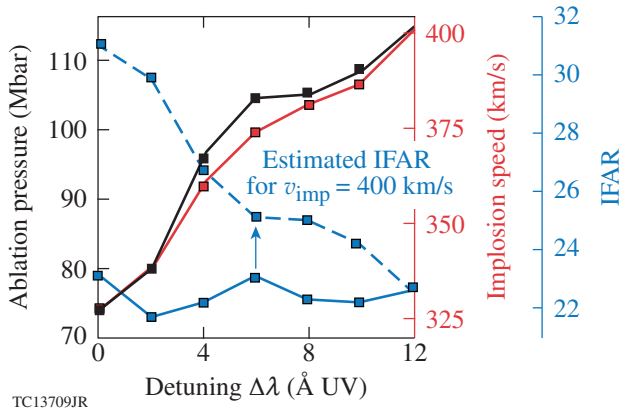

Figure 152.6
The ablation pressure and implosion speed are shown for the ignition design as functions of wavelength-detuning separation. Also shown (dashed line) is the approximate in-flight aspect ratio (IFAR) expected for a shell with mass reduced by the amount needed to recover the original 400-km/s implosion speed.

The two PDD designs presented in this article—the alpha-burning design and the lower-adiabat ignition design—address the twin constraints of sufficient shell kinetic energy and implosion uniformity. These are the first ignition-scale direct-drive designs of any dimensionality to include the effects of nonlocal heat transport and CBET. Previous ignition designs did not incorporate this important physics and modeled these processes in an approximate way by using an *ad hoc* flux limiter applied to the classical expression for heat conduction.[13] In these designs, the loss of drive related to CBET is mitigated by detuning the laser-beam wavelengths relative to one another.[14,15] As with previous PDD designs for the NIF, the drive asymmetries caused by the disposition of the beams are controlled through a combination of independent pulse shapes for different groups of beams, tailored laser beam spot shapes, and beam repointing. The alpha burner has a shell adiabat of almost 5 for greater hydrodynamic stability. In a simulation that models only drive perturbations caused by beam geometry, the alpha burner is predicted to generate bootstrap heating with a yield enhancement of 5× by means of alpha deposition, producing over 10^{17} fusion neutrons. The lower-adiabat ignition design (~3) achieves a gain close to 30.

PDD designs have seen vast improvement since the original concept was first proposed by Skupsky *et al.*[4] While that earlier design was not capable of ignition, it included components that have been used in most other laser PDD designs: use of different pulse shapes for different laser beams, repointing of beams toward the equatorial region of the target, and equatorial spot shapes that concentrate energy toward the equator. Each of these components compensates for the reduction in equatorial ablative drive because of the greater angles of incidence and resulting energy deposition at lower densities for the laser light driving that region. Marozas *et al.*[5] presented the first igniting PDD design. Their design improved on the earlier design by using an automated tuning process for the pulse shape designs. Reference 5 also presented a general process for tuning PDD designs and demonstrated the importance of the time dependence of the relative beam-group energies. Their design also made use of spot shapes apertured by a high-order super-Gaussian envelope, reducing the amount of energy flowing around the target [spot-masking apodization (SMA)[5,16]]. The first design to use a shell of DT ice with a CH ablator rather than a foam/DT shell was that of Collins *et al.*[17] It also applied the previously introduced beam conditioning through smoothing by spectral dispersion (SSD),[18] employing multiple-frequency modulators[19] applied selectively prior to the main "drive" portion of the laser pulse.[20] The more-recent designs of Lafon *et al.*[21] use ablators composed of mid-*Z* elements to reduce perturbation growth resulting from laser imprint by increasing the size of the conduction zones between the laser absorption and ablation regions. PDD designs have also been developed for the shock-ignition scheme,[22] in which a high-intensity laser spike at the end of the drive pulse drives a strong shock, thereby initiating ignition.[23,24] These designs do not include any mechanism for mitigating CBET, nor do they model nonlocal electron heat transport; the work presented in this article includes the first such designs. Finally, an intermediate-energy PDD detuning design for CBET mitigation has been fielded for the first time on the NIF, demonstrating the effectiveness of this approach and exploring the physical mechanism of wavelength detuning.[15] Observables such as the shapes and trajectories of the in-flight shell inferred through radiographs are well modeled with the CBET model described below. These validated models are used in the designs presented in this work.

The consistent result of each of these investigations is that the low equatorial drive can be successfully compensated for in a number of ways. The design of Collins *et al.*[17] is the basis of the designs described here, which employs equatorial pulses with 50%-higher power (within the NIF laser performance envelope) than the polar beams, repoints beams toward the equator, and uses SMA to offset the loss of equatorial drive caused by PDD.

For direct-drive targets of sufficient density scale length and laser intensity, the SBS process responsible for CBET is dynamically important. As mentioned above, this process entails the parametric coupling of incident light with an ion-acoustic wave and a backscattered electromagnetic wave. The efficiency

of energy transfer is determined by a resonance function of the parameter $\eta = \left[\left(\omega_{\text{pump}} - \omega_{\text{probe}}\right) - \mathbf{k}_a \cdot \mathbf{v}\right] \big/ \left(c_a k_a\right)$, where ω_{pump} and ω_{probe} are the ray frequencies of the beams losing and gaining energy, respectively; c_a is the outflow sound speed; $\mathbf{k}_a = \mathbf{k}_{\text{pump}} - \mathbf{k}_{\text{probe}}$ is the ion-acoustic wave vector; and $\mathbf{v}$ is the outflow plasma velocity. Energy transfer from the incoming ray to the outgoing ray occurs as $\eta > 0$ is satisfied in backscatter mode under normal circumstances.[15] CBET is well known in indirect-drive ICF experiments on the NIF, where it has been used to transfer energy between cones of beams to affect low-mode capsule symmetry by means of wavelength detuning,[25] but this forward-scatter mode is unimportant for direct drive.[15] In direct-drive ICF, CBET backscatter typically occurs when an outbound ray is refracted into the path of the central, high-energy region of an inbound beam and the ion-acoustic phase-matching conditions are near resonance. The energy transferred between beams by CBET over a distance ds attenuates the incident laser light by $1 - e^{-\mathrm{d}\tau}$, where $\mathrm{d}\tau_{\text{CBET}} \propto \zeta_{\text{pol}} P(\eta) I_{\text{pump}} \mathrm{d}s$, the resonance function is given by $P(\eta) = \eta \cdot v_a \big/ \left[(\eta v_a)^2 + (1 - \eta^2)^2\right]$, and I_{pump} is the intensity of the "pump" beam. Reduction in energy transfer caused by mismatched inbound–outbound polarization is represented by the factor ζ_{pol}.

CBET is particularly effective at scattering energy from incoming rays and significantly reducing ablation pressure because the matching condition can be met over a large volume, where $|\eta| \approx 1$ and the resonance function $P(\eta)$ peaks. Consider this region in the absence of wavelength detuning: the shift in a ray's frequency resulting from the changing plasma refractive index n_r is small enough that $\omega_{\text{pump}} \approx \omega_{\text{probe}}$ (Ref. 26). The mass flow in the corona is nearly radial, so CBET backscatter is greatest in a region where $M\mathbf{k}_a \cdot \mathbf{r} \equiv M\cos\theta_a \approx 1$ (where M is the flow Mach number and θ_a is the angle between $\mathbf{k}_a$ and $\mathbf{r}$). This region is largely exterior to the Mach-1 surface where, as M increases radially outward, θ_a decreases so the product is still approximately unity. As a result of the beam angles in the PDD configuration and the lack of usable equatorial beam ports, this resonance region occurs preferentially over the equator where repointed beams from each hemisphere overlap. The CBET power density during the drive pulse for the ignition design, but without detuning, is plotted in Fig. 152.7(a). Note that the CBET power density includes the transferred power resulting from both sidescatter between incoming rays, which has little effect on the target drive, and backscatter between inbound and outbound rays, which is of primary interest here.

The target designs presented here were simulated using the 2-D radiation hydrocode *DRACO*.[27] *DRACO* uses a 3-D ray-based inverse bremsstrahlung energy deposition model

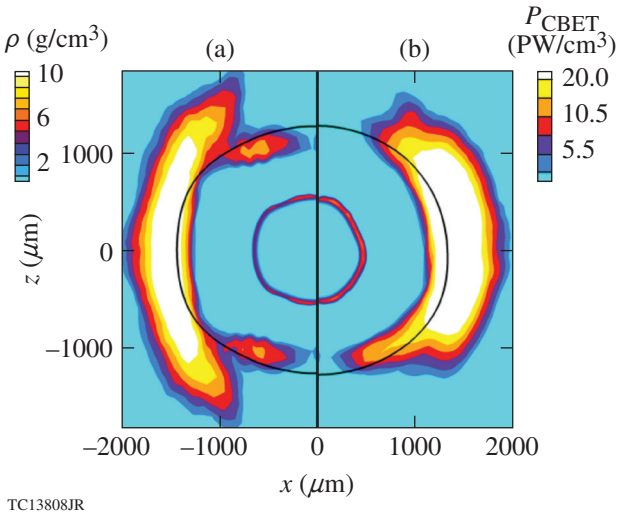

Figure 152.7
The CBET (cross-beam energy transfer) power density during the drive pulse for simulation of the ignition design (a) without wavelength detuning for CBET mitigation and (b) with hemispheric wavelength detuning. With hemispherical detuning, the interaction volume is reduced in extent in the polar angle. The CBET power density includes both backscatter and sidescatter, which accounts for the higher level of power density in (b). The shell mass density is also indicated (with a radius ~500 to 600 μm), showing the greater convergence with wavelength detuning (right). The Mach-1 surface is indicated by the solid black circle.

(*Mazinisin*).[5] The CBET model in *DRACO*, *Adaawam*,[15] uses an angular-spectrum representation (ASR) in which the ASR captures, for each computational zone, the accumulated intensity as a function of direction and color from all the beams that enter that cell, representing the field of pump rays. A pump ray traversing a cell interacts with the other rays, which cross the zones by means of the ASR, using the formalism above. A proportional-integral-differential (PID) predictor–corrector controller iterates until a self-consistent, energy-conserving solution is found. Since the ray-trace approach used in *DRACO* does not presently include the polarization state of the light, random polarization is included by setting $\zeta_{\text{pol}} = (1/4)\left[1 + \left(\hat{\mathbf{k}}_{\text{pump}} \cdot \hat{\mathbf{k}}_{\text{probe}}\right)^2\right]$ (Ref. 28). This model for CBET has been shown to accurately predict the large-scale morphology of implosions on the NIF when a constant multiplier of 1.5 is applied to $\mathrm{d}\tau_{\text{CBET}}$ (Refs. 9 and 15). Since experiments have yet to probe plasma conditions (density scale lengths, flow speeds, and electron temperature) relevant to NIF PDD ignition, the equations above for the attenuation caused by CBET are used here without an *ad hoc* multiplier. Using a 1.5 multiplier would reduce the shell speed and require a redesign of the target and likely a reduction in shell mass and corresponding increase in the IFAR. Simulations indicate it is also possible to compensate for an increase in CBET multiplier

by increasing drive power, even though peak drive power is limited by optics damage considerations.

DRACO uses the implicit Schurtz–Nicolaï–Busquet (iSNB) nonlocal heat-transport model,[29] based on the Schurtz–Nicolaï–Busquet (SNB) model.[30] The SNB model computes the nonlocal heat flux using multigroup diffusion by means of a multidimensional convolution integral, which has the effect of delocalizing the Spitzer–Härm heat flux. The iSNB model improves on SNB by solving the diffusion equations implicitly for improved robustness and numerical accuracy. Because of sensitivity in direct-drive ignition to fast-electron preheat, modified mean free paths are used to bring results closer to predictions by more complex but computationally expensive nonlocal models (e.g., Ref. 11). These mean free paths are such that nonlocal electron thermal transport overwhelmingly affects the drive rather than the fuel adiabat. The iSNB model has demonstrated predictive capability for shock timing[29] and shell shape[31] in numerous experiments on OMEGA.

In the wavelength-detuning approach to CBET mitigation, the laser cavities are detuned slightly for different collections of beams to increase the frequency separation, which in turn alters the region over which the CBET efficiency is greatest. The detuning magnitude considered here for the designs presented here is $\Delta\lambda \pm 12$ Å (UV). Extension of these results to ±6 Å is discussed below. The designs presented here will require modifications to the NIF, including the ability to extend the wavelength tunability of the laser drive and enhanced beam conditioning such as multifrequency-modulated SSD and distributed polarization rotators. Future target designs that mitigate laser beam imprint may reduce or alter the requirements for enhanced beam smoothing. A cryogenic handling system that reduces the time between when the target is extracted from the cryostat and the start of the laser pulse will also be necessary. It should also be recognized that PDD would also enable the use of external magnetic fields that may enhance fusion performance by reducing thermal conduction losses from the hot spot and more efficiently trapping the alpha particles.[32]

If the outgoing probe rays are detuned to shorter wavelengths (blue-shifted) relative to the pump field, the resonance region moves to greater Mach numbers and correspondingly larger radii, where the beam overlap and corresponding energy transfer are reduced.[15] If the probe rays are red-shifted relative to the pump field, the resonance region moves radially inward, reducing the overlap between the resonance region and the region reached by the rays. Figure 152.7(b) shows the CBET power density for the ignition design but with the simpler hemispheric wavelength-detuning configuration. Over time, for red-detuned outgoing rays, this resonance region is exposed,[15] reducing the CBET mitigation.

The effectiveness of this approach depends on the choice of which beam groups to "detune" and by how much. Several detuning configurations were investigated (see Fig. 152.8). The

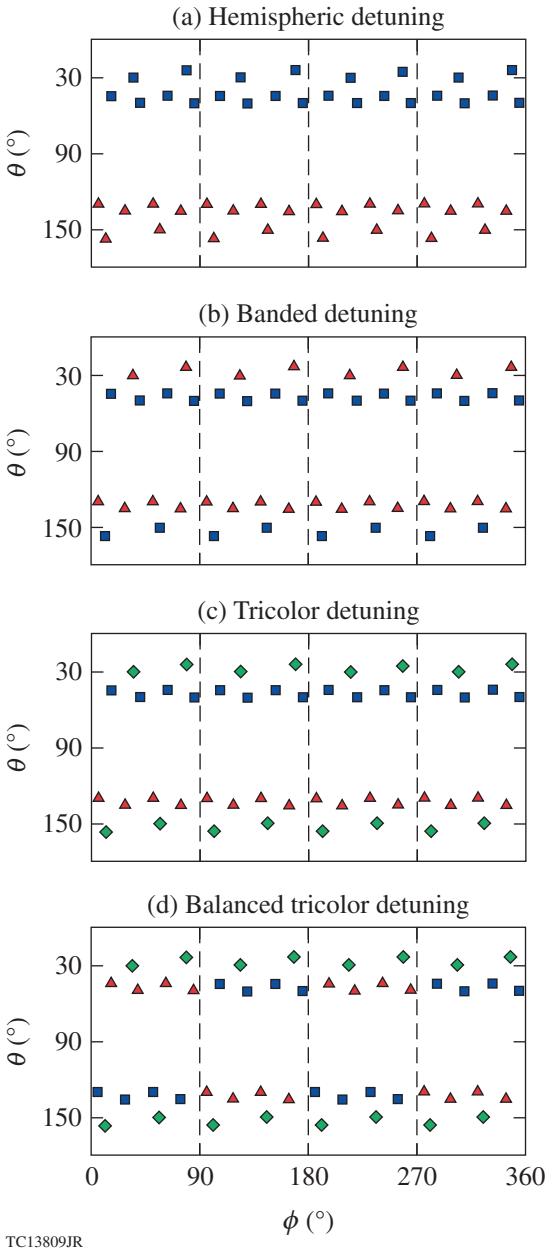

Figure 152.8
Four of the wavelength-detuning configurations explored in this study. The wavelength shift of each port is indicated by the color of the symbols (where green corresponds to a zero wavelength shift).

laser-absorption efficiency for four of these configurations is shown in Fig. 152.9. Per Fig. 152.8, the hemispheric scheme detunes the beams by hemisphere.[14] This scheme greatly reduces the energy loss caused by the beams interacting across the equator, which is where the greatest scattering occurs, but does not reduce losses caused by interactions between beams from the same hemisphere. The beams on the NIF are divided into four cones for each hemisphere: two inner cones nearer the pole and two outer cones nearer the equator. The banded scheme reverses the sign of the detuning for the two inner cones of beams in each hemisphere, thereby increasing the coupling.

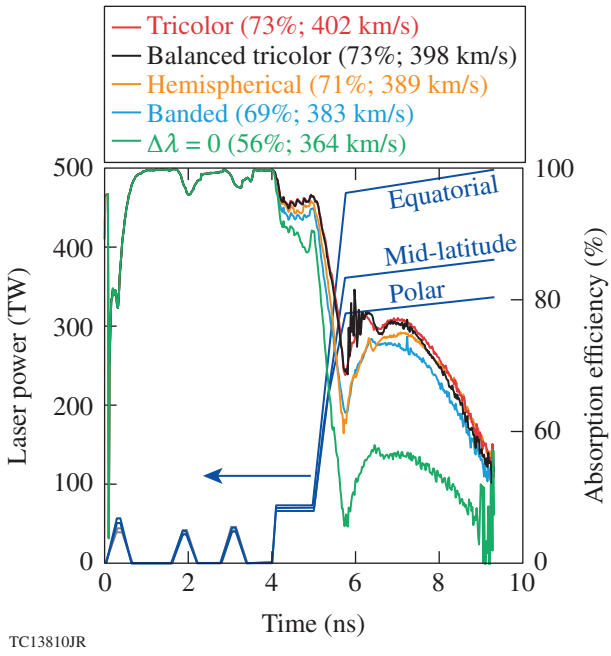

Figure 152.9
Absorption efficiency is shown as a function of time for four detuning configurations for the polar-direct-drive ignition design, modeled by including the effects of CBET and nonlocal electron thermal transport. The case without detuning is also shown. The legend shows the cumulative absorption efficiency as well as the peak implosion speed. Shown in blue are the pulse shapes used in the inner-cone beams (which preferentially illuminate the polar and mid-latitude regions on the target) and the outer-cone (equatorial) beams for the ignition (blue) and alpha-burning (gray, visible only at ~400 ps) designs.

The tricolor configuration improves on both of these by not detuning the inner cones. The tricolor scheme is more effective than the banded scheme because the inner cones interact with both the equatorial beams in the same hemisphere and with the equatorial beams in the opposite hemisphere; by not detuning the inner cones, more energy is regained from the interaction across the equator than is lost to the intrahemispherical interaction. Figure 152.9 also shows the primary effect of nonlocal heat transport: an increase in absorption efficiency, which occurs especially near the equator where the radial thermal gradient is greater. A comparison between the implosions with and without nonlocal heat transport, shows an increase of ~30% in the absorbed laser energy for the tricolor scheme, resulting in a much higher implosion speed. All three of these schemes introduce a north–south asymmetry, as described above. This asymmetry is greatly reduced by using a fourth configuration, balanced tricolor, in which the tricolor scheme is inverted, north to south, in alternating quadrants.[33,34]

The two designs shown here use a 194-μm DT shell with a 36-μm CH ablator and an outer radius of 1482 μm. Each design uses a triple-picket pulse shape to shape the adiabat.[35] The incident laser energy is 1.8 MJ. Both designs achieve a high implosion speed of ~400 μm/ns, sufficient to generate burn-averaged hot-spot pressures of 190 Gbar for the ignition design and 215 Gbar for the alpha burner, which is higher because of the delayed disassembly. It is important to recognize that x-ray–driven implosions on the NIF have achieved inferred hot-spot pressures well in excess of those calculated in these designs.[36] Both designs have moderately low in-flight aspect ratios (IFAR's), given by the maximum ratio during the implosion of the shell radius to its thickness. The IFAR is an indicator of shell stability, with lower values being less unstable.[37] The ignition design has an IFAR of 23 and a minimum end-of-pulse, density-weighted adiabat of 2.8, and the alpha burner has a somewhat lower IFAR of 21 with a larger ablator adiabat, resulting in an end-of-pulse, density-weighted adiabat of 4.8. Both of these IFAR's are lower than that of their flux-limited predecessor,[17] which also used a CH ablator and was calculated to withstand the effects of laser imprint. (The simulations presented here include only nonuniformities related to port geometry, repointing, CBET, and nonlocal heat transport; sensitivity to other illumination nonuniformities, such as beam power imbalance, and to target imperfections will be investigated in the near future.) The higher fuel adiabat of the alpha burner is reflected in a lower hot-spot convergence fuel ratio of 25, compared to 28 for the ignition design, and a lower peak total fuel areal density of 1.4 g/cm^2, compared to 1.7 g/cm^2 for the ignition design. The ion temperature and density of these designs are shown around the time of peak convergence in Fig. 152.10. The alpha burner achieves a total neutron yield of 1.2×10^{17} (~320 kJ of fusion energy) and the ignition design achieves a yield of 1.8×10^{19}, with 1.8 MJ of incident energy, for a gain of 27. While the alpha burner does not ignite, it operates at a moderate adiabat for acceleration-phase stability, and the neutrons generated by bootstrap heating are over 5× that generated by compression alone. Since this design

lacks an "ignition cliff," it is also less sensitive to drive and target nonuniformities, making this design an ideal platform for initial study; initial estimates suggest the neutron yield for the alpha burner varies approximately linearly with the implosion speed, rather than the much-steeper dependence of an ignition design.

The use of a $\Delta\lambda = \pm 12$ Å (UV) detuning bandwidth would require significant modifications to the NIF laser chain as presently understood. It may be possible, however, to obtain ignition-relevant hot-spot conditions for lower values of $\Delta\lambda$. Figure 152.6 shows, for the ignition design, the dependence of ablation pressure and implosion speed on $\Delta\lambda$. (The pointing and detuning configurations are held constant.) The volume over which CBET is active changes as $\Delta\lambda$ is varied; this is the most likely cause of the second-order nonlinearities in the dependence on $\Delta\lambda$. This plot makes clear the effectiveness of detuning as a mitigation scheme; detuning by ±12 Å increases the drive pressure by over 50% and the implosion speed by ~10%. As expected, the CBET efficiency increases as $\Delta\lambda$ decreases, reducing the coupling and raising $E_{\min}$. This reduction in coupling may, in principle, be offset by a reduction in fuel mass at the cost of increased IFAR. Figure 152.6 also shows the IFAR that would result from reducing the fuel mass in order to obtain the original shell speed of 400 km/s. Reducing $\Delta\lambda$ to ±6 Å corresponds to an increase in the IFAR from 23 to 25 and may require greater beam smoothing to achieve ignition. However, the alpha burner is already on a high shell adiabat and is less sensitive to imprint. Development of a PDD alpha burner with a thinner shell and $\Delta\lambda = \pm 6$ Å is a natural next step.

The two designs presented here—the first of their kind—demonstrate a promising approach to generating high-energy densities on the NIF and offer a useful research platform for ICF ignition. These designs have peak equatorial intensities of $\sim 1.4 \times 10^{15}$ W/cm^2 and are likely to experience some degree of fast-electron preheat because of two-plasmon decay and stimulated Raman scattering. A solution for this preheat has already been proposed and will be explored, in which the ablator is doped with mid-Z elements, in order to raise the electron temperature and the instability threshold and increase absorption efficiency.[9,21,38] This is likely to be far less of a design issue for the alpha burner, which already operates on a high adiabat. This is, in part, because of the lack of the ignition cliff mentioned above. It is also true because an increase of $\Delta\alpha = 1$ (where α is the adiabat) is a $\delta\ln\alpha = 50\%$ increase for an $\alpha = 2$ ignition design but only a $\delta\ln\alpha = 20\%$ increase for an $\alpha = 5$ alpha burner, and the factional increase in hot-spot pressure (in the absence of alpha heating, which is relevant for achieving ignition-scale conditions needed for both target designs) is $\delta\ln p_{\rm hs} \approx -0.9\,\delta\ln\alpha$ (Ref. 22), where $p_{\rm hs}$ is the hot-spot pressure. Furthermore, the designs presented here are modeled in 2-D, although nonaxisymmetric perturbations are expected from both the laser-port geometry (which introduces a perturbation with azimuthal mode number $m = 4$) and the detuning configuration ($m = 2$). While these low modes may be compensated by using azimuthal target "shimming,"[39,40] other detuning configurations that do not introduce nonaxisymmetric modes are also being developed. As mentioned above, an embedded external magnetic field may also improve the target performance.

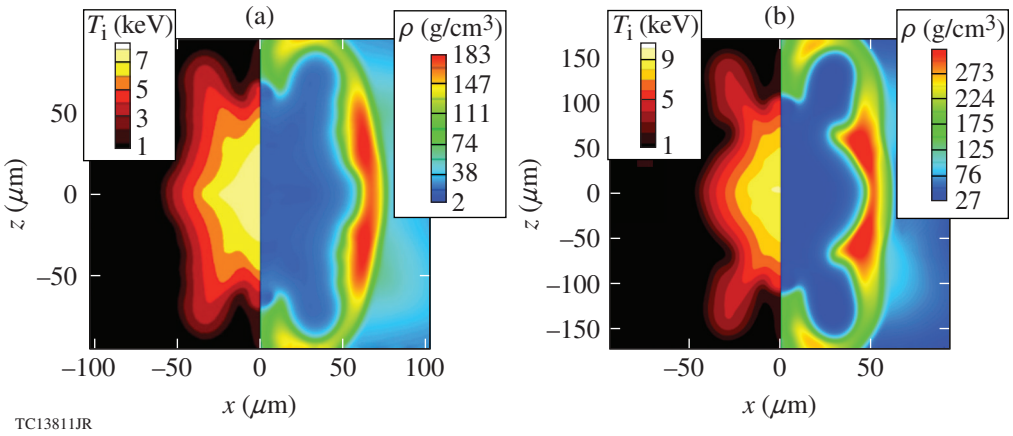

Figure 152.10
(a) The alpha-burning and (b) ignition designs are shown near peak compression. On the left of each contour plot is the ion temperature and on the right is the mass density.

ACKNOWLEDGMENT

The authors thank S. Skupsky, K. Anderson, and J. Delettrez for useful discussions during the development of these designs. This material is based upon work supported by the Department of Energy National Nuclear Security Administration under Award Number DE-NA0001944, the University of Rochester, and the New York State Energy Research and Development Authority.

REFERENCES

1. M. C. Herrmann, M. Tabak, and J. D. Lindl, Nucl. Fusion **41**, 99 (2001).

2. E. M. Campbell, V. N. Goncharov, T. C. Sangster, S. P. Regan, P. B. Radha, R. Betti, J. F. Myatt, D. H. Froula, M. J. Rosenberg, I. V. Igumenshchev, W. Seka, A. A. Solodov, A. V. Maximov, J. A. Marozas, T. J. B. Collins, D. Turnbull, F. J. Marshall, A. Shvydky, J. P. Knauer, R. L. McCrory, A. B. Sefkow, M. Hohenberger, P. A. Michel, T. Chapman, L. Masse, C. Goyon, S. Ross, J. W. Bates, M. Karasik, J. Oh, J. Weaver, A. J. Schmitt, K. Obenschain, S. P. Obenschain, S. Reyes, and B. Van Wonterghem, Matter and Radiation at Extremes **2**, 37 (2017).

3. E. M. Campbell and W. J. Hogan, Plasma Phys. Control. Fusion **41**, B39 (1999).

4. S. Skupsky, J. A. Marozas, R. S. Craxton, R. Betti, T. J. B. Collins, J. A. Delettrez, V. N. Goncharov, P. W. McKenty, P. B. Radha, T. R. Boehly, J. P. Knauer, F. J. Marshall, D. R. Harding, J. D. Kilkenny, D. D. Meyerhofer, T. C. Sangster, and R. L. McCrory, Phys. Plasmas **11**, 2763 (2004).

5. J. A. Marozas, F. J. Marshall, R. S. Craxton, I. V. Igumenshchev, S. Skupsky, M. J. Bonino, T. J. B. Collins, R. Epstein, V. Yu. Glebov, D. Jacobs-Perkins, J. P. Knauer, R. L. McCrory, P. W. McKenty, D. D. Meyerhofer, S. G. Noyes, P. B. Radha, T. C. Sangster, W. Seka, and V. A. Smalyuk, Phys. Plasmas **13**, 056311 (2006).

6. V. N. Goncharov, S. P. Regan, E. M. Campbell, T. C. Sangster, P. B. Radha, J. F. Myatt, D. H. Froula, R. Betti, T. R. Boehly, J. A. Delettrez, D. H. Edgell, R. Epstein, C. J. Forrest, V. Yu. Glebov, D. R. Harding, S. X. Hu, I. V. Igumenshchev, F. J. Marshall, R. L. McCrory, D. T. Michel, W. Seka, A. Shvydky, C. Stoeckl, W. Theobald, and M. Gatu-Johnson, Plasma Phys. Control. Fusion **59**, 014008 (2017).

7. T. J. Murphy, N. S. Krasheninnikova, G. A. Kyrala, P. A. Bradley, J. A. Baumgaertel, J. A. Cobble, P. Hakel, S. C. Hsu, J. L. Kline, D. S. Montgomery, K. A. D. Obrey, R. C. Shah, I. L. Tregillis, M. J. Schmitt, R. J. Kanzleiter, S. H. Batha, R. J. Wallace, S. D. Bhandarkar, P. Fitzsimmons, M. L. Hoppe, A. Nikroo, M. Hohenberger, P. W. McKenty, H. G. Rinderknecht, M. J. Rosenberg, and R. D. Petrasso, Phys. Plasmas **22**, 092707 (2015).

8. M. Hohenberger, P. B. Radha, J. F. Myatt, S. LePape, J. A. Marozas, F. J. Marshall, D. T. Michel, S. P. Regan, W. Seka, A. Shvydky, T. C. Sangster, J. W. Bates, R. Betti, T. R. Boehly, M. J. Bonino, D. T. Casey, T. J. B. Collins, R. S. Craxton, J. A. Delettrez, D. H. Edgell, R. Epstein, G. Fiksel, P. Fitzsimmons, J. A. Frenje, D. H. Froula, V. N. Goncharov, D. R. Harding, D. H. Kalantar, M. Karasik, T. J. Kessler, J. D. Kilkenny, J. P. Knauer, C. Kurz, M. Lafon, K. N. LaFortune, B. J. MacGowan, A. J. Mackinnon, A. G. MacPhee, R. L. McCrory, P. W. McKenty, J. F. Meeker, D. D. Meyerhofer, S. R. Nagel, A. Nikroo, S. Obenschain, R. D. Petrasso, J. E. Ralph, H. G. Rinderknecht, M. J. Rosenberg, A. J. Schmitt, R. J. Wallace, J. Weaver, C. Widmayer, S. Skupsky, A. A. Solodov, C. Stoeckl, B. Yaakobi, and J. D. Zuegel, Phys. Plasmas **22**, 056308 (2015).

9. P. B. Radha, M. Hohenberger, D. H. Edgell, J. A. Marozas, F. J. Marshall, D. T. Michel, M. J. Rosenberg, W. Seka, A. Shvydky, T. R. Boehly, T. J. B. Collins, E. M. Campbell, R. S. Craxton, J. A. Delettrez, S. N. Dixit, J. A. Frenje, D. H. Froula, V. N. Goncharov, S. X. Hu, J. P. Knauer, R. L. McCrory, P. W. McKenty, D. D. Meyerhofer, J. Moody, J. F. Myatt, R. D. Petrasso, S. P. Regan, T. C. Sangster, H. Sio, S. Skupsky, and A. Zylstra, Phys. Plasmas **23**, 056305 (2016).

10. C. J. Randall, J. R. Albritton, and J. J. Thomson, Phys. Fluids **24**, 1474 (1981).

11. V. N. Goncharov, O. V. Gotchev, E. Vianello, T. R. Boehly, J. P. Knauer, P. W. McKenty, P. B. Radha, S. P. Regan, T. C. Sangster, S. Skupsky, V. A. Smalyuk, R. Betti, R. L. McCrory, D. D. Meyerhofer, and C. Cherfils-Clérouin, Phys. Plasmas **13**, 012702 (2006).

12. V. N. Goncharov, T. C. Sangster, R. Betti, T. R. Boehly, M. J. Bonino, T. J. B. Collins, R. S. Craxton, J. A. Delettrez, D. H. Edgell, R. Epstein, R. K. Follet, C. J. Forrest, D. H. Froula, V. Yu. Glebov, D. R. Harding, R. J. Henchen, S. X. Hu, I. V. Igumenshchev, R. Janezic, J. H. Kelly, T. J. Kessler, T. Z. Kosc, S. J. Loucks, J. A. Marozas, F. J. Marshall, A. V. Maximov, R. L. McCrory, P. W. McKenty, D. D. Meyerhofer, D. T. Michel, J. F. Myatt, R. Nora, P. B. Radha, S. P. Regan, W. Seka, W. T. Shmayda, R. W. Short, A. Shvydky, S. Skupsky, C. Stoeckl, B. Yaakobi, J. A. Frenje, M. Gatu-Johnson, R. D. Petrasso, and D. T. Casey, Phys. Plasmas **21**, 056315 (2014).

13. W. L. Kruer, in *The Physics of Laser Plasma Interactions*, Frontiers in Physics, Vol. 73, edited by D. Pines (Westview, Boulder, CO, 2003).

14. J. A. Marozas, T. J. B. Collins, J. D. Zuegel, P. B. Radha, F. J. Marshall, and W. Seka, presented at the 44th Annual Anomalous Absorption Conference, Estes Park, CO, 8–13 June 2014.

15. J. A. Marozas, M. Hohenberger, M. J. Rosenberg, D. Turnbull, T. J. B. Collins, P. B. Radha, P. W. McKenty, J. D. Zuegel, F. J. Marshall, S. P. Regan, T. C. Sangster, W. Seka, E. M. Campbell, V. N. Goncharov, M. W. Bowers, J.-M. G. DiNicola, G. Erbert, B. J. MacGowan, L. J. Pelz, and S. T. Yang, "First Observation of Cross-Beam Energy Transfer Mitigation for Direct-Drive Inertial Confinement Fusion Implosions Using Wavelength Detuning at the National Ignition Facility," submitted to Physical Review Letters.

16. J. A. Marozas, T. J. B. Collins, J. D. Zuegel, P. W. McKenty, D. Cao, S. Fochs, and P. B. Radha, J. Phys.: Conf. Ser. **717**, 012107 (2016).

17. T. J. B. Collins, J. A. Marozas, K. S. Anderson, R. Betti, R. S. Craxton, J. A. Delettrez, V. N. Goncharov, D. R. Harding, F. J. Marshall, R. L. McCrory, D. D. Meyerhofer, P. W. McKenty, P. B. Radha, A. Shvydky, S. Skupsky, and J. D. Zuegel, Phys. Plasmas **19**, 056308 (2012).

18. S. Skupsky and T. Kessler, Opt. Commun. **70**, 123 (1989).

19. J. A. Marozas, J. D. Zuegel, and T. J. B. Collins, Bull. Am. Phys. Soc. **53**, 249 (2008).

20. P. W. McKenty, J. A. Marozas, V. N. Goncharov, K. S. Anderson, R. Betti, D. D. Meyerhofer, P. B. Radha, T. C. Sangster, S. Skupsky, and R. L. McCrory, Bull. Am. Phys. Soc. **51**, 295 (2006).

21. M. Lafon, R. Betti, K. S. Anderson, T. J. B. Collins, R. Epstein, P. W. McKenty, J. F. Myatt, A. Shvydky, and S. Skupsky, Phys. Plasmas **22**, 032703 (2015).

22. R. Betti, C. D. Zhou, K. S. Anderson, L. J. Perkins, W. Theobald, and A. A. Solodov, Phys. Rev. Lett. **98**, 155001 (2007).

23. K. S. Anderson, R. Betti, P. W. McKenty, T. J. B. Collins, M. Hohenberger, W. Theobald, R. S. Craxton, J. A. Delettrez, M. Lafon, J. A. Marozas, R. Nora, S. Skupsky, and A. Shvydky, Phys. Plasmas **20**, 056312 (2013).

24. M. Temporal *et al*., High Power Laser Sci. Eng. **2**, e37 (2014).

25. P. Michel *et al*., Phys. Plasmas **16**, 042702 (2009).

26. T. P. Gill, *The Doppler Effect: An Introduction to the Theory of the Effect* (Logos, London, 1965).

27. P. B. Radha, V. N. Goncharov, T. J. B. Collins, J. A. Delettrez, Y. Elbaz, V. Yu. Glebov, R. L. Keck, D. E. Keller, J. P. Knauer, J. A. Marozas, F. J. Marshall, P. W. McKenty, D. D. Meyerhofer, S. P. Regan, T. C. Sangster, D. Shvarts, S. Skupsky, Y. Srebro, R. P. J. Town, and C. Stoeckl, Phys. Plasmas **12**, 032702 (2005).

28. P. Michel, Lawrence Livermore National Laboratory, private communication (2014).

29. D. Cao, G. Moses, and J. Delettrez, Phys. Plasmas **22**, 082308 (2015).

30. G. P. Schurtz, Ph. D. Nicolaï, and M. Busquet, Phys. Plasmas **7**, 4238 (2000).

31. S. P. Regan, V. N. Goncharov, I. V. Igumenshchev, T. C. Sangster, R. Betti, A. Bose, T. R. Boehly, M. J. Bonino, E. M. Campbell, D. Cao, T. J. B. Collins, R. S. Craxton, A. K. Davis, J. A. Delettrez, D. H. Edgell, R. Epstein, C. J. Forrest, J. A. Frenje, D. H. Froula, M. Gatu Johnson, V. Yu. Glebov, D. R. Harding, M. Hohenberger, S. X. Hu, D. Jacobs-Perkins, R. T. Janezic, M. Karasik, R. L. Keck, J. H. Kelly, T. J. Kessler, J. P. Knauer, T. Z. Kosc, S. J. Loucks, J. A. Marozas, F. J. Marshall, R. L. McCrory, P. W. McKenty, D. D. Meyerhofer, D. T. Michel, J. F. Myatt, S. P. Obenschain, R. D. Petrasso, R. B. Radha, B. Rice, M. Rosenberg, A. J. Schmitt, M. J. Schmitt, W. Seka, W. T. Shmayda, M. J. Shoup III, A. Shvydky, S. Skupsky, A. A. Solodov, C. Stoeckl, W. Theobald, J. Ulreich, M. D. Wittman, K. M. Woo, B. Yaakobi, and J. D. Zuegel, Phys. Rev. Lett. **117**, 025001 (2016); **117**, 059903(E) (2016).

32. L. J. Perkins *et al*., Phys. Plasmas **20**, 072708 (2013).

33. J. A. Marozas, T. J. B. Collins, P. W. McKenty, and J. D. Zuegel, Bull. Am. Phys. Soc. **60**, 167 (2015).

34. T. J. B. Collins, J. A. Marozas, P. W. McKenty, and S. Skupsky, Bull. Am. Phys. Soc. **60**, 29 (2015).

35. V. N. Goncharov, T. C. Sangster, T. R. Boehly, S. X. Hu, I. V. Igumenshchev, F. J. Marshall, R. L. McCrory, D. D. Meyerhofer, P. B. Radha, W. Seka, S. Skupsky, C. Stoeckl, D. T. Casey, J. A. Frenje, and R. D. Petrasso, Phys. Rev. Lett. **104**, 165001 (2010).

36. R. Betti and O. A. Hurricane, Nat. Phys. **12**, 435 (2016).

37. S. Atzeni and J. Meyer-ter-Vehn, *The Physics of Inertial Fusion: Beam Plasma Interaction, Hydrodynamics, Hot Dense Matter*, 1st ed., International Series of Monographs on Physics, Vol. 125 (Oxford University Press, Oxford, 2004).

38. R. K. Follett, J. A. Delettrez, D. H. Edgell, V. N. Goncharov, R. J. Henchen, J. Katz, D. T. Michel, J. F. Myatt, J. Shaw, A. A. Solodov, C. Stoeckl, B. Yaakobi, and D. H. Froula, Phys. Rev. Lett. **116**, 155002 (2016).

39. S. Skupsky, R. S. Craxton, F. J. Marshall, R. Betti, T. J. B. Collins, R. Epstein, V. N. Goncharov, I. V. Igumenshchev, J. A. Marozas, P. W. McKenty, P. B. Radha, J. D. Kilkenny, D. D. Meyerhofer, T. C. Sangster, and R. L. McCrory, J. Phys. IV France **133**, 233 (2006).

40. D. S. Clark *et al*., Phys. Plasmas **23**, 072707 (2016).

Readout Models for General Electric BAS-MS Image Plates

Introduction

The performance of inertial confinement implosions on OMEGA is potentially limited by the production of hot electrons.[1] The hard x-ray image-plate (HXIP) diagnostic[2] is used to determine the energy distribution of the hot electrons by estimating the spectrum of the x rays that are generated through bremsstrahlung with the target. Simulations and data from this diagnostic agree with a bi-Maxwellian shape for the total time-integrated hot-electron spectrum, which for low-Z targets generates an x-ray energy spectrum that is approximately the sum of two exponentials.[3]

HXIP is a time-integrated multichannel x-ray spectrometer. X rays incident on the detector are attenuated by different high-pass filters for each channel and are then recorded by a General Electric (GE) BAS-MS image plate,[4] whose active layer is $BaFBr_{0.85}I_{0.15}:Eu^{2+}$ and is structured as described in Table 152.I. After an experiment, the image plates are removed from the detector and the photostimulated luminescence (PSL) is scanned out by a Typhoon FLA 7000 flying spot scanner. Since the initial signal level for some channels is often higher than the saturation limit of the scanner, image plates are repeatedly scanned until all signal levels are below saturation.

The signal on image plates fades both with time and through readout. The time fading of BAS-MS image plates has been characterized by Ohuchi and Hatano, who measured the signal fading given elapsed time and ambient temperature.[6] The decay rate of the signal on an image plate based on readout number alone has been estimated several times, although never for the BAS-MS image plate with the Typhoon FLA 7000 scanner.[7–9] A model covering the relationship between the depth of deposited energy and the contribution to signal was provided by Bonnet *et al*., who exponentially weighted the deposited energy distribution with a falloff length.[10] Thoms provides a theoretical model of the readout process over any number of scans based on the photon diffusion equation and finds a triple exponential decay for PSL centers as a function of integrated photon flux.[11–13]

Image-plate scan sequences for HXIP indicate a small variation in fade ratio (defined as the current signal value divided by the preceding signal value) between channels and a larger variation between different experiments. A data set of 200 scan sequences for HXIP with at least two scans (see, for example, Fig. 152.11) is used to determine the parameters for a new model of the readout fading.

The following sections: (1) explain the nonapplicability of existing image-plate models to the BAS-MS image plate; (2) derive two basic image-plate models; (3) present methods of determining the model parameters from the HXIP experimental data; and (4) discuss the results.

Table 152.I: Layers of a BAS-MS–type image plate. The first four columns are transcribed from vendor documents.[5] The empirical formulas are calculated from the fifth column, using estimates for unknown values such as the composition of "plastic."

Layer	Width (μm)	Material	Density (g/cm^3)	Calculated empirical formula
Surface	9	Polyethylene terephthalate (PET)	1.4	$C_{10}H_8O_4$
Phosphor	115	25:1 mix $BaFBr_{0.85}I_{0.15}$:urethane	3.3	$Ba_{2263}F_{2263}Br_{1923}I_{339}C_{741}H_{1730}N_{247}O_{494}$
Back	12	Plastic	1.4	$C_{10}H_8O_4$
Base	190	PET	1.4	$C_{10}H_8O_4$
Ferrite	80	MnO, ZnO, Fe_2O_3, plastic	3.0	$Mn_{1015}Zn_{885}Fe_{902}C_{1315}H_{1315}O_{4568}$
Back protective	25	PET	1.4	$C_{10}H_8O_4$

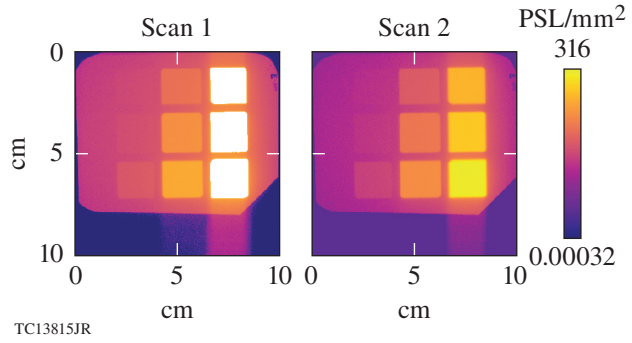

Figure 152.11
Two successive image plate scans for the wide-aperture hard x-ray image plate (HXIP) configuration. Some channels are initially saturated.

Image-Plate Models

1. Review of Existing Image-Plate Models

A first model for the readout process for image plates was derived by Thoms[11] and later extended to include a triple-exponential fading function for the excitation centers in the image plate, which are referred to as photostimulable F-centers.[12] Photon propagation in the image plate is modeled using a 3-D photon diffusion equation and solved numerically. While this may be appropriate for the Fuji ST III image plate for which parameters were determined,[12] the light transport equation used requires that (1) photons are scattered isotropically, (2) the absorption length is much larger than the scattering length, and (3) the scattering length is small compared to the sensitive layer thickness so that photons can immediately be treated as diffuse. Since the estimated parameters for a $BaFBr_{0.85}I_{0.15}$:Eu image plate that are similar in structure to the BAS-MS indicate significant absorption and weak and anisotropic scattering of photons,[14] this model is not applicable.

A variation on the Thoms model using the four-flux model[15] for light transport comes from Masalovich *et al.*, who considered KCl:Eu and KBr:Eu image plates.[16] The four-flux model invokes fewer assumptions than the photon diffusion equation used by Thoms,[11] although it requires the F-center distribution to be uniform along all but the depth coordinate. The four-flux model is used to estimate the readout light flux distribution and the PSL escape probability, from which the image-plate response can be calculated. Since readout light and PSL have different wavelengths, the many free parameters for the four-flux model must be specified for both wavelengths. In practice, the two functions can usually be approximated by much simpler linear or exponential functions.

Finally, Vedantham and Karellas[14] construct a comprehensive image-plate model with more than 20 parameters that relies on simulations of photon transport, taking into account grain sizes and binder material within the image plate. If all the parameters were measured and the structural assumptions of the optical simulations were correct, the model would be appropriate for the BAS-MS image plate. However, many of the model parameters were measured for BaFBr:Eu and assumed to match for $BaFBr_{0.85}I_{0.15}$:Eu, and most information on the internals of the BAS-MS image plate has been kept proprietary.

2. Image-Plate Readout Process

Two image-plate models are introduced in the following sections. In the fixed-distribution model, it is assumed that the shape of the distribution of F-centers in the image plate at any time is unchanged and only its magnitude decreases. In the fading-distribution model, the fading of the F-center distribution as a function of time and depth is structured around the interaction of laser photons and F-centers, which generates PSL.

Figure 152.12 summarizes the readout process of a given distribution $\eta(z)$:[1/mm^3] of F-centers within the image plate's sensitive (phosphor) layer. Laser photons at 650 nm pass into the sensitive layer from the front of the image plate, and the photon flux $\phi(z)$ is reduced (by absorption or scattering) deeper in the image plate. A single cross section σ:[cm^2] describes the interaction between laser photons and the photostimulable F-centers to produce a 390-nm photon and remove an F-center.

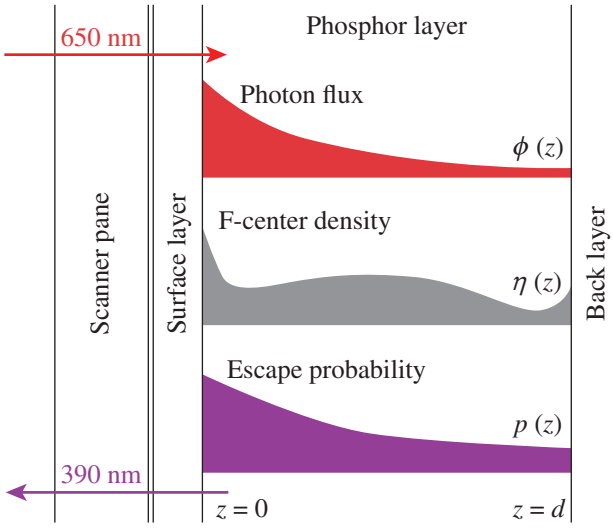

Figure 152.12
Typical shapes of the photon flux distribution, F-center density distribution, and photostimulated luminescence (PSL) escape-probability function within the sensitive layer of an image plate.

[Note that $F(Br^-)$ and $F(I^-)$ centers are treated identically.] The density $\eta(z)$ is assumed to be small enough that absorption by F-centers does not significantly alter the laser photon flux. PSL generated at a given depth z escapes the image plate and is recorded by the scanner optics with probability $p(z)$.

Because a detailed and accurate optical analysis of the BAS-MS plates is difficult, the readout laser photon flux can instead be approximated by the function

$$\phi(z) = Ie^{-z/L_R}, \tag{1}$$

which is defined over $z \in [0,d]$ for the d sensitive layer depth. I:[1/cm^2 • s] is the average photon flux density at the surface of the sensitive layer and L_R is a length factor accounting for the readout photon scattering and absorption effects within the sensitive layer. Similarly, the escape probability can be approximated by

$$p(z) = \frac{1}{2}e^{-z/L_B} \tag{2}$$

in which L_B is another length factor accounting for PSL photon scattering and absorption in the sensitive layer. The F-center distribution $\eta(z)$ can be estimated by assuming that the density of F-centers is proportional to the energy deposited by incident high-energy particles. Separate proportionality constants may apply for each particle type.[10]

3. Fixed-Distribution Model

Under the fixed-distribution model, the total signal S_1 for the first scan is

$$S_1 \propto \int_0^d \phi(z)\sigma\eta(z)p(z)\mathrm{d}z, \tag{3}$$

where σ:[cm^2] is the cross section of photostimulated luminescence with an F-center. Because both $p(z)$ and $\phi(z)$ contain exponentials, defining a combined absorption and scattering length $L = \left(L_R^{-1} + L_B^{-1}\right)^{-1}$ reduces this expression to

$$S_1 = \alpha\int_0^d \eta(z)e^{-z/L}\mathrm{d}z. \tag{4}$$

The factor α:[PSL] is a scale factor encompassing the cross section σ, average laser photon flux density I, illumination time τ, the factor 1/2 from $p(z)$, and the conversion from photostimulated luminescence photons to FLA 7000 intensity units (which are also labeled "PSL").

To account for readout fading, the fixed-distribution model uses an empirical fading formula that has been used for other scanner and image-plate combinations.[7–9] The signal for the nth scan is then

$$S_n = S_1\prod_{i=2}^{n}\left[f_{max} - \left(f_{max} - f_{min}\right)e^{-(i-2)/\mathcal{T}_{fade}}\right]. \tag{5}$$

The fade ratio S_n/S_{n-1} decays exponentially with time. For the first two scans, the fade ratio is f_{min}; for large n it approaches f_{max}; and in between, the falloff in fade ratio has an exponential time constant $\mathcal{T}_{fade}$.

The controlling parameters for the fixed-distribution model are the minimum and maximum fade ratios f_{min} and f_{max}, time constant $\mathcal{T}_{fade}$, falloff length L, and scale factor α.

4. Fading-Distribution Model

In the fading-distribution model, the F-center distribution $\eta(z)$ changes with readout time according to

$$\frac{d}{dt}\eta(z) = -\phi(z)\sigma\eta(z). \tag{6}$$

If τ is the total readout time for a given area over a single scan, the change in the number of F-centers during the nth scan is

$$\eta(z)\left[e^{-(n-1)\sigma\tau\phi(z)} - e^{-n\sigma\tau\phi(z)}\right], \tag{7}$$

where $\phi(z)$ is the photon flux-density approximation from Eq. (1). Since the change in the F-centers equals the PSL generation, the nth scan signal is

$$S_n = \beta\int_0^d \eta(z)w_1(z)e^{(n-1)\sigma\tau\phi(z)}\mathrm{d}z, \tag{8}$$

$$w_1(z) = p(z)\left[1 - e^{-\sigma\tau\phi(z)}\right], \tag{9}$$

where β:[PSL] is a scale factor including the PSL photon to scanner PSL conversion and a factor 1/2 from $p(z)$, which in Eq. (2) gives the PSL escape probability.

The fading-distribution model expression for the first scan signal reduces to Eq. (4) when the number of readout photons is small [$\phi(z)\sigma\tau \ll 1$]. The empirical time decay formula in Eq. (5) can be derived as an approximation for small n if the shape of $\eta(z)$ is fixed, although the expression for $\mathcal{T}_{fade}$ is complicated.

The fading-distribution model is parameterized by falloff lengths L_R and L_B, scale factor β, and unitless product $I\sigma\tau$

encompassing the average incident photon flux density I [see Eq. (1)], F-center cross section σ, and illumination time τ.

Parameter Estimation

1. Scanner-Induced Image-Plate Errors

The Typhoon FLA 7000 scanner used to scan the image plates uses GE software, 50-μm resolution, a 650-nm laser, and a special calibration procedure as described in Williams *et al.*[17] As a result of a lossy conversion from exponential scaling to the offset quadratic scale used by the scanner software, precision at low intensities is reduced. Time fading is not an issue, however, for the HXIP data set: over the 90 s used to scan a 10-cm × 10-cm region, the change in signal caused by time fading is less than 1% for scans begun at least 20 min after exposure.

Streaking effects along one axis of the HXIP images are visible below the image plate boundaries in Fig. 152.11. One possible explanation is that stray readout laser light (possibly reflecting off the front image-plate surface or off scanner components) interacts with regions of the image plate far away from the currently illuminated spot. Only the generated PSL aligned with the light guide of the scanner is recorded, so that the signal at a given location is proportional to the F-center density at that location plus a small fraction of the F-center density along the scan line. If this hypothesis is correct, the streaking effects are linear and can be accounted for.

2. Bounds on Parameter Values

Bounds on the model parameters can be determined using extremal values from the HXIP data set. In this example and for all other parameter estimation, the signal values have been corrected for time fading (assuming a constant 20°C temperature).[6] The observed maximum fade ratio between successive scans is 0.85 for the change in channel signal from the 11th to the 12th scan of a scan sequence, and the minimum fade ratio is 0.15, measured for the least-filtered channel between the first and second scans.

If the time-fading correction does not introduce any significant errors, then for the image-plate readout models to be consistent with this information, the entire range of fade ratios from 0.15 to 0.85 must be attainable for some F-center distribution. For the fixed-distribution model, this condition requires that the parameters $f_{\min} < 0.15$ and $f_{\max} > 0.85$. With the fading-distribution model, the minimum-possible fade ratio $\mathcal{F}_{\min} < 0.15$ is obtained for an F-center distribution concentrated at the front of the sensitive layer [$\eta(z) = \delta(z)$] and the maximum $\mathcal{F}_{\max} > 0.85$ for a concentration at the back of the layer [$\eta(z) = \delta(z–d)$]. Evaluating the fading-distribution model for these two extreme cases yields $I\sigma\tau = -\log \mathcal{F}_{\min} > 1.9$ and $L_R = d \big/ \log\left(\log \mathcal{F}_{\max} \big/ \log \mathcal{F}_{\min}\right) < 100\ \mu$m. The parameter L_B cannot be determined without constraining the shape of the depth distribution of the F-centers.

3. Determining Parameters by an Error Minimization Fit

For a given model m, the model parameters Ω_m are determined by minimizing the errors between the available data and a fit to that data based on the assumption that the x-ray energy spectra incident on HXIP are sums of two exponentials. The average error χ_s^2 for a specific scan sequence s is computed using

$$\chi_s^2 = \sum_{\substack{n \in \text{scans} \\ c \in \text{scans}}} w_c \left(\log \frac{v_{n,c}\left[\Psi_s;\Omega_m\right]}{x_{s,n,c}} \right)^2, \tag{10}$$

where w_c is a weight inversely proportional to the number of scans for which a channel is neither saturated nor read out below the noise threshold. The values $x_{s,n,c}$ are the measured signals for scan sequence s, the nth scan, and the cth channel. The function $v_{n,c}[\Psi_s;\Omega_m]$ calculates the expected channel signal as a function of scan sequence parameters Ψ_s and model parameters Ω_m [see the **Appendix** (p. 190) for details]. The mean square log deviation is chosen as a measure of error because the data are always positive and often a factor of 2 distant from the fit values, so the assumption of normally distributed errors under which minimizing squared (linear) errors yields a maximum-likelihood solution does not apply.

Because the errors χ_s^2 have a long-tailed distribution, the geometric mean is used to combine them into a single cost function C, over which the model parameters Ω_m can be minimized. (The arithmetic mean would overemphasize scan sequences whose errors are large for reasons unrelated to the readout model; using it shifts the final model parameter estimates only slightly). Therefore,

$$C = \sqrt[N_s]{\prod_{s \in \text{seqs}} \left(\chi_s^2\right)}, \tag{11}$$

where N_s is the number of scan sequences used for the fit.

Due to the large number of total parameters, the fit procedure is performed in two loops: in the outer loop, the minimi-

zation over model parameters Ω_m uses a global optimization method for C based on a surrogate function using linear interpolation on a Delaunay triangulation;[18] in the inner loop, for each scan sequence, the values Ψ_s minimizing χ_s^2 are found by brute force followed by gradient descent. The simplex mesh surrogate is chosen because it can handle both fine detail (near the minima) and coarse detail (for the global shape) without requiring tuning. Computations on the surrogate are efficient since they reduce to computations on linear functions.

Applying the fit procedure to the fixed-distribution and fading-distribution models over a data set of 212 image-plate scan series with at least two scans provides the model parameters and error measures given in Table 152.II. The error bars and limits on individual parameters are computed from the region of parameter space where the surrogate function is less than $1.1C$. An alternative approach to estimating the error for the parameters is to minimize C repeatedly, each time using a variation on the original data set perturbed according to the measurement errors of each value, and use the distribution of parameters found to compute the error for each parameter. For the HXIP data set, such Monte Carlo error estimation yields extremely narrow error bars when only accounting for statistical errors. Accurately modeling the systematic errors involved in the estimation of $v_{n,c}[\Psi_s;\Omega_m]$ is beyond the scope of this article.

Table 152.II: Best-fit parameters for the fixed-and fading-distribution models. See **Determining Parameters by an Error Minimization Fit** (p. 187) for an explanation of the error bars and bounds.

Model	Parameters	Bounds
Fixed distribution	$f_{\max} = 0.83 \pm 0.10$	(0.65,1.00)
	$f_{\min} = 0.36 \pm 0.02$	(0.35,0.38)
	$\mathcal{T}_{\text{fade}} = 3.75 \pm 1.0$	(0.31,11.0)
	$L = 136 \pm 43\ \mu$m	(39 μm, ∞)
Fading distribution	$I\sigma\tau = 2.8 \pm 0.3$	(2.3,3.3)
	$L_{\text{B}} = 220 \pm 90\ \mu$m	(200 μm, 680 μm)
	$L_{\text{R}} = 51 \pm 28\ \mu$m	(39 μm, 136 μm)

Plotting the minimum C while fixing a single parameter at a time does not capture the complex trade-off between parameters; see Fig. 152.13 for the minimum model errors when fixing two of the parameters. The practical difference between best-fit models is shown in Fig. 152.14. The scale factors α and β for the two models cannot be determined since the absolute intensity of the x rays recorded by HXIP is uncertain.

Discussion

The fading-distribution model yields a significantly lower average error ($C = 0.133$) than the fixed-distribution model ($C = 0.170$). Since the cost function C is a relative measure, neither value implies a quantifiable certainty in the parameter values. However, C can be used as a proxy for the likelihood of a given combination of model parameters, assuming the model in question is correct.

For instance, with the fading-distribution model, L_{R} is constrained to the range (39 μm, 136 μm). While lower values of L_{R} do not significantly increase C, they are unphysical, especially for L_{R} less than the phosphor particle size of 5 μm (Ref. 4). For large L_{R}, the error increases up to the point where the fading-distribution model reduces to a simpler one with a fixed fade ratio. The other length parameter L_{B} induces only gradual changes in error as it varies; it follows that the minimization of C only weakly constrains L_{B}. To determine L_{B} with any more precision would require a different method of estimation. The combined parameter $I\sigma\tau$, which encompasses the photon flux, PSL cross section, and illumination time, has estimated bounds $2.3 \lesssim I\sigma\tau \lesssim 3.3$, outside which L_{R} and L_{B} can no longer effectively compensate for the extreme value of $I\sigma\tau$.

The interaction between parameters for the fixed-distribution model is more complicated, but it is also more clearly influenced by features of the HXIP data set. For instance, most of the scan sequences available are between two and five scans in length. The variation in fade ratios between channels and between scan sequences is largest for the initial scans and smaller for the final scans in a sequence. As Fig. 152.13 shows, C quickly increases on deviating from the minimized $f_{\min} = 0.36 \pm 0.02$. The error on $f_{\min}$ is small since changes to it directly alter the first fade ratio for about 200 scan sequences. Meanwhile, fade ratios approaching $f_{\max}$ are obtained only for the few sequences with more than five scans, and correspondingly the change in C is more gradual, yielding a larger error on $f_{\max} = 0.83 \pm 0.10$. The bias toward short scan sequences also affects parameter $\mathcal{T}_{\text{fade}}$ since for the first three or four scans in a sequence, increasing $\mathcal{T}_{\text{fade}}$ in conjunction with $f_{\max}$ only slightly increases C. Finally, without the influence of differing fade ratios on the length parameter (as for the fading-distribution model), the value of C is largely independent of L, whose value, like that of L_{B}, must be determined by another method.

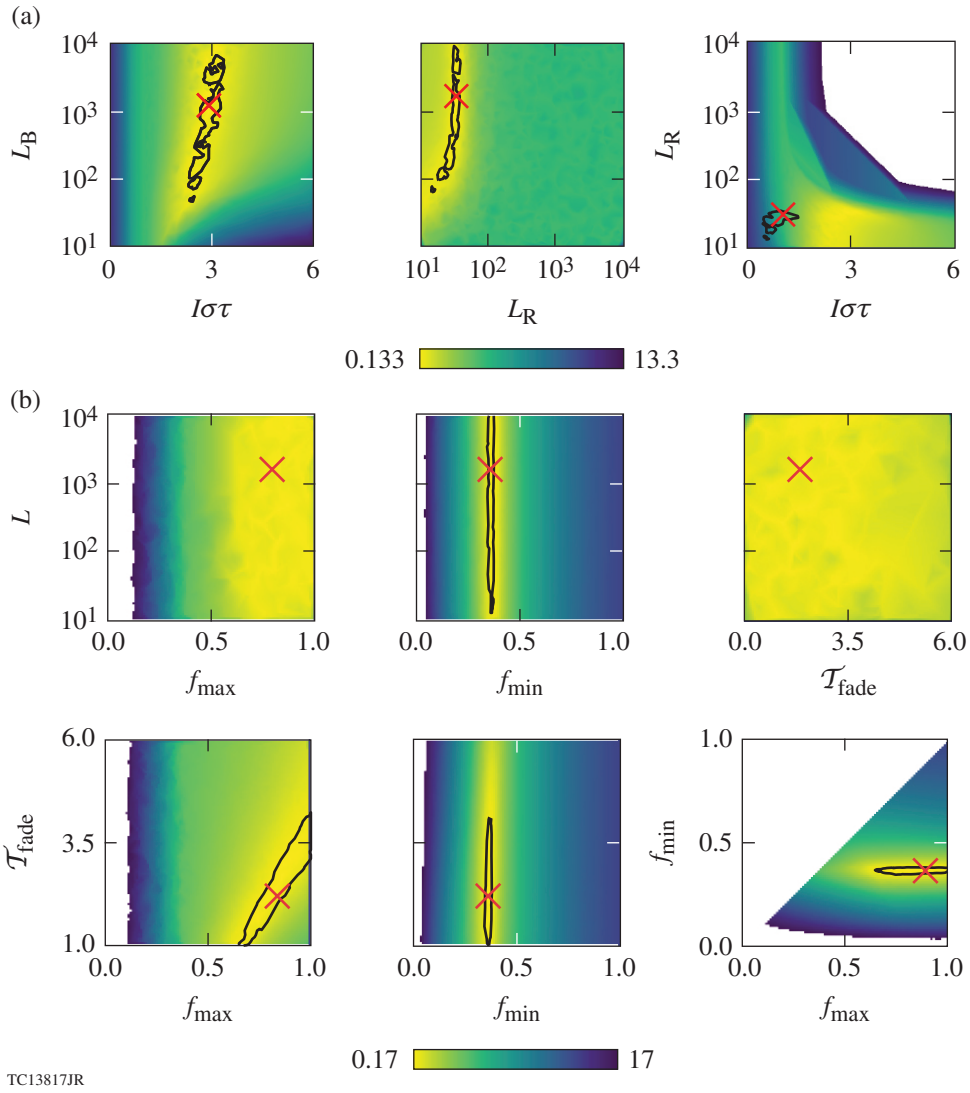

Figure 152.13
Plot of the cost function C for the (a) fading-distribution model and (b) fixed-distribution model when two parameters are fixed and the rest are minimized. The black line is the contour of the surrogate function at $1.1C$, and × marks the minimum. The contour is omitted where it is too convoluted.

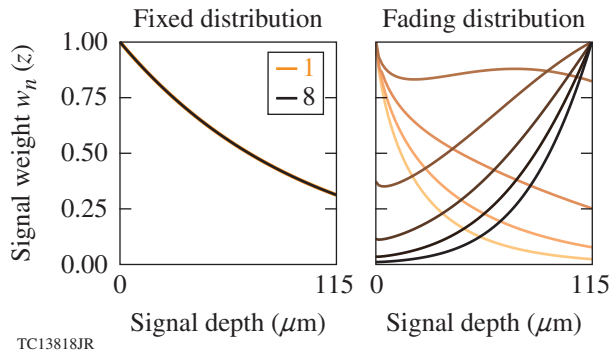

Figure 152.14
Normalized weight functions $w_n(z)$ for the two models defined so that the equation $S_n = \alpha_n \int_0^d w_n(z)\eta(z)\mathrm{d}z$ describes the nth scan signal S_n as a function of the F-center distribution $\eta(z)$ in the image plate, where α_n is a scale parameter. For the fixed-distribution model, all normalized weight functions are identical.

Not all inferred model parameters agree with previous work on the BAS-MS image plate. For instance, the fading-distribution model parameter $L_R = 51\pm28$ μm $\in$ (39 μm, 136 μm) implies strong attenuation of the incident readout laser. Although the fading-distribution and fixed-distribution models have different equations, the distorting effect of the depth-dependent fading is small enough for the first scan only that the parameters of the two models can be compared to find $L \approx \left(L_R^{-1} + L_B^{-1}\right)^{-1}$, which implies $L \lesssim L_R$. Both the length $L = 125\pm35$ μm from Boutoux *et al.*[19] and the length $L = 222\pm72$ μm found by Bonnet *et al.*[10] are higher than expected given the value of L_R. Moreover, the error plot in Fig. 152.13 indicates that while smaller L_R values are plausible, larger values of L_R significantly increase the average error.

Conclusion

In summary, a simple model for BAS-MS image plates that accounts for readout fading has been proposed and found to improve the Bonnet *et al.* model[10] combined with an empirical treatment of readout fading. Model parameters are inferred that minimize errors on a collection of experimental HXIP data. The model implies that the response of the second image-plate scan may not be proportional to the response of the first scan, especially when large variations in the depth distribution of F-centers within the image plate are present. The procedure to determine model parameters accurately determines fading parameters but yields little certainty on values related to the transportation of PSL photons and cannot provide any of the scale factors involved in an absolute calibration.

ACKNOWLEDGMENT

The authors thank D. Edgell and C. Stoeckl for insightful discussions.

This material is based upon work supported by the Department of Energy National Nuclear Security Administration under Award Number DE-NA0001944, the University of Rochester, and the New York State Energy Research and Development Authority.

Appendix: Estimating Signal Values for a Specific Scan Sequence

The expected signal for channel c of scan n of sequence s given model parameters Ω_m and spectrum parameters Ψ_s, $v_{n,c}[\Psi_s;\Omega_m]$ are defined as a product of operators,

$$v_{n,c}\left[\Psi_s;\Omega_m\right] = \mathcal{I} \times M_n\left[\Omega_m\right] \times R_{c,s} \times \left[f\left(E;\Psi_s\right)\right], \quad \text{(A1)}$$

where $\mathcal{I}$ approximates the additional signal from F-centers in different regions of the image plate caused by stray readout light in the scanner. This correction is performed on estimated signals rather than the image plates themselves in order to avoid negative values. $M_n[\Omega_m]$ provides the signal recorded by the scanner for a given depth distribution of F-centers, using the formulas derived in **Image-Plate Models** (p. 185). $R_{c,s}$ converts an arbitrary x-ray spectrum to the resulting depth distribution $\eta(z)$ within the region of the image plate corresponding to the channel. It is calculated for each HXIP configuration using a *Geant*[20] simulation of the detector. The simulation accounts for backscattering from the aluminum image-plate holder and Compton-scattered photons from the channel filters, which contribute to the F-center distribution in other channels' regions of interest. Finally, $f(E;\Psi_s)$ is the approximated x-ray energy spectrum given by

$$f\left(E;\Psi_s\right) = A_1 e^{-E/kT_1} A_2 e^{-E/kT_2}, \quad \text{(A2)}$$

where A_1, A_2, kT_1, and kT_2 are the spectrum parameters encompassed by Ψ_s.

REFERENCES

1. D. H. Froula, D. T. Michel, I. V. Igumenshchev, S. X. Hu, B. Yaakobi, J. F. Myatt, D. H. Edgell, R. Follett, V. Yu. Glebov, V. N. Goncharov, T. J. Kessler, A. V. Maximov, P. B. Radha, T. C. Sangster, W. Seka, R. W. Short, A. A. Solodov, C. Sorce, and C. Stoeckl, Plasma Phys. Control. Fusion **54**, 124016 (2012).
2. A. A. Solodov, B. Yaakobi, D. H. Edgell, R. K. Follett, J. F. Myatt, C. Sorce, and D. H. Froula, Phys. Plasmas **23**, 102707 (2016).
3. R. Follett, "The Multiple-Beam Two-Plasmon-Decay Instability," Ph.D. thesis, University of Rochester, 2015.
4. Storage Phosphor Screen BAS-IP, GE Healthcare Bio-Sciences, Pittsburgh, PA 15264-3065, http://www.gelifesciences.com/webapp/wcs/stores/servlet/productById/en/GELifeSciences-us/28956474 (19 October 2017).
5. U. D. Chalasani, GE Healthcare Scientific Support, private communication (24 August 2017).
6. H. Ohuchi and L. C. Ha, Proc. Radiochim. Acta **1**, 49 (2011).
7. B. Hidding *et al.*, Rev. Sci. Instrum. **78**, 083301 (2007).
8. H. Ohuchi and A. Yamadera, Nucl. Instrum. Methods Phys. Res. A **490**, 573 (2002).
9. A. Taniyama, D. Shindo, and T. Oikawa, J. Electron. Microsc. **45**, 232 (1996).
10. T. Bonnet *et al.*, Rev. Sci. Instrum. **84**, 013508 (2013).
11. M. Thoms, Appl. Opt. **35**, 3702 (1996).
12. M. Thoms, Nucl. Instrum. Methods Phys. Res. A **378**, 598 (1996).

13. M. Thoms and H. von Seggern, J. Appl. Phys. **81**, 5887 (1997).

14. S. Vedantham and A. Karellas, IEEE Trans. Med. Imaging **29**, 790 (2010).

15. B. Maheu, J. N. Letoulouzan, and G. Gouesbet, Appl. Opt. **23**, 3353 (1984).

16. S. Masalovich *et al*., Nucl. Instrum. Methods Phys. Res. A **539**, 236 (2005).

17. G. J. Williams *et al*., Rev. Sci. Instrum. **85**, 11E604 (2014).

18. R. Paulavičius and J. Žilinskas, in *Simplicial Global Optimization*, SpringerBriefs in Optimization, edited by P. M. Pardalos *et al*. (Springer, New York, 2014), Chap. 1, pp. 1–19.

19. G. Boutoux *et al*., Rev. Sci. Instrum. **87**, 043108 (2016).

20. J. Allison *et al*., Nucl. Instrum. Methods Phys. Res. A **835**, 186 (2016).

A Time-To-Frequency Converter for Measuring the Shape of Short Optical Pulses

Introduction

First noted in the 1960s, a mathematical equivalence exists between paraxial beam diffraction and dispersive pulse broadening.[1–3] This equivalence, known as space–time duality, has led to the development of temporal analogs of several optical devices. An important component of such devices is the time lens,[4,5] which is designed to impose a time-dependent parabolic phase across an optical pulse passing through it, just as a traditional lens provides a parabolic phase in space. The development of such a time lens has led to applications such as temporal imaging,[4–7] spectral phase conjugation,[7] and temporal cloaking.[7,8]

Most modern time lenses produce the required parabolic phase using nonlinear effects such as four-wave mixing (FWM),[7–10] which requires a highly nonlinear waveguide and careful control of the pump dispersion and timing. Using an electro-optic phase modulator driven by a phase-locked sinusoidal radio-frequency (rf) signal, we must adjust the timing of our test pulse within only one cycle of the rf signal, a task that can be accomplished with commercially available phase shifters. Additionally, the electro-optic phase shift does not have the intensity dependence of FWM and can be used for test pulses of any energy.[11–16]

One of LLE's diagnostic needs is to measure the shape of infrared (λ = 1053-nm) pulses with durations in the range of 1 to 30 ps. Pre-shot characterization of such short-pulse beams is important for preventing damage to the system. Optical streak cameras have been used at LLE for this purpose;[17–19] however, several challenges to streak cameras limit their use. First, time-of-flight broadening occurs because of variations in the kinetic energy of the generated photoelectrons. These variations in kinetic energy lead to different electron velocities and, therefore, different amounts of time to reach the other end of the streak tube. For an infrared-sensitive Ag-O-Cs photocathode (designated S-1 photocathode) used in a streak camera, this leads to impulse responses of several picoseconds in width. Second, space-charge effects cause the electrons generated from short, intense pulses to repel each other. This produces broadening of the electron pulse in the drift region of the streak tube, which causes the measured pulse to be longer.[19–22] The space-charge effects can be reduced by using lower-power pulses, but lower powers lead to signal-to-noise issues. The combination of these two factors means that streak cameras are not particularly well suited to measuring pulses of durations <10 ps. Finally, and perhaps most importantly, recent experience at LLE has shown that current optical streak tubes based on S-1 photocathodes have such a limited lifetime that the long-term costs of operating such streak cameras are not realistic. Therefore, it would be beneficial to develop new diagnostic techniques as alternatives to the streak cameras.

Temporal imaging systems are of particular interest because they can be run in both single-shot and averaging modes without changing the aperture and resolution of the time lens.[9] They are also well suited to imaging picosecond to tens-of-picosecond pulses.[7] In particular, electro-optic phase modulators driven by GHz-rf signals can have apertures in the tens of picoseconds. As a proof of concept, we have developed a pulse-imaging system that uses an electro-optic phase modulator as a time lens in a time-to-frequency converter configuration. Our device maps the pulse shape onto the spectrum, allowing us to record the pulse shape with an optical spectrum analyzer. In the following sections, we address the design of our system, compare its performance to streak-camera and autocorrelator traces, and discuss how the system can be scaled up to cover a range of 1 to 30 ps.

Theory and System Design

We use a time lens in a time-to-frequency conversion system in which the input pulse first propagates inside an optical fiber before passing through the time lens.[10,23,24] For a linear system, the electric field at the output of the dispersive medium of length L can be related to the input electric field in the frequency domain as[25]

$$\tilde{E}_1(\omega) = \tilde{E}_0(\omega)\exp\left[\frac{i\beta_2 L}{2}\left(\omega-\omega_0\right)^2\right], \tag{1}$$

where $\tilde{E}_1(\omega)$ is the Fourier transform of the output electric field and the dispersion effects inside the fiber are included by

the second derivative, $\beta_2 = d^2\beta/d\omega^2$, of the modal propagation constant β at the central frequency ω_0 of the pulse spectrum. The parameter β_2 takes into account the group-velocity dispersion (GVD) and affects both the duration of the input pulse and its chirp. The pulse duration and chirp after the fiber are determined by the group-delay dispersion (GDD), given by $D_1 = \beta_2 L$.

When an electro-optic phase modulator driven by a sinusoidal voltage is used as a time lens, the phase shift applied to the pulse has the form

$$\Phi(t) = \phi_0 \cos(2\pi\nu_m t), \tag{2}$$

where ϕ_0 is the amplitude of the phase modulation and ν_m is frequency of the rf signal used to drive the modulator. The phase amplitude is determined by $\phi_0 = \pi V/V_\pi$, where V is the amplitude of the rf voltage used to drive the modulator and V_π is the voltage required for the modulator to produce a phase shift of π, a known quantity for commercial modulators. The electric field after the phase modulator is then related to the electric field at the output of the dispersive medium as

$$E_2(t) = E_1(t)\exp[-i\Phi(t)]. \tag{3}$$

In close analogy to the focal length of a traditional lens, a focal GDD is used to describe a time lens; it is defined as[5,26]

$$D_f = [(2\pi\nu_m)^2\phi_0]^{-1}. \tag{4}$$

For a time-to-frequency converter, the length of the dispersive medium is chosen such that the GDD of the medium, $D_1 = \beta_2 L$, is equal to the focal GDD of the time lens, D_f (Ref. 7). Therefore, the required length in our case is $L = D_f/\beta_2$. When this condition is satisfied, the output-pulse spectrum maps the temporal shape of the input pulse according to the scaling relation[10,23]

$$t = D_f(\omega - \omega_0). \tag{5}$$

As with a traditional lens, it is useful to define a time aperture and temporal resolution for our time lens. The time aperture is the longest Gaussian pulse that can be imaged by our system without significant distortion of its measured full width at half maximum (FWHM) and has the form[5]

$$\Delta T = \frac{1}{2\pi\nu_m}. \tag{6}$$

The time resolution is the shortest FWHM pulse duration that can be generated by compressing a pulse that fits within the time lens aperture and is given by[7]

$$\delta t = \frac{4\ln(2)}{2\pi\nu_m\phi_0}. \tag{7}$$

A schematic of the experimental setup is shown in Fig. 152.15. A mode-locked laser (High Q femtoTrian IC-1053-400 fs Yb) producing 150-fs pulses at 1053 nm with a 38-MHz

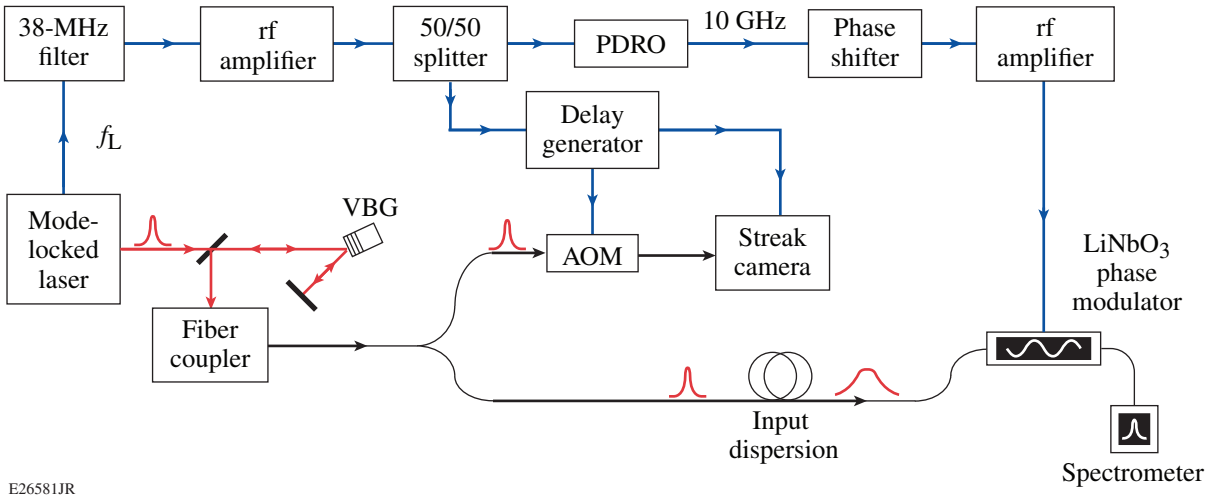

Figure 152.15
Experimental setup for a time-to-frequency converter using a phase modulator as a time lens and an optical fiber for the input dispersion. AOM: acousto-optic modulator; PDRO: phase-locked dielectric resonator oscillator; rf: radio frequency; VBG: volume Bragg grating.

repetition rate was used as the source of optical pulses. The time lens was implemented using a high-efficiency electro-optic phase modulator designed to operate at 800 nm but usable at 1053 nm (EOSPACE PM-5K4-10-PFU-PFU-800-LV-S). A fast photodiode (>100-MHz bandwidth) created an electronic signal of the laser pulse train, which was split into two parts with a 50/50 splitter. The first arm of the splitter was filtered with a 76-MHz bandpass filter to produce a synchronization signal at the second harmonic of the 38-MHz laser repetition rate. This 76-MHz signal matches the resonant frequency of a commercially available phase-locked dielectric resonator oscillator (PDRO), which uses phase locking to synchronize the pulse train to a high harmonic of the 76-MHz signal near 10 GHz (Ref. 27). The 10-GHz output was sent through a phase shifter, which allows one to adjust the timing between the 10-GHz signal and the pulse train so the time lens could be properly aligned. The resulting rf signal was amplified by a 33-dBm microwave amplifier and used to drive the phase modulator. This allowed our phase modulator to produce a sinusoidal phase modulation with a maximum phase amplitude of $\phi_0 = 16$ rad.

Using $\nu_m = 10$ GHz and a maximum phase amplitude of $\phi_0 = 16$ rad in Eqs. (6) and (7) gives a time aperture of $\Delta T = 15.9$ ps and a resolution of $\delta t = 2.75$ ps. The minimum focal dispersion for the time lens is then found using Eq. (4) to be $D_f = 15.8$ ps^2. To calibrate the time lens, the sinusoidal phase modulation is scanned across the pulse using a phase shifter and the amplitude of the rf voltage is adjusted until the peak of the pulse spectrum oscillates over a 1.2-nm range. To create the input GDD, a single-mode fiber (Corning HI1060) was used. Using the value of $\beta_2 = 23.8$ ps^2/km at 1053 nm, 667 m of this fiber was required to give the input dispersion of $D_1 = 15.8$ ps^2. The chirped pulse was then sent through the phase modulator and the spectrum was recorded using an optical spectrum analyzer (Yokogawa AQ6370D).

Because the laser source produces pulses shorter than the resolution of the time lens, a spectral filter must be applied to the laser signal to broaden the pulse in time. A volume Bragg grating (VBG) with a 0.5-nm bandwidth was used to filter the spectrum. The VBG was used in a double-pass configuration to better attenuate the wings of the spectrum, resulting in a final spectral bandwidth of 0.254 nm.

The second arm of the rf line was filtered to 38 MHz and was used as a clock for a digital delay generator (Stanford Instruments DG645), which triggered an acousto-optic modulator (AOM) and a Rochester Optical Streak System (ROSS).[17] The AOM was used to gate the pulse train to achieve a 0.1-Hz repetition rate to prevent damage to the photocathode of the ROSS and to allow only a single pulse to be captured in the streak camera image, thereby eliminating jitter. The ROSS then captured images of the pulse shape, which were used as a comparison for the time-lens measurements.

Although the time lens has a theoretical aperture of 15.9 ps, this value was found, based on the FWHM of the measured pulse, to be largely the same as the FWHM of the actual pulse. However, even if pulses shorter than the time aperture are used, the wings of the pulse, which extend outside of the time aperture, can still see significant distortions. To explore this effect, numerical simulations of the pulse shape measured by a time-to-frequency converter with the same parameters as our experimental time lens were performed. The input dispersion and phase modulation were modeled using Eqs. (1) and (3), respectively. The frequency axis is scaled to the time axis using the relation given in Eq. (5).

Figure 152.16 shows the results for Gaussian input pulses with a FWHM of (a) 15 ps, (b) 12 ps, and (c) 10 ps. The pulse shape is plotted on a logarithmic scale to better show the behavior in the pulse wings. Comparing the three plots, it is shown that the 12-ps and 10-ps pulses in Figs. 152.16(b) and 152.16(c), respectively, are well imaged in the wings, while the 15-ps pulse has significant errors. Note that the wings are beginning to distort for the 12-ps pulse in Fig. 152.16(b), so the effective aperture is close to 12 ps. Also note that the FWHM of the 15-ps pulse is largely unchanged, with the errors arising from a suppression of the wings. A similar problem occurs for the time resolution, with the simulations showing that the resolution is closer to $\delta t = 3$ ps.

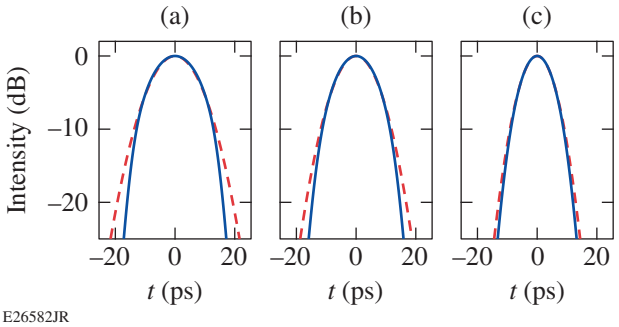

Figure 152.16
Numerical simulations showing the pulse shapes at the input (dashed red curve) and output (solid blue curve), respectively, of the time-to-frequency converter. Initial pulse widths are (a) $T_{FWHM} = 15$ ps, (b) $T_{FWHM} = 12$ ps, and (c) $T_{FWHM} = 10$ ps. The time axis for the output pulse was obtained using the scaling from Eq. (5).

Experimental Results

Three experimentally recorded spectra (dashed red curves) are shown in Fig. 152.17. The wavelength axis has been converted to a time axis by first converting wavelength to frequency and then using the focal GDD, $D_f = 15.8$ ps^2, as a conversion factor to time. A Gaussian fit (solid blue curves) for each pulse provides a measure of the FWHM duration of the pulse. Our measurements show a typical pulse width of around 7.2 ps, with a few traces showing FWHM pulse durations near 7.32 ps, as in Fig. 152.17(a).

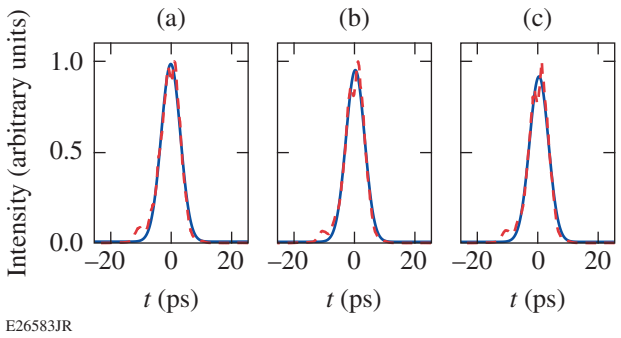

Figure 152.17
Measurement of the pulse shape produced by the volume Bragg grating using the time-to-frequency converter (dashed red curves) for (a) T_{FWHM} = 7.32 ps, (b) T_{FWHM} = 7.13 ps, and (c) T_{FWHM} = 7.24 ps. The time axis is obtained using the scaling from Eq. (5). A Gaussian fit to the data is shown as the solid blue curves.

We first compare these measurements to an autocorrelation trace of the pulse as shown in Fig. 152.18(a). Because the autocorrelation signal was very weak as a result of the low peak intensity of our filtered pulses, the oscilloscope trace was averaged over 512 traces. The autocorrelation was then fitted with a Gaussian profile and found to have a FWHM duration of 10.31 ps. Using the known decorrelation factor of 0.707 for Gaussian pulses, a pulse width of T_{FWHM} = 7.29 ps was obtained, which agreed very well with the FWHM calculated from the time-lens measurements in Fig. 152.17 of 7.20±0.08 ps. To obtain this value, it was assumed that the input pulse shape was approximately Gaussian. While this was a good assumption in this case, the decorrelation factor can change drastically for different pulse shapes, taking a value of 0.65 for sech-shaped pulses. This is the reason why autocorrelation is not a useful technique for pulses of unknown shapes. For our time-lens technique, no assumptions are necessary for the pulse shape; as a result, it can be used for pulses of arbitrary shapes. Finally, the pulses measured by our time lens have a small asymmetric peak located near $t = -9$ ps. This peak is likely caused by a secondary reflection in the VBG. It is not

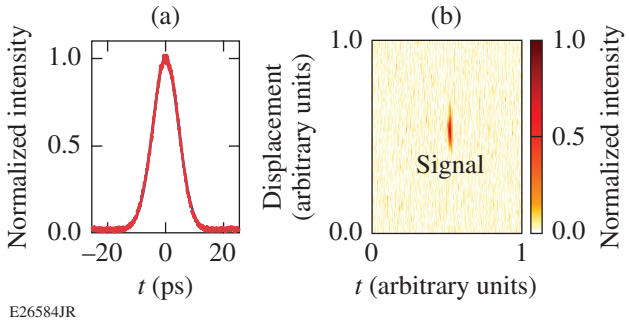

Figure 152.18
(a) Autocorrelation of pulses used to generate Fig. 152.17 has a width of T_{FWHM} = 10.32 ps; (b) streak-camera image of the same pulses. The signal is labeled in the image.

present in the autocorrelation trace because autocorrelation involves the overlap of two copies of the same pulse, resulting in a symmetric trace. The ability of the time lens to measure asymmetries in the pulse shape is a major benefit of our technique over an autocorrelation-based technique.

Figure 152.18 compares these results to measurements from the ROSS. Figure 152.18(b) shows the image produced by the streak camera using the fastest sweep of 1.75 ns, where the region of the image corresponding to the signal pulse is zoomed in on. Each image is averaged along the displacement axis to produce a temporal profile for a single pulse. Figure 152.19 shows the resulting temporal profiles from three independent streak-camera traces, using 0.85 ps per pixel for the 1.75-ns sweep. After multiple shots, the pulse width measured on the streak camera was found to be 9.29±0.76 ps, which does not agree with the 7.20±0.08-ps value deduced from the time-to-frequency converter. There are several reasons behind this discrepancy: First, the signal is inherently noisier compared

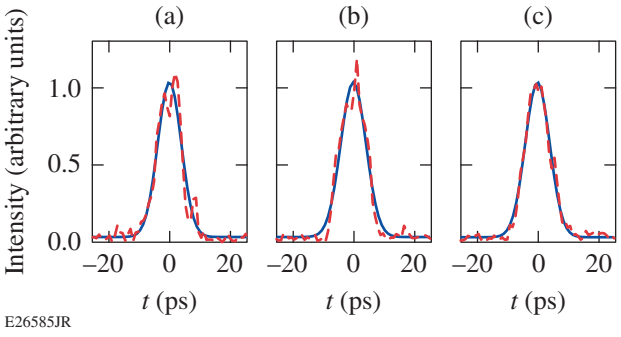

Figure 152.19
ROSS measurements of the pulse used to generate Fig. 152.17 (dashed red curves) and a Gaussian fit to the data (solid blue curves) for three different shots: (a) T_{FWHM} = 9.01 ps, (b) T_{FWHM} = 9.63 ps, and (c) T_{FWHM} = 9.38 ps.

to the other two techniques owing to the single-shot nature of the streak camera. Second, the peak power of the pulses was considerably reduced to prevent the space-charge effects, which also decreased the signal-to-noise ratio. The primary reason the streak camera measurements are consistently over a picosecond longer than those found with either the time lens or the autocorrelator is related to the time-of-flight broadening. For an impulse response τ, the measured pulse width will be $T_m = \sqrt{T_0^2 + \tau^2}$. The measured impulse response of 5.78±0.63 ps accounts for the observed discrepancy between the streak camera and the other two methods of measuring the pulse duration. Furthermore, even though the streak camera can potentially see the asymmetries in the pulse shape, the impulse response of the camera is longer than the asymmetry, which can no longer be resolved. Therefore, the same consistent bump in the pulse shape that could be clearly seen in the time-lens measurements is no longer seen.

Conclusions

A time-to-frequency converter using an electro-optic phase modulator acting as a time lens was built. Such a device was used to record the temporal shape of infrared pulses at a wavelength of 1053 nm (width of ~7 ps) and these measurements were compared to those made by using both a streak camera and an autocorrelator. Although the proof-of-concept system has successfully demonstrated the time-to-frequency conversion process, several improvements must be made before its use becomes practical. The most-challenging task is to expand the range of pulse durations that can be successfully imaged to cover the entire 1- to 30-ps range. As seen earlier, the current time lens can only accurately image pulses of less than 12 ps, so the time aperture must be expanded by lowering the drive frequency, ν_m. To reliably image the wings of 30-ps pulses, the drive frequency must be less than $\nu_m = 4$ GHz, with a time aperture of $\Delta T = 40$ ps.

By lowering the rf frequency, the time resolution will be expanded by the same factor according to Eq. (7). Therefore, the peak phase modulation must also increase by the same factor to maintain the same time resolution. However, it is also desired to lower the resolution from 3 ps to 1 ps, and the amplitude of the phase modulation must be increased to $\phi_0 =$ 120 rad. The first step to accomplishing this will be to use a phase modulator designed for the 1053-nm wavelength. Such modulators can produce phase amplitudes of up to $\phi_0 = 30$ rad. If four of these modulators are connected in series, the required phase amplitude can be achieved. With the new frequency and amplitude for the time lens, the focal dispersion becomes $D_f =$ 13.2 ps^2 , requiring only 554 m of single-mode fiber. This gives a theoretical time resolution of 0.92 ps. However, numerical simulations show that the actual resolution of the time lens is closer to 2 ps. This is likely caused by the aperture of the time lens being smaller than predicted in Eq. (6). Therefore, the resolution will actually be larger than the predicted value according to Eq. (7). Indeed, a 2-ps pulse should be well imaged by this time lens. To image pulses with durations down to 1 ps, it would be necessary to double the total phase amplitude. This would require eight phase modulators connected in series, and the insertion losses would begin to affect the signal-to-noise ratio.

For the OMEGA EP Laser System in particular, this limitation can be worked around because the longer pulses are formed by chirping a shorter pulse with diffraction gratings. Because optical fiber has the opposite GVD as that of the diffraction gratings, the 30-ps pulse will actually recompress during propagation through the input fiber, allowing it to fit within the aperture of the time lens. The drive frequency can therefore be increased to $\nu_m = 7$ GHz to obtain a time aperture of $\Delta T = 21$ ps, while keeping the phase amplitude at $\phi_0 = 120$ rad. Using these parameters, our simulations show that the full 1- to 30-ps range can be well imaged with only slight errors for the 1-ps pulse. Therefore, we can image much longer pulses with a considerably weaker time lens if the long pulses are properly chirped.

Once the time-to-frequency converter is able to image the proper range of pulses, the system can be converted to a single-shot mode. This can be accomplished by feeding the output of the time lens into a single-shot spectrometer. For the above system with $\nu_m = 7$ GHz and $\phi_0 = 120$ rad, the spectrometer must be able to resolve spectral widths as small as 160 pm. Using a diffraction grating with a line density of 1200 g/mm and a charge-coupled device with 13.5-μm pixels, this resolution can be achieved with a spectrometer that is less than 30 cm long.

ACKNOWLEDGMENT

This material is based upon work supported by the Department of Energy National Nuclear Security Administration under Award Number DE-NA0001944, the University of Rochester, the New York State Energy Research and Development Authority, and the National Science Foundation under award ECCS-1505636.

REFERENCES

1. P. Tournois, C. R. Acad. Sci. **258**, 3839 (1964).
2. A. Papoulis, *Systems and Transforms with Applications in Optics* (McGraw-Hill, New York, 1968), p. 379.
3. S. A. Akhmanov, A. P. Sukhorukov, and A. S. Chirkin, Sov. Phys. JETP **28**, 748 (1969).

4. B. H. Kolner and M. Nazarathy, Opt. Lett. **14**, 630 (1989).
5. B. H. Kolner, IEEE J. Quantum Electron. **30**, 1951 (1994).
6. C. V. Bennett and B. Kolner, IEEE J. Quantum Electron. **36**, 430 (2000).
7. R. Salem, M. A. Foster, and A. L. Gaeta, Adv. Opt. Photon. **5**, 274 (2013).
8. M. Fridman *et al*., Nature **481**, 62 (2012).
9. D. H. Broaddus *et al*., Opt. Express **18**, 14,262 (2010).
10. A. Pasquazi *et al*., IEEE J. Sel. Top. Quantum Electron. **18**, 629 (2012).
11. J. E. Bjorkholm, E. H. Turner, and D. B. Pearson, Appl. Phys. Lett. **26**, 564 (1975).
12. T. Kobayashi *et al*., IEEE J. Quantum Electron. **24**, 382 (1988).
13. B. H. Kolner, Appl. Phys. Lett. **52**, 1122 (1988).
14. A. A. Godil, B. A. Auld, and D. M. Bloom, Appl. Phys. Lett. **62**, 1047 (1993).
15. M. T. Kauffman *et al*., Electron. Lett. **29**, 268 (1993).
16. A. A. Godil, B. A. Auld, and D. M. Bloom, IEEE J. Quantum Electron. **30**, 827 (1994).
17. W. R. Donaldson, R. Boni, R. L. Keck, and P. A. Jaanimagi, Rev. Sci. Instrum. **73**, 2606 (2002).
18. R. A. Lerche, J. W. McDonald, R. L. Griffith, G. Vergel de Dios, D. S. Andrews, A. W. Huey, P. M. Bell, O. L. Landen, P. A. Jaanimagi, and R. Boni, Rev. Sci. Instrum. **75**, 4042 (2004).
19. J. Qiao, P. A. Jaanimagi, R. Boni, J. Bromage, and E. Hill, Rev. Sci. Instrum. **84**, 073104 (2013).
20. B.-L. Qian and H. E. Elsayed-Ali, J. Appl. Phys. **91**, 462 (2002).
21. B. J. Siwick *et al*., J. Appl. Phys. **92**, 1643 (2002).
22. A. Verna *et al*., J. Electron. Spectrosc. Relat. Phenom. **209**, 14 (2016).
23. M. T. Kauffman *et al*., Appl. Phys. Lett. **64**, 270 (1994).
24. M. A. Foster, R. Salem, and A. L. Gaeta, Opt. Photonics News **22**, 29 (2011).
25. G. P. Agrawal, *Nonlinear Fiber Optics*, 5th ed. (Elsevier, Amsterdam, 2013).
26. B. H. Kolner, J. Opt. Soc. Am. A **11**, 3229 (1994).
27. I. Kang, C. Dorrer, and F. Quochi, Opt. Lett. **28**, 2264 (2003).

The Ninth Omega Laser Facility Users Group Workshop

Introduction

The Ninth Omega Laser Facility Users Group (OLUG) Workshop was held at the Laboratory for Laser Energetics (LLE) on 26–28 April 2017. It was attended by 110 researchers, including scientists, postdoctoral fellows (postdocs), and students (Fig. 152.20). The attendees represented institutions from five countries, including the U.S., UK, France, Spain, and Hungary. As has been the case for previous workshops, postdocs and students received travel support to attend the workshop from the Department of Energy's (DOE's) National Nuclear Security Administration (NNSA).

The Workshop Program

The OLUG program included the following four invited talks: "Exploring the Structure of Extra Solar Planets Using the OMEGA Laser," by Tom Duffy (Princeton University) (Fig. 152.21); "Systematic Fuel Cavity Asymmetries in

U2183JR

Figure 152.21
Tom Duffy (Princeton University) gave a talk on exploring the structure of extrasolar planets using the OMEGA Laser System.

U2182JR

Figure 152.20
A group photo of the Ninth Omega Laser Facility Users Group Workshop attendees.

Directly Driven ICF Implosions," by Rahul Shah [Los Alamos National Laboratory (LANL)] (Fig. 152.22); "Fast-Electron Transport in Warm and Hot Dense Plasmas," by Farhat Beg [University of California, San Diego (UCSD)] (Fig. 152.23); and "Using Multi-Hohlraum Arrays for Studying the Pillars of Creation," by David Martinez [Lawrence Livermore National Laboratory (LLNL)] (Fig. 152.24). DOE's NNSA perspective was presented by ICF Program Director Njema Frazier. Other highlights included an evening tutorial, "X-Ray Imaging at OMEGA," offered by Chuck Sorce (LLE); a facility talk, "Omega Facility Update and Progress on OLUG Recommendations," by Sam Morse (LLE); research talks by representatives from LLE and the national laboratories [Mike Campbell, LLE; Peter Celliers, LLNL; Kirk Flippo, LANL; and Kyle Peterson, Sandia National Laboratories (SNL)]; a lunch round-table discussion on career opportunities in high-energy-density science, the student and postdoc panel; and a discussion of OLUG's Findings and Recommendations with LLE management. In addition, LLE staff organized tours of the OMEGA and OMEGA EP lasers (Fig. 152.25). The lunch round-table discussion on career opportunities followed up on the talks from laboratory representatives on Thursday morning and gave the students and postdocs an opportunity to engage in a relaxed and productive discussion with laboratory researchers (Fig. 152.26). The round-table discussion was a new activity of the workshop introduced this year. It was very well received by

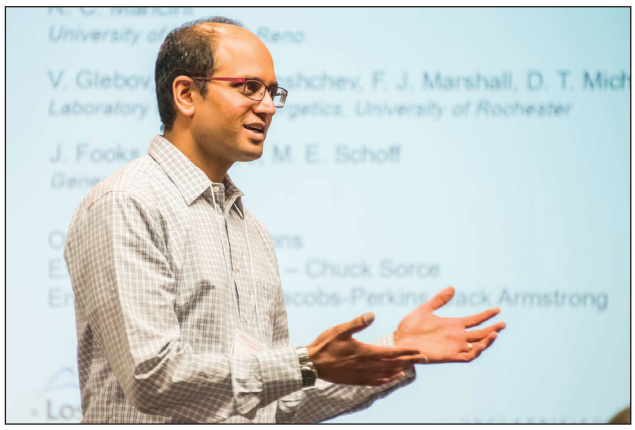

U2184JR

Figure 152.22
Rahul Shah (LANL) gave a talk on systematic fuel cavity asymmetries in directly driven ICF implosions.


U2186JR

Figure 152.24
David Martinez (LLNL) gave a talk on using multi-hohlraum arrays for studying the pillars of creation.


U2185JR

Figure 152.23
Farhat Beg (UCSD) gave a talk on fast-electron transport in warm and hot dense plasmas.


U2192JR

Figure 152.25
LLE staff organized tours of OMEGA and OMEGA EP. In this photo David Canning explains the OMEGA EP Laser System to a group of students and postdocs.

U2190JR

Figure 152.26
A lunch round-table discussion on career opportunities in high-energy density followed up on talks by national laboratory representatives.

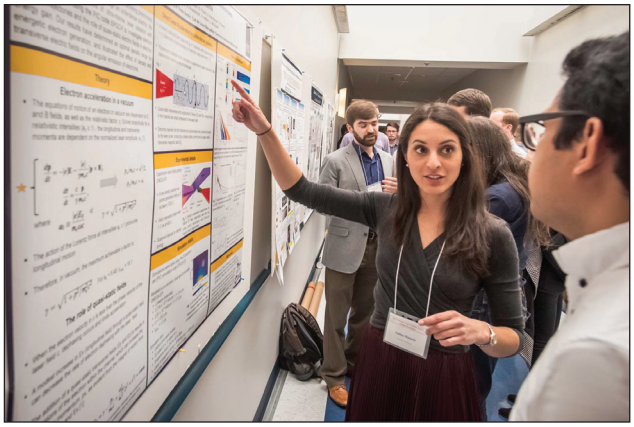

U2187JR

Figure 152.27
Amina Hussein (University of Michigan) discusses her poster on particle-in-cell simulations of laser-accelerated electrons in underdense plasmas.

students and postdocs, and it will be continued and expanded in future workshops to include scientists working in universities and industry.

Student, postdoc, scientist, and facility posters comprised a total of 62 poster presentations that were organized in three poster sessions. Of the total number, 46 posters were presented by graduate students and postdocs. In addition, six posters were presented by undergraduate students, and two posters were presented by high school students who had participated in LLE's 2016 Summer High School Research Program (Figs.152.27–152.29).

Student and Postdoc Poster Awards

In an effort to promote and reward excellence in young researchers, the posters presented at the OLUG Workshop by students and postdocs were reviewed and ranked by a committee of scientists. As a result, honorable mentions and prizes were

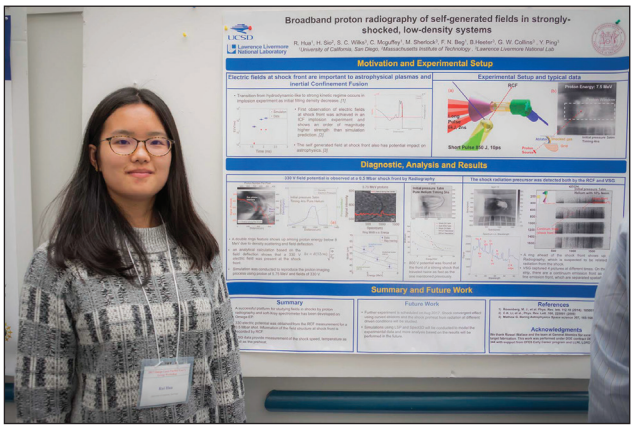

U2188JR

Figure 152.28
Rui Hua (UCSD) presented a poster on broadband proton radiography of self-generated fields in strongly shocked, low-density systems.

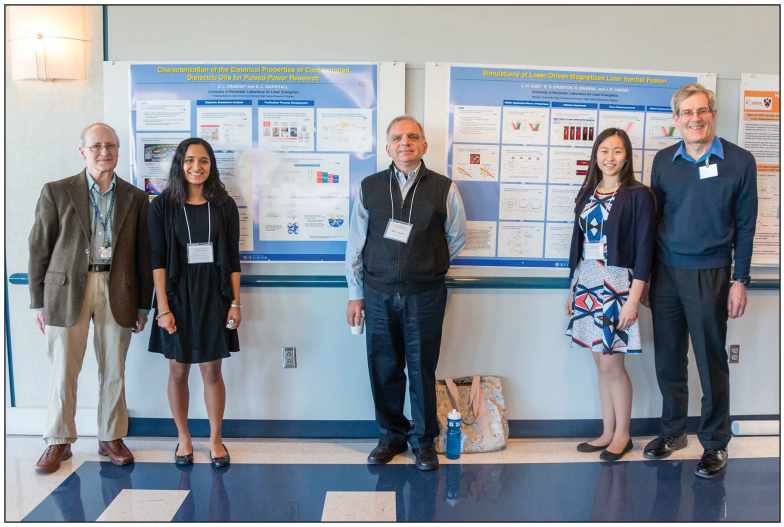

U2191JR

Figure 152.29
Sapna Ramesh from Pittsford Mendon High School and her mentor Kenneth Marshall (left) and Leah Xiao from Webster Schroeder High School and her mentor Stephen Craxton (right) presented posters based on their summer internships at LLE. In the center is OLUG chair Roberto Mancini.

awarded to those posters at the top of the ranking. The following are the awards granted during this OLUG Workshop (Fig. 152.30).

U2193JR

Figure 152.30
Student and postdoc poster awardees. From left to right: Craig Sangster, Derek Nasir, Hans Rinderknecht, Hong Sio, Archie Bott, Luke Ceurvorst, Paul Campbell, Samuel Totorica, and Maria Gatu Johnson. Craig Sangster and Maria Gatu Johnson led the poster awardees selection process.

Undergraduate Students

First place ($250): Katelyn Cook and Micah Coates, Houghton College, "Measurement of the ^{6}He Decay Produced by the ^{9}Be(n,α)^{6}He Reaction"

Honorable Mention ($75): Hannah Harrison, Hannah Visca, David Chin, and Praveen Wakwella, State University of New York (SUNY), Geneseo, "Characterizing Neutron Diagnostics on the nTOF Line at SUNY Geneseo" (Fig. 152.31)

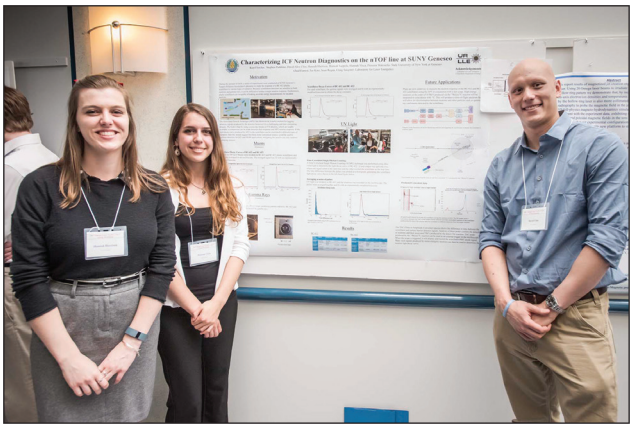

U2189JR

Figure 152.31
Undergraduate students Hannah Harrison, Hannah Visca, and David Chin (left to right) presented a poster on characterizing ICF neutron diagnostics on the neutron time-of-flight line at the SUNY, Geneseo.

Graduate Students

First place ($250): Hong Sio, Massachusetts Institute of Technology (MIT), "Probing Kinetic and Multi-Ion Fluid Effects in ICF Implosions Using DT and D^{3}He Reaction Time-Histories on OMEGA"

Second place ($175): Archie Bott, University of Oxford, "Proton Imaging of Stochastic Magnetic Fields"

Third place ($100): Paul Campbell, University of Michigan, "X-Ray and Electron Measurements of Relativistic Magnetic Reconnection in Layered Targets and Preformed Plasmas"

Honorable mentions ($75): Derek Nasir, Ohio State University, "Enhanced Laser Plasma Interaction Using Micro-Structured Targets"

Luke Ceurvorst, University of Oxford, "Implications for Channel Formation in ICF from Observations of mm-Scale Plasmas at Omega EP"

Samuel Totorica, Stanford University, "Plasmoid Formation and Particle Acceleration in Laser-Driven Magnetic Reconnection"

Postdoctoral Fellows

First place ($250): Hans Rinderknecht, LLNL, "Measurements of Shock-Front Structure in Multi-Species Plasmas"

Honorable mention ($75): Edward Marley, LLNL, "Development of a Buried Layer Platform at the OMEGA Laser to Study Non-Equilibrium Coronal Plasmas"

Nominations and Election

In the winter of 2017, a nominating committee was established to request nominations for the election of three new executive committee (EC) members according to the guidelines of OLUG's bylaws. The nominating committee was comprised of Mark Koepke [West Virginia University (WVU), Chair] (Fig. 152.32), Ray Leeper (LANL), and Chris McGuffey (UCSD). The nominations for the three new members of OLUG's EC were to include one representative from a U.S. university/small business, one representative from a national laboratory/major business, and one representative from non-U.S. researchers. Once again, we had an excellent group of nominees who agreed to put their name on the ballot and were willing to serve on the EC if elected. The election resulted in the selection of Maria Gatu Johnson from MIT, Channing Huntington from LLNL, and Alexis Casner from the University of Bordeaux, France, as new members of the EC. Taking

U2194JR

Figure 152.32
Mark Koepke (WVU) explained the annual nominations and election process carried out in the winter of 2017 that led to the election of three new members of OLUG's Executive Committee.

into account the newly elected members as well as those who continue from the previous year, the EC of OLUG for the year April 2017–April 2018 will comprise the following members:

- U.S. university/small business: Roberto Mancini [University of Nevada, Reno (UNR), Chair], Mark Koepke (WVU, Vice Chair), Maria Gatu Johnson (MIT), and Johan Frenje (MIT)
- National laboratory/major business: Peter Celliers (LLNL), Channing Huntington (LLNL), and Mingsheng Wei [General Atomics (GA)]
- Junior researcher: Alex Zylstra (LANL)
- Non-U.S. researcher: Alexis Casner (University of Bordeaux, France)
- LLE, ex-officio: Jim Knauer

The three new EC members replaced Paul Drake (University of Michigan), Kirk Flippo (LANL), and Peter Norreys (Rutherford Laboratory, UK) who stepped down from the EC after completing their terms. The OLUG EC is very grateful to Paul Drake, Kirk Flippo, and Peter Norreys for their service in the EC and their contributions to the success of OLUG (Fig. 152.33).

Summary of Findings and Recommendations

An important outcome of OLUG's annual workshop is the list of Findings and Recommendations that OLUG submits for consideration to LLE's management every year. The 2017 Findings and Recommendations are summarized below, including those put forward by the student and postdoc panel (Fig. 152.34).

1. An increase in the NLUF shot allocation to advance fundamental high-energy-density science and student/postdoc training.

2. An opposing beam configuration for OMEGA EP.

3. Development of the capability for an absolute measurement of Raman backscattered light.

4. A distributed phase plate (DPP)–smoothed, nanosecond-duration beam with small focal spot on OMEGA EP.

5. Additional heated tritium-fill cells for filling glass capsules.

6. A facility-owned ten-inch manipulator (TIM)–mounted, DMX-type instrument to spectrally characterize x-ray drives on OMEGA EP.

U2195JR

Figure 152.33
OLUG Executive Committee members and ICF Program Director Njema Frazier from NNSA. From left to right, front row: Maria Gatu Johnson (MIT), Mingsheng Wei (GA), Roberto Mancini (UNR, Chair), Njema Frazier (NNSA), Johan Frenje (MIT), and Peter Celliers (LLNL). From left to right, back row: Alex Zylstra (LANL), Kirk Flippo (LANL), Mark Koepke (WVU, Vice Chair), and Peter Norreys (Rutherford Laboratory, UK).

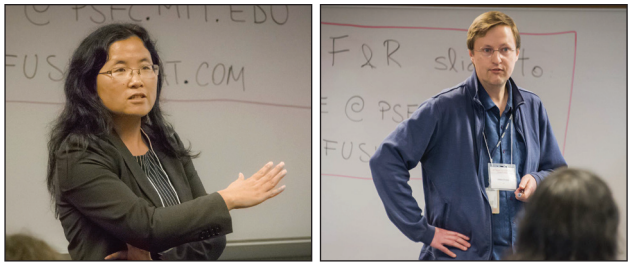

U2304JR

Figure 152.34
(a) Mingsheng Wei (GA) and (b) Johan Frenje (MIT) led the Findings and Recommendations discussion and presentation to LLE management on Friday morning.

7. More options of spectral range coverage for the imaging x-ray Thomson spectrometer (IXTS) and high-resolution spectrometer 2 (HRS2).

8. An optical Thomson-scattering capability for OMEGA EP.

9. An update/expansion of the flat-fielding database of x-ray framing cameras.

10. A Dante radiation temperature analysis and time-history result available during shot day.

11. Several upgrades and improvements of the active shock breakout (ASBO) and streak optical pyrometer diagnostics, including (a) suppressing the "wiggles" in OMEGA EP ASBO, (b) a smaller field of view to accommodate smaller targets, (c) an absolute calibration of OMEGA EP ASBO, (d) faster timing combs, and (e) a centralized server to archive and make available all necessary calibration details.

12. A three-wavelength VISAR (velocity interferometer system for any reflector) for OMEGA EP.

13. Improving the beam combiner optic lifetime and/or replacement capability to support year-round interleaved joint OMEGA–OMEGA EP shots.

14. The option of taking photos of OMEGA EP shots.

15. Investigating the extension of the duration of OMEGA EP UV beams to 15 to 20 ns.

16. Investigating the feasibility of splitting one of the OMEGA EP short-pulse beams into two focal spots.

17. Continuing the work to improve the Principal Investigator (PI) portal and web-based resources, in particular, with emphasis on data permission access.

18. A web-based system and better microphones for pre-shot briefings so offsite attendees can improve their involvement and participation in the discussions.

19. The addition of a web-based meeting option to Monday morning's experiment briefings so PI's who want to join the meeting after their experiment can do so.

U2196JR

Figure 152.35
OLUG Chair Roberto Mancini (UNR) adjourned the workshop with the announcement of the "mid-year" meeting of OLUG at the 2017 APS Division of Plasma Physics conference and the next annual OLUG Workshop in April 2018.

ACKNOWLEDGMENT

This OMEGA Laser Facility Users Group Workshop was made possible in part by the generous support of the National Nuclear Security Administration of the U.S. Department of Energy for travel expenses of students and postdocs; by the Physics Department at the University of Nevada, Reno; and by the Laboratory for Laser Energetics at the University of Rochester for the use and availability of critical resources and support. In addition, OLUG thanks the LLE management for their responsiveness to our Findings and Recommendations. For capturing through his lens the workshop ambiance, OLUG thanks Eugene Kowaluk. Roberto Mancini is the editor for this Proceeding.

LLE's Summer High School Research Program

During the summer of 2017, 11 students from Rochester-area high schools participated in the Laboratory for Laser Energetics' Summer High School Research Program. The goal of this program is to excite a group of high school students about careers in the areas of science and technology by exposing them to research in a state-of-the-art environment. Too often, students are exposed to "research" only through classroom laboratories, which have prescribed procedures and predictable results. In LLE's summer program, the students experience many of the trials, tribulations, and rewards of scientific research. By participating in research in a real environment, the students often become more excited about careers in science and technology. In addition, LLE gains from the contributions of the many highly talented students who are attracted to the program.

The students spent most of their time working on their individual research projects with members of LLE's technical staff. The projects were related to current research activities at LLE and covered a broad range of areas of interest including laser physics, computational modeling of implosion physics, experimental diagnostic development, laser system diagnostics, physical chemistry, cryogenic target characterization, and web-based data analysis (see Table 152.III).

Table 152.III: High School Students and Projects—Summer 2017.

Name	High School	Supervisor	Project Title
Viknesh Baskar	Webster Schroeder	J. P. Knauer and C. J. Forrest	Ion Temperature Analysis of Neutron Time-of-Flight Data
Nikhil Bose	Pittsford Sutherland	M. J. Guardalben	Compensation for Self-Focusing on OMEGA EP by Use of Frequency Conversion
Benjamin Chaback	Byron Bergen	J. P. Knauer and C. J. Forrest	Modeling and Analysis of Cherenkov Radiation Detectors
Meshach Cornelius	Gates Chili	T. Walker and G. Brent	Characterization and Detection of the Deterioration of Electrical Connectors in a Flash-Lamp System
Griffin Cross	Pittsford Sutherland	W. T. Shmayda	Studying the Hydrogen-Palladium System at Low Temperatures
Matthew Galan	Fairport	R. W. Kidder	Data Services for Scientific Analysis on OMEGA and OMEGA EP
Claire Guo	Penfield	A. Bose and R. Epstein	Analysis of Asymmetries of the Hot Spot Using Synthetic X-Ray Images
Joyce Luo	Pittsford Mendon	K. L. Marshall	Ambient-Temperature Ammonia Removal Process for Sol-Gel Coating Solutions
Jonathan Moore	Pittsford Sutherland	M. D. Wittman and A. Kalb	Predetermination of DT Fuel Mass in Cryogenic Target Capsules from Any Viewing Angle
Arian Nadjimzadah	Brighton	W. T. Shmayda	Modifying Stainless-Steel Surfaces by Electropolishing
Yujia Yang	Brighton	R. S. Craxton	Improving the Uniformity of *Revolver* Designs for the National Ignition Facility

The students attended weekly seminars on technical topics associated with LLE's research. Topics this year included laser physics, fusion, holography, nonlinear optics, atomic force microscopy, laser focusing, and pulsed power. The students also received safety training, learned how to give scientific presentations, and were introduced to LLE's resources, especially the computational facilities.

The program culminated on 30 August with the "High School Student Summer Research Symposium," at which the students presented the results of their research to an audience including parents, teachers, and LLE staff. The students' written reports will be made available on the LLE Website and bound into a permanent record of their work that can be cited in scientific publications.

Three hundred and sixty-four high school students have now participated in the program since it began in 1989. This year's students were selected from approximately 60 applicants.

At the symposium LLE presented its 21st annual William D. Ryan Inspirational Teacher Award to Mrs. Lois Houlihan, a chemistry teacher at Pittsford Mendon High School. This award is presented to a teacher who motivated one of the participants in LLE's Summer High School Research Program to study science, mathematics, or technology and includes a $1000 cash prize. Teachers are nominated by alumni of the summer program. Mrs. Houlihan was nominated by Sapna Ramesh, a participant in the 2016 program. Sapna wrote, "Mrs. Houlihan cares deeply about all her students and does everything she can to help them succeed… She goes above and beyond to encourage her students… Her teaching style is also very unique and practical. Whenever we went over a new topic in class, Mrs. Houlihan would start off by asking us about the practical uses of the concept, such as in medicine or industry. She makes a point of learning about each student's interests and background… Instead of teaching to the test, Mrs. Houlihan wants to spark an interest in science and technology in her students." Sapna acknowledged her personal debt to Mrs. Houlihan: "In terms of encouraging students, Mrs. Houlihan is the reason that I applied to the summer internship at the Laser Lab… I feel blessed to have had Mrs. Houlihan as a teacher, because she was the first teacher I really connected with. The thing with Mrs. Houlihan is that she has high expectations for each and every student she teaches, but also helps everyone individually to push their limits and reach her expectations." Sapna concluded by saying, "All in all, Mrs. Houlihan has inspired me and many of her other students to love chemistry and science in general. Not only that, but she has opened my eyes to the practical applications of chemistry in the world. I think the best thing about Mrs. Houlihan is that it is obvious that she enjoys teaching, but her greatest joy is seeing her students succeed in college and beyond." Ms. Houlihan also received strong support from Mr. Karl Thielking, Principal of Pittsford Mendon High School, who described her as a caring and dedicated teacher with a passion for chemistry.

FY17 Laser Facility Report

During FY17, the Omega Laser Facility conducted 1353 target shots on OMEGA and 785 target shots on OMEGA EP for a total of 2138 target shots (see Tables 152.IV and 152.V). OMEGA averaged 10.7 target shots per operating day with Availability and Experimental Effectiveness averages for FY17 of 95.7% and 94.4%, respectively.

OMEGA EP was operated extensively in FY17 for a variety of internal and external users. A total of 773 target shots were taken into the OMEGA EP target chamber and 12 joint target shots were taken into the OMEGA target chamber. OMEGA EP averaged 8.7 target shots per operating day with Availability

Table 152.IV: OMEGA Laser System target shot summary for FY17.

Laboratory	Planned Number of Target Shots	Actual Number of Target Shots	ICF	Shots in Support of ICF	Non-ICF
CEA	39	47	—	—	47
CELIA	17	18	—	—	18
HED	418	471	—	—	471
LBS	121	132	—	—	132
LLE	396	377	—	377	—
LLNL	77	78	78	—	—
NLUF	154	180	—	—	180
SNL	11	15	15	—	—
ARPA-E	17	10	—	—	10
Calibration	0	25	—	25	—
Total	1250	1353	93	402	858

Table 152.V: OMEGA EP Laser System target shot summary for FY17.

Laboratory	Planned Number of Target Shots	Actual Number of Target Shots	ICF	Shots in Support of ICF	Non-ICF
CEA	7	12	—	—	12
HED	210	296	—	—	296
LBS	49	67	—	—	67
LLE	98	132	—	132	—
LLNL	28	35	35	—	—
NLUF	112	139	—	—	139
NRL	21	24	24	—	—
SNL	21	29	29	—	—
Calibration	0	51	—	51	—
Total	546	785	88	183	514

and Experimental Effectiveness averages for FY17 of 95.8% and 96.6%, respectively.

Highlights of Achievements in FY17

1. 100-Gbar Campaign

The OMEGA Laser System is the preeminent direct-drive laser facility. It capitalizes on the benefits of a spherically symmetric laser configuration and high-uniformity focal spots to conduct implosion and high-energy-density–physics experiments. In FY16, LLE embarked on a campaign to seek higher implosion pressures through improved laser power balance and a cryogenic fill-tube target system. In FY17, significant progress was made in these two areas.

LLE has continued the effort to temporally balance the energy over 100-ps sections of the pulse shape. To achieve this, each of the beamlines of OMEGA must balance passive transmission losses and active gain between each of the 60 beams. During earlier characterization of transmission, amplifier losses were directly linked to observed surface scattering. In FY17, 23 amplifier disks were precision cleaned, resulting in a direct increase in transmission and improved balance of passive transmission in the amplifier stages. After a study of the frequency-conversion process was concluded, the second tripler optics were removed since the current three-color-cycle smoothing by spectral dispersion (SSD) does not require a dual-tripler setup. This removal eliminated a source of loss and imbalance in the system. A set of 15 rover calorimeters has been deployed to expedite System Science measurements of the gain and loss of each stage. With dedicated system time, the power imbalance has been cut in half to 3%. Numerous efforts have begun to expand our capability to characterize the system: LLE is working on a full-beam-in-tank (FBIT) diagnostic to observe the focal spot after UV transport; a modification to the streak-camera diagnostic that will improve signal integrity by eliminating fluorescence in the fiber; stage-F digital alignment cameras (to characterize losses caused by pre-shot optics damage); and a passive IR beam-transmission diagnostic that will not require amplified laser shots.

In FY17 significant strides were made on two additional efforts required to reach our goal of 100-Gbar pressure. Achieving the highest uniformity is dependent on the target placement at the time of the implosion. Vibrations have been a major source of target offsets. The moving cryostat transfer carts were outfitted with a vibration isolation stage that uses eddy current feedback to actively damp vibrations. It is difficult to quantify the effect of just these isolators because other changes were also made but the overall improvement is sufficient to achieve ~60% of all targets positioned to less than 10 μm (see Fig. 152.36).

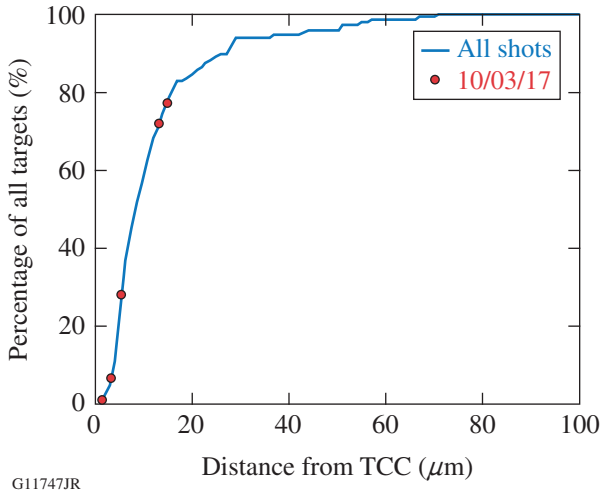

Figure 152.36
Cryogenic DT target positioning accuracy for FY15–FY17, including position data for the five most-recent shots. TCC: target chamber center.

Early theoretical predictions showed that the targets must have nonpermeable capsules to optimize the ablator.[1] A cryogenic fill-tube project is underway to provide for this need on OMEGA and to augment the permeation fill system. In FY17, a DT fill-tube target was successfully layered in the laboratory. By FY20, this system will be able to fill, characterize, and deliver a target to OMEGA.

2. Cross-Beam Energy Transfer Mitigation Study

Longer-term improvements to the laser–plasma interaction physics will require mitigation of cross-beam energy transfer (CBET). This phenomena must be characterized to fully understand how to design a system that minimizes the coupling loss to direct-drive capsules that diverts ~30% of the hydrodynamic drive of implosion capsules. LLE chose to utilize OMEGA EP to produce a tunable UV beam and inject it into the OMEGA target chamber to study CBET. This is an efficient design because it utilizes many of the existing OMEGA EP subsystems with little or no modifications. This effort consists of two main subprojects: (1) The installation and activation of a tunable wavelength source laser injected into the optical parametric amplifier (OPA) system on Beamline 1. The tunable laser was installed in Q3 and is being activated. (2) Transport of the UV beam from the OMEGA EP Bay to port P9 in the OMEGA target chamber. Final design of this project was completed in FY17, and fabrication and installation are underway. Closely tied to this effort, a gas-jet target system has been deployed on OMEGA to produce highly uniform, low-density plasma. This produces the optimum environment to study the interactions of OMEGA beams with the new tunable laser.

3. Improvements to the Laser Systems

The OMEGA EP short-pulse diagnostic package was augmented with a new ultrafast temporal diagnostic able to measure pulse widths between best compression and 100 ps. This feat—achieved with a phase-diversity technique in a fiber pulse stacker[2]—has increased the permissible energy on target for pulses between best compression and 10 ps. This diagnostic is utilized in shot preparations for ensuring proper configuration and also for an on-shot measurement with improved accuracy. Other front-end improvements include the expansion of a time-multiplexed pulse-shaping system to OMEGA EP. Currently deployed on Beamlines 3 and 4, this subsystem allows a single higher-resolution waveform generator to feed the independent OMEGA EP beams and will minimize jitter between pulses. On OMEGA, an improved SSD spectrometer is being used to monitor bandwidth up to the time of shot and to ensure that the phase modulators are operating to specification.

4. Improvements to Target Diagnostics

Diagnostic improvements continue to expand the capabilities of the laser systems. On OMEGA EP, a high-resolution spectrometer has been deployed with the ability to measure time-resolved x-ray spectra over a range that includes the Cu K_α lines. This diagnostic is housed in a 4π lead enclosure to optimize the signal-to-noise ratio (SNR) by preventing scattered x-ray signals from reaching the sensor. The 4ω probe diagnostic has been upgraded with an interferometry arm.

A single-line-of-sight, time-resolved x-ray imager (SLOS-TRXI), developed in conjunction with General Atomics, Lawrence Livermore National Laboratory, Sandia National Laboratories, and Kentech Instruments Ltd., has been deployed on OMEGA to measure hot-spot self-emission with a temporal resolution of 40 ps and spatial resolution of 10 μm. Unique in its ability to take multiple pinhole images along a single axis, this hardware represents the first phase in development with improvements in the areas of throughput and spatial resolution to follow.

LLE continues to design and develop improved diagnostics for characterizing experiments. A neutron time-of-flight diagnostic is being deployed on the H10 port with significant improvement to the SNR. The powder x-ray diffraction diagnostic is being upgraded to acquire time-resolved images.

REFERENCES

1. V. N. Goncharov, T. C. Sangster, R. Betti, T. R. Boehly, M. J. Bonino, T. J. B. Collins, R. S. Craxton, J. A. Delettrez, D. H. Edgell, R. Epstein, R. K. Follet, C. J. Forrest, D. H. Froula, V. Yu. Glebov, D. R. Harding, R. J. Henchen, S. X. Hu, I. V. Igumenshchev, R. Janezic, J. H. Kelly, T. J. Kessler, T. Z. Kosc, S. J. Loucks, J. A. Marozas, F. J. Marshall, A. V. Maximov, R. L. McCrory, P. W. McKenty, D. D. Meyerhofer, D. T. Michel, J. F. Myatt, R. Nora, P. B. Radha, S. P. Regan, W. Seka, W. T. Shmayda, R. W. Short, A. Shvydky, S. Skupsky, C. Stoeckl, B. Yaakobi, J. A. Frenje, M. Gatu-Johnson, R. D. Petrasso, and D. T. Casey, Phys. Plasmas **21**, 056315 (2014).

2. C. Dorrer, L. J. Waxer, A. Kalb, E. M. Hill, and J. Bromage, Opt. Express **23**, 33,116 (2015).

National Laser Users' Facility and External Users' Programs

Under the facility governance plan implemented in FY08 to formalize the scheduling of the Omega Laser Facility as a National Nuclear Security Administration (NNSA) User Facility, Omega Facility shots are allocated by campaign. The majority (68.1%) of the FY17 target shots were allocated to the Inertial Confinement Fusion (ICF) Campaign conducted by integrated teams from Lawrence Livermore National Laboratory (LLNL), Los Alamos National Laboratory (LANL), Naval Research Laboratory (NRL), Sandia National Laboratories (SNL), and LLE; and to the High-Energy-Density (HED) Campaigns conducted by teams led by scientists from the national laboratories, some with support from LLE.

The Fundamental Science Campaigns accounted for 24.2% of the Omega Laser Facility target shots taken in FY17. Nearly 62% of these shots were dedicated experiments under the National Laser Users' Facility (NLUF) Program, and the remaining shots were allotted to the Laboratory Basic Science (LBS) Program, comprising peer-reviewed fundamental science experiments conducted by the national laboratories and by LLE.

The Omega Laser Facility was also used for several campaigns by teams from the Commissariat à l'énergie atomique et aux énergies (CEA) of France. These programs are conducted at the facility on the basis of special agreements put in place by Department of Energy (DOE)/NNSA and participating institutions.

In this section, we briefly review all the external user activity at the Omega Laser Facility during FY17.

FY17 NLUF Program

During the first quarter of fiscal year 2017 (FY17), the Inertial Fusion Office of DOE/NNSA completed a solicitation, review, and selection process for NLUF experiments to be conducted at the Omega Laser Facility during calendar years (CY's) 2017 and 2018. Twenty-eight proposals were submitted in response to the call for proposals, and the shot requests totaled 60.5 shot days at the Omega Laser Facility. The proposals were peer reviewed by an independent review committee, and ICF/NNSA selected 13 proposals for funding and shot allocation for CY17–CY18.

CY17 was the first of a two-year period of performance for these 13 NLUF projects (Table 152.VI). In addition, several NLUF campaigns completed experiments during FY17 that had been approved during the FY15–FY16 NLUF cycle. In total, 319 target shots were taken for NLUF projects during FY17. The NLUF experiments conducted at the facility during FY17 are summarized in this section.

A critical part of the NLUF program is the education and training of graduate students in high-energy-density physics. During the year, 33 graduate students from nine universities participated in experiments conducted under the NLUF program at the Omega Laser Facility (Table 152.VII).

Transport of Relativistic Electrons in Cylindrically Imploded Magnetized Plasmas

Principal Investigator: F. N. Beg [University of California, San Diego (UCSD)]

Co-investigators: P. Forestier-Colleoni, M. Dozières, and C. McGuffey (UCSD); M. S. Wei and C. M. Krauland [General Atomics (GA)]; P. Gourdain, J. R. Davies, and E. M. Campbell (LLE); S. Fujioka (University of Osaka); and J. J. Santos and D. Batani (University of Bordeaux)

In the fast-ignition (FI) scheme of ICF, fuel compression to high densities and temperatures is achieved in separate processes. A high-energy (≥100-kJ), high-intensity ($\geq 10^{20}$-W/cm^2) short-pulse (~10-ps) laser is first used to create high-energy (~MeV) electrons (or ions), which then heat the precompressed fuel plasma to initiate ignition. One critical issue is the knowledge of the energy and number of relativistic electrons that can reach, and effectively heat, the core plasma. This unresolved issue warrants a new approach to observe the spatial energy deposition of relativistic electrons.

The objective of the UCSD NLUF project in collaboration with GA, LLE, the University of Bordeaux, and the University

of Osaka is to systematically investigate the propagation and energy deposition of relativistic electrons in a preassembled cylindrical plasma under controlled conditions of density and temperature with and without an external magnetic field. Understanding the role of an external magnetic field in relativistic electron transport and energy deposition is important for several applications including ICF FI, isochoric heating, and the study of warm dense matter.

Our first NLUF experiment in 2017, which measured the time-dependent plasma conditions of an imploded cylinder with and without an external magnetic field, was successfully performed in the OMEGA chamber. This will be useful for the second experiment, which will reveal the temporal evolution of the plasma conditions with fast-electron energy deposition. In the first experiment, 36 beams (0.3 TW/beam, 1.5-ns square pulse) of the OMEGA laser were used to compress a Cl-doped CH foam cylinder to reach densities close to 7 g/cm^3. This implosion was characterized by two main diagnostic techniques: proton deflectometry and Cl spectroscopy. A schematic of the experimental layout is shown in Fig. 152.37. The cylinder (600-μm outer diameter and 540-μm inner diameter) was filled with 0.1 g/cm^3 of CH foam doped with 1% of Cl. In addition, one Cu foil and one Zn foil were attached to the cylinder's surface to decrease the magnetic mirror effect and allow K_α emissions during the second shot day. The protons used in proton deflectometry were created by a compressed D^{3}He capsule producing two energy populations: 3.5 MeV and 13 MeV. These protons, collected by CR-39, provided an image of the imploded cylinder deformed by the presence of the magnetic field. The Cl spectroscopy focused on the x-ray absorption of Cl 1*s*–2*p* transitions detected on axis. The back-

Table 152.VI: NLUF projects approved for FY17–FY18 funding and Omega Laser Facility shot allocations.

Principal Investigator	Institution	Title
A. Battacharjee	Princeton University	Dynamics of Magnetic Reconnection in High-Energy-Density Plasmas
F. N. Beg	University of California, San Diego	Transport of Relativistic Electrons in Cylindrically Imploded Magnetized Plasmas
R. P. Drake	University of Michigan	Experimental Astrophysics on the OMEGA Laser
T. S. Duffy	Princeton University	Phase Transitions and Crystal Structure of Tin Dioxide at Multi-Megabar Pressures
R. Jeanloz	University of California, Berkeley	High-Energy-Density Chemical Physics and Planetary Evolution
H. Ji	Princeton University	Particle Acceleration Resulting from Magnetically Driven Reconnection Using Laser-Powered Capacitor Coils
K. Krushelnick	University of Michigan	X-Ray Measurements of Laser-Driven Relativistic Magnetic Reconnection Using OMEGA EP
D. Q. Lamb	University of Chicago	Properties of Magnetohydrodynamic Turbulence in Laser-Produced Plasmas
R. Mancini	University of Nevada, Reno	Development of a Photoionized Plasma Experiment on OMEGA EP
R. D. Petrasso	Massachusetts Institute of Technology	Explorations of Inertial Confinement Fusion, High-Energy-Density Physics, and Laboratory Astrophysics
A. Spitkovsky	Princeton University	Study of Magnetized Collisionless Shocks in Laser-Produced Plasmas
D. Stutman	Johns Hopkins University	Demonstration of Talbot–Lau X-Ray Deflectometry Electron Density Diagnostic in Laser–Target Interactions
M. S. Wei	General Atomics	Hot-Electron Generation with 10^{16}-W/cm^2 Infrared Lasers in Shock-Ignition–Relevant Conditions

Table 152.VII: Graduate students participating in NLUF experiments in FY17.

Name	University	PI
Rui Hua	UCSD	Beg
Jonathan Peebles	UCSD	Beg
Shu Zhang	UCSD	Beg
Adrianna Angulo	University of Michigan	Drake
Patrick X. Belancourt	University of Michigan	Drake
Shane Coffing	University of Michigan	Drake
Joshua Davis	University of Michigan	Drake
Laura Elgin	University of Michigan	Drake
Jeff Fein	University of Michigan	Drake
Heath LeFevre	University of Michigan	Drake
Alex Rasmus	University of Michigan	Drake
Robert Vandervort	University of Michigan	Drake
Joseph Levesque	University of Michigan	Drake/ Hartigan
Rachel Young	University of Michigan	Drake/ Hartigan
Rajkrishna Dutta	Princeton	Duffy
Donghoon Kim	Princeton	Duffy
Han Sirus	Princeton	Duffy
Jack Matteucci	Princeton	Fox/ Schaeffer
Peter Heuer	UCLA/Princeton	Schaeffer
Abraham Chien	Princeton	Ji
Andrew Liao	Rice University	Hartigan
Thomas Batson	University of Michigan	Krushelnick
Paul Campbell	University of Michigan	Krushelnick
Amina Hussein	University of Michigan	Krushelnick
Archie Bott	Oxford University/ University of Chicago	Lamb
Alexandra Rigby	Oxford University/ University of Chicago	Lamb
Patrick Adrian	MIT	Petrasso
Neel Kabadi	MIT	Petrasso
Brandon Lahmann	MIT	Petrasso
Raspberry Simpson	MIT	Petrasso
Hong Sio	MIT	Petrasso
Graeme Sutcliffe	MIT	Petrasso
Cole Holcomb	Princeton	Spitkovsky

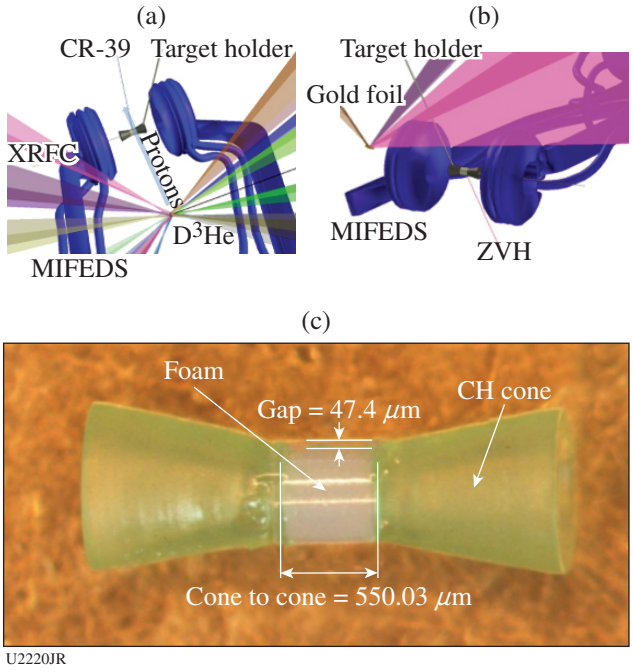

Figure 152.37
Schematic of (a) the proton deflectometry setup of the experiment in the OMEGA chamber and (b) the Cl-spectroscopy setup of the experiment in the OMEGA chamber; (c) a cylinder target with cones (made by GA) to prevent plasma interaction with the cylinder's surface. XRFC: x-ray framing camera; MIFEDS: magneto-inertial fusion electrical discharge system; ZVH: zinc von Hamos detector.

lighter for the absorption measurement was a gold foil irradiated by two pairs of stacked (0.3-TW/beam, 1.5-ns) OMEGA beams, creating a 3-ns x-ray source.

Our results show a cylindrical compression of the cylinder by the 36 OMEGA beams. The most important result is the impact of the external magnetic field on the compression. Figure 152.38 shows the temporally and spectrally resolved x-ray signal from the plasma with and without an external magnetic field. The compression time seems to be 0.5 ns later with a magnetic field, and we infer the electron temperature from the spectra of Cl. Another spectrometer [zinc von Hamos (ZVH)] was used to detect the Cu and Zn foil emissions with and without an external magnetic field. Furthermore, the x-ray pinhole charge-coupled device (CCD) shows a more-homogenous x-ray emission for the compression in the presence of an external magnetic field, indicating a more-homogenous compression. For proton deflectometry, the protons interacted with the cylinder at two different delays: 0.3 ns before and 2 ns after the

time of laser incidence on the cylinder (the latter approximately corresponds to the implosion time). Figures 152.39(a) and 152.39(b) show the proton radiography of the cylinder deflected by the external magnetic field (estimated ~5.4 T), 0.3 ns before laser incidence and 2 ns after the laser pulse (after implosion time); the thermoelectric effect appears at the surface of the cone [Figs. 152.39(c) and 152.39(d)]. At this time, the cylinder's diameter can be observed and is directly related to the plasma density, revealing a difference in compression with or without the external magnetic field.

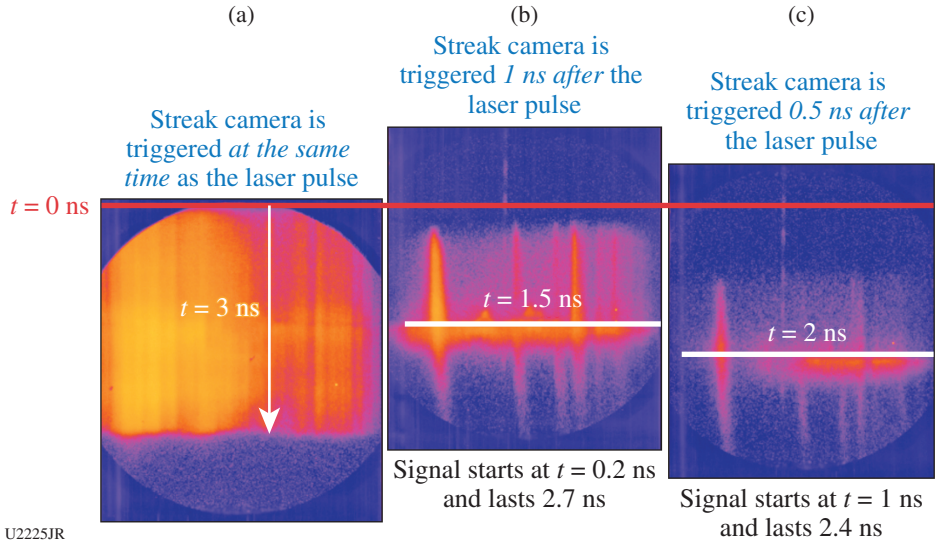

Figure 152.38
Temporally and spectrally resolved absorbed Cl signal (a) with backlighter only, (b) without an external magnetic field, and (c) with a magnetic field.

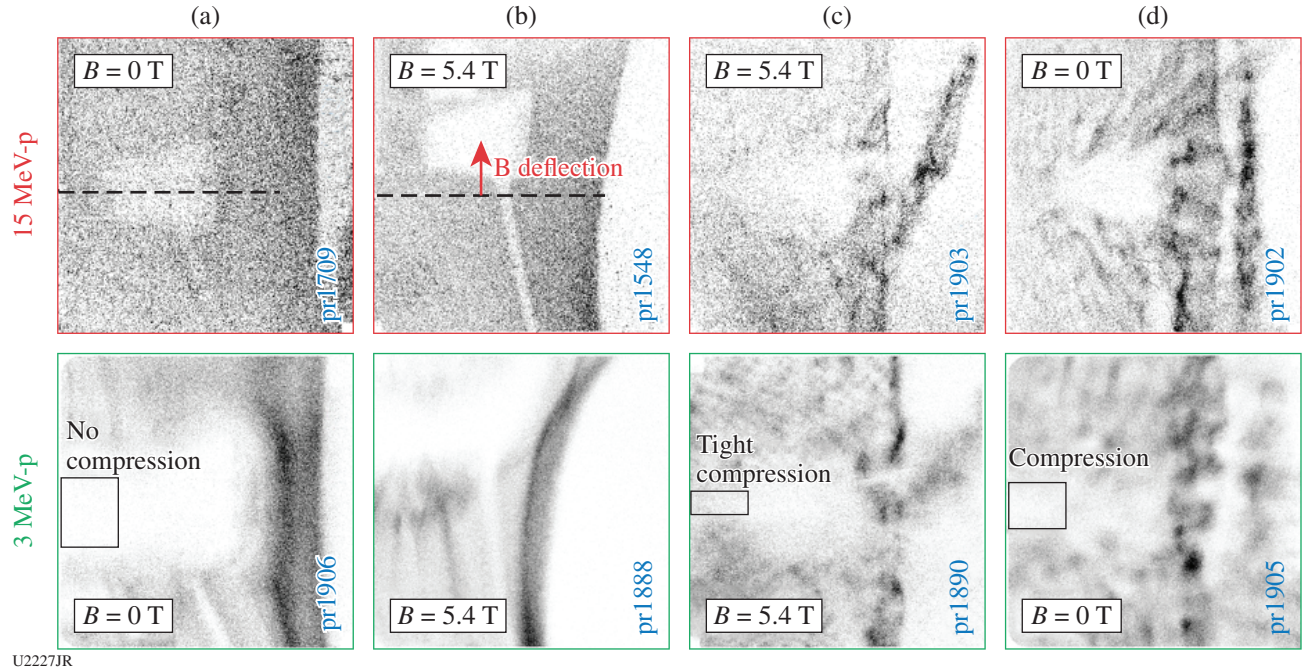

Figure 152.39
Proton deflectometry results for two delays (–0.3 and +2 ns from the laser) and with or without an external magnetic field: (a) 0.3 ns before the laser without a magnetic field, (b) 0.3 ns before the laser with a magnetic field, (c) 2 ns after the laser with a magnetic field, and (d) 2 ns after the laser without a magnetic field.

The data analysis and simulations are ongoing. Magnetohydrodynamic (MHD) simulations will be used to retrieve the compression history by matching the diagnostics at different times, and atomic physics codes will be used to determine the time-resolved plasma temperature inside the cylinder. Together, these will determine the best delay for the OMEGA EP beam on the second shot day.

Experimental Astrophysics on the OMEGA EP Laser
Principal Investigator: R. P. Drake (University of Michigan)

We study hydrodynamic processes by creating long-duration (tens of nanoseconds) steady shocks using the long-pulse UV laser beams on the OMEGA EP laser. Shocks encountering an interface with a density gradient generate shear or vorticity, depending on the geometry, which will induce either the Kelvin–Helmholtz instability (KH) or the Richtmyer–Meshkov (RM) process. Previously, we have independently studied the KH and RM processes; however, both processes will be induced if the interface is at an oblique angle. The contribution from each process depends on the interface angle. Our initial work aims to minimize the RM growth so that the KH growth dominates over time. We will do this by maximizing the parallel (shear) velocity and minimizing the perpendicular velocity.

The experimental target is shown in Fig. 152.40. Three UV laser beams are incident on an ablator package that includes a plastic layer and a plastic-doped bromine thermal insulator layer. This layer absorbs any laser preheat so it cannot adversely affect the target. The laser beams have a 1.1 full-width-at-half-maximum (FWHM) laser spot and a total energy of ~12 J; also, each of the 10-ns pulses is stacked in time to create an almost 30-ns laser pulse for an overall irradiance of ~4.2 × 10^{13} W/cm^2. This long, steady laser pulse creates a strong shock in the ablator package, is then driven into a 100-mg/cm^3 carbon foam, and is finally incident on an oblique interface in a plastic material. The interface has a precision-machined sinusoidal pattern that is either a single mode (λ = 100 μm, a = 5 μm) or dual mode (λ_1 = 100 μm, a_1 = 2.5 μm, λ_2 = 50 μm, a_2 = 5 μm). Our goal is to compare the developing structure with a single mode (where no merger is expected) and the dual-mode case. We also have experimental targets with a planar interface.

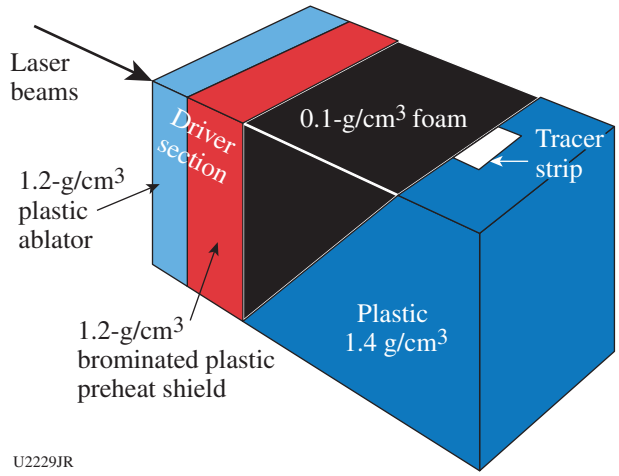

Figure 152.40
Schematic of vortex merger target showing the unstable interface between the low- and high-density material at 40°.

The evolution of the vertical structures was imaged with a spherical crystal imager (SCI) using Cu K_α radiation at 8.0 keV. Figure 152.41 shows an example of a high-resolution, high-

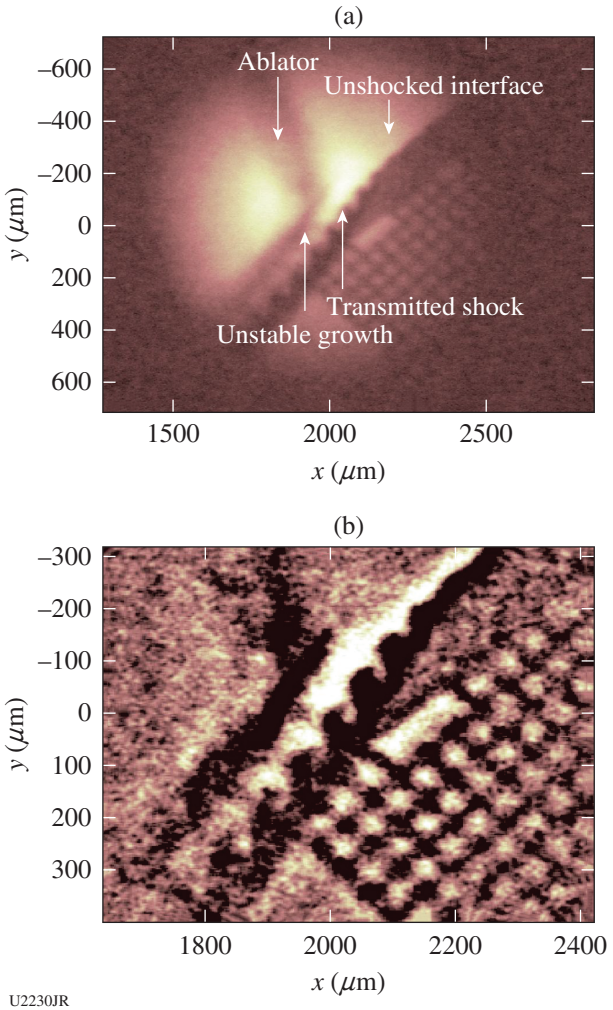

Figure 152.41
(a) X-ray radiograph of an experimental target using a single-mode initial condition at an oblique interface. (b) The radiograph has been cropped and processed to better visualize the unstable growth at the interface.

signal-to-background x-ray radiograph with several notable features indicated. The unperturbed interface is in the upper right portion of the image in Fig. 152.41(a). The shock front is barely visible in the foam, but the position can also be determined from the transmitted shock in the plastic component. The dark, curved feature on the left in Fig. 152.41(a) is the ablator package, which collided with the interface in the lower part of the image and is approaching the interface in the upper part of the image. Between the ablator and shock front, vortex structures can be seen growing. This experimental target had a single-mode interface and was imaged at 65 ns from the start of the main laser pulse. Future experiments will vary the angle of the oblique interface in order to change the contributions of the RM and KH processes.

Phase Transitions and Crystal Structure of Tin Dioxide at Multimegabar Pressures

Principal Investigator: T. S. Duffy (Princeton University)
Co-investigators: R. F. Smith and F. Coppari (LLNL);
J. K. Wicks (Princeton University); and T. R. Boehly (LLE)
Graduate Students: D. Kim and R. Dutta (Princeton University)

Silica is the most abundant oxide component of terrestrial mantles and serves as an archetype for the dense, highly coordinated silicates of planetary interiors. Understanding the behavior of silica at ultrahigh pressure is necessary to model the structure and dynamics of large rocky exoplanets known as super-Earths. Pressures in the mantles of such exoplanets may exceed 1 TPa, which is beyond the range of standard static high-pressure experimental techniques. Dynamic compression using the OMEGA laser offers an alternative means to explore structures and equations of state of planetary materials at these extreme conditions.

SiO_2 is one of a family of dioxides whose high-pressure behavior has been of strong interest because of their extensive polymorphism, highly coordinated structures, and varied transition pathways. The challenge in structure determination of silicates and oxides at exoplanet interior pressures is to obtain sufficient x-ray diffraction intensity from weakly diffracting, low-symmetry phases at ultrahigh pressures. The use of analog materials that undergo similar phase transition sequences at lower pressures has a long history in geoscience and high-pressure research and provides a useful pathway for the exploration of high-pressure structures. In this study, we have examined the behavior of SnO_2 at exoplanetary conditions using OMEGA and OMEGA EP. In addition to its role as an analog material, tin oxide is also of interest since its high-pressure phases have been predicted to be potential ultra-incompressible materials.

Our ramp compression experiments use a target package consisting of a thin sample foil sandwiched between a diamond pusher and a LiF window. The OMEGA laser is used to ablate the diamond front surface driving a ramp compression wave into the sample. A quasi-monochromatic x-ray source is generated by irradiating a metal foil to create predominately He-like x rays. *In-situ* x-ray diffraction is performed using the powder x-ray diffraction image-plate (PXRDIP) diagnostic. The pressure is determined from measurements of the free-surface velocity of the sample/lithium fluoride interface.

We have carried out density-functional-theory calculations that indicate that tin oxide is expected to transform from the orthorhombic cotunnite-type phase to the hexagonal Fe_2P-type structure above 200 GPa. Our measured x-ray diffraction data for SnO_2 are ~300 GPa and are shown in Fig. 152.42. We observe multiple diffraction lines from the sample, indicating that we have the potential to constrain high-pressure structures and equations of state at multi-megabar pressures for SnO_2. Analysis to distinguish among the possible crystal structure at this pressure is ongoing. In future work, we will extend these measurements to higher pressure as well as study the behavior of other dioxides including GeO_2 and SiO_2.

Dynamics of Magnetic Reconnection in High-Energy-Density Plasmas

Principal Investigators: W. Fox (Princeton Plasma Physics Laboratory); D. Schaeffer and A. Bhattacharjee (Princeton University); G. Fiksel (University of Michigan); and D. Haberberger (LLE)

We have developed and conducted experiments on the OMEGA and OMEGA EP Laser Systems to study the related phenomena of magnetic reconnection and collisionless shocks. Magnetic reconnection occurs when regions of opposite directed magnetic fields in a plasma can interact and relax to a lower-energy state; it is an essential plasma-physics process that governs the storage and explosive release of magnetic energy in systems such as the Earth's magnetosphere, the solar corona, and magnetic-fusion devices. The energy thereby liberated can produce heat flows and can enable the acceleration of a large number of particles to high energies. During previous NLUF reconnection experiments on OMEGA EP, we also unexpectedly observed the formation of magnetized collisionless shocks. Like reconnection, collisionless shocks are common in space and astrophysical systems. Magnetized shocks form from the nonlinear steepening of a magnetosonic wave and convert highly kinetic supersonic inflows to high-pressure subsonic outflows. In the process, they can also accelerate particles to

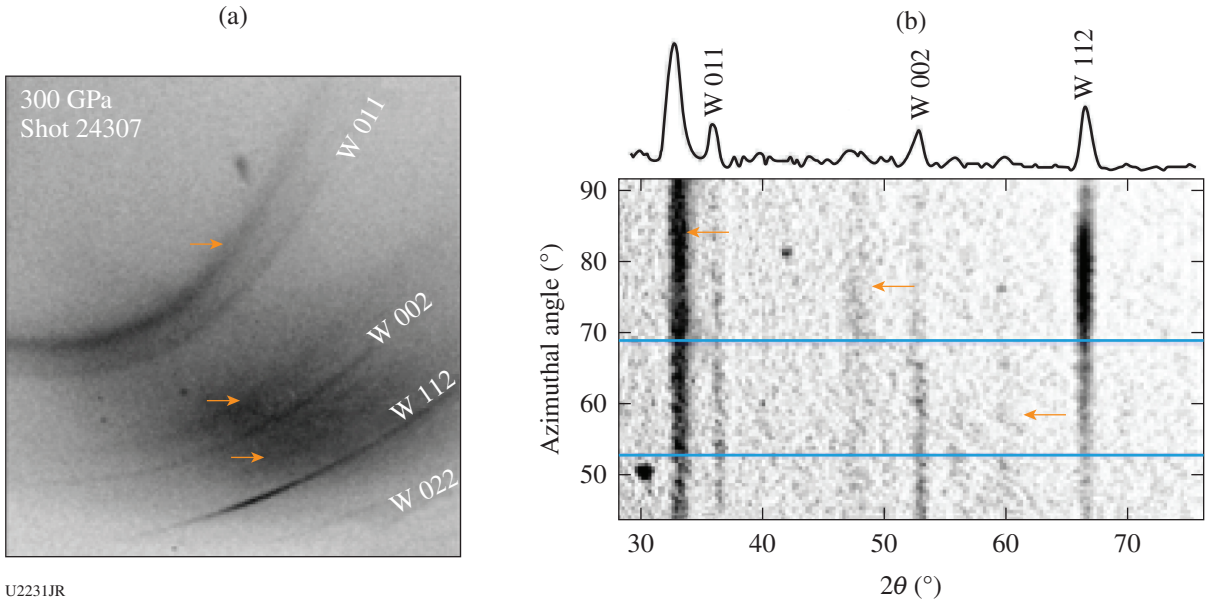

Figure 152.42
Diffraction data for SnO_2 at 300 GPa. (a) One of the image plates for shot 24307. Lines from the tungsten pinhole (used for collimation and calibration) are labeled. Diffraction lines from the sample are indicated with orange arrows. (b) Image-plate data transformed to ϕ, 2θ coordinates, where ϕ is the azimuthal angle around the incident x-ray beam and 2θ is the diffraction angle. A lineout from the region between the blue horizontal lines is shown at the top of (b). Again, peaks from SnO_2 are indicated with orange arrows. These results demonstrate that diffraction data can be obtained from weakly scattering, low-symmetry oxide samples at high pressures using the OMEGA laser.

extremely high energies. Those experiments were recently published in Ref. 1 and are under review in Ref. 2 as part of an invited talk at the 58th APS DPP meeting.

In this campaign we successfully carried out two experimental shot days on OMEGA EP and one shot day on OMEGA. The experiments on OMEGA EP utilized a new flat-foil platform for studying Biermann-mediated reconnection, while the experiments on OMEGA ported the magnetized colliding plasmas platform developed previously by our group and first published in Ref. 3.

The experiments on OMEGA EP used magnetic fields generated by the Biermann battery effect as the seed field for reconnection. Two oppositely directed Biermann fields were driven by the interaction of two lasers with a flat-foil target. Unlike previous Biermann-mediated experiments, our experiments utilized a flat target with a gap between the laser spots to provide a low-density region where the two laser plumes collide. The experiments on OMEGA used a single MIFEDS-driven coil but were otherwise similar to our MIFEDS platform developed for our previous NLUF campaigns on OMEGA EP.

The first shot day (March 2017) on OMEGA EP used proton radiography and the recently developed single-channel electron spectrometer (SC-ESM) to study the interaction between expanding plasma plumes and the resulting electron acceleration. We obtained spectacular proton radiography images that measure the magnetic field (see Fig. 152.43). Proton radiographs showed significant generation of Weibel filamentation and plasmoid formation in the gap region, which indicates fast reconnection. The SC-ESM also observed a population of energized electrons. This population was consistent with reconnection-accelerated particles but could also be caused by laser–plasma interaction (LPI) effects.

The second shot day (July 2017) on OMEGA used the Thomson-scattering diagnostic to measure the temperature and density of a single plasma plume interacting with a background magnetic field and ambient plasma (see Fig. 152.44). These measurements complement previous efforts on OMEGA EP that used proton radiography and angular filter refractometry (AFR) to diagnose large-scale magnetic topology and density profiles. They also provided information on conditions necessary for magnetized collisionless shock formation. We successfully obtained data at a range of times, distances from the target, ambient plasma conditions, and magnetic-field conditions. The results filled in several previous gaps. The measurements directly give plasma parameters and agree well with the 2-D radiation–hydrodynamics code *DRACO*. They also indicate

that the formation of magnetized shocks is sensitive to the configuration of the main laser beams. The experiments, and their extension to counter-streaming plumes, will be continued on an upcoming NLUF shot day.

The third shot day (August 2017) on OMEGA EP continued the previous experiments on Biermann-mediated reconnection. We used AFR, which was unavailable on the previous shot day, proton radiography, and the SC-ESM to study the interaction of the colliding plumes. We obtained excellent AFR images, which show a complex interplay between magnetic turbulence and reconnection (see Fig. 152.43). The combination of proton and AFR images are currently being analyzed and compared to particle-in-cell simulations. We saw similar energized electron populations as on the first OMEGA EP day, but we also confirmed using the sub-aperture backscatter (SABS) diagnostics that LPI may play a significant role in energizing particles. This will be pursued in upcoming NLUF experiments.

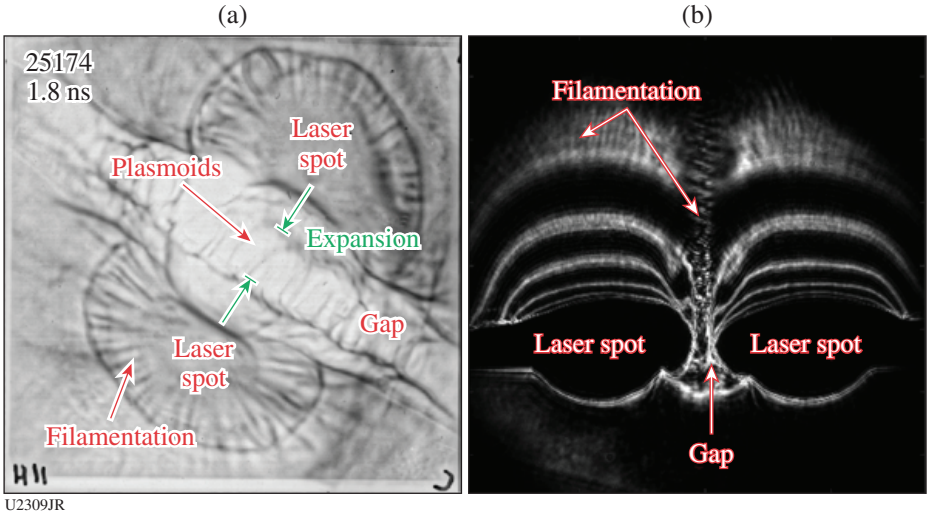

Figure 152.43
Interaction of two Biermann-generated magnetic plumes 1.8 ns after laser ablation on OMEGA EP. The gap in the flat-foil target can be seen between the laser spots. (a) Proton radiography reveals the formation of Weibel filaments at the edge of the Biermann fields and plasmoids in the gap region. (b) AFR also shows the formation of filamentation at the plume edges and in the gap region.

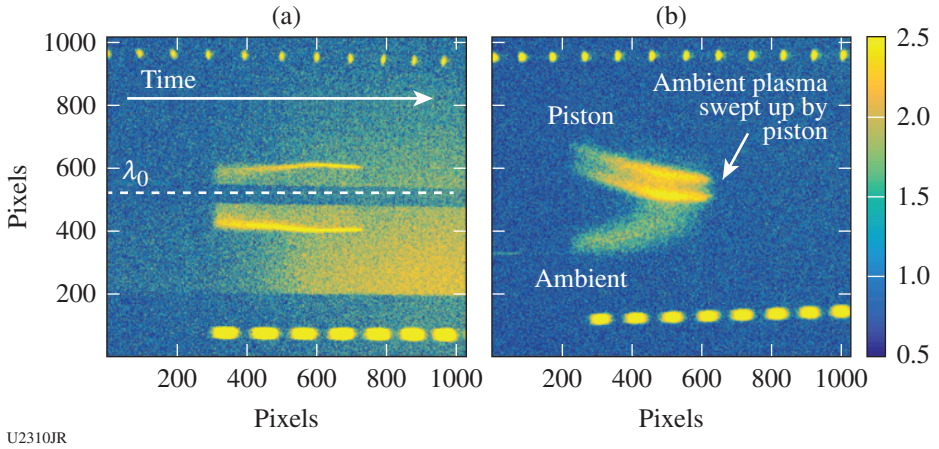

Figure 152.44
Streaked Thomson-scattering measurements of the interaction of a piston plasma with a magnetized ambient plasma: (a) electron plasma wave feature and (b) ion-acoustic wave feature. The scattered spectra show that the ambient ions are swept up by the piston and form a hot, high-density downstream region.

Magnetized Accretion Shocks and Magnetospheres in the Laboratory

Principal Investigator: P. Hartigan (Rice University)
Co-investigators: C. C. Kuranz, G. Fiksel, J. Levesque, and R. Young (University of Michigan); J. Foster and P. Graham [Atomic Weapons Establishment (AWE)]; A. Frank (University of Rochester); A. Liao (Rice University); C. K. Li and R. D. Petrasso [Massachusetts Institute of Technology (MIT)]; and D. H. Froula (LLE)

The goal of our NLUF campaign is to use the magneto-inertial fusion electrical discharge system (MIFEDS) on OMEGA to create analogs of magnetized, hypersonic plasma flows that are ubiquitous in astrophysics. In previous experiments we explored several related topics, including the dynamics of magnetized star-forming clouds, magnetized supersonic Kelvin–Helmholtz instabilities, stellar magnetospheric infall, and planetary magnetospheres. Our current experiments relate most closely to stellar wind interactions with atmospheric outflows from magnetized exoplanets. The experimental setup drives a supersonic flow that impinges upon a current-carrying wire, producing a bow shock. Ablation flow from the wire encounters the supersonic flow, creating a working surface where the flows meet. Altering the amount of current in the wire changes the strength of the magnetic field in the ablation flow.

Last year we succeeded in producing a layer of concentrated magnetic flux embedded in the strongly shocked plasma of the working surface. However, the optical imaging diagnostics we used did not spatially resolve this layer well, and parts of the shocked layers were optically thick, preventing us from directly probing this layer where the two flows collide. To improve upon this design, in FY17Q1 we deployed two new diagnostic techniques that both penetrate into the working surface. First, we used spatially resolved Thomson scattering as a means to map how the velocities and densities vary across the shocked layers. In the spectra shown in Fig. 152.45(a) both the ablation flow from the wire (left side of the image in blue) and the incident flow that is driven from the laser target (right side of image in blue) are traced as a function of position. The two flows collide to generate a shocked layer with high temperature and density. According to theoretical models, the field in the wire should be swept by the ablation flow into a compressed layer that coincides with the working surface.

To diagnose the field geometry and strength, we employed proton radiography (Fig. 152.46). The results, which are quite striking, show the two main characteristics predicted by the simulations: (1) a voided area caused by protons being deflected away from the wire by the toroidal field caused by the current in the MIFEDS wire, and (2) a caustic produced by the

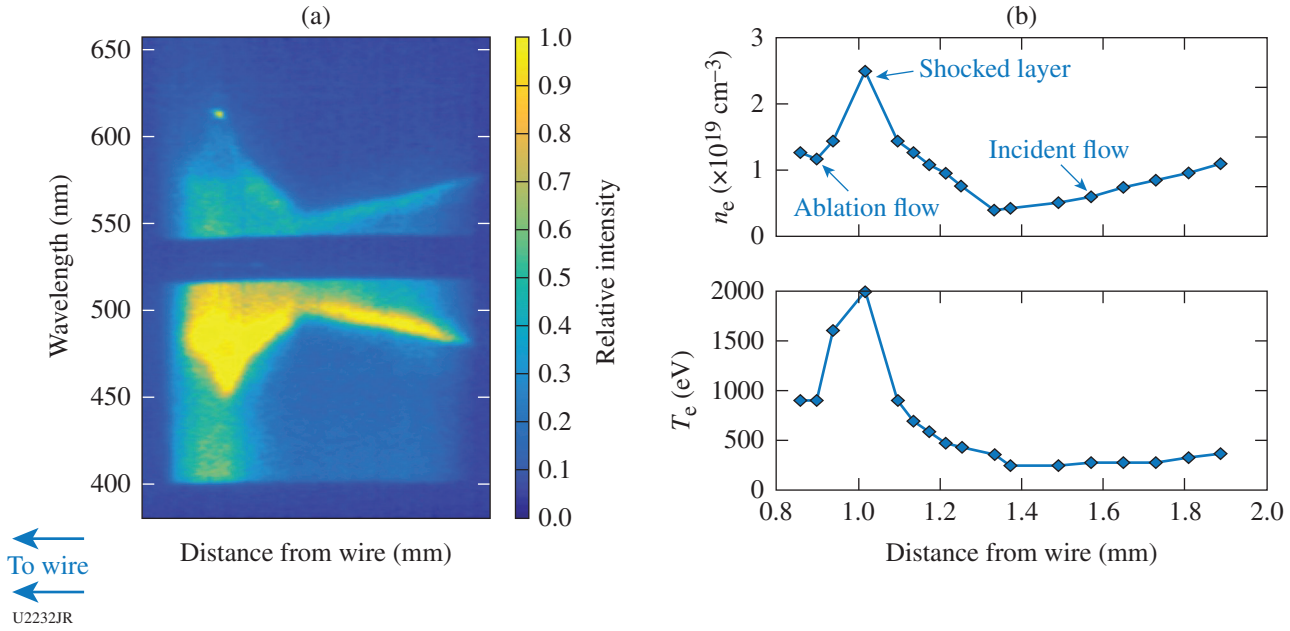

Figure 152.45
(a) Electron wave spectra resolved across the magnetized shock and (b) derived quantities. The density profile indicates a shock at the d = 1-mm position of ~100-μm thickness at half maximum.

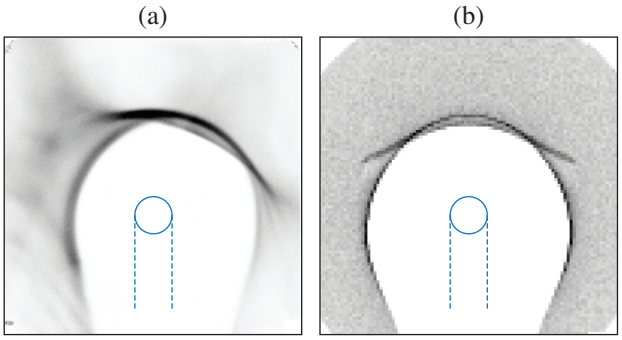

Figure 152.46
(a) Real and (b) synthetic 3-MeV proton radiographs with a fiducial, indicating the actual location of the wire (blue). The synthetic image (b) was constructed by placing a flux layer in the deprojected magnetic-field model with the position and thickness indicated by the electron plasma wave–derived shock structure (see Fig. 152.45). The apparent position of the flux layer (brimmed hat) defines the magnetized flux layer coincident with the shocked gas.

accumulation of magnetic flux in the working surface. These observations allowed us to characterize the thickness and density of the magnetized flux sheet. Interestingly, the flux density we derived from the proton radiography was significantly less than that predicted by pressure equilibration; diffusion of the magnetic field resulting from inertial ions is a likely cause of these differences.

This experiment will serve as a template for future studies of magnetized shock layers. Following the temporal evolution of the system is a promising area of research, and with small changes to the experimental setup we should be able to further improve the spatial resolution and possibly measure the degree of mixing between the two fluids within the working surface.

Our NLUF research currently supports the thesis preparation of three graduate students in laboratory astrophysics: A. Liao (Rice University), and J. Levesque and R. Young (University of Michigan).

Influence of Plasma Density on the Generation of Hundreds of MeV Electrons via Direct Laser Acceleration

Principal Investigators: A. E. Hussein, T. Batson, K. Krushelnick, and L. Willingale (University of Michigan); A. V. Arefiev (UCSD); P. M. Nilson, D. H. Froula, R. S. Craxton, A. Davies, and D. Haberberger (LLE); and H. Chen and G. J. Williams (LLNL)

The OMEGA EP Laser System was used to study the acceleration of electrons to many times the ponderomotive energy by high-energy, picosecond-duration laser pulses interacting with an underdense plasma target. A high-intensity picosecond pulse propagating through underdense plasma will expel electrons along its path, forming a positively charged plasma channel.[4] Electrons that are injected into this channel can gain significant energy through direct acceleration by the laser field.[5] This acceleration mechanism is known as direct laser acceleration (DLA). Experiments on the OMEGA EP laser employed four of the chamber beams to study, optimize, and diagnose the influence of plasma density on the DLA mechanism. The existence of an optimal plasma density for the generation of high-energy, low-divergence electron beams was demonstrated. This result is consistent with results from 2-D particle-in-cell (PIC) simulations using the code *EPOCH*.

A schematic of the experiments on OMEGA EP is given in Fig. 152.47. A long-pulse UV beam (2.5 ns, 1200 J) ionized a CH flat-foil target to generate an expanding plasma plume. The backlighter beam (1 ps, 400 J) interacted with the plasma plume in an oblique geometry to generate a channel and accelerate an electron beam. The plasma density was varied by changing the timing between the long-pulse UV beam and the short-pulse (backlighter) beam. The sidelighter beam (1 ps, 200 J) was focused onto a Cu foil to generate a proton probe via target normal sheath acceleration (TNSA) for imaging electromagnetic fields onto a stack of radiochromic film (RCF). Shadowgraphy imaging, polarimetry of magnetic-field formation, and plasma density measurements by angular filter refractometry (AFR) were fielded using the 4ω optical diagnostic probe. The electron spectrum along the axis of the short-pulse beam was measured

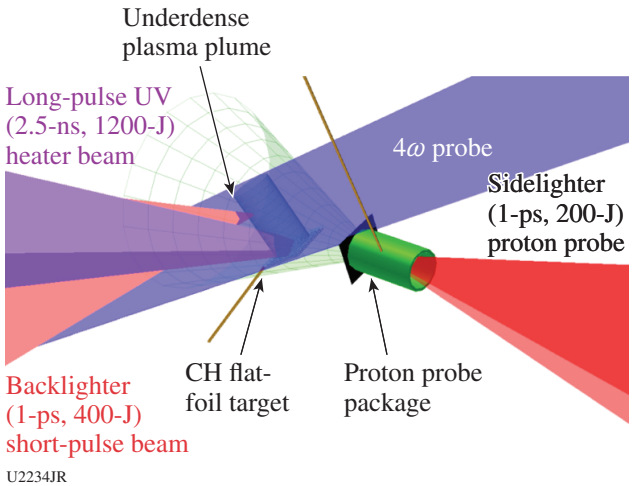

Figure 152.47
Experimental configuration. A long-pulse beam generated an expanding CH plasma plume as the target of the short-pulse beam for channel formation and electron acceleration by direct laser acceleration.

using an absolutely calibrated magnetic spectrometer [electron positron proton spectrometer (EPPS)].

Previous experiments explored the formation and evolution of plasma channels on an RCF film stack.[4,5] In these images, the upward deflection of DLA-accelerated electrons was observed as a result of the refraction of the laser pulse in the plasma-plume density gradient.[5] AFR measurements of plasma-plume expansion were used to extract a 2-D Gaussian density profile. This density profile agreed reasonably with density profiles of a CH expanding plasma plume obtained using the 2-D hydrodynamic code *SAGE*.

Two-dimensional PIC simulation conditions were designed to match the OMEGA EP Laser System. A 1.053-μm-wavelength laser, with coincident focal spots of 3.4 μm and 17 μm, with intensities of 3.776×10^{19} W/cm^2 and 2.81×10^{18} W/cm^2, respectively, was simulated. The plasma density profile was defined by the Gaussian profile from AFR measurements. Simulations were performed with a resolution of 30 cells per wavelength in the longitudinal direction (x) and six cells per wavelength in the transverse direction (y). The laser was linearly polarized in y and propagated in x. Ions were treated as mobile, and the plasma (electron) density was varied to simulate the temporal evolution of the plasma plume in experiments. Simulated densities ranged between 0.1 n_c and 0.008 n_c, where the quoted value corresponds to the peak density along the laser trajectory and n_c is the critical density.

Simulated electron spectra are shown in Fig. 152.48(a) and reveal the existence of an optimal plasma density for electron acceleration to energies exceeding 230 MeV. Experimental electron spectra are shown in Fig. 152.48(b). The quoted density in this figure refers to the peak electron density along the trajectory of the main interaction beam, as estimated by *SAGE* simulations and AFR measurements. Experimental measurements revealed an enhancement of peak electron energy at a peak density of 0.01 n_c. The enhancement of peak electron energy, up to nearly 600 MeV, was significantly higher than predicted by 2-D simulations.

The proton-probe diagnostic captured electromagnetic-field structures of the plasma channel. Although the initial time t_0 of the short-pulse interaction cannot be exactly determined because of timing jitter of the order of 20 ps, relative timing between each film in the RCF stack can be calculated from proton time-of-flight calculations. An example radiograph is given in Fig. 152.49(a), where clear formation and filamentation can be observed using a normal film pack, 8 cm from the interaction region. The centroid of the resultant electron beam on another RCF stack was found to deflect above the axis of laser propagation, as shown in Fig. 152.49(b). This is consistent with upward refraction of the laser pulse in the density gradient. Information about beam pointing and angular divergence as a function of plasma density could be extracted from the on-axis RCF stack. Beam divergence tends to decrease as a function of plasma density, with some evidence of channel filamentation, creating multiple beamlets, at lower densities.

These experiments demonstrated the existence of an optimal plasma density for the generation of high-energy electron beams by the interaction of a high-intensity picosecond pulse with underdense plasma. Experimental results also indicate a relation between plasma density and beam divergence. Continued work will focus on the role of quasi-static channel fields on

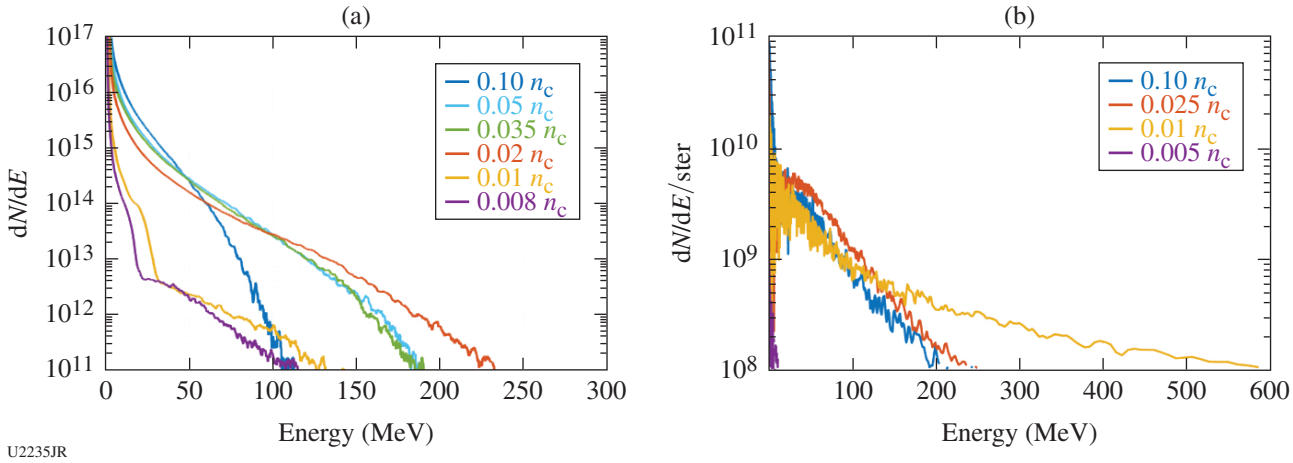

Figure 152.48
(a) Electron spectra simulated for various peak densities and (b) experimental measurements of electron spectra along the axis of the short-pulse beam.

electron energy enhancement, beam pointing, and divergence to elucidate the mechanisms and action of DLA at different plasma densities.

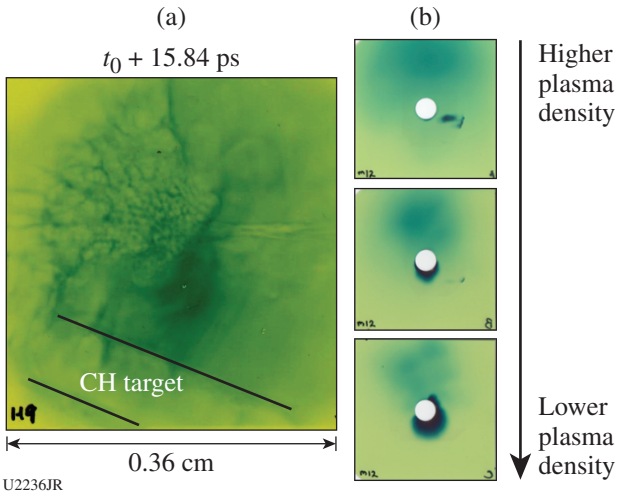

Figure 152.49
(a) Proton probe image of a plasma channel. (b) Radiochromic film along the axis of short-pulse (backlighter) beam propagation can be used to study electron beam pointing and divergence as a function of plasma density.

High-Energy-Density Chemical Physics and Planetary Evolution

Principal Investigator: R. Jeanloz (University of California, Berkeley)

Co-investigators: M. A. Millot, D. E. Fratanduono, P. M. Celliers, and J. H. Eggert (LLNL); S. Brygoo and P. Loubeyre (CEA); and T. R. Boehly, G. W. Collins, and J. R. Rygg (LLE)

During FY17, our international research team conducted two campaigns with diamond-anvil cell targets on the OMEGA laser (DirectDAC17A and 17B) for a total of 16 shots. The configuration is a direct-drive geometry (Fig. 152.50), with up to 12 beams delivering up to 6 kJ in 1-ns square pulses to the 1-mm aperture in the tungsten carbide seats holding the diamond anvils. VISAR (velocity interferometer system for any reflector) velocimetry and streaked optical pyrometry monitored the shock propagation in the sample pressure chamber to diagnose the pressure–density equation of state and the optical properties (reflectivity, absorption coefficient) using a quartz reference.[6] Most of the shots were dedicated to the study of the metallization of hydrogen (deuterium) using the combination of high precompression (6 to 13 GPa) and double shock

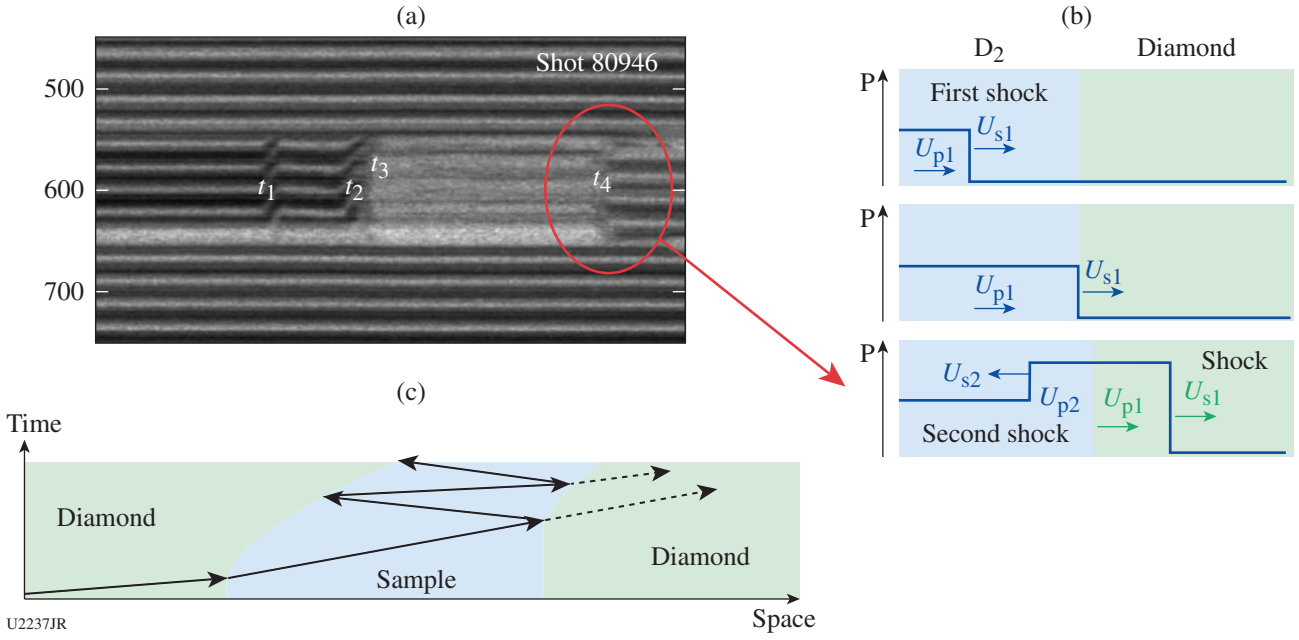

Figure 152.50
(a) Typical VISAR velocimetry record and (b) sketches of the re-shock experimental configuration showing the arrival of the elastic wave at the diamond/sample interface (t_1), followed by the arrival of the inelastic wave (t_2) and the catchup of these two waves inside the D_2 sample, transforming it in an opaque fluid. (c) Impedance mismatch at the arrival of the shock wave at the sample/diamond interface induces the generation of a second shock wave into the deuterium sample (t_4). The bright fringes after t_4 indicate that deuterium becomes a good reflector upon reshock, indicative of high electrical conductivity.

compression to access high-density states in the vicinity of the predicted first-order transition from the insulating molecular fluid to a metallic atomic fluid.

Our team also successfully demonstrated the feasibility of using diamond-anvil cell targets on the OMEGA EP laser during a one-day campaign. Preliminary analysis of the data indicates that OMEGA EP makes it possible to reach higher shock pressures using longer pulse durations. Future experiments might also benefit from the excellent pulse-shape capability available on OMEGA EP to generate multishock compression and map out the metallization transition of several key planetary constituents.

Prepared by LLNL under Contract DE-AC52-07NA27344. LLNL-TR-739623.

Particle Acceleration Resulting from Magnetically Driven Reconnection Using Laser-Powered Capacitor Coils

Principal Investigator: H. Ji (Princeton University)
Co-investigator: L. Gao (Princeton Plasma Physics Laboratory)

Magnetic reconnection is a ubiquitous astrophysical phenomenon in which magnetic energy is rapidly converted into plasma kinetic energy in the form of flow energy and thermal energy as well as nonthermal energetic particles. Energy particles are often regarded as an observational signature of the magnetic reconnection, which can be a more-efficient generation mechanism than other competing processes such as collisionless shocks. Despite its long history, most laboratory work in this area has focused on the mechanisms of fast reconnection as well as the generation of plasma flow and thermal energy during magnetic reconnection, mostly resulting from the limitations in either experimental setups or diagnostic capabilities. The goal of our research is to build an effective new platform to achieve and measure conspicuous particle acceleration by magnetically driven axisymmetric reconnection using laser-powered capacitor coils. In FY14, our team successfully measured and reported the first direct measurement of the magnetic fields generated by these laser-powered capacitor coils. With strong magnetic fields approaching the MG level and by tuning plasma parameters, we will be able to access magnetically driven, collisionless reconnection for efficient particle acceleration.

In FY17, we successfully carried out one experimental shot day on OMEGA EP to study the above-mentioned physics goals. A schematic of the experimental setup on OMEGA EP is shown in Fig. 152.51. The main interaction target is comprised of two parallel copper plates connected by two copper wires. Two OMEGA EP 2.5-kJ, 1-ns laser pulses pass through the laser entrance holes on the front plate and are focused on the back foil, generating a beam of superthermal hot electrons. The hot electrons stream onto the front plate and build up an electrical potential between the plates. This in turn drives

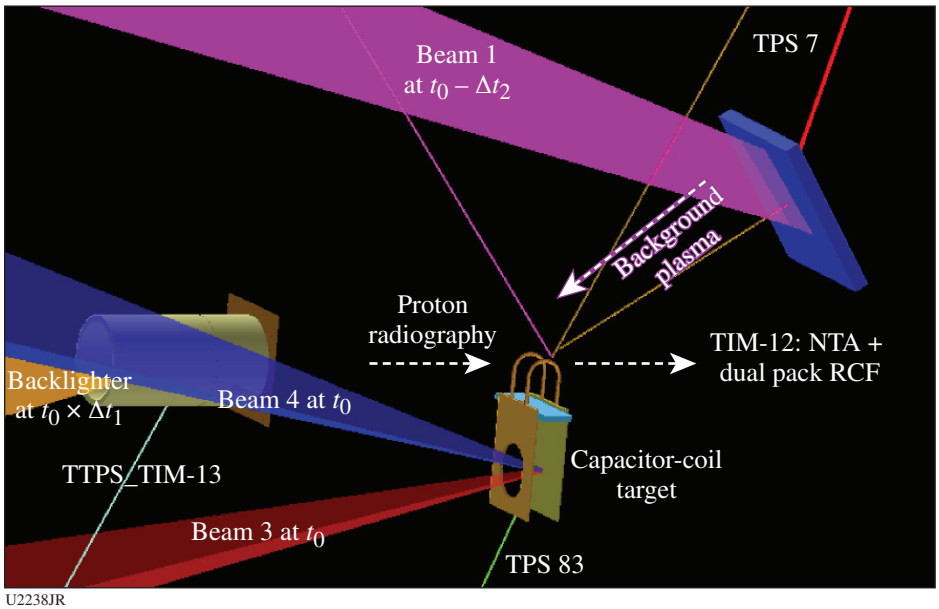

Figure 152.51
Experimental setup for the recent reconnection experiments on OMEGA EP based on the laser-powered capacitor coils. BL: backlighter; NTA: near-target arm; TIM: ten-inch manipulator; TPS: target positioner system; TTPS: TIM target positioner system.

large currents in both wires and creates magnetic reconnection because antiparallel magnetic-field lines exist in the middle plane. Another OMEGA EP 50-J, 1-ns laser pulse irradiates a plastic target and generates a tenuous background plasma for the reconnection region.

A suite of existing OMEGA EP diagnostics were fielded to identify quantitative confirmation of reconnection. Ultrafast proton radiography was utilized to probe the reconnection process at various times with high spatial and temporal resolutions. The new OMEGA EP high-resolution x-ray spectrometer (HiRes) was fielded to monitor Cu K_α emission from both front and back Cu plates. Three fixed port x-ray pinhole cameras viewed the time-integrated x-ray emission from the entire target. The Osaka University electron spectrometer was used to measure the particle spectrum from reconnection. The HiRes data showed strong Cu K_α emission from the front Cu plate, indicating hot electrons generated during the main interaction streaming onto the front plate and exciting these K-shell emissions. This measurement is a direct confirmation of the charging mechanism for building the electrical potential between the two plates. The hot electrons therefore have energies of at least 8 keV. Detailed atomic physics analysis is ongoing to understand the spectrum of hot electrons generated when the two main laser pulses hit the back copper foil. This will facilitate a better understanding of the mechanism for creating these strong magnetic fields. Our electron spectrometer data consistently showed a peak in the electron power spectrum with maximum electron energy ~1 MeV from reconnection. These experimental results are being compared with our PIC simulations.

X-Ray Measurements of Laser-Driven Relativistic Magnetic Reconnection Using OMEGA EP

Principal Investigators: K. Krushelnick, P. Campbell, L. Willingale, and G. Fiksel (University of Michigan); and P. M. Nilson and C. Mileham (LLE)

Recent experiments were conducted on the OMEGA EP Laser System to study a magnetic-reconnection geometry established by firing a short-pulse laser alongside a long-pulse UV beam onto solid targets. A 1-ns, 1250-J UV beam was focused to an intensity of 2×10^{14} W/cm^2 onto a 25-μm-thick copper target. Misalignment of temperature and density gradients in the ablated plasma plume generated azimuthal Biermann battery magnetic fields (of the order of MG). As this long-pulse–produced plasma developed, a 10-ps pulse containing 500 J was focused to relativistic intensity ($I > 10^{18}$ W/cm^2) in close proximity. In contrast to the slowly expanding Biermann battery fields ($v \approx c_s$), relativistic currents driven by the short-pulse laser generate a strong azimuthal magnetic field (of the order of 10 to 100 MG) that spreads radially with a velocity near the speed of light. This dramatic difference in scales yields a highly asymmetric field geometry, with the rapidly expanding short-pulse–generated field driving into a quasi-static Biermann battery field.

Proton radiography was implemented to diagnose the magnetic-field dynamics of the interaction. A second short-pulse laser (300 J in 1 ps) accelerated protons via the TNSA mechanism from 20-μm-thick gold targets to energies exceeding 60 MeV. A stack of RCF detected the deflection of the proton beam by the electromagnetic fields of the target. The time of flight for a proton depends on the kinetic energy. Because of the Bragg peak in the proton stopping power, each layer in the RCF stack detects a different energy and therefore a different time in the interaction.

As shown in Fig. 152.52, the proton radiography captures the rapid expansion of the short-pulse–generated magnetic field

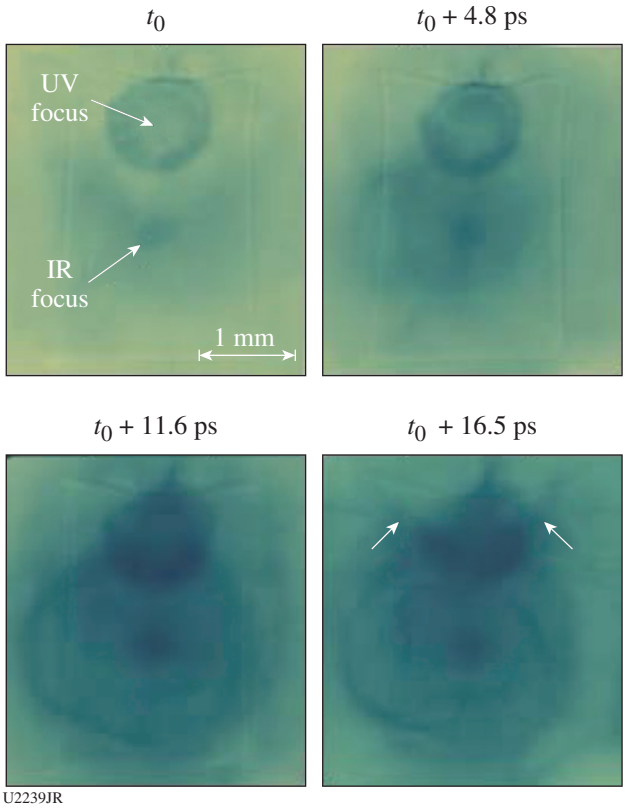

Figure 152.52
Proton radiography captures the interaction of the rapidly expanding, short-pulse–generated magnetic field with the quasi-static Biermann battery field. Superimposed arrows at time = t_0 + 16.5 ps indicate the regions of enhanced signal potentially associated with outflows.

into the quasi-static Biermann field. At t_0, the Biermann field has evolved for 750 ps when the short-pulse IR beam arrives on target and the focal-spot separation is 1.25 mm. After 11.6 ps, there is a local enhancement in proton flux along the edge of the Biermann field structure as the fields meet and interact, indicating a strengthening of the field gradient. At later times, there is evidence of outflow structures emanating from the magnetic-field interaction.

In future experiments, the relative beam timing and focal-spot separation will be tuned to optimize and study these features of the interaction. The copper targets will be replaced with a lower-Z material to improve the quality of the proton radiography, and the dimensions will be increased to mitigate target-edge effects. In addition to the experiments, our future work will include a quantitative analysis of the proton-radiography results, moving toward full 3-D PIC simulations.

Properties of Magnetohydrodynamic Turbulence in Laser-Produced Plasmas

Principal Investigator: D. Q. Lamb (University of Chicago)

During the first shot day (19 April 2017) of our experiments (TDYNO NLUF Campaign) we used the OMEGA laser to study the turbulent dynamo amplification of magnetic fields, a ubiquitous process in astrophysical systems. The experiments employed a platform (Fig. 152.53) similar to the one we fielded on OMEGA for our very successful first TDYNO Campaign (FY15–FY16), during which we demonstrated nonlinear amplification by turbulent dynamo for the first time in a laboratory environment. The main goal of our first shot day was to map the time history of the magnetic-field amplification, probing the various phases of turbulent dynamo: the kinematic phase, when fields are weak with respect to the turbulent motions; the nonlinear phase, when the Lorentz force back-reacts on the plasma's momentum; and the saturation phase, when the magnetic energy reaches a sizable fraction of the kinetic reservoir and amplification stops (Fig. 152.54). We designed the experimental platform using numerical simulations on one of the nation's leadership supercomputers (Fig. 152.55). The platform is uniquely suited to generating turbulent plasmas in the large magnetic Reynolds numbers regime, where the dynamo can operate. The configuration consists of two diametrically opposed foil targets that are backlit with temporally stacked beams, delivering 5 kJ of energy on each side in a 10-ns span. The beams drive a pair of counter-propagating plasma flows that carry seed magnetic fields generated by the Biermann battery effect. The flows propagate through a pair of grids that destabilize the flow and define the driving scale of the turbulence. The flows meet at the center of the chamber to form a hot, turbulent interaction region where the weak seed magnetic fields are amplified to saturation values.

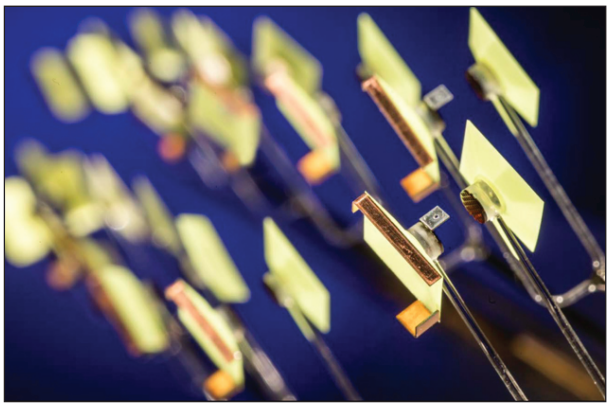

U2240JR

Figure 152.53
Experimental platform for the NLUF campaign to study turbulent dynamo amplification, a ubiquitous astrophysical process. The target assembly consists of two polystyrene foils and a pair of meshes, held together by a pair of cylindrical shields and a "tuning-fork" stalk. The foils and meshes were carefully designed to optimize the conditions in the interaction region for turbulent field amplification. The shields and flaps protect the interaction region, the imploding D^3He capsule, and the diagnostics from direct view of the laser spots.

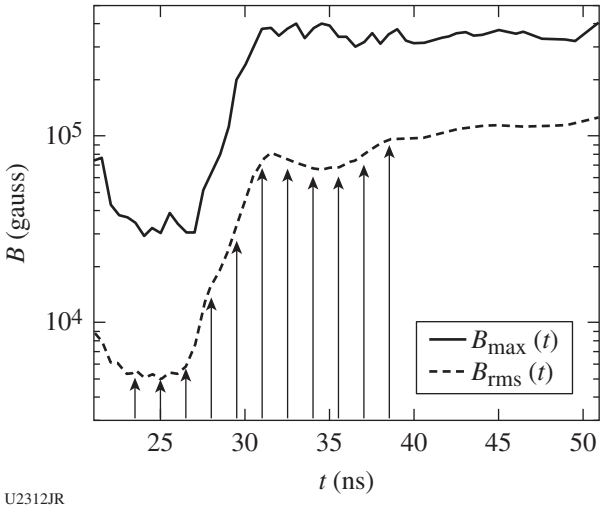

U2312JR

Figure 152.54
Simulated time history of the magnetic field's strength (in gauss) in the interaction region, showing the kinematic (exponential), nonlinear, and saturation phases of the dynamo for root mean square (rms) and peak values of the magnetic field. The arrows denote the different times at which we fired the proton radiography diagnostic: the 1.5-ns cadence allowed us to collect enough experimental data to temporally resolve the rise of the magnetic field.

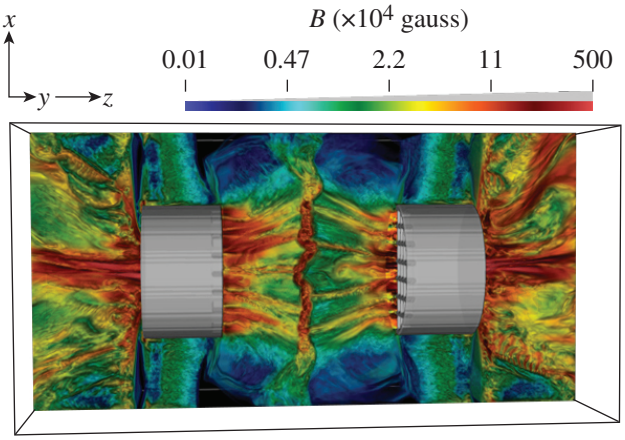

Figure 152.55
Three-dimensional radiation magnetohydrodynamic simulation of the experimental platform, performed with the multi-physics code *FLASH*. A large simulation campaign on Argonne National Lab's *Mira* BG/Q supercomputer guided us in the design of a platform capable of probing the turbulent dynamo regime. The figure displays a 3-D rendering of the magnetic field's magnitude (in gauss) after the jets collide.

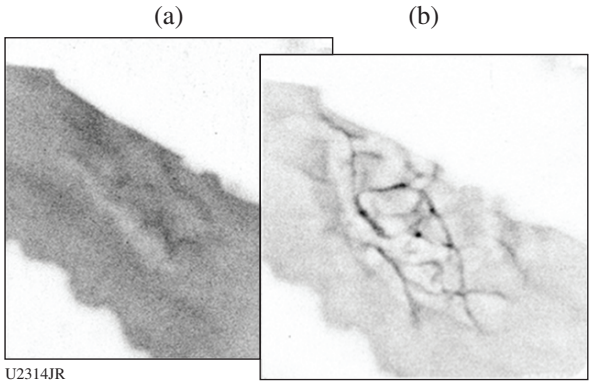

Figure 152.56
Proton radiographs (14.7 MeV) at $t = 25$ ns and $t = 29.5$ ns, corresponding to the times when the turbulent region first forms and weak seed fields are advected in (a) the center and (b) halfway through the exponential amplification phase when the filamentary structures start to develop. Analysis of the radiographs will reveal the topology and magnetic-field strength that the protons traversed on their way to the CR-39 film pack. The wealth of experimental diagnostics has enabled us to characterize the magnetized plasma, study the turbulent dynamo mechanism, and map its temporal evolution.

With a modest redesign of our original experimental platform, we were able to develop a faster and more-accurate alignment procedure; this enabled us to perform *15* shots during our first shot day—a record number given the complexity of our platform. The shots yielded a wealth of experimental data. The diagnostics we fielded allowed us to fully characterize the turbulent interaction region and quantify its plasma properties in space and time. More specifically, x-ray imaging enabled us to directly visualize the formation and evolution of the turbulent region. From the x-ray intensity fluctuations we reconstructed the density power spectrum of the magnetized turbulence and inferred its power law. Moreover, the spatially resolved spectrum from the Thomson-scattering diagnostic yielded clear ion-acoustic and electron features—at different times—that allowed us to characterize the plasma properties, including the ion and electron temperatures; the bulk flow and turbulent velocities; and the electron density in a 1.5-mm field of view. Therefore, we were able to probe for the first time both the turbulent interaction region *and* the inflowing plasma. Finally, to recover the time history of the magnetic-field amplification, we fielded the proton radiography diagnostic in all shots (Fig. 152.56). Utilizing the proton-radiography data and the novel magnetic-field mapping techniques we have developed, we are able to reconstruct the strength and topology of the magnetic field during *all* phases of dynamo amplification, with a 1.5-ns cadence (Fig. 154.54). This plenitude of experimental data is under analysis and promises to greatly expand our understanding of the puzzle that is astrophysical turbulence.

Creation of a Magnetized Jet Using a Hollow Ring of Laser Beams

Principal Investigator: E. Liang (Rice University)

Progress toward the objectives of this NLUF project as listed in the original application far exceeded expectations in its second year. We carried out a one-day joint OMEGA and OMEGA EP laser experiment in November 2016, using 20 OMEGA beams to form a hollow ring focal pattern to create a magnetized jet from a flat plastic target. Some of the targets were doped with 2% Fe. The hollow ring radius varied from 800 to 1200 μm. Twelve shots were successfully completed, half of which were joint shots with OMEGA EP. The Thomson-scattering (TS) diagnostic was used to measure the on-axis electron and ion density, temperature, and flow velocity at 2.5 mm from the laser target for each shot. The TS results confirmed the predictions of new *FLASH* 3-D simulations, after allowance was made for the TS probe beam's heating of the electrons. The on-axis densities, temperatures, and velocities are comparable for the 800- and 1200-μm-radius rings, suggesting that the optimal OMEGA ring radius lies between 800 and 1200 μm. In six of the shots, we used 3-MeV and 14-MeV monoenergetic protons from D^3He capsule implosions to measure the magnetic fields in the jet via proton radiography. For the other six shots we used continuum OMEGA EP protons to probe the magnetic fields. Both sets of proton radiography images gave consistent results, which compare favorably with 3-D *FLASH* simulation predictions

of approximately megagauss axial fields for both the 800- and 1200-μm cases. This shows that the plasma properties of the hollow ring jet, including its collisionality and MHD properties, will be significantly impacted by the self-generated magnetic fields. We used an x-ray framing camera to take x-ray images of the jet at 1-ns time intervals. The images show well-collimated laminar outflows for both the 800- and 1200-μm cases. This is in excellent agreement with 3-D *FLASH* predictions. When we compare the x-ray images of the undoped and 2% Fe-doped jets, we find that the Fe-doped jet is narrower and the x-ray emission stronger, as predicted by *FLASH*. A poster on the 2016 results was presented at the Omega Laser Facility Users Group (OLUG) Workshop in April 2017. The Principal Investigator (PI) also gave invited talks on the NLUF results at the NNSA symposium in Chicago in April 2017 and at LANL in July 2017. Updated results on both the OMEGA data and *FLASH* simulations will be presented at the American Physical Society Division of Plasma Physics (APS DPP) meeting in Milwaukee in October 2017. A National Ignition Facility (NIF) Discovery Science proposal based on the OMEGA results and *FLASH* simulations was submitted to the NIF in September 2017.

Development of a Photoionized Plasma Experiment on OMEGA EP

Principal Investigator: R. C. Mancini (University of Nevada, Reno)

Experiments on basic high-energy-density science on OMEGA EP provide a unique opportunity to create states of matter at extreme conditions of temperature, density, and radiation flux relevant to astrophysics. The focus of this project is to study the fundamental atomic and radiation physics of plasmas driven by a broadband intense flux of x rays; i.e., photoionized plasmas. Most laboratory work performed to date on high-energy-density laboratory plasmas pertains to collisional plasmas; i.e., those where electron collisional processes play a dominant role in the plasma ionization and atomic kinetics. However, relatively little attention has been paid to studying and understanding the fundamental properties of laboratory photoionized plasmas, where both photoionization and photoexcitation driven by a broadband x-ray flux are dominant. These plasmas are important for understanding a myriad of astrophysical sources including x-ray binaries, active galactic nuclei, and the accreting disks formed in the vicinity of black holes. The information that we obtain on these objects is based on the analysis of spectroscopic measurements recorded by orbiting telescopes such as Chandra and XMM-Newton. Yet, the analysis of the spectra relies on sophisticated atomic and radiation physics models that have been developed only on a best-theory effort. Therefore, there is a critical need for performing systematic photoionized plasma laboratory experiments to benchmark theory and modeling codes.

We are developing a silicon photoionized plasma experiment on OMEGA EP in which a plastic-tamped silicon foam is ionized by the 30-ns-duration, broadband x-ray flux produced by the "gatling-gun" radiation source. This source is comprised of three copper hohlraums that are driven by three OMEGA EP beams, each delivering 4 kJ of UV energy in a 10-ns square pulse shape. The laser beams sequentially illuminate one hohlraum at a time, thereby producing an x-ray drive characteristic of 90-eV radiation temperature for a time period of 30 ns. The silicon sample is placed at a distance of 7 mm from the source. It has an initial mass density of 100 mg/cm^3 and a thickness of 0.1 mm and is coated with two 1-μm-thick layers of plastic. Heated by the x-ray flux, the silicon sample expands by a factor of 10 and ionizes into the L-shell range of silicon ions, thereby producing a photoionized plasma with an atom number density of a few times 10^{19} atoms/cm^3 and a relatively uniform spatial distribution.

In the first phase of the experiment's development, we performed OMEGA EP shots in which the expansion and ionization of the tamped silicon foam was monitored with a gated imaging x-ray spectrometer that recorded the L-shell self-emission of the plasma. The radiation temperature of the gatling source was measured with a VISAR diagnostic. The expansion to 1-mm thickness and ionization of the silicon sample were both confirmed by the observations during the experiment.

Figure 152.57 displays L-shell emission from line transitions in B- and Be-like silicon ions recorded at $t = 6$ ns and $t = 9$ ns. No measurable line emission in these ions is noted before $t =$ 6 ns. The x-ray flux starts at $t = -15$ ns and lasts until $t = +15$ ns. Therefore, these observations are taken during the second half of the x-ray drive duration. This is reasonably consistent with the pre-shot expectation based on radiation–hydrodynamics modeling of the experiment. This observation is now being used to refine the numerical simulation. The spectra demonstrate the formation of a highly ionized silicon plasma driven by the x-ray flux. It also provides data to extract the electron temperature.

The next step in the experiment's development is to perform x-ray K-shell transmission spectroscopy of the silicon photoionized plasma with a streaked instrument and a separate titanium backlighter driven by the fourth beam of OMEGA EP. The transmission spectroscopy will permit the extraction of the silicon charge-state distribution and an independent check on the temperature from the L-shell emission spectra analysis.

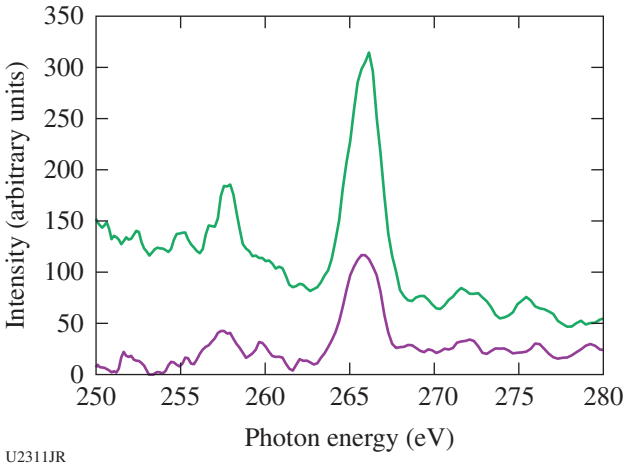

Figure 152.57
Photoionized silicon plasma L-shell self-emission recorded in OMEGA EP shot 26079 with a gated spectrometer at t = 6 ns (purple curve) and t = 9 ns (green curve). The emission spectral features at photon energies of 257 eV and 266 eV are caused by L-shell line transitions in B-like and Be-like silicon ions.

Explorations of Inertial Confinement Fusion, High-Energy-Density Physics, and Laboratory Astrophysics
Principal Investigators: R. D. Petrasso, C. K. Li, and J. A. Frenje (MIT)
Co-investigators: F. H. Séguin and M. Gatu Johnson (MIT)
Graduate students: N. Kabadi, B. Lahmann, H. Sio, R. Simpson, G. Sutcliffe, and C. Wink (MIT)
Undergraduate Student: M. Manzin (MIT)

MIT work in FY17 included a wide range of experiments applying proton radiography, charged-particle spectrometry, and neutron spectrometry methods developed by MIT and collaborators to the study of laboratory astrophysics, high-energy-density physics (HEDP), and ICF plasmas.[7–17] This was an outstanding year for the HEDP Division's scientists and students and their work on NLUF-related research. Based on NLUF work resulting in the development of the multiple-monoenergetic-particle source (MMPS) and its application to a wide range of physics experiments involving the observation and measurement of laboratory plasma phenomena and associated electromagnetic fields through radiography and other means, Drs. C. K. Li, R. D. Petrasso, and F. H. Séguin (Fig. 152.58) were chosen as recipients of the APS 2017 John Dawson Award for Excellence in Plasma Physics Research.* The MMPS is a laser-driven capsule containing D^3He fuel that produces monoenergetic charged-fusion products including 3.0-MeV protons, 14.7-MeV protons, and 3.6-MeV alpha particles during a 0.1-ns time interval, used either as a backlighter for multiple-monoenergetic-particle radiography or as a source of monoenergetic particles for other nonimaging experiments. The many subjects MIT has studied with the MMPS during the NLUF program include ICF experiments, plasma jet propagation, and magnetic reconnection, utilizing the MMPS as a backlighter for radiography, and quantitative studies of ion stopping and ion-electron equilibration in plasmas. These NLUF-developed techniques have also recently been ported to the NIF (LLNL).

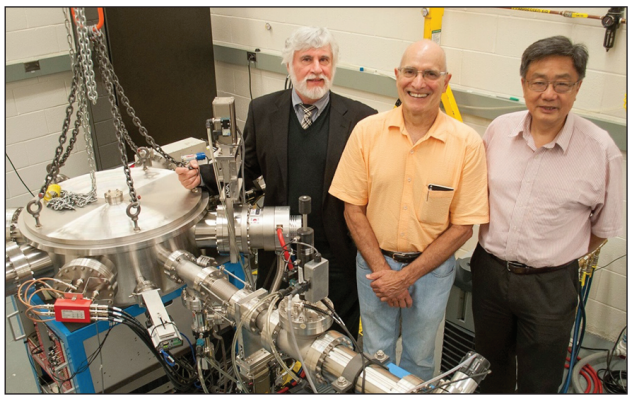

Figure 152.58
The three MIT scientists chosen as recipients of the American Physical Society's 2017 John Dawson Award for Excellence in Plasma Physics Research, standing next to the target chamber of the MIT-PSFC HEDP Division's accelerator facility (left to right: F. H. Séguin, R. D. Petrasso, and C. K. Li). The accelerator facility played a crucial role in the development and calibration of the multiple-monoenergetic-particle–source diagnostic platform used in the research cited in the Dawson Award.

The MMPS has been used by several MIT students in research critical to their outstanding Ph.D. theses. These include Drs. M. Manuel and M. Rosenberg, who received the APS *Rosenbluth Outstanding Doctoral Thesis Award* in 2014 and 2016, respectively, and Dr. A. Zylstra, who has now been nominated for the same award. In addition to the HEDP Division's own students, investigators from many other institutions have enlisted MIT's collaboration in their HEDP experiments on OMEGA to gain the unique information supplied by radiography with the MMPS. Those institutions include LANL, the University of Rochester, LLNL, the University of Chicago, Princeton University, UCSD, the University of Michigan, and the University of Oxford.

*The MIT scientists shared the Dawson Award with three scientists at other institutions (A. MacKinnon, Lawrence Livermore National Laboratory; M. Borghesi, The Queen's University, Belfast; and O. Willi, Heinrich Heine University, Düsseldorf). Those scientists had applied a different kind of proton source to radiography of plasmas, using TNSA, in which a laser pulse strikes a planar target and generates a strong electric field, charge separation, and a resultant picosecond-duration proton beam with a continuous energy spectrum.

In the meantime, other important NLUF accomplishments have included experimental measurements of nuclear reactions relevant to stellar and big-bang nucleosynthesis using high-energy-density plasmas on OMEGA and extensive experiments on kinetic physics. Many of these experiments have been enhanced by MIT student H. Sio's development of the new particle x-ray temporal diagnostic (PXTD) on OMEGA for simultaneous time-resolved measurements of several nuclear products as well as the x-ray continuum produced in HEDP. The PXTD system makes it possible, for the first time, to take accurate and simultaneous measurements of x-ray emission histories, nuclear reaction histories and their time differences along with measurements of $T_i(t)$ and $T_e(t)$ for studies of kinetic, multi-ion effects, and ion-electron equilibration rates in ICF plasmas.

Study of Magnetized Collisionless Shocks in Laser-Produced Plasmas

Principal Investigator: A. Spitkovsky (Princeton)
Co-investigator: C. M. Huntington (LLNL)

The FY17 MagShock EP Campaign was dedicated to the study of collisionless magnetized shocks in ablated plasma flows and exploration of new experimental concepts. Collisionless shocks commonly form in supernova remnants and in the heliosphere. The shock thickness is determined by the Larmor radius of the incoming protons, and the collisional mean free path must be much longer. The setup is shown in Fig. 152.59(a). The experiments used the OMEGA EP Laser System in which a 3-D–printed Helmholz coil powered by MIFEDS was inserted; two targets were mounted on MIFEDS. A 400- to 800-J, 1-ns pulse was used to ablate plasma that propagated along the coil's magnetic field (this component is called "background" plasma). A 1.3-kJ, 1-ns pulse was used to drive a fast-flow orthogonal to the magnetic field [this component is called "piston" plasma; see Fig. 152.59(b)]. The interaction between the flows was expected to drive a compression in the background plasma and the magnetic field [see Fig. 152.59(c)]. At a strong enough drive, this compression becomes a collisionless shock. This compression was diagnosed using proton radiography with TNSA from a short 1-ps laser pulse. The protons were recorded on CR-39 film, which was our primary diagnostic. On some shots, the 4ω optical probe was also utilized.

The experiments resulted in the detection of a magnetized collisionless shock propagating through the plasma. The main feature of the magnetic compression in the data was the appearance of a white band in the proton image, indicating additional deflection of the protons. The band was followed by a sharp

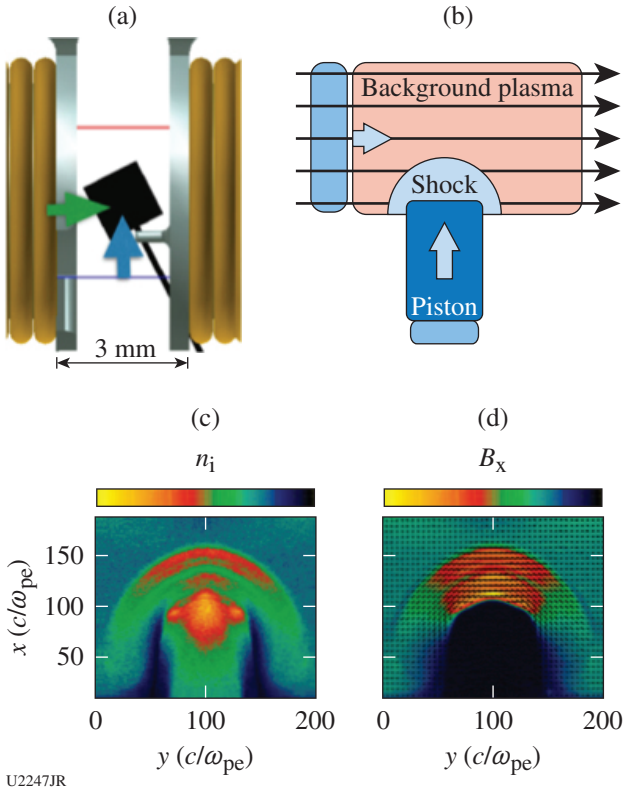

Figure 152.59
(a) Experimental setup for MagShock-EP-16AB, (b) schematic of fast-piston plasma interacting with a magnetized background plasma, and [(c),(d)] particle-in-cell (PIC) simulations of density and magnetic compression launched by a piston plasma.

caustic of enhanced proton concentration [Figs. 152.60(a)–152.60(c); shots separated by 2 ns]. The band and the caustic propagated at 300 km/s. The thickness of the band made it possible to constrain the magnetic compression ratio to 2.3, and the caustic was interpreted as the signature of the contact discontinuity between the piston and compressed background plasma [Fig. 152.60(d) lineout along the blue line in Fig. 152.60(b)]. This compression ratio corresponds to a Mach-3.4 shock. The shock is in the collisionless regime since the mean free path of the background protons is larger than the size of the plasma. These results were confirmed on several shots that performed the time-series study. Several time offsets were also tried before the piston plasma was launched, presumably probing different background densities. Extensive numerical simulations of the experiment were performed with 3-D PIC simulations [Figs. 152.59(c) and 152.59(d)], including simulated proton radiography through the fields of the simulation. The experimental results agree quite well with the predictions of the simulations. These findings will be presented at APS DPP Meeting in October 2017 as an oral contribution.

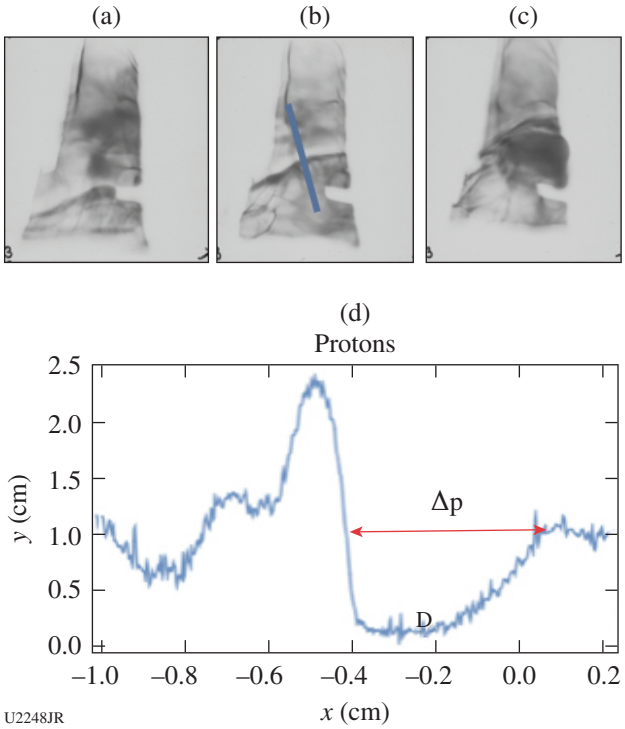

Figure 152.60
[(a)–(c)] Proton radiography of the interaction at different times. Notice the movement of the white band and the sharp caustic feature behind it. (d) Proton density in a cross-section cut, indicated by the blue line in Fig. 152.60(b).

In a second campaign in August, we attempted to probe the configuration through the orthogonal direction, resulting in rotation of the entire apparatus. The results are currently being analyzed. A clear shock signature was not seen, most likely because the background plasma density was lower than expected.

We thank the OMEGA EP personnel for their assistance in planning and executing this campaign.

Demonstration of Talbot–Lau X-Ray Deflectometry Electron Density Diagnostic in Laser–Target Interactions
Principal Investigator: D. Stutman (Johns Hopkins University)

An experiment aimed at demonstrating Talbot–Lau x-ray deflectometry (TXD) in high-energy-density plasmas was performed on the Multi-Terawatt (MTW) laser, where a laser-produced x-ray backlighter was used to illuminate a Talbot–Lau interferometer and obtain electron density maps of solid targets. These experiments confirmed that the TXD technique has the potential to become a basic and widespread diagnostic for HEDP experiments. To benchmark the technique in the HED environment, the interferometer must be tested in the presence of a plasma target. To this aim, a CH foil will be radiated by three UV OMEGA EP beams. A fourth beam will be used to obtain an x-ray backlighter source to illuminate the Talbot–Lau deflectometer, which will provide an electron density map of the ablated foil. Simulation and theory have failed to accurately predict the electron density profile from the ablation dynamics. TXD will provide electron density information in ranges not available today ($<n_c$) and will therefore advance the field of HED.

The proposed two-year research includes the implementation of a TXD on the OMEGA EP laser (FY18Q4). Preparatory experiments have been performed on MTW to test and optimize the x-ray backlighter. The first year has focused on diagnostic conceptual design and preparation of the experiment in collaboration with S. P. Regan and C. Stoeckl from LLE. The diagnostic design and implementation in the OMEGA EP laser are underway and being directed by C. Sorce and C. Mileham from the LLE Experimental Support Group. The conceptual design is shown in Fig. 152.61. Similar to the MTW setup, all the gratings will be mounted on a common optical base or rail. The common rail will allow us to accurately pre-align the gratings on site during pre-shot setup. The experiments will be defined and optimized in collaboration with P. A. Keiter (University of Michigan), so that the main goal of benchmark-

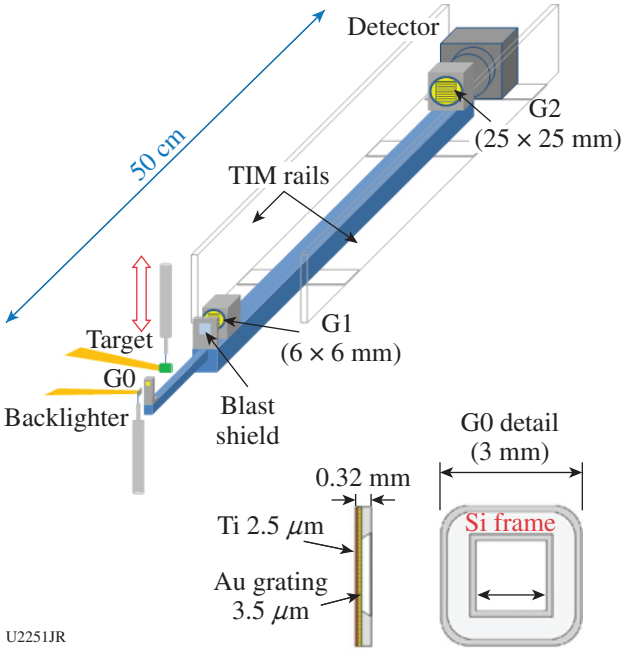

Figure 152.61
Conceptual design of the Talbot–Lau x-ray deflectometry (TXD) diagnostic for the OMEGA EP experiments. The inset shows source grating details. TIM: ten-inch manipulator

ing TXD as an electron density diagnostic for HEDP will be compatible with the goal of advancing the understanding of plasma ablation of plasma-irradiated foils.

Hot-Electron Generation with 10^{16}-W/cm^2 Infrared Lasers in the Shock-Ignition–Relevant Conditions

Principal Investigator: M. S. Wei (GA)
Co-investigators: C. M. Krauland (GA); S. Zhang, J. Li, and F. N. Beg (UCSD); C. Ren, W. Theobald, D. Turnbull, D. Haberberger, C. Stoeckl, R. Betti, and E. M. Campbell (LLE); and J. Trela and D. Batani (CELIA)

Shock ignition (SI) is an alternative ICF scheme that achieves ignition with a strong convergent shock launched by a high-intensity (~10^{16}-W/cm^2) laser spike at the end of the low-intensity (~10^{14}-W/cm^2) assembly pulse. SI spike-pulse energy coupling to the fusion target is uncertain because of laser–plasma instability (LPI) such as filamentation, stimulated Brillouin scattering (SBS), stimulated Raman scattering (SRS), two-plasmon decay (TPD), and the resultant hot-electron generation. Therefore, it is important to characterize the LPI and the hot-electron beam energy, temperature, and divergence in SI-relevant conditions to further assess the SI scheme.

This GA-led NLUF HotEScaleEP-17A Campaign conducted on OMEGA EP in August 2017 is an extension of our previous experiments (HotEScaleEP-15A), where we successfully demonstrated the propagation of an infrared (IR) laser beam (1.053 μm, 100 ps, up to 2.5 kJ, ~10^{16} W/cm^2) over a long-scale plasma (1.4-keV, 450-μm scale length) and the generation of a hot-electron beam with small divergence and moderate energies ($T_{hot} \sim 90$ keV). This year we continued using the IR laser with two beams (up to 2.3 kJ) in the co-propagating (co-prop) geometry to extend the pulse duration to 200 ps. The IR pulse (i.e., 200 ps with the co-prop beams or 100-ps single beam) had a nominal vacuum laser intensity of ~2×10^{16} W/cm^2 at the quarter- or tenth-critical density (n_c) surface. We used three-layer (25 μm CH/20 μm Cu/50 μm Al) solid disk targets designed to stop hot electrons up to 200 keV. A hot, large-scale CH plasma was created by a 2-ns, 2.2-kJ UV laser (B3 or B4) with 750-μm distributed phase plates (DPP's) ($I \sim 2 \times 10^{14}$ W/cm^2) to mimic the large corona plasma in SI. At 1.5 ns after the start of the UV pulse, the single or co-prop IR beams were injected. A suite of optical (the 10-ps 4ω probe and the newly available OMEGA EP SABS) and x-ray diagnostics [e.g., SCI, ZVH, bremsstrahlung MeV x-ray spectrometer (BMXS), and hard x-ray detector (HXRD)] were utilized to characterize LPI and the hot-electron energy, spectral, and angular distribution.

In our HotEScaleEP-17A experiments, we found that hot-electron generation by the co-prop IR beams (200 ps) was sensitive to the plasma temperature as shown in Fig. 152.62. Such dependence was not observed in the single IR beam (100-ps) interaction. With the higher-temperature (1.5-keV) plasma, the Cu K_α photon yield produced by the co-prop IR beams increased 170% compared to the data with 1.0-keV plasma. Meanwhile, the measured hard x-ray signal was also increased about 130% to 180% in the 17- to 200-keV energy range. HXRD data suggested a hot-electron temperature of less than 100 keV. The AFR image obtained from the 4ω probe diagnostic showed that the co-prop IR beams propagated beyond the $n_c/4$ in high-temperature plasma and produced a bright self-emission spot at the n_c surface as shown in Fig. 152.63. Resonance absorption may have contributed to hot-electron generation at the n_c surface. The bright self-emission spot was not observed from the interaction of either the co-prop IR beam with the 1.0-keV plasma or the single IR beam (100 ps) with the same density scale plasma with a temperature from 1.0 to 1.4 keV. The AFR image also captured the density perturbation between $n_c/10$ and $n_c/4$ surface as the result of strong nonlinear LPI's. OMEGA EP SABS recorded spectrally resolved sidescattering of the IR beam in the 400- to 750-nm spectrum range showing SRS. The 4ω self-emission observed at the n_c surface indicated that SRS and TPD were saturated since the co-prop IR beams propagated beyond the $n_c/4$ surface (TPD and SRS boundary). The data analysis and PIC modeling are ongoing.

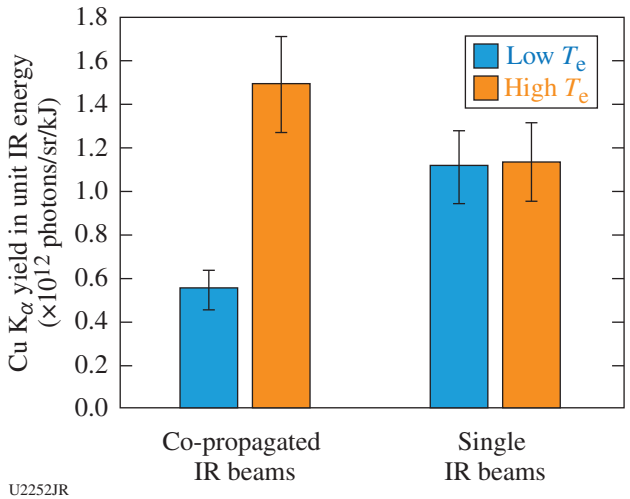

Figure 152.62
The Cu K_α yield (normalized to the IR beam energy) from the interaction of the single and two co-prop IR beams with low- (1.0-keV) and high- (1.4- to 1.5-keV) temperature plasmas was measured using a zinc von Hamos x-ray spectrometer.

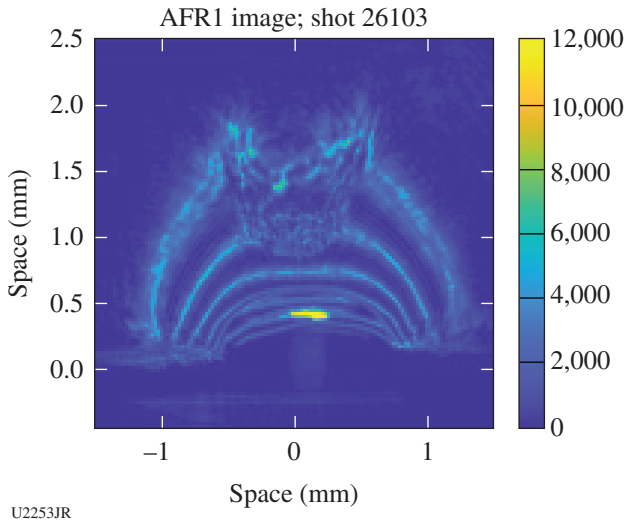

Figure 152.63
The 4ω probe–measured AFR image of the co-prop IR beams in the high-temperature (1.5-keV) plasmas The co-prop IR beams strongly interacted with the long-scale plasma and reached the critical-density surface, producing bright self-emission.

FY17 Laboratory Basic Science (LBS) Program

Sixteen LBS projects previously approved for FY17 target shots were allotted Omega Laser Facility shot time and conducted a total of 199 target shots at the Omega Laser Facility in FY17 (see Table 152.VIII). The FY17 LBS experiments are summarized in this section.

During FY17, LLE issued a solicitation for LBS proposals to be conducted in FY18. A total of 28 proposals were submitted. An independent committee reviewed and ranked the proposals; on the basis of these scores, 16 proposals have been allocated 21 shot days at the Omega Laser Facility in FY18. Table 152.IX lists the approved FY18 LBS proposals.

Exploring Pair Plasmas and Their Applications
Principal Investigator: H. Chen (LLNL)

In FY17, an LLNL/SLAC/University of Michigan team continued this project on OMEGA EP with one LBS shot day. These experiments use the short-pulse beams to produce jets of electron–positron antimatter pairs. The FY17 campaign focused

Table 152.VIII: LBS experiments approved for target shots at the Omega Laser Facility in FY17.

Principal Investigator	Institution	Title
H. Chen	LLNL	Exploring Pair Plasmas and Their Applications
A. R. Christopherson	LLE	Shock-Ignition Timing Measurements on OMEGA
J. R. Davies	LLE	Measuring the Nerst Effect and the Thermal Dynamo
S. Jiang	LLNL	Characterizing Pressure Ionization in Ramp-Compressed Materials with Electron-Induced Fluorescence
E. V. Marley	LLNL	Time-Resolved Measurement of the Radiative Properties of Open L-Shell Zinc
D. A. Martinez	LLNL	Optimizing Backlighters for Imaging Low-Density Plasmas for Eagle Pillar Studies
M. A. Millot	LLNL	Equation of State, Structure, and Optical Properties of Silicates at Multi-Mbar Pressure for Super-Earth Mantle and Accretion Modeling
A. Pak	LLNL	Laser-Driven Collisionless Shock Acceleration of Ions (E-Shock)
H.-S. Park	LLNL	Astrophysical Collisionless Shock Experiments with Lasers
H. G. Rinderknecht	LLNL	Measuring Strong Plasma Shock-Front Structure Using Thomson-Scattering Imaging
M. J. Rosenberg	LLE	Electron Energization During Magnetic Reconnection in High-Energy-Density Plasmas
A. M. Saunders	LLNL	Absolute Equation-of-State Measurements from Spherical Converging Shock Waves on the OMEGA Laser
R. F. Smith	LLNL	Determining the High-Pressure Properties of Silicon Carbide Using Decaying Shocks in *In-Situ* X-Ray Diffraction
R. F. Smith	LLNL	Experimentally Constraining the High-Pressure Thermal Conductivity of Iron
C. E. Wehrenberg	LLNL	Recovery of Dynamically Compressed Samples
A. B. Zylstra	LANL	Charged-Particle Stopping Power and Scattering Measurements in a Warm Dense Plasma

on measuring the pair yield enhancement with nanostructured targets. The experiments successfully demonstrated that the laser-positron energy conversion can be improved by using novel structured targets. A total of 12 shots were performed.

The OMEGA EP short-pulse beams (~1 kJ in 10 ps) irradiated 1-mm-thick Au targets with and without the nanostructure on the laser-interaction surface. It was found that for the same laser energy, positron yields and acceleration both were increased dramatically by using a nanostructure. This finding is important to future experiments and applications using laser pair jets. Previous experiments used primarily gold targets and showed that quasi-monoenergetic relativistic positron jets are formed during high-intensity irradiation of thick gold targets,[18,19] and also that these jets can be strongly collimated[20] using the magneto-inertial fusion electrical discharge system (MIFEDS).[21] The external field produces a 40-fold increase in the peak positron and electron signal.[20] The positron yield was found to scale as the square of the laser energy[22,23] in this regime. The yield also increases with the Z of the target material. Together with the nanostructured target yield enhancement, these favorable scalings are expected to enable the laboratory study of relativistic pair plasmas to aid one's understanding of some of the most exotic and energetic systems in the universe.[23,24]

Shock-Ignition Timing Measurements on OMEGA

Principal Investigators: A. R. Christopherson, D. T. Michel, R. Betti, A. K. Davis, S. Depierreux, W. Seka, C. Stoeckl, and W. Theobald (LLE); and J. Trelou, A. Casner, M. Lafon, C. Neuville, and X. Ribeyre (CEA)

The objective of the Shock-Ignition Timing Campaign was to measure the ablation pressure and hot-electron preheat from the ignitor spike. Small [650-μm-outer-diam (OD)] CH shells were irradiated with two pulse shapes—one with a spike and one without a spike—as shown in Fig. 152.64(a). The compression of the shell resulting from the ignitor shock was measured by the x-ray framing camera (XRFC). This is illustrated in Fig. 152.64, where (a) represents the ablation-front trajectories of the implosions with and without a spike, while (b) is an image from the XRFC showing how the ablation front and hot-

Table 152.IX: LBS experiments approved for target shots at the Omega Facility in FY18.

Principal Investigators	Institution	Title
S. J. Ali	LLNL	Effect of Grain Size on the Dynamic Failure of Diamond
H. Chen	LLNL	Exploring the Applications of Laser-Produced Relativistic Electron–Positron Pair-Plasma Jets
T. Doeppner	LLNL	Equation-of-State Measurements of Shock-Heated Foams Using X-Ray Thomson Scattering and Fluorescence
S. Jiang	LLNL	Characterizing Pressure Ionization in Ramp-Compressed Materials with Electron-Induced Fluorescence
G. Kagan	LANL	Separation of Ion Species in Collisional Plasma Shocks
A. Krygier	LLNL	Shock Metamorphism and Lattice Deformation Kinetics in Meteor Impacts
T. Ma	LLNL	Proton Isochoric Heating for Warm-Dense-Matter Studies
E. V. Marley	LLNL	Radiative Properties of an Open L-Shell, Non-LTE Plasma
P. M. Nilson	LLE	Applying Marshak Waves to the Iron Opacity Problem
H.-S. Park	LLNL	Study of High Alfvénic Mach Number Plasma Dynamics and Magnetized Shocks
D. N. Polsin	LLE	Structure and Melting of High-Pressure Sodium
M. J. Rosenberg	LLE	Electron Energization During Magnetic Reconnection in High-Energy-Density Plasmas
J. R. Rygg	LLE	Atomic and Electronic Structure of Warm Dense Silicon
R. F. Smith	LLNL	Thermal Conductivity of Fe and Fe-Si at Earth Core Conditions
W. Theobald	LLE	Shock Formation and Hot-Electron Preheating in Planar Geometry at Shock-Ignition–Relevant Laser Intensities
A. B. Zylstra	LANL	Charged-Particle Stopping Power Near the Bragg Peak

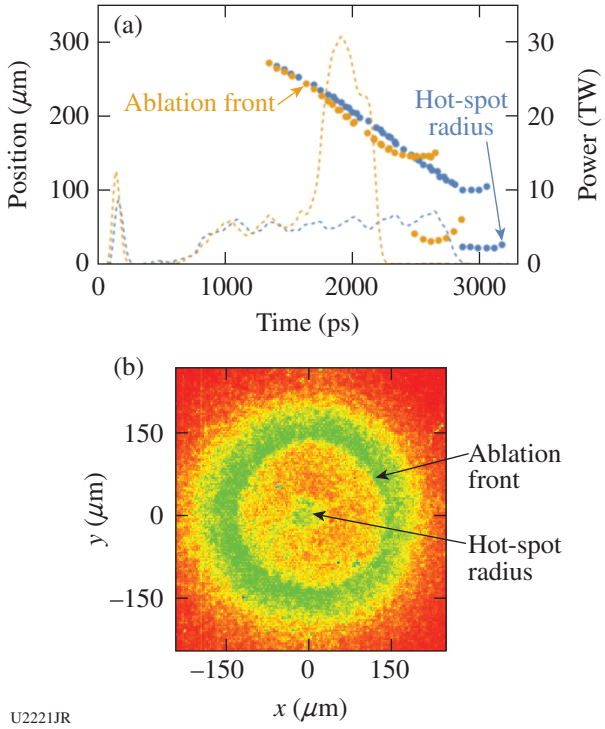

Figure 152.64
(a) The ablation-front trajectories for the implosion with (dotted orange curve) and without (dashed blue curve) the spike, which clearly accelerates faster after the shock has been launched. The dashed lines represent the laser power in TW. (b) An x-ray framing-camera image that is used to determine the ablation-front position and the hot-spot radius.

spot radius are measured. A maximum ignitor shock ablation pressure of ~180 Mbar was inferred from a post-shot *LILAC* simulation approximately constrained to the data.

One way to experimentally determine preheat by hot electrons is to measure the premature expansion of the shell before the ignitor shock breaks out. This preheat causes the hot spot to emit earlier than it would without preheat. In Fig. 152.64(a), the implosion with the ignitor shock starts emitting earlier than the no-spike case. Understanding the relative importance of hot-electron preheat versus ignitor shock breakout time on the earlier emission is the subject of an ongoing investigation.

Measuring the Nerst Effect and the Thermal Dynamo

Principal Investigator: J. R. Davies (LLE)

The objective of this experiment was to observe the dynamo effect caused by cross-field heat flow. The dynamo effect occurs because of sheared rotation of plasma around magnetic-field lines, which acts to twist the field lines, generating a component in the direction of the rotation. The dynamo effect has been extensively studied in the context of astrophysical jets.

A magnetic field in a plasma moves not only with the bulk plasma motion but also with the electron heat flow, which can be ascribed to the field being preferentially frozen to the electrons responsible for heat flow because of their lower collision frequency. In magnetized plasma there exists heat flow perpendicular to the temperature gradient and the magnetic field, known as cross-field heat flow. Cross-field advection of the field has largely been ignored, but it could readily lead to a dynamo effect in the absence of plasma rotation.

To generate a thermal dynamo, we placed a carbon disk inside a MIFEDS coil, giving an axial magnetic field, and irradiated the edge of the disk with ten OMEGA beams, five from each side, creating a radial temperature gradient, which will lead to an azimuthal cross-field heat flow and the generation of an azimuthal magnetic field. To probe the magnetic field, we used D^3He protons passing through a grid on one side of the target.

Unfortunately, MIFEDS started to trigger erratically and only one magnetized shot was obtained, at maximum field, which deflected all of the protons out of the detection angle, as shown in Fig. 152.65. The grid is not visible, which may be a result of being attached to the target or simply being too close to the target or backlighter. Although this one shot indicates that the thermal dynamo effect does occur, shots with lower magnification, a lower magnetic field, and a working grid setup would be required to confirm and quantify the effect.

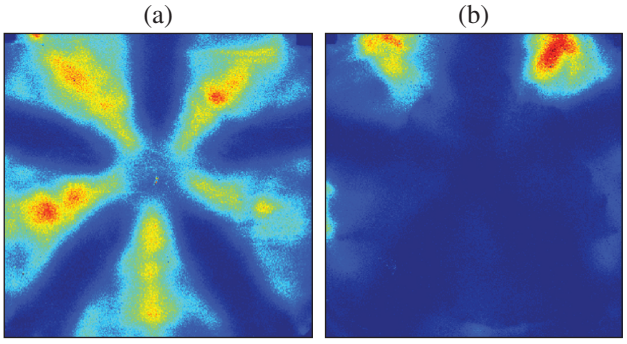

Figure 152.65
Proton radiographs of (a) unmagnetized and (b) magnetized disks irradiated at the edges by five OMEGA beams on each side. The empty regions (blue) in the unmagnetized case correspond to the beam paths. In the magnetized target, almost all of the protons have been deflected away from the detector.

Characterizing Pressure Ionization in Ramp-Compressed Materials with Electron-Induced Fluorescence

Principal Investigator: S. Jiang (LLNL)

Co-investigators: Y. Ping, R. F. Smith, A. Jenei, and J. H. Eggert (LLNL)

This campaign used one day on OMEGA EP to measure ionization in compressed materials as a function of density, using K-shell fluorescence spectroscopy. The K-shell line emissions were induced by hot electrons generated through short-pulse laser–solid interactions. The high pressure was achieved by ramp compression using the long-pulse drivers while keeping the temperature low. A large, thick target was used to avoid heating from the short pulse, as shown in Fig. 152.66(a). The configuration is intended to compress the material up to 1.5× to 2× its original density without raising the thermal ionization effect. There is still little consensus on pressure ionization under these conditions despite extensive theoretical and experimental efforts.

A schematic of the experimental setup is displayed in Fig. 152.66(a). The main diagnostic used in this campaign was the high-resolution imaging x-ray Thomson spectrometer (IXTS). The Cu K_α and Co K_β fluorescence lines were successfully observed with a high signal-to-noise ratio, as can be seen in Fig. 152.66(b). Under the designed experimental conditions, pressure ionization has a negligible effect on the innermost electron shells (K,L), but it can affect the M shell. Therefore, the Cu K_α line is not subject to an energy change and can be used as a reference. On the other hand, the Co K_β line is more prone to a shift. Figure 152.66(b) shows the measured Co K_β peaks under different driver energies and time delays. While some differences can be observed between the undriven and driven conditions, the energy shifts are small enough that they are close to the resolution of the spectrometer (~4 eV). In a future experiment, we will increase the driver energy to reach a higher pressure and also probe other materials.

Time-Resolved Measurement of the Radiative Properties of Open L-Shell Zinc

Principal Investigator: E. V. Marley (LLNL)

Co-investigators: L. C. Jarrott, M. B. Schneider, G. E. Kemp, M. E. Foord, R. F. Heeter, D. A. Liedahl, K. Widmann, C. W. Mauche, G. V. Brown, and J. A. Emig (LLNL)

This campaign was designed to measure the emitted L-shell zinc spectrum from a well-characterized and uniform plasma for comparison to atomic kinetic models. Recent studies have shown a discrepancy between atomic kinetic models and high-Z M-shell spectral data. This study was done to test the accuracy of models for L-shell emission.

Planar buried layer targets were illuminated evenly on both sides (Fig. 152.67) to heat the sample composed of Ti and Zn. The sample was buried between two 6.7-μm-thick layers of Be, which inertially tamps the sample, slowing its expansion.

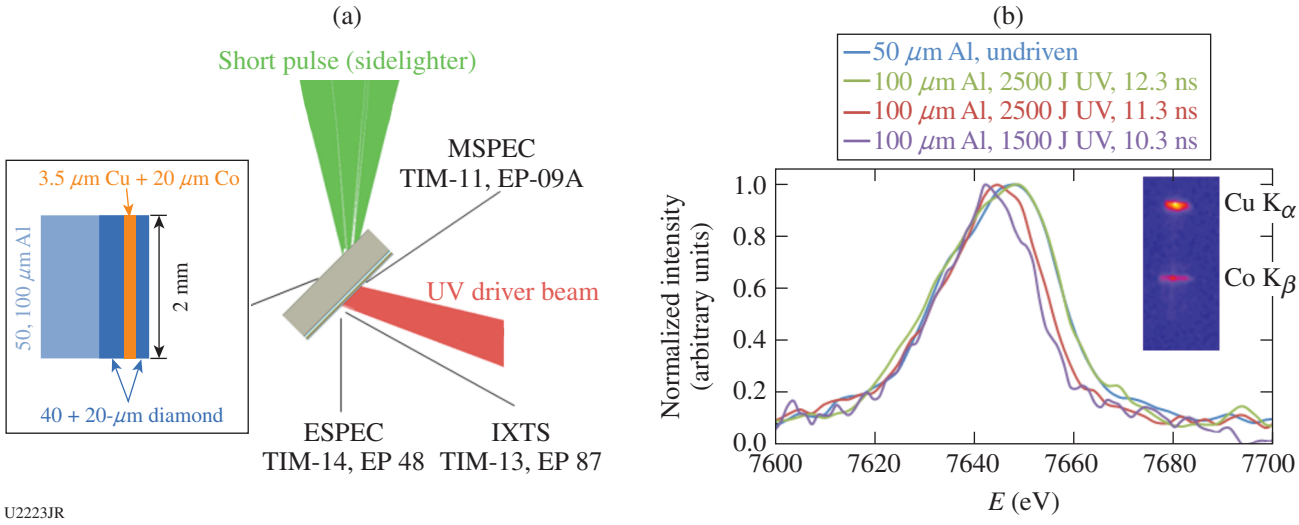

Figure 152.66

(a) A schematic of the experimental configuration. The inset shows the target geometry. (b) Measured IXTS spectra of Co K_β (normalized with the peak intensity). The lineouts are from different driver conditions. An example of the raw image is shown in the inset in (b).

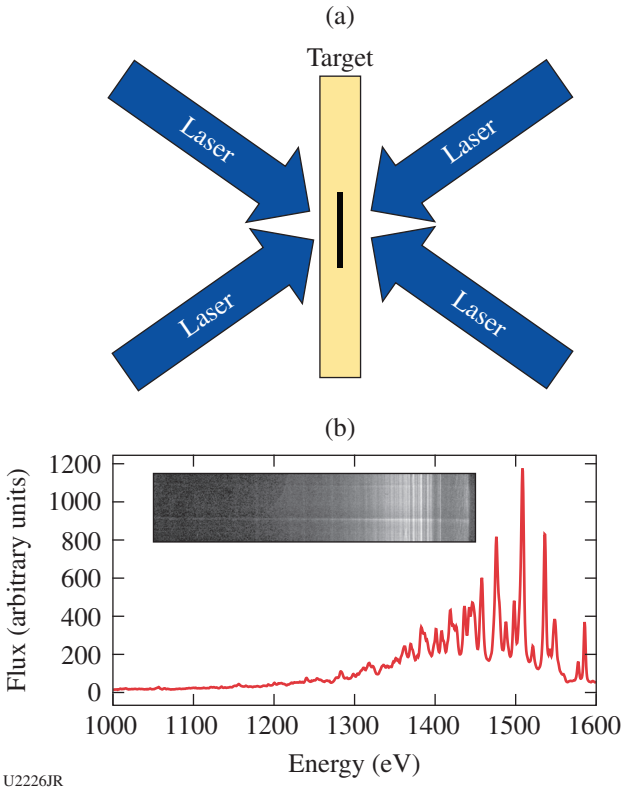

Figure 152.67
(a) Experimental configuration; (b) time-resolved Zn L-shell spectrum with data inset at 2.8 ns of shot 85317.

Time-resolved 2-D images of the target's x-ray emission, viewed both face-on and side-on, were recorded using pinhole cameras coupled to framing cameras. The K-shell spectrum from the Ti was used to determine the electron temperature of the plasma. The time-resolved spectrum was recorded using a crystal spectrometer coupled to a framing camera. A second crystal spectrometer/framing-camera system was used to record time-resolved zinc L-shell emission. More L-shell spectra were recorded with a spectrometer coupled to a streak camera to give a continuous record of the ion population shifts over time. A third spectrometer, which utilized a variably spaced grating and a slit, was coupled to a framing camera to give a temporally and spatially resolved spectral measurement of the zinc L shell. This measurement will help to verify the uniformity of the plasma at different times during the experiment. All of the framing cameras, used for imaging as well as for spectroscopy, were co-timed on the shot day so that plasma conditions could be determined for the measured zinc L-shell spectra.

Two different pulse shapes were used: a 3.2-ns square pulse and a 3.0-ns square pulse with a 100-ps picket preceding it by 1 ns. The second pulse tested whether creating a pre-plasma before the main pulse would create a smoother interface, allowing for a more-efficient coupling of energy into the target. The results look promising. A complete set of data from all six co-timed diagnostics was recorded for both pulse shapes during the campaign at sample temperatures ~1 keV.

Optimizing Backlighters for Imaging Low-Density Plasmas for Eagle Pillar Studies

Principal Investigator: D. A. Martinez (LLNL)
Co-investigators: J. Kane and R. F. Heeter (LLNL); and B. Villette and A. Casner (CEA)

The LBS Eagle Pillar experiments were designed to optimize the backlighter for imaging the plasma plume created by an ablated CH solid-density cone target in conditions similar to counterpart NIF Discovery science experiments. The CH target was driven for 30 ns using three Cu hohlraums (Fig. 152.68) heated in succession, which will eventually create

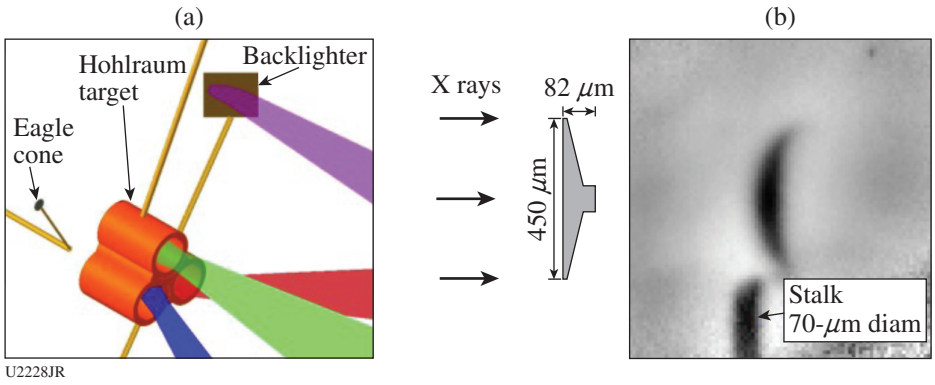

Figure 152.68
(a) Layout of the experiment showing all beams on target. (b) A hohlraum drives a cone target for 30 ns and is imaged with a Ti (shown) or U backlighter.

a comet-like flow behind the solid target (away from the drive). This flow is expected to coalesce behind the solid target, and the hohlraum x-ray drive will confine the plasma to generate a plasma pillar. To observe this requires a backlighter with sufficiently low photon energy to image the warm, low-density plasma. This campaign used Ti (4.7-keV) and U (1.2-keV) area backlighters to try to image the ablating CH target. Seven shots were taken with a backlighter delay between 20 and 35 ns with respect to the start of the drive, using both U and Ti backlighters. Because of debris risk, the experiment used image plates with a 200-μm Be blast shield, increasing the average photon energy for the U backlighter to the 3- to 4-keV range. Images obtained from the U backlighter were comparable to the Ti backlighter, both suggesting this photon energy was too high. The U backlighter also showed significant structure in the backlighter profile as shown in Fig. 152.69. More work is needed to sufficiently reduce the photon energy to image the ablated plasma.

Equation of State, Structure, and Optical Properties of Silicates at Multi-Mbar Pressures for Super-Earth Mantle and Accretion Modeling

Principal Investigator: M. A. Millot (LLNL)
Co-investigators: F. Coppari, D. E. Fratanduono, and S. Hamel (LLNL); N. Dubrovinskaia and L. Dubrovinsky (Bayreuth University, Germany); and R. Jeanloz (University of California, Berkeley)

During FY17, our international research team conducted two campaigns at the Omega Laser Facility to investigate the equation of state, structure, and optical properties of silicates at multi-Mbar pressures using shock compression.

Following our previous study on the melting line of SiO_2 using stishovite crystals,[25] we conducted a shock compression study of $MgSiO_3$ bridgmanite (perovskite) samples synthesized at Bayreuth University, Germany, to investigate the pressure–density–temperature equation of state and the melting temperature of $MgSiO_3$, representative of the material making up the interiors of rocky planets and the cores of gas giants. Preliminary analysis of the velocity interferometry (VISAR) and streaked optical pyrometry (SOP) data indicates that we successfully observed reflecting shocks up to 15 Mbar.

Another set of experiments used OMEGA EP pulse-shaping capabilities to launch a carefully timed series of two steady shocks into stishovite samples to make it possible to determine the atomic structure of SiO_2 at Neptune core conditions using x-ray diffraction. Composite three-beam pulse shapes enabled us to generate the complex drive conditions, while focusing Beam 1 on a Ge foil was used to generate a 1-ns pulsed x-ray source. Preliminary analysis indicates that x-ray diffraction (XRD) patterns (Fig. 152.70) for single- and double-shock compressed silica were obtained up to 9 Mbar.

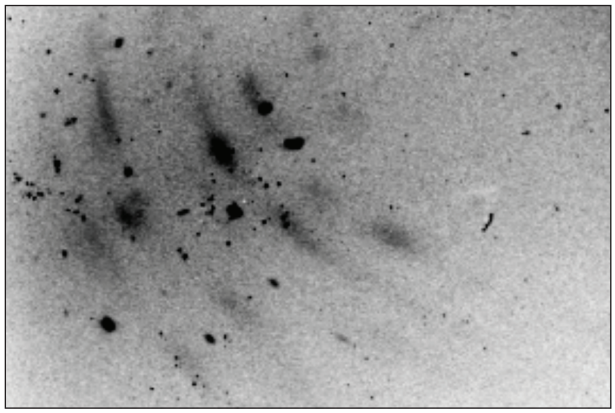
U2242JR

Figure 152.70
Example of an x-ray–diffraction pattern of silica shock compressed to ~3 Mbar along the stishovite Hugoniot.

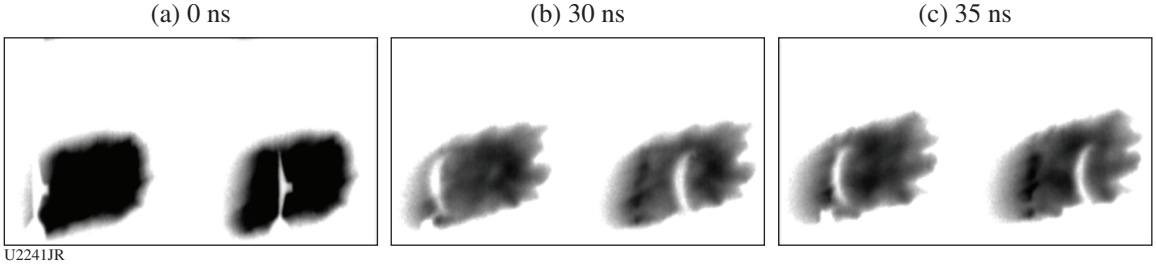

U2241JR

Figure 152.69
Time sequence of the target imaged through a pinhole array backlit with a U backlighter. Multiple images were obtained to remove the backlighter structure. The (a) 0-ns image had lower filtering but the (b) 30- and (c) 35-ns images had 200 μm Be.

Laser-Driven Collisionless Shock Acceleration of Ions (E-Shock)

Principal Investigator: A. Pak (LLNL)
Co-investigators: A. J. Link (LLNL); D. Haberberger and D. H. Froula (LLE); S. Tochitsky, C. Joshi, and F. Fiuza (University of California, Los Angeles)

This LBS shot day explored the acceleration of ions into narrow energy distributions caused by the reflection from the strong electrostatic field of a collisionless shock wave. As Fig. 152.71(a) indicates, a near-critical-density CH target was first produced by the x-ray drive generated from the ablation of a gold foil by a 1-ns-long laser pulse (UV Beamline 3). After waiting for the CH target to expand to a peak density of $\sim 10 \times 10^{21}$ cm^{-3}, the ultra-intense backlighter beam was used to irradiate the target and drive the collisionless shock wave. Nearly simultaneously, the sidelighter beam produced a beam of protons through target normal sheath acceleration (TNSA) to radiograph the shock-formation process.

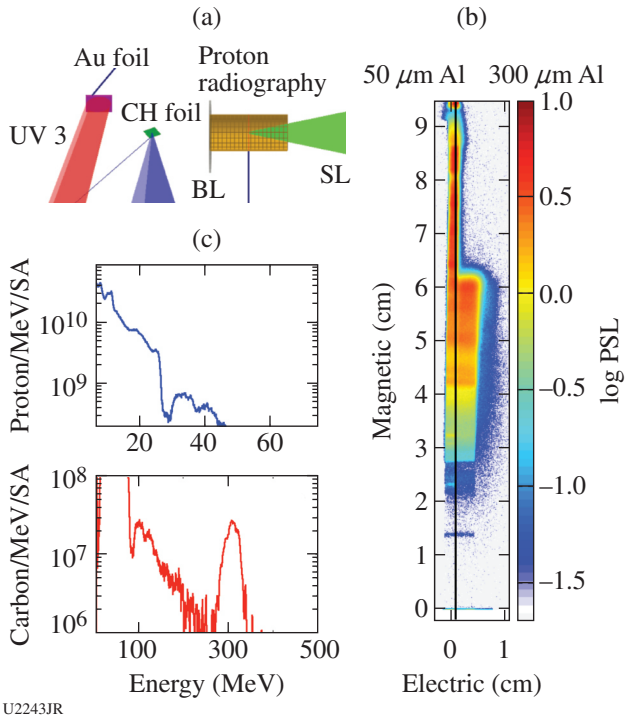

Figure 152.71
(a) Experimental configuration. (b) Data from the modified Thomson parabola ion energy (TPIE) setup with differential filtering and no electrical bias. The vertical black line denotes filter change. (c) The proton and carbon spectra. BL: backlighter; SL: sidelighter; PSL: photostimulated luminescence.

In these experiments, the pinhole of the Thomson parabola ion energy (TPIE) diagnostic was replaced with a new ~5-mm-wide × 0.25-mm-long slit to extend the angular acceptance of the diagnostic. The electric bias of the TPIE was turned off, and differential filtering of 50 μm and 300 μm Al was used at the image-plate detector to differentiate between ion species. TPIE data from this configuration are shown in Fig. 152.71(b).

In this experiment, narrow energy distributions of both protons and carbon ions were observed to be accelerated to similar velocities of ~0.25 c. The acceleration of disparate charge to mass ratio ion species to similar velocities is consistent with acceleration from the moving near-relativistic electric field associated with a collisionless shock wave. A distribution of protons centered at 36 MeV (velocity = 0.28 c), and with an energy range $\Delta E/E$ of ~30% was observed, as well as a distribution of C^{6+} ions centered at 308 MeV (velocity = 0.23 c) and $\Delta E/E$ of ~12%. The difference in velocity between the two ion species is thought to arise from the remaining sheath field of the expanded target, which preferentially accelerates the lighter species. Analysis of the radiography and accelerated beam profile data is in progress.

Astrophysical Collisionless Shock Experiments with Lasers

Principal Investigator: H.-S. Park (LLNL)
Shot Principal Investigator: G. F. Swadling (LLNL)

Experiments ACSEL-17A and 17B investigated the physical processes that lead to the formation of astrophysical collisionless shocks. These shots continued a broad, long-running, cross-institutional collaboration. A total of 26 target shots were completed in two shot days, primarily investigating interactions between beryllium ablation outflows; this material was selected to provide a low-Z, single-species plasma, which greatly simplifies Thomson-scattering interpretation and analysis, while maintaining the large collisional scale lengths required to observe the development of interpenetrating flow instabilities. In these experiments, the OMEGA beams heat the surfaces of a pair of opposed planar disk targets (see Fig. 152.72), ablating counter-propagating plumes of high-velocity (up to 1.5×10^6 ms^{-1}), high-temperature (~keV) plasma. The outflow parameters are such that the coulomb mean-free path for interflow collisions is long, but the interaction of the flows is still susceptible to the growth of the interstream instabilities that are believed to mediate the formation of collisionless shocks.

This year, experiments focused on taking spatially resolved Thomson-scattering measurements across the interaction

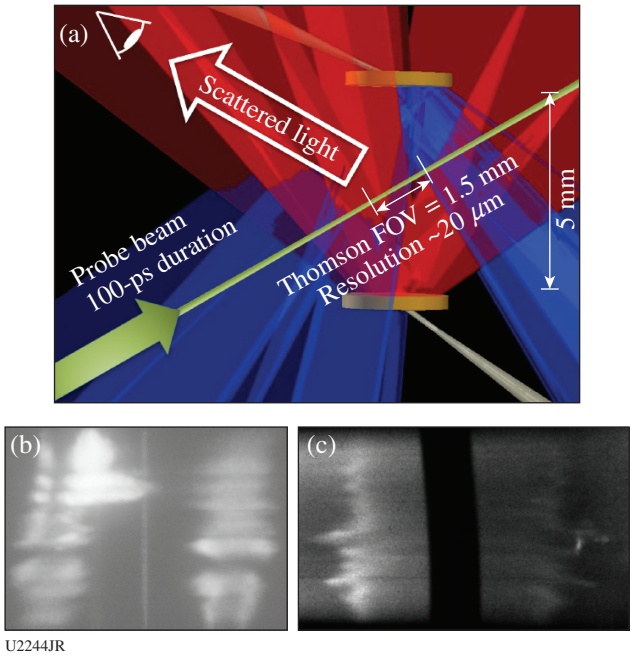

U2244JR

Figure 152.72
(a) Diagram of experimental setup for spatially resolved Thomson-scattering measurements. (b) Ion-acoustic wave (IAW) and (c) electron plasma wave (EPW) data. The vertical direction in the spectrograms is the direction of spatial displacement along the probe beam, as shown in the diagram. The horizontal direction is the direction of spectral dispersion. Striations in the vertical direction in the IAW image are characteristic of Weibel filamentation. Modulations in the EPW image indicate strong transverse modulations in the electron density across the interaction region. FOV: field of view.

region to quantitatively investigate the development of the ion-Weibel instability. Thomson scattering was combined with proton radiography measurements; a D^3He exploding-pusher capsule provided a dichromatic (3.3- and 14.4-MeV) proton source for radiography, probing the plasma at two separate times during each experiment. Images were recorded on CR-39, with processing and analysis of the CR-39 plates carried out by collaborators at MIT.

The OMEGA Thomson-scattering diagnostic records both ion-acoustic and electron plasma wave features of the Thomson-scattering spectrum. Analysis of the detailed shape of these spectra made it possible to extract information about the spatial variation in electron temperature, electron density, ion temperature, and flow velocity across the interaction of the two flows. The primary goal in FY17 was to make a direct measurements of spatial density modulations of the ion flows and the underlying electron density of the plasma. High-quality data were recorded and are expected to provide a wealth of data on the development of the ion-Weibel instability in these experiments; examples of the spectrograms are shown in Fig. 152.72. Striations in the intensity of the ion-acoustic feature along the probe beam are characteristic of the development of the ion-Weibel instability, while the presence of modulations in the electron plasma wave data suggests that the ion-Weibel instability is in the nonlinear growth phase.

Measuring Strong Plasma Shock-Front Structure Using Thomson-Scattering Imaging

Principal Investigator: H. G. Rinderknecht (LLNL)
Co-investigators: H.-S. Park and J. S. Ross (LLNL); and D. H. Froula (LLE)

This series of shots was designed to directly measure for the first time the spatial structure of a strong shock front in a plasma. The experiments were intended to develop a platform for kinetic plasma studies using the new gas-jet system on OMEGA to quantify collisional phenomena in high-energy-density plasmas and to benchmark high-fidelity physics codes. These experiments were also the first use of the gas-jet system on OMEGA.

The KineticShockLBS-17A Campaign on 24 August used the new gas-jet system to inject a column of hydrogen or neon gas into the OMEGA target chamber. A 1-μm Si_3N_4 foil positioned near the gas-jet nozzle was driven by ten beams with 2.5 kJ in 0.6 ns, exploding the foil to drive a strong shock into the low-density (~5×10^{18} cm^{-3}) gas. A 526.5-nm probe beam with 40 J in a 100-ps impulse was injected normal to the ablator foil at a 4- to 6-ns delay from the drive beams, and Thomson-scattered light from the probe was imaged along the probe axis. The imaged region was 3.25 to 4.75 mm from the ablator, with a resolution of 20 μm. Despite operational difficulties with the gas-jet system on its first shot day, six shots were completed and excellent data collected on all shots for which the gas-jet successfully operated.

Figure 152.73 shows ion-acoustic wave (IAW) and electron plasma wave (EPW) Thomson-scattering images from shot 86801. Fits to the EPW data demonstrate the characteristics of strong shock formation: heating of electrons in the pre-shock region, followed by an increase in density as the ion shock forms. IAW data appear to show streaming protons in advance of the shock front, heating, and slowing down on the pre-shocked plasma; analysis of these results is underway. These exciting results will be presented in an invited talk at the APS DPP meeting in October 2017 to demonstrate the high value of this platform for future kinetic plasma studies on OMEGA.

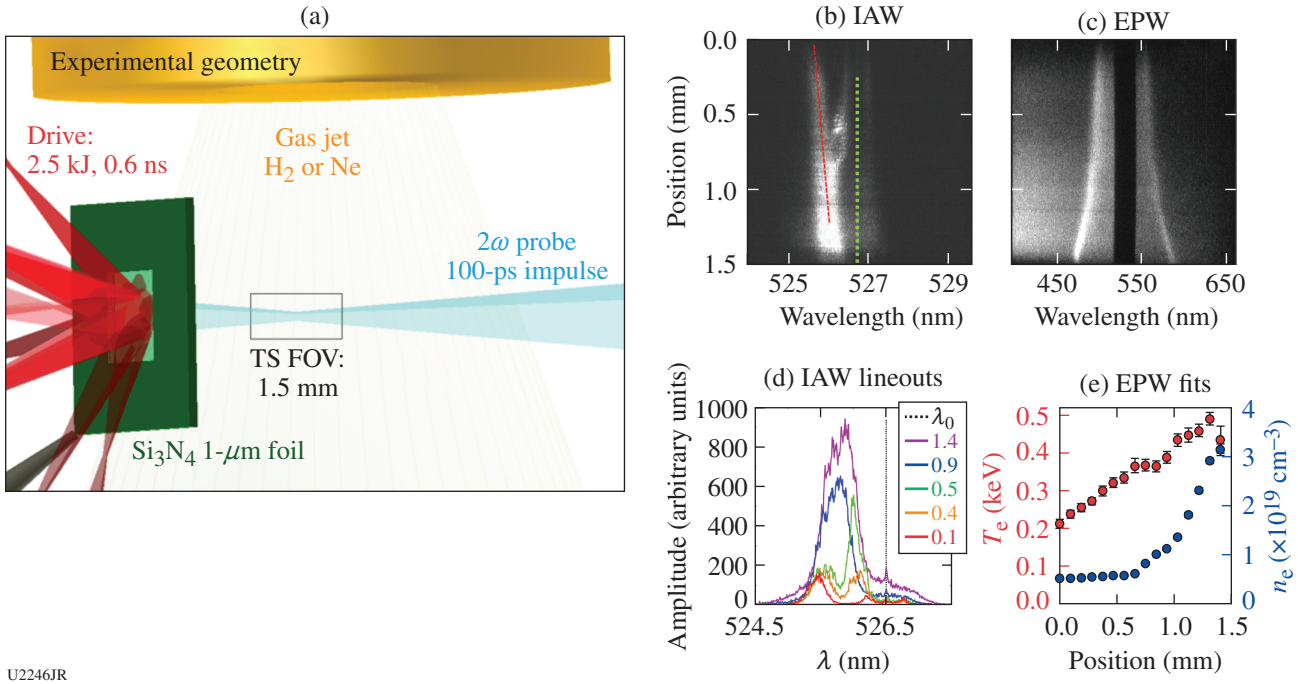

Figure 152.73
(a) Experimental layout; [(b),(c)] raw Thomson-scattering (TS) images; (d) lineouts from ion-acoustic wave (IAW) data showing merging of ion populations in shock; and (e) fits to electron plasma wave (EPW) spectrum showing heating and density jump resulting from shock in shot 86801. FOV: field of view.

Electron Energization During Magnetic Reconnection in High-Energy-Density Plasmas

Principal Investigator: M. J. Rosenberg (LLE)

The MagReconnection-17A shot day on OMEGA (14 March 2017) through the LBS program successfully diagnosed the spectrum of energetic electrons generated in laser-plasma experiments in which magnetic reconnection was driven. These experiments utilized a well-established platform for studying the generation, interaction, and reconnection of magnetic fields in plasmas created by the interaction of multiple laser-produced plasma plumes adjacent to each other using foil targets. The energization of particles during the annihilation of magnetic fields is a common process in astrophysical plasmas, but it is poorly understood and has rarely been investigated in the laboratory. The new, compact single-channel electron spectrometer microscope (SC-ESM) obtained electron spectra over the energy range of ~50 to 300 keV.

Spectra obtained perpendicular to the foil and parallel to the reconnection current sheet that supports the magnetic fields are shown in Fig. 152.74. Experiments with two beam spots [Figs. 152.74(b) and 152.74(c)] drove magnetic reconnection, while experiments with only one beam spot [Fig. 152.74(d)] did not. Energetic electron spectra were measured, with characteristic temperatures of ~30 to 50 keV. Notably, a single-beam experiment [Fig. 152.74(d)] generated energetic electrons, suggesting that additional mechanisms beyond magnetic reconnection, such as laser–plasma instability (LPI), may be producing the energized particles. In addition, Thomson-scattering measurements were successfully obtained to diagnose plasma conditions in the reconnection region, and monoenergetic proton radiography was used to confirm the interaction and reconnection of magnetic fields, as have been observed in previous experiments. Another LBS shot day has been awarded to this campaign, during which we will attempt to determine the source of energetic electrons and obtain spectra unambiguously from magnetic reconnection by eliminating LPI.

Absolute Equation-of-State Measurements from Spherically Converging Shock Waves on the OMEGA Laser

Principal Investigator: A. M. Saunders (LLNL)
Co-investigators: T. Doeppner and R. Nora (LLNL); W. Theobald (LLE); and A. Jenei, D. Swift, J. Nilsen, and R. W. Falcone (Lawrence Berkeley National Laboratory, University of California, Berkeley)

X-ray Thomson scattering (XRTS) is an experimental technique that directly probes the physics of warm dense mat-

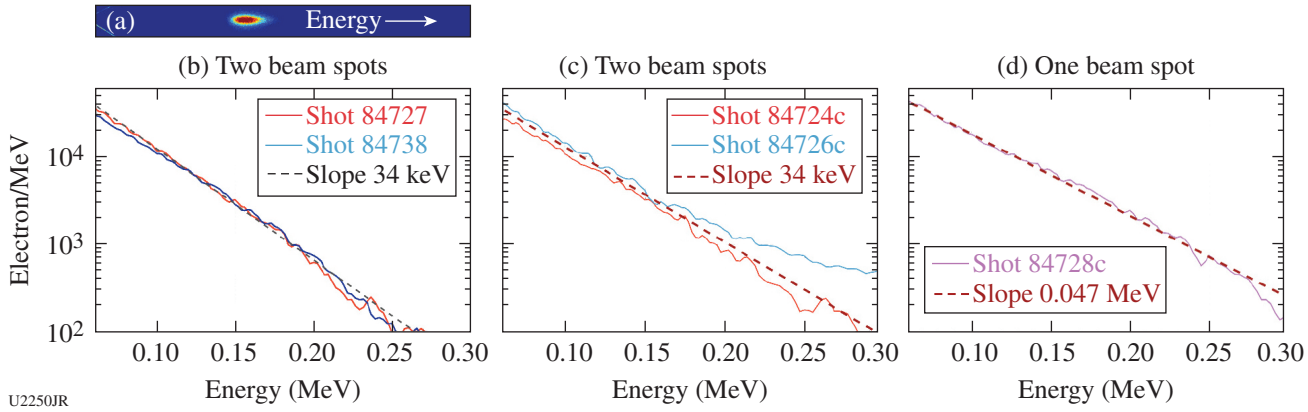

Figure 152.74
(a) A sample raw image-plate scan from SC-ESM; [(b)–(d)] spectra from various laser drive conditions.

ter by measuring electron density, electron temperature, and ionization state. XRTS in combination with x-ray radiography offers a unique ability to measure the absolute equation of state (EOS) of material in extreme conditions.

The OMEGA GbarIPD-17A Campaign took XRTS and x-ray radiography measurements from directly driven carbon-containing spheres compressed to electron densities of the order of 1×10^{24} cm^{-3} and temperatures of ~30 eV. X-ray radiography measurements were obtained for both plastic (CH) and high-density carbon (HDC) spheres. Fifty-two beams compressed the spheres, and six beams drove a foil backlighter. The x rays from the foil backlighter were observed in transmission through the sphere using a gated x-ray framing camera (Fig. 152.75). They show that the shock front travels inward as predicted by simulations. The radial lineouts make it possible to obtain the shock velocity. A more-complicated analysis of post-shock density at each time step will also be performed; the combination of density and shock velocity will allow for an absolute measurement of the EOS.

In conjunction with the radiography measurements, XRTS spectra were obtained from HDC spheres. A zinc He$_\alpha$ x-ray source was used to scatter x rays from the imploding spheres at a scattering angle of 135°. The scattered x rays were collected by a crystal spectrometer in conjunction with a gated x-ray framing camera. Figure 152.76 shows an example of the raw data collected and a lineout of one of the strips. The

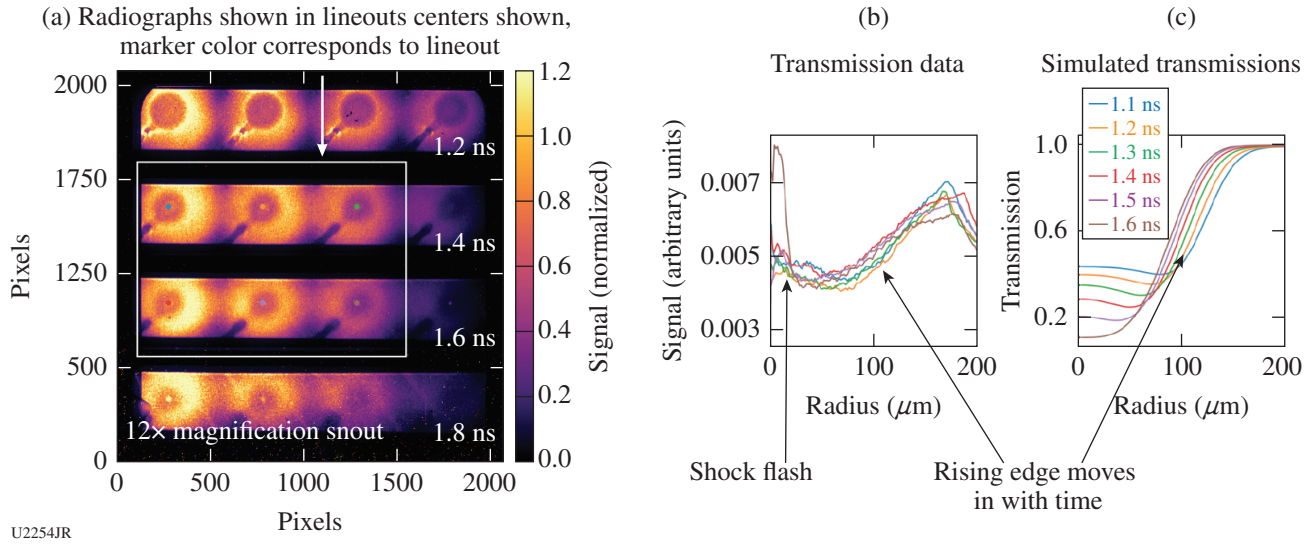

Figure 152.75
X-ray radiography measurements of shock-compressed CH spheres (shot 85691). (a) Example of the raw data obtained from the imploding CH spheres and [(b),(c)] radial lineouts from several of the radiography images, each at a different point in the implosion time.

XRTS data will provide an independent measurement of the mass-averaged electron temperature of the imploding sphere. The temperature measurement will further constrain the EOS measurement obtained from the radiography analysis. In summary, the data obtained in this campaign shed light on the EOS of matter under compression and support EOS measurements previously taken on the NIF.

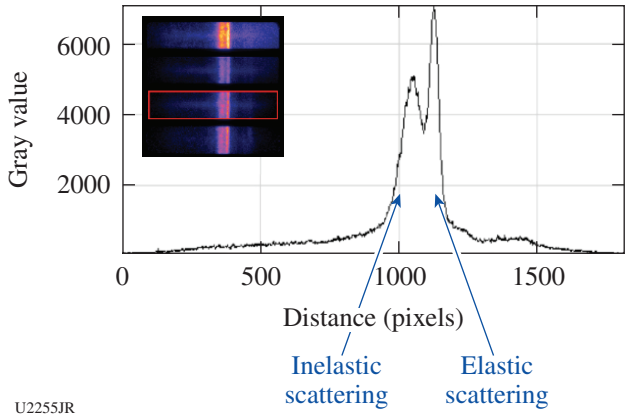

Figure 152.76
X-ray Thomson-scattering measurements from high-density carbon spheres (shot 85696).

Determining the High-Pressure Properties of Silicon Carbide Using Decaying Shocks in In-Situ *X-Ray Diffraction*

Principal Investigators: R. F. Smith (LLNL) and J. K. Wicks (Johns Hopkins University)

The goal of this campaign was to determine the high-pressure properties of single-crystal SiC along the Hugoniot, using a combination of shock decay[25] and nanosecond x-ray diffraction techniques.[26] Silicon carbide is an important material in geology and planetary science. It may be a host of reduced carbon in the Earth's interior since it is found in rocks from the mantle and in inclusions in deep diamonds.[27] It also occurs in meteorites and impact sites. The target design in Fig. 152.77 is modeled off previous campaigns on OMEGA.[25] The raw active shock breakout (ASBO) (shock velocity) and streaked optical pyrometer (SOP) (shock front thermal emission) data make it possible to determine the pressure–temperature onset of melt (see Fig. 152.78). During this shot day the powder x-ray

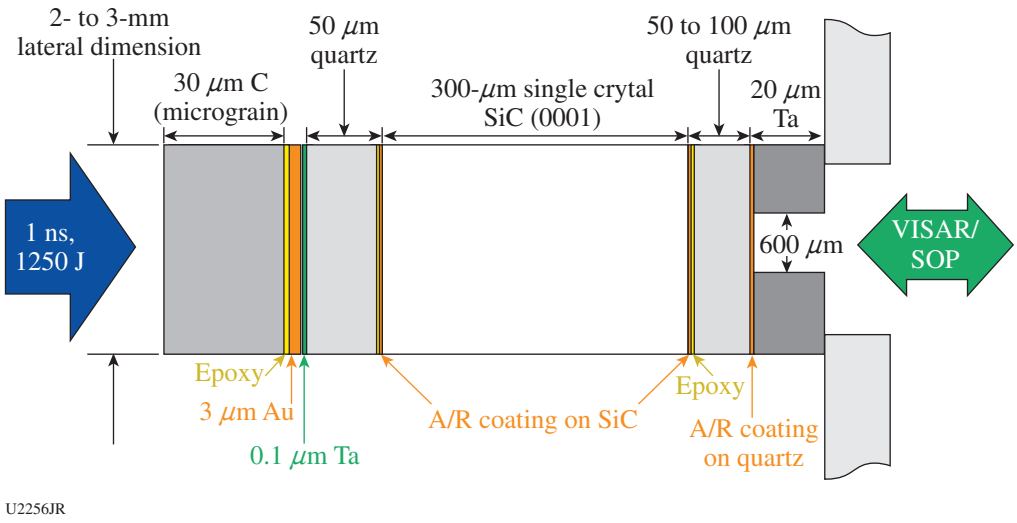

Figure 152.77
Target design for shock-decay experiments in SiC using a 1250-J drive in 1 ns (1100-μm phase plate). The quartz layers serve as calibrants for the OMEGA EP SOP.[25]

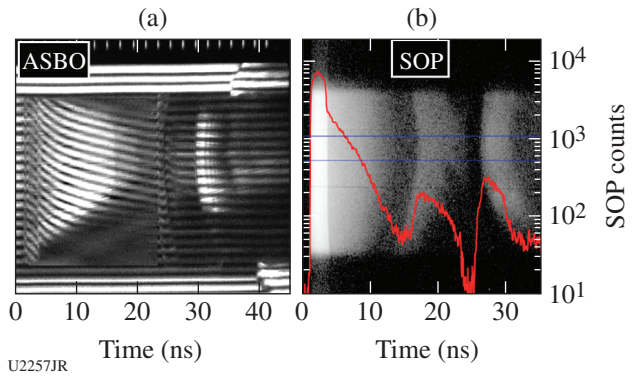

Figure 152.78
(a) Active shock breakout (ASBO) data provided the SiC shock velocity versus time. (b) The OMEGA EP SOP provided the temperature of the shock front as a function of time.

diffraction image-plate (PXRDIP) diagnostic was also used to determine the high-pressure crystal structure (pre-melt).

Experimentally Constraining the High-Pressure Thermal Conductivity of Iron

Principal Investigator: R. F. Smith (LLNL)
Co-investigator: J. K. Wicks (Johns Hopkins University)

High-pressure thermal conductivity is one of the most important and yet most difficult to measure physical property of materials. Within the Earth's interior the thermal conductivity k of Fe and Fe-rich alloys at core pressure–temperature conditions (135 to 360 GPa, 2500 to 5000 K, respectively) is a key parameter for heat transport models and plays an important role in determining the temperature profile and energy balance of our planet. The thermal conductivity of the Earth's core remains poorly constrained because of the extreme difficulty in making thermal transport measurements under the relevant pressure and temperature conditions. Two experimental studies published in Nature in 2016 report values of k for Fe that vary by a factor of 7 at ~130 GPa (34 → 225 W/mK) (Refs. 28 and 29). The goal of the OMEGA experiments was to constrain the thermal conductivity at high pressures, using a ramp-compression platform previously developed on OMEGA[30] (Fig. 152.79), where (1) stagnating plasma simultaneously launches a ramp-compression and heat wave in the sample, (2) a "cool" ramp-compression wave runs ahead of the heat wave (the sample pressure can be constrained using VISAR), and (3) LLE's SOP makes it possible to measure the heat-wave transit time. The raw ASBO/SOP data provide velocity and thermal transport information through stepped Fe samples (Fig. 152.80). Analysis is underway to translate this data into a measurement of thermal conductivity.

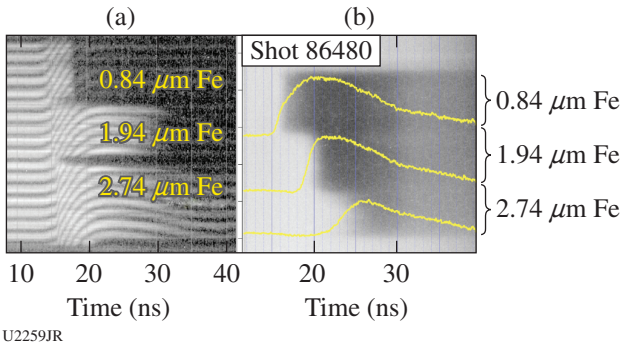

Figure 152.80
(a) ASBO and (b) SOP data for 0.84-/1.94-/2.74-μm Fe step samples provide sufficient information to constrain the high-pressure thermal conductivity of Fe.

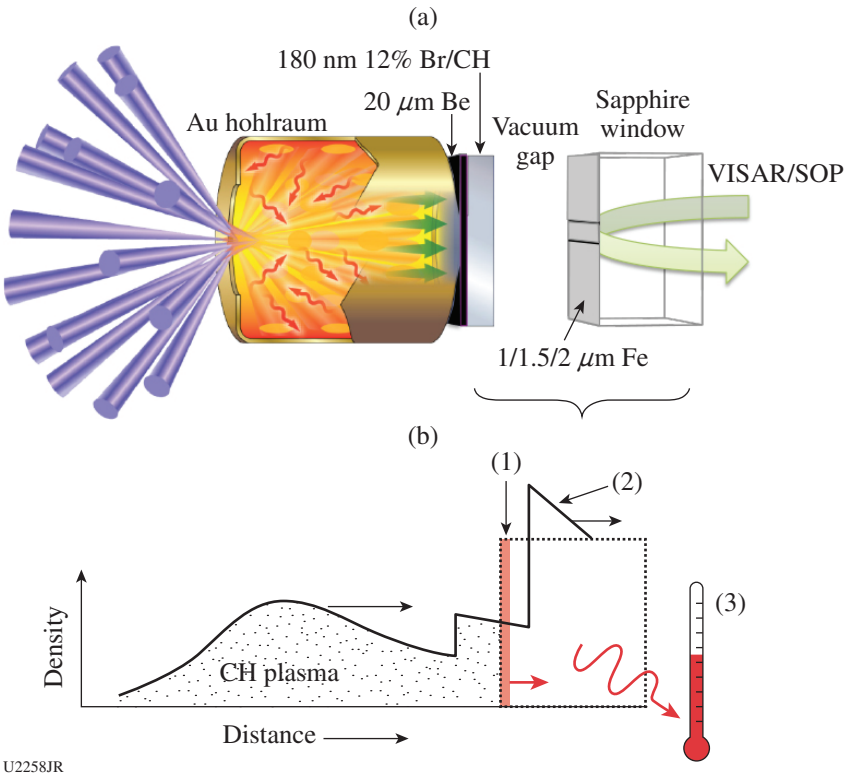

Figure 152.79
(a) Target design used to (b) measure heat flow in a ramp-compression stepped Fe sample.

Recovery of Dynamically Compressed Samples
Principal Investigator: C. E. Wehrenberg (LLNL)
Co-investigators: S. Zhao and M. Meyers (UCSD); and B. Remington and A. Krygier (LLNL)

This LBS campaign studied the deformation response of a variety of materials to shock compression. Sample materials were mounted onto the front of steel recovery tubes that were in turn mounted on a ten-inch manipulator (TIM). A single OMEGA beam is used to drive a shock into the sample material, and the sample remains in the recovery tube after the shot so that it can be recovered for further *ex-situ* study. Two recovery tubes and a VISAR target were fielded for each shot. Consequently, a large data set of 12 recovered samples and six VISAR traces was produced using only a half-day of shots.

A wide variety of samples were recovered during this campaign. Previous iterations of this campaign have been very successful in studying the deformation response of semiconductors (Si and Ge) to shock compression, producing a series of high-profile papers on pressure-shear–induced amorphization.[31,32] The FY17 campaign studied GaAs, graphite, and olivine and generated the first dynamic compression data on a new class of materials—high-entropy alloys. These samples will be taken to Oak Ridge National Laboratory for TEM (transmission electron microscopy) study.

Charged-Particle Stopping Power and Scattering Measurements in a Warm Dense Plasma
Principal Investigator: A. B. Zylstra (LANL)

The d*E*d*x* Campaign is developing a platform to perform high-precision measurements of charged-particle stopping power (d*E*/d*x*). Stopping power in dense plasmas is important for ICF self-heating and propagating burn, particularly for particles near and below the peak in d*E*/d*x* ("Bragg peak"). While the stopping power has been measured in hot-spot–relevant plasmas using an exploding pusher platform, the current data cannot distinguish between models of interest;[33] for example, the Maynard–Deutsch and Brown–Preston–Singleton theories. This campaign uses shocked-foam targets probed by a separate source of fusion particles to achieve higher precision. The d*E*d*x*-17A shot day demonstrated the viability of this platform, shown in Fig. 152.81. Good data using 3-MeV protons from the D–D fusion reaction were acquired, shown in Fig. 152.81(b). A similar downshift is observed in both shocked (warm) and undriven (cold) foam, which is expected from stopping theory. Future experiments will be modified to use the lower-velocity particles, particularly D^3He_α, which are more sensitive to d*E*/d*x* and will be able to differentiate between stopping models in this regime.

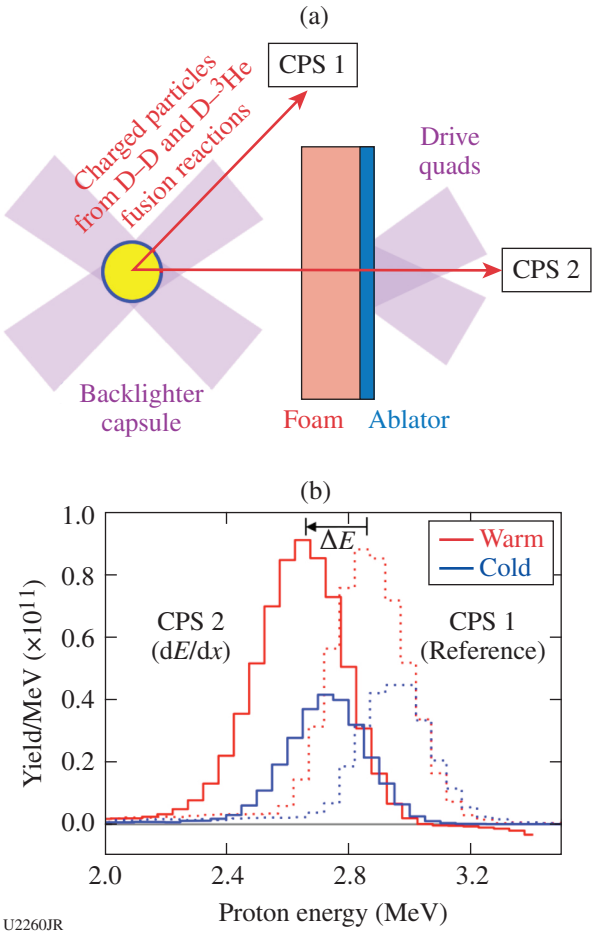

Figure 152.81
(a) Diagram of the experimental geometry. A backlighter capsule produces particles from the D–D and D–^{3}He fusion reactions, which probe a planar shock-compressed foam. (b) Example data of protons from the D–D fusion reaction slowing through warm and cold foams.

FY17 LLNL Omega Facility Experimental Programs
Principal Investigators: R. F. Heeter, F. Albert, S. J. Ali, H. Chen, F. Coppari, T. Doeppner, A. Fernandez Panella, D. E. Fratanduono, E. Gumbrell, C. M. Huntington, L. C. Jarrott, S. Jiang, A. Krygier, A. E. Lazicki, S. LePape, E. V. Marley, D. A. Martinez, J. M. McNaney, M. A. Millot, A. Pak, Y. Ping, B. B. Pollock, P. Poole, H. G. Rinderknecht, M. B. Schneider, R. F. Smith, G. F. Swadling, C. E. Wehrenberg, O. L. Landen, A. Wan, and W. Hsing (LLNL); J. Benstead and M. Rubery (AWE); R. Hua (UCSD); C. C. Kuranz (University of Michigan); and A. Saunders (University of California, Berkeley)

In FY17, LLNL's Indirect-Drive Inertial Confinement Fusion (ICF-ID) and High-Energy-Density (HED) Physics Programs conducted numerous campaigns on the OMEGA and OMEGA EP Laser Systems. Overall these LLNL programs led

413 target shots in FY17, with 282 shots using only the OMEGA Laser System and 131 shots using only the OMEGA EP Laser System. Approximately 27% of the total number of shots (78 OMEGA shots and 35 OMEGA EP shots) supported the ICF-ID Campaign. The remaining 73% (204 OMEGA shots and 96 OMEGA EP shots) were dedicated to experiments for HED Physics. Highlights of the various ICF-ID and HED Campaigns are summarized in the following reports.

In addition to these experiments, LLNL Principal Investigators (PI's) led a variety of LBS Campaigns using OMEGA and OMEGA EP, including 85 target shots using only OMEGA and 70 shots using only OMEGA EP.

Overall, LLNL PI's led a total of 568 shots at LLE in FY17. In addition, LLNL PI's also supported 30 NLUF shots on OMEGA and 46 NLUF shots on OMEGA EP, in collaboration with the academic community.

Indirect-Drive Inertial Confinement Fusion Experiments

Hydrodynamic Response from Nonuniformities in Plastic, High-Density Carbon, and Beryllium

Principal Investigator: S. J. Ali
Co-investigators: P. M. Celliers, S. W. Haan, S. Baxamusa, M. Johnson, H. Xu, N. Alexander, H. Huang, V. A. Smalyuk, and H. F. Robey

The goal of the Capseed Campaign (comprising Capseed 17A, 17B, and 17C) is to measure shock-front velocity nonuniformities in ICF ablator materials and quantify the level of nonuniformity caused by intrinsic effects. This is done using the OMEGA high-resolution velocimeter (OHRV) to obtain velocity maps of the optically reflecting shock front following release of the ablator material into either PMMA [poly(methyl methacrylate)] for the warm experiments or cryogenic deuterium for the cryogenic experiments. For three half-days in FY17 the focus was twofold: (1) complete measurements on the impact of oxygen heterogeneity and oxygen mitigation layers for glow-discharge polymer (GDP); and (2) begin measuring velocity nonuniformities on deep release from Be, GDP, and high-density carbon (HDC) into D_2 with improved velocity sensitivity.

Performance and yield from fusion capsules at the National Ignition Facility (NIF) are highly dependent on the uniformity of the capsule implosion, and hydrodynamic instabilities are a significant source of performance degradation during the implosion. A possible explanation for unexpectedly large in-flight modulations observed during NIF capsule implosions was a surface oxygenation of GDP; laboratory tests of GDP samples under controlled conditions confirmed the heterogeneous surface oxygenation effect. In FY16 the OHRV was used to test this idea further by obtaining 2-D velocity maps for both oxygen-modulated and unmodulated samples. Modulated samples showed clear evidence of the propagation of a rippled shock wave as a result of the photo-induced oxygen heterogeneity. To mitigate this effect, the target fabrication team proposed depositing a 20-nm oxygen barrier layer of alumina. Tests of the mitigation in the 17A and 17B campaigns determined, via OHRV measurements on warm GDP samples, that this barrier layer introduced no additional perturbations in the shock velocity. In 17C the velocity roughness on deep release from GDP into D_2 with and without this barrier layer was also measured and no significant difference was determined. The velocity nonuniformities in both samples were close to the detection limit of the diagnostic, as described in Fig. 152.82.

The remaining shots in 17A were used to measure velocity nonuniformities slightly below the first shock level in HDC and

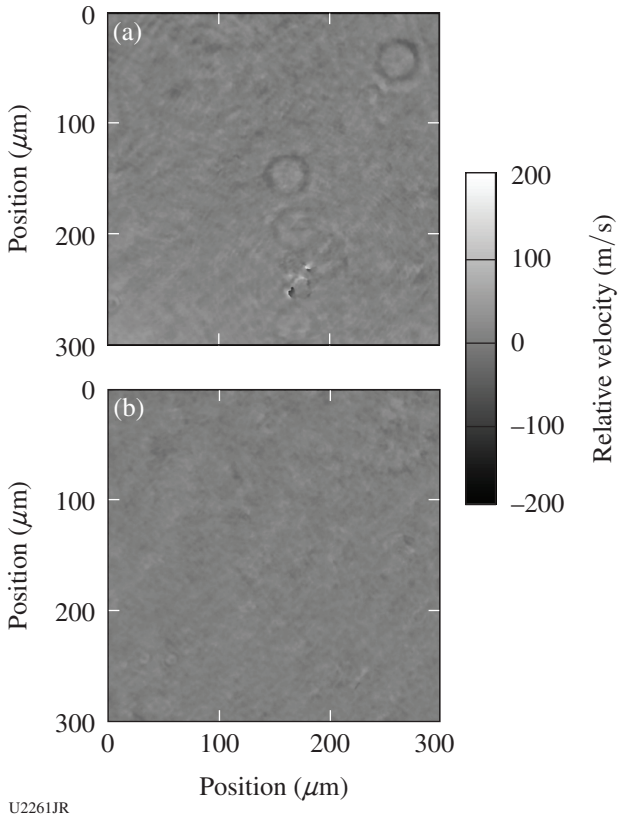

Figure 152.82
Velocity maps from (a) alumina-protected and (b) unprotected glow-discharge polymer (GDP) releasing into D_2. Root mean square (rms) velocity roughness was 8.6 m/s for (a) and 6 m/s for (b), with a diagnostic detection limit of 6 m/s.

at the first shock level in sputtered Be, both releasing into D_2. The velocity nonuniformity for the Be shots varied significantly (35±6 m/s and 24±6 m/s) but in both cases, was ~3 to 5× larger than would be expected from the surface roughness. Nonuniformity in HDC was measured at 7 and 10 Mbar and was found to decrease with increasing pressure (from 124±17 m/s for 7 Mbar to 85±17 m/s for 10 Mbar) but was again a few times larger than predicted from surface roughness alone. These experiments are continuing into FY18, with further cryogenic measurements planned.

Diamond Sound-Speed Measurements Between 8 and 14 Mbar

Principal Investigator: A. Fernandez-Panella
Co-investigators: D. E. Fratanduono and P. M. Celliers

This half-day on the OMEGA laser was designed to collect high-quality data on the sound speed of diamond in the multi-Mbar range, where currently little data exist, for the purpose of constraining equation-of-state models. It was the continuation of the DiamondSS-15B Campaign, where two data points were obtained at 10 Mbar.

The DiamondSS-17A Campaign used planar targets and a direct-drive configuration with a CH ablator, a quartz pusher, and two targets side by side [quartz (standard) and diamond]. The velocity profiles at the free surface were recorded using VISAR as the primary diagnostic (Fig. 152.83). Throughout the day, the laser drive energy was changed in order to probe different shocked pressure states in diamond. The laser pulse was designed to produce a small pressure perturbation that propagated through both the standard and the sample. The wave propagation analysis described in Ref. 34 was applied to extract the sound speed of both materials, quartz and diamond, from their velocity profiles (Fig. 152.84).

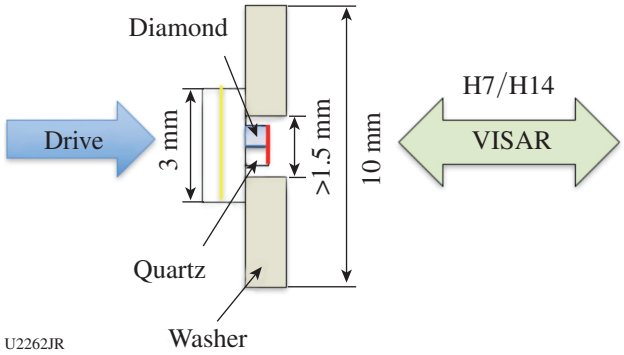

Figure 152.83
Experimental setup and target design for the DiamondSS-17A Campaign.

The results indicate that sound-speed measurements are sensitive enough to constrain EOS models. The Livermore LEOS table 9061 shows good agreement with the data. Further measurements in an extended pressure range are desirable in order to better constrain the models. The results of this campaign are being used to optimize the design for the DiamondSS-18A Campaign, where Be ablators will be used instead of CH to reach higher pressure states; a different pair of etalons will be chosen to increase the accuracy of the velocity measurements to enable extraction of not only the sound speed but also the Grüneissen coefficient.

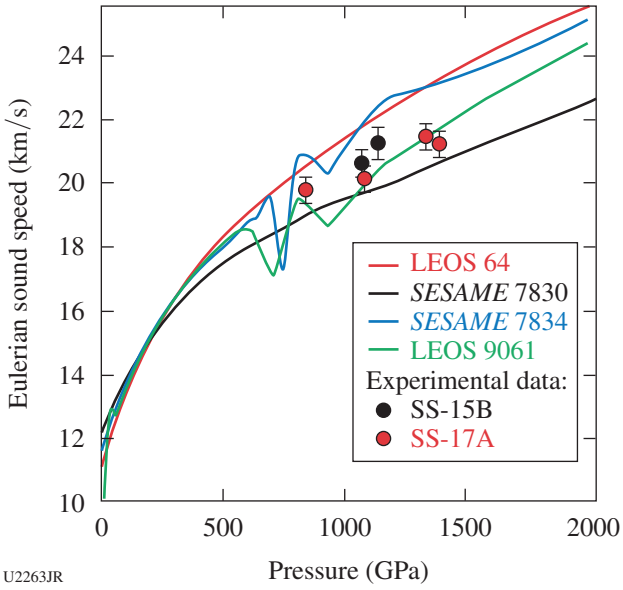

Figure 152.84
Plot of the diamond sound speed versus pressure.

Thomson-Scattering Measurements from Foam- and Gas-Covered Gold Spheres

Principal Investigator: G. F. Swadling
Co-investigators: J. S. Ross, M. Rosen, K. Widmann, and J. D. Moody

The FoamCoSphere-17A Campaign performed foam- and gas-covered high-Z sphere experiments illuminated in direct-drive geometry to investigate atomic physics models, radiative properties of the laser-spot plasma, and the interpenetration of

multi-ion species plasmas relevant to ICF indirect-drive–ignition hohlraums. These experiments use laser irradiation at 10^{14} to 10^{15} W/cm^2, similar to the intensities found in hohlraums fielded on the NIF.

For the foam experiments the Au sphere was embedded in a low-density (3.8-mg/cm^3) CH foam [Fig. 152.85(a)]. For the gas-covered experiments, the spheres were located inside a gas bag filled to 1 atm of propane, or 1 atm of a 70/30 mix of propane and methane, to achieve initial electron densities of 4.0% of the critical density of the 3ω drive beams and to mimic the interaction of the hohlraum Au wall with the low-density hohlraum fill gas. Significant target development work was required to prepare the open-geometry foam-covered targets; we look forward to leveraging this target development work in future shot days.

The plasma temperature and density at various radial positions in the blowoff plasma are characterized using Thomson scattering, while x-ray flux from the gold sphere was recorded using the Dante and DMX soft x-ray spectrometer diagnostics. The laser beams use a shaped laser pulse (1-ns square foot, 1-ns square peak) designed to pre-ionize the gas/foam before the main drive pulse.

The electron temperature and density, the plasma-flow velocity, and the average ionization state are measured by fitting the theoretical Thomson-scattering form factor to the observed data. An example of the Thomson-scattering data from ion-acoustic fluctuations is shown in Fig. 152.85. Continued data analysis and simulations are in progress to better understand the plasma evolution and heat transport.

Study of Interpenetrating Plasmas on OMEGA
Principal Investigator: S. LePape

This campaign is designed to study the dynamics of plasma interpenetration in an environment relevant to hohlraums used on the NIF to drive HDC capsules. The question this campaign is trying to answer is whether a fluid description of plasma flows in a low-gas-fill hohlraum (<0.3 mg/cm^3 of helium gas in the hohlraum) is accurate, or if a kinetic description of the flows must be used. Following the first series of shots in 2016 that looked at the time evolution in one point in space in the gap between the two flows, this series of shots focused on 1-D spatially resolved Thomson-scattering data in addition to looking at the effect of helium gas density on the flows' interaction. During this series of shots the helium gas density was changed as well as the ring material (carbon, aluminum, and gold) and the laser energy used to drive the target.

Two main diagnostics are fielded on these experiments: (1) a soft x-ray time-resolved imager looking at the self-emission of the plasmas along the ring axis (Fig. 152.86) and (2) a spatially resolved Thomson-scattering diagnostic (Fig. 152.87) to diagnose electron and ion temperature, flow velocities, and densities.

Time-resolved x-ray images [Figs. 152.86(c) and 152.86(d)] indicate that the helium gas holds the plasma expansion and as time goes by when helium is present, a bright layer appears, presumably being the helium compressed between the low-Z and high-Z plasma.

Figure 152.87 shows a 1-D spatially resolved spectrum acquired on a carbon/carbon shot without helium, providing

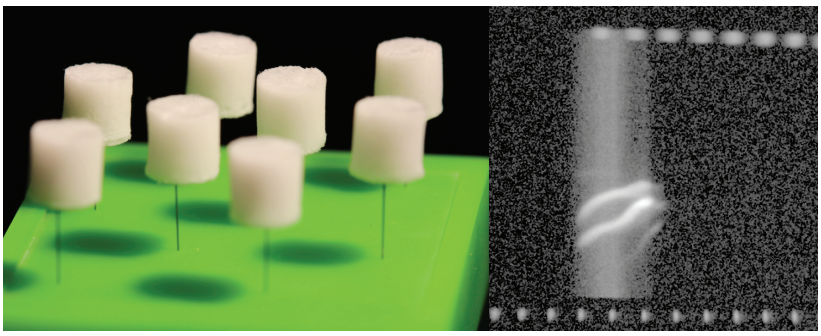

U2264JR

Figure 152.85
(a) Au spheres (1-mm diameter) centered in a 5-mm-diam foam. (b) Example of the Thomson-scattering ion feature, where the Thomson-scattering k vector is directed radially, giving sensitivity to the ablation velocity of the Au plasma.

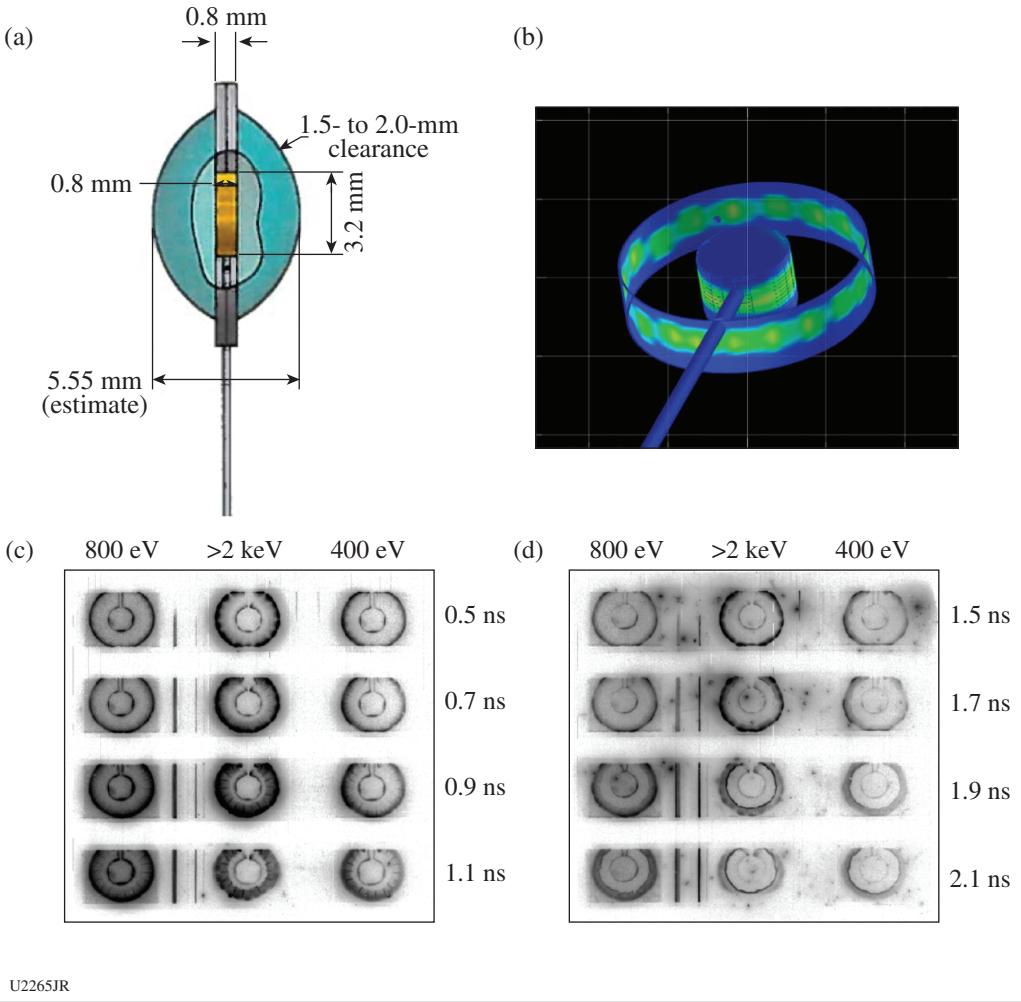

Figure 152.86

(a) Schematic of a gas-bag target. The ring and rod with which the laser interacts are enclosed into a gas bag that holds the helium gas. (b) *VISRAD* calculation of the laser-deposited energy on the ring and high-density carbon (HDC) rod. [(c),(d)] Time-resolved x-ray images of the plasma self-emission. The inner feature is the carbon rod; the outer feature is the low- or high-*Z* ring. In (c), gold ablates into HDC without a helium fill; in (d), gold ablates into HDC with 0.2 mg/cm^3 of helium gas.

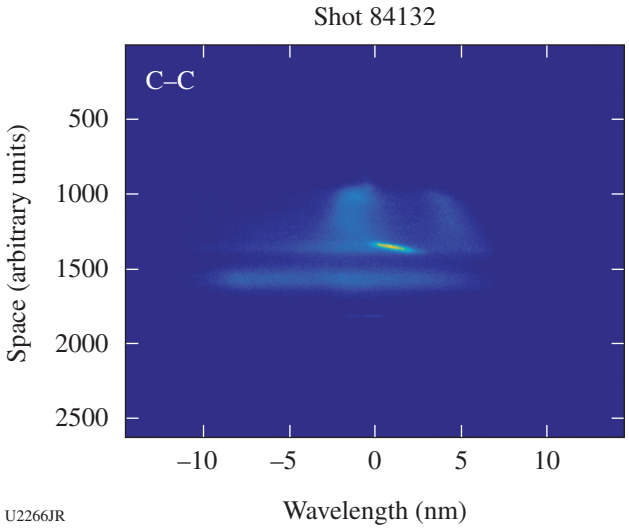

Figure 152.87

One-dimensional spatially resolved Thomson-scattering data of a carbon plasma flowing into a carbon plasma.

information on plasma temperature, densities, and plasma stagnation length. High-quality data were obtained. The results of this campaign are being analyzed.

Measurements of Anisotropy in Non-LTE Low-Density Iron–Vanadium Plasmas

Principal Investigator: L. C. Jarrott
Co-investigators: M. E. Foord, R. F. Heeter, D. A. Liedahl, M. A. Barrios Garcia, G. V. Brown, W. Gray, E. V. Marley, C. W. Mauche, K. Widmann, and M. B. Schneider

Accurate characterization of the effects of geometrical anisotropies on K-shell line emission is very important for improving line-ratio–based temperature measurements in low-density, non-LTE (local thermodynamic equilibrium) plasmas. OpticalDepth-17A built on the OpticalDepth-16A Campaign, which established a working platform for accurately characterizing low-density, mid-Z, non-LTE plasmas. Specific goals of this platform included a characterization of heat conduction in the nominal target point design by comparing a layered sample target material to a mixed sample target material. Additionally, this campaign attempted to improve on-target laser drive efficiency by virtue of a picketed pulse shape to improve the laser–target interaction interface. Both OpticalDepth Campaigns used three laser–target configurations, varying target angle to verify the accuracy of data acquired. The primary target was a 10-μm-thick, 1000-μm-diam beryllium tamper with an embedded volumetrically equal mixture of iron and vanadium, 0.2 μm thick and 250 μm in diameter. The second target type was identical to the primary target except that the sample material was layered (50 nm Fe/100 nm V/50 nm Fe) rather than mixed. The third target type was a null target where the beryllium tamper contained no sample material. Three beam-target orientations were used over the course of 14 experimental shots (Fig. 152.88).

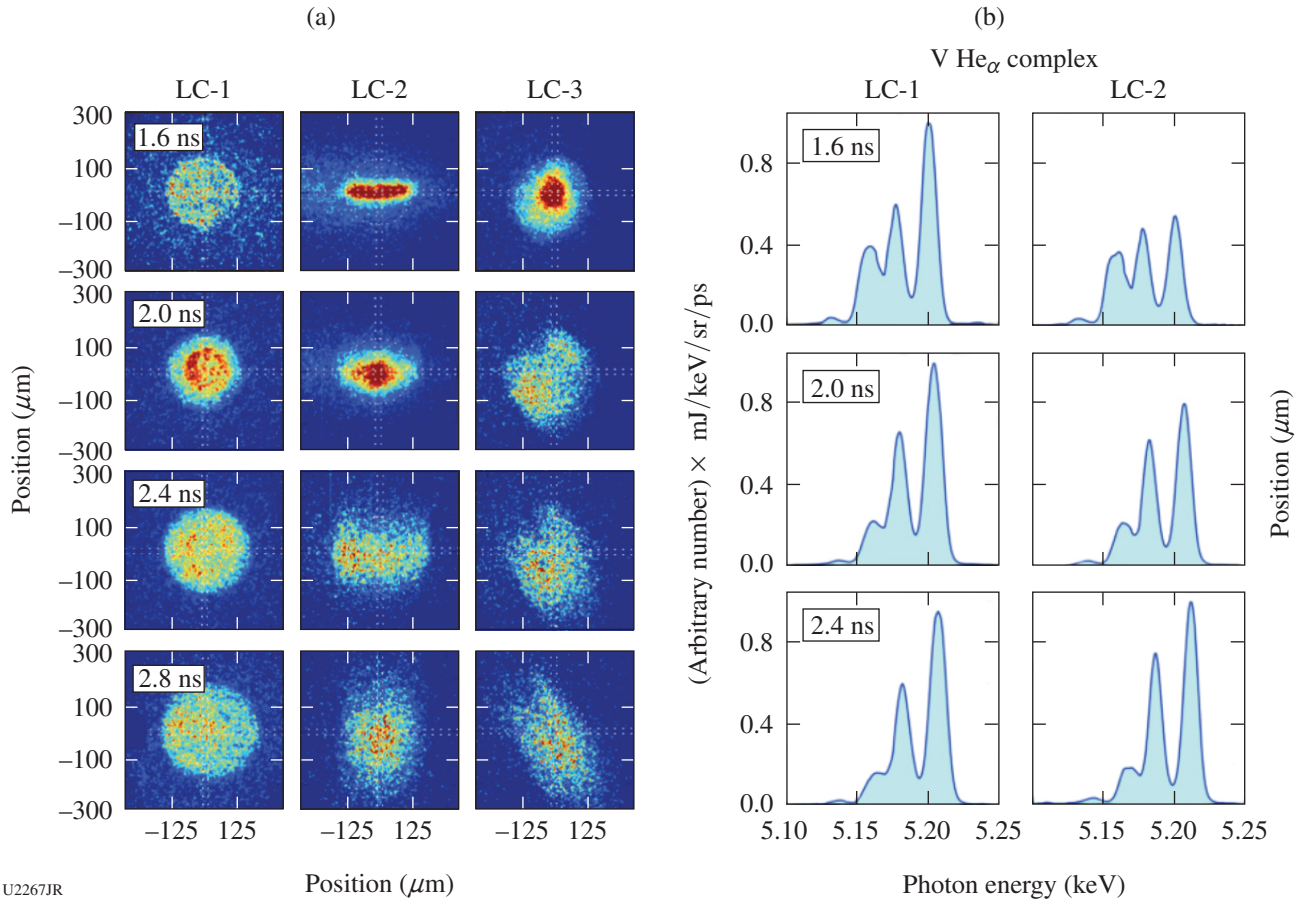

Figure 152.88
(a) X-ray framing-camera images (all from TIM-3) using our three laser/target orientation configurations, showing a face-on view (LC-1), side-on view (LC-2), and 45° view (LC-3). (b) Spectrum measured by the MSPEC spectrometer of the x-ray emission from K-shell transitions in highly charged vanadium and iron using laser/target configurations 1 and 2.

In the first configuration (LC-1), the multipurpose gated x-ray spectrometer (MSPEC) situated in TIM-2 had an edge-on view of the target, while an identical MSPEC in TIM-6 had a face-on view. In the second configuration (LC-2), the target orientation with respect to TIM-2 and TIM-6 was reversed compared with the first configuration. In the third configuration (LC-3), all primary ten-inch–manipulator (TIM)-based diagnostics had a viewing angle of 45° with respect to target normal. Using multiple target-beam orientations resulted in an *in-situ* cross-calibration of the spectrometers and pinhole imagers. The data included simultaneous measurements of (1) time-resolved iron and vanadium K-shell spectra viewed from both the target edge and the target face, and (2) time-resolved images of the expanding plasma, viewed from both the target edge and target face, to infer plasma density for both layered and mixed sample target materials. The K-shell spectral data provided time-resolved electron temperature measurements of the expanding plasma, with preliminary analysis implying a plasma temperature above 2 keV.

Imaging Electric-Field Structure in Strong Plasma Shocks

Principal Investigator: H. G. Rinderknecht
Co-investigators: H.-S. Park, J. S. Ross, S. C. Wilks, and P. A. Amendt

This series of shots was designed to measure the electric fields produced by strong shocks in single- and multi-species plasmas. Strong shocks ($M > 1.6$) produce electric fields as a result of streaming of the electron precursor ahead of the ion shock, which is not accurately reproduced in hydrodynamic models. This experiment is intended to quantify electric-field strength and position in a shock platform previously characterized in FY16 (Ref. 35) to be used to constrain high-fidelity physics codes.

The KineticDynamics-17A Campaign performed proton radiography of a shock-tube target platform developed in the KineticShock-16 series. Ten beams with 2.5 kJ in a 0.6-ns impulse drove a 2-μm-thick SiO_2 ablator attached to one end of the tube, launching a strong shock into the 1 atm of gas contained in the tube. A D^3He-filled backlighter capsule was imploded to produce 3.0- and 14.7-MeV protons, which transited perpendicular to the shock front and were recorded using CR-39. Deflections of the protons caused by electric fields were recorded as changes in the proton fluence with position on the detector, as shown in Fig. 152.89. Gas fills of H_2 (two shots), Ne (three shots), and H_2 + 2% Ne (six shots) were probed while varying the backlighter timing relative to the shock.

Radiographs were collected on all shots, demonstrating electric-field formation at both the shock front and the ablator/gas interface. X-ray framing-camera images recorded perpendicular to the radiography axis confirm that the flow velocity is consistent with previous experiments (450 μm/ns) and identify

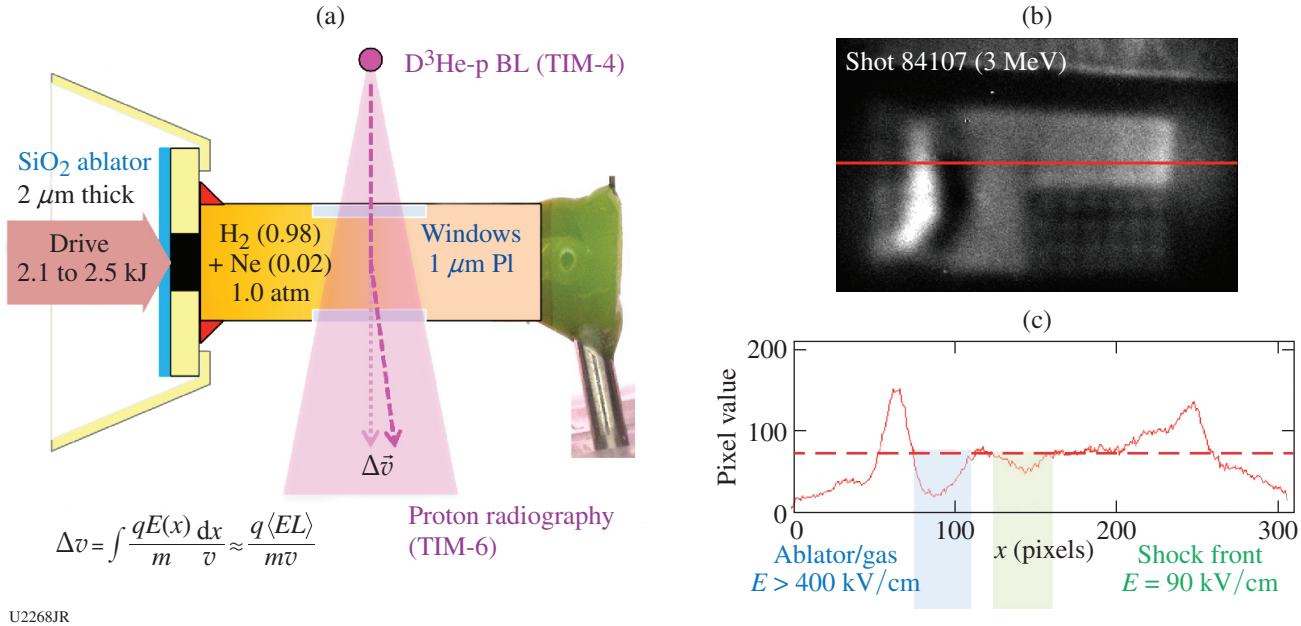

Figure 152.89
(a) Experimental configuration, (b) 3-MeV proton radiograph, and (c) lineout of proton fluence for shot 84107.

the position of the SiO_2 ablator at the radiography sample time on each shot. Analysis is ongoing and results were presented at the APS DPP Meeting in October 2017.

Measuring Thermal Conductivity of D_2

Principal Investigators: S. Jiang and Y. Ping
Co-investigators: P. M. Celliers and O. L. Landen

This campaign successfully developed a platform of refraction-enhanced x-ray radiography for planar cryogenic targets and obtained usable radiographs. The campaign fielded two half-days on OMEGA during FY17. The series of cryogenic shots was designed to measure the thermal conductivity of liquid D_2 at 1 to 10 eV, which helps to benchmark different transport models used in ICF ignition target design. Figure 152.90 shows the experimental configuration. The CH and liquid D_2 were heated to different temperatures by the x rays generated from heating lasers incident on a thin Zn foil. This builds up a density gradient because of thermal conduction. The evolution of the CH/D_2 interface was measured using refraction-enhanced x-ray radiography with high spatial resolution. The temperature can be constrained by the wave velocities in CH/D_2. A vanadium foil backlighter was used to generate the probing x rays. The backlit x-ray images were collected with a four-strip framing camera. Useful radiographs at different delays were recorded (shown in Fig. 152.90), including undriven and driven data at 0.5 ns, 1.5 ns, 2 ns, and 2.5 ns. Analysis of the measured data is in progress.

Characterization of Laser-Driven Magnetic Fields

Principal Investigator: B. B. Pollock
Co-investigators: C. Goyon, G. J. Williams, D. Mariscal, G. F. Swadling, J. S. Ross, S. Fujioka, H. Morita, and J. D. Moody

BFieldLoop-17A and -17B continued the laser-driven magnetic-field experimental campaign on OMEGA EP. The goal for 17A was to study the impact on the magnetic-field–generation process of modifying the target geometry, while the primary

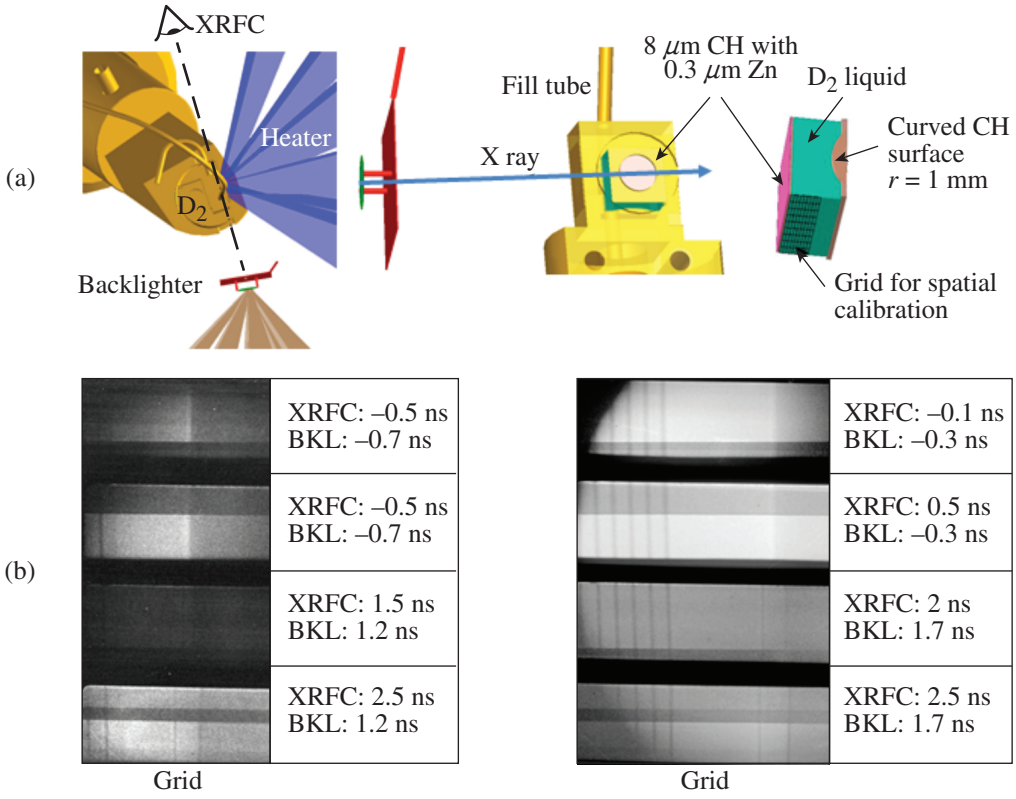

Figure 152.90
(a) The experimental configuration, target geometry, and (b) raw radiographs from an x-ray framing camera (XRFC). The delays of both the framing camera and the x-ray backlighter (BKL), with respect to the heating pulses, are shown in the table next to each radiograph.

objective for 17B was the extension of the probing time for the field. Figure 152.91 shows the general experimental geometry. The field is produced by currents flowing in a U-shaped gold foil target. One or two long-pulse beams are directed through holes in the front side of the target to produce a plasma on the interior rear side of the target. Plasma produced in this region expands toward the front side, setting up a voltage across the target that drives the current. The fields are measured by proton deflectometry, where the protons are produced through target normal sheath acceleration by the OMEGA EP backlighter beam incident on a separate, thin Au foil.

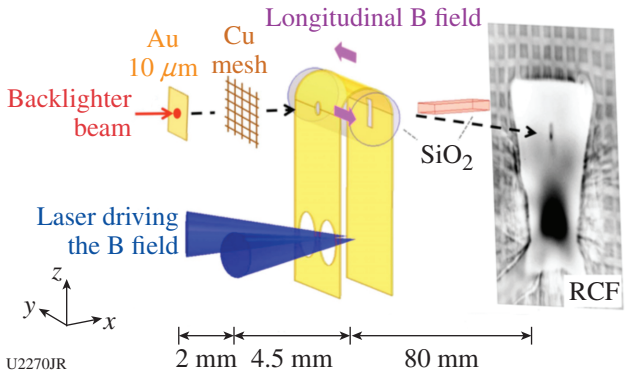

Figure 152.91
Experimental configuration for BFieldLoop experiments. RCF: radiochromic film.

Previous experiments showed that for a 1-TW long-pulse laser drive, fields of ~200 T can be produced in the interior of the loop portion of the target. The 17A experiment modified the front of the target by removing the bottom portion where the laser holes are located. This target modification showed a difference in the resulting proton images recorded on the radiochromic film (RCF), and modeling is ongoing to quantify the modification to the field strength and topology.

For 17B, a gold shield was added between the main target and the backlighter target to protect the rear surface of the backlighter and allow for late-time probing of the magnetic fields. Prior to 17B the ability to measure magnetic fields after the long-pulse beams turned off had been limited. By using a 750-ps long-pulse B-field drive beam, the addition of this shield allowed the probe time to be extended from 750 ps (the end of the drive beam) to 16 ns. Preliminary analysis of these results indicates that the magnetic field persists long after the drive laser turns off, decaying exponentially with a time constant of ~2 ns. This is consistent with a circuit theory treatment of the interaction, where the drive laser acts as a voltage source while turned on; after the voltage is turned off, the current (and consequently the magnetic field) decays with the L/R time constant of the target. For the geometry of the 17B targets, this L/R time is ~2.6 ns.

Study of Shock Fronts in Low-Density Single- and Multi-Species Systems

Principal Investigator: R. Hua (UCSD)
Co-investigators: Y. Ping, S. C. Wilks, R. F. Heeter, and J. A. Emig (LLNL); H. Sio (MIT); C. McGuffey, M. Bailly-Grandvaux, and F. N. Beg (UCSD); and G. W. Collins (LLNL, LLE)

This series of shots is designed to study the shock-front structure of low-density single- and multi-species systems in a planar geometry, using proton radiography from a broadband TNSA source and x-ray emission spectroscopy. Unlike most other low-density shock experiments that are mostly carried out in convergent geometry with near-monoenergetic D^3He proton radiography, the planar geometry of these experiments enables one to distinguish the shock front from its pusher, and the TNSA protons provide broadband energy measurements.

In this platform, the strong shock of interest is initiated by launching three long-pulse beams from OMEGA EP onto a 2-μm SiO_2 foil (Fig. 152.92). By ablation, the foil pushes into a cylindrical kapton tube that is prefilled with either pure helium or a helium/neon mixture. A short-pulse beam is fired a few nanoseconds after the shock-driving beams, onto a TNSA proton target normal to the axis of the kapton tube. The protons are driven through two windows on the tube into a stack of RCF's on the other side. Photons emitted from the shock front through another window are recorded by a 1-D spatially resolved soft x-ray spectrometer [called variable-spaced grating (VSG)]. The details of the design and its feasibility have been published.[7]

With pure helium fill, a proton accumulation layer at the shock front, resulting from a self-generated electric field, has been recorded on the RCF. A discussion of the field information inferred from the proton behavior was published recently.[12] Shocks in the mixed gas displayed different features. Not one, but two proton accumulation layers are observed. In addition, line emission from the added neon gas is recorded by the VSG, which provides the potential to constrain the temperature and density of the shock front. Further analysis of these results is in progress. Results of these campaigns are being used to further optimize the platform to make more measurements in FY18.

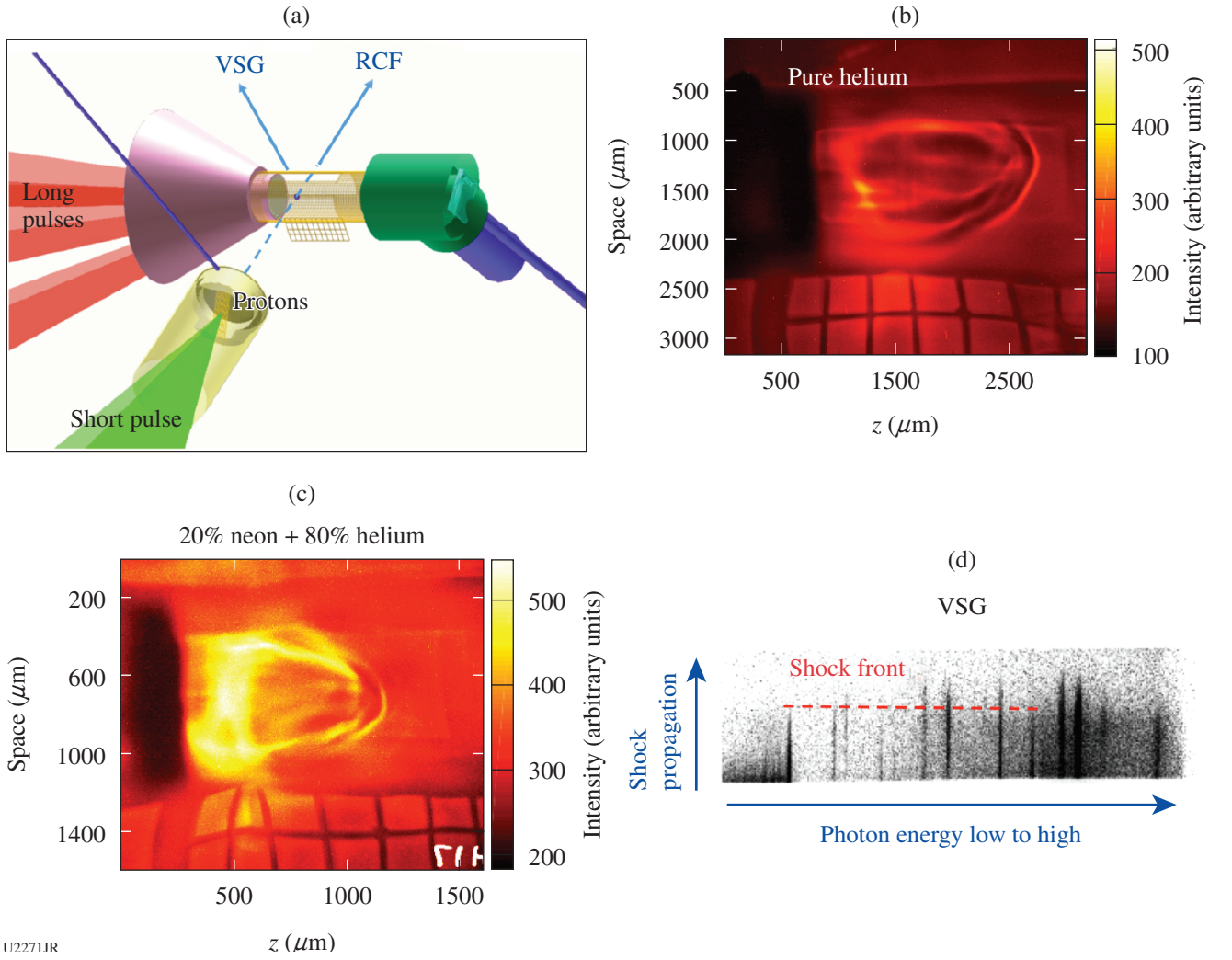

Figure 152.92
(a) Experimental setup; RCF data from (b) a pure helium shot and (c) a mixture shot (20% neon and 80% helium); (d) VSG spectrometer data from a mixture shot.

High-Energy-Density Experiments

1. Material Equation of State and Strength Measured Using Diffraction

Measurement of Pb Melt Curve Along the Hugoniot Using* In-Situ *Diffraction

Principal Investigator: C. E. Wehrenberg
Co-investigators: R. Kraus, F. Coppari, J. M. McNaney, and J. H. Eggert

This series of shots was designed to measure the melt curve of Pb on the Hugoniot using *in-situ* x-ray diffraction on OMEGA EP's PXRDIP diagnostic. The physics package consists of a 40-μm epoxy ablator, a 12.5-μm lead foil, and a 100-μm LiF window for VISAR. A single UV beam is used to drive a steady shock through the ablator and into the Pb sample. A separate beam drives a Ge x-ray source target, and the diffracted x rays are collected on image plates mounted on the inside of the PXRDIP box. The solid or liquid state of the shock-compressed lead is determined by the presence of a diffraction signal as either sharp lines (solid) or a single diffuse line (liquid). Figure 152.93 shows a diffraction pattern containing both the diffuse liquid signal from lead under 47 GPa of shock compression and sharp diffraction lines generated by the Pt pinhole.

This campaign is performed in conjunction with similar campaigns on the NIF and the Linac Coherent Light Source

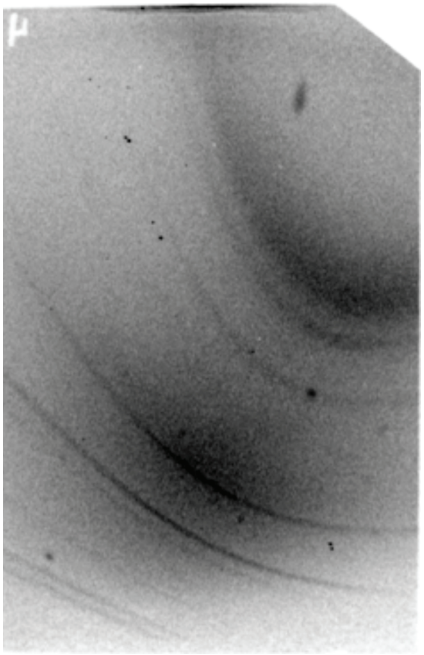

U2272JR

Figure 152.93
Example diffraction image showing a diffuse signal generated by liquid Pb under shock compression at 47 GPa and sharp diffraction lines generated by the Pt pinhole.

(LCLS). The epoxy ablator setup, which eliminates reverberations between the ablator and any glue layers, and the Ge x-ray source target were developed on the NIF campaign before being applied on these shots. On this OMEGA EP day, alternating beams to increase the shot rate achieved 11 shots that provided a large data set to map the melt curve on the Hugoniot. This data will be compared with similar experiments performed on LCLS, making it possible to compare shots done with greater x-ray diffraction precision (because of the x-ray free-electron laser) with the greater-precision shock drive available on OMEGA EP. In addition, these melt curve measurements will be used in the design of future NIF shots using shock-ramp combination drives to measure melt curves in off-Hugoniot states.

Development of a New Platform for Measuring Recrystallization

Principal Investigator: F. Coppari
Designer: R. Kraus
Co-investigators: C. E. Wehrenberg and J. H. Eggert

This campaign seeks to develop a platform for measuring recrystallization of Pb through shock-ramp compression. By first launching an initial shock to compress the sample along the Hugoniot close to the melting pressure, letting the sample release into the liquid phase, and then recompressing it with ramp compression across the solid–liquid phase boundary, one can measure high-pressure melting lines of materials. The structure of the Pb upon shock, release, and ramp compression is monitored by x-ray diffraction. The onset of melting is identified by the appearance of a diffuse scattering pattern and the disappearance of the Bragg diffraction lines characteristic of the solid. The pressure is monitored by VISAR looking at the interface between the Pb and a LiF window.

Building upon the successful use of Be ablators initiated in FY16, the FY17 series used a slightly modified target design that included a Ge preheat shield (Fig. 152.94). Hydrocode simulations allowed us to design a suitable laser pulse shape to compress the Pb sample along this complicated shock–release–ramp path.

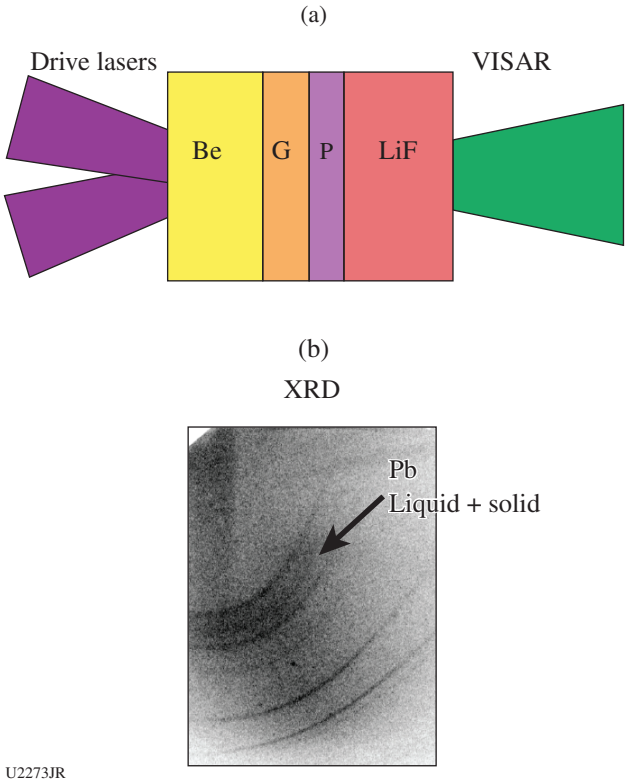

U2273JR

Figure 152.94
(a) Target schematic and (b) example of a diffraction image showing diffuse (liquid) and sharp (solid) features from the Pb sample. VISAR: velocity interferometer for any reflector; XRD: x-ray diffraction.

Diffraction data indicate that Pb completely melts above 50 GPa along the Hugoniot. Resolidification into a structure consistent with the bcc lattice has been observed upon subsequent ramp compression to higher pressures. Data analysis is ongoing and will provide valuable information for future OMEGA and NIF campaigns.

High-Pressure Crystal Structure of Ramp-Compressed Pb and Ta to Resolve Known or Potential High-Pressure Phase Transformations

Principal Investigator: A. E. Lazicki
Co-investigators: F. Coppari, R. Kraus, C. E. Wehrenberg, J. M. McNaney, D. Swift, D. Braun, and J. H. Eggert (LLNL); and J. R. Rygg, D. N. Polsin, and G. W. Collins (LLE)

Several previous experiments on OMEGA, OMEGA EP, and the NIF in the past five years have examined the crystal structure of Pb and Ta at high pressure. Pb is of specific interest because its high-pressure/high-temperature phase diagram, including two phase transformations, is well constrained between 0 to 100 GPa from diamond-anvil cell experiments. Therefore, it provides an opportunity to test for the effects of rapid compression and heating, inherent from ramped laser drives, on phase boundaries. Although very high quality data have already been collected in the 100- to 500-GPa pressure regime, previous measurements have failed to reach sufficiently low pressures to cross the two known phase boundaries. Meanwhile, measurements of Ta structure have suggested a possible new high-pressure phase, but contamination of the diffraction pattern by diamond, a material that has always been present in the target packages, has made the determination ambiguous. The goals of this OMEGA EP campaign were to capture the low-pressure phase transformations in Pb and, in the case of Ta, to eliminate all diamond from the target and examine the pressure regime where previously a new phase was suggested. Both target packages used beryllium ablators and LiF windows, with thin (3- to 5-μm) layers of Pb. The shots used a combination of Cu and Ge backlighter sources.

Very high quality diffraction data were collected on all shots and the low-pressure phases of Pb were clearly observed and followed with pressure, constraining the phase boundaries (Fig. 152.95). The diagnostic damage incurred from the explosive ablation of beryllium made it impossible to reach the desired pressure regime for the Ta measurements, but the measurements provided at least a clear lower bound to the transition. These results were presented at an invited talk at the 55th meeting of the European High-Pressure Research Group and are being prepared for publication.

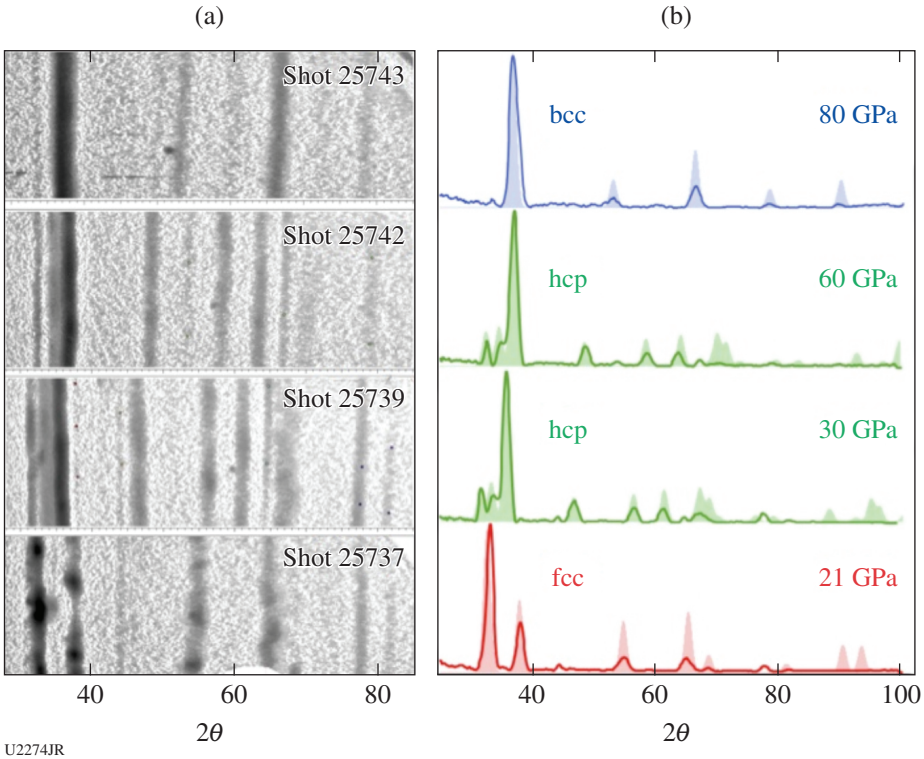

Figure 152.95
(a) Raw data and (b) integrated diffraction patterns from three phases of Pb. A Cu He_α x-ray source was used.

Development of an* In-Situ *Pressure Standard for Diffraction Experiments

Principal Investigator: F. Coppari
Co-investigators: J. H. Eggert and R. Kraus

The goal of this campaign is to develop a new way of determining pressure in diffraction experiments, based on the use of an *in-situ* pressure gauge. By measuring the diffraction signal of a standard material (whose equation of state is known) compressed together with the sample, one can determine the pressure reached during ramp compression.

Currently, pressure is determined from VISAR measurements of diamond free-surface velocity or particle velocity through a transparent window (such as LiF or MgO). This method is, in some cases, ambiguous (lack of reflectivity or shock formation) or relies on assumptions and equation-of-state models. Cross-checking the VISAR measurement with *in-situ* pressure determination using the diffraction signal of a standard material will improve the diffraction platform by providing a complementary way of determining the pressure state within the sample, with great impact to the programmatic effort of determining structures and phase transitions at high pressure and temperature. In addition, combining pressure determination from VISAR and from the *in-situ* gauge can provide information about the temperature of the sample by measuring the calibrant thermal expansion.

Building upon the results obtained in FY16, this FY17 campaign focused on the study of Au, Ta, Pt, and W pressure standards ramp compressed to 2 Mbar on OMEGA. Data were collected on eight successful shots in a half-day, including diffraction patterns of the Au/Ta and Pt/W pairs. All shots provided useful data (Fig. 152.96). Comparison of the pressures obtained from VISAR analysis and from the diffraction patterns will yield information on the accuracy of the VISAR method as well as on the existence of preheating.

Future directions of this work will look at characterizing the pressure standards at higher pressure and implementing this technique into other diffraction experiments. This platform still requires additional development before it can be used routinely in diffraction experiments, but the data collected so far are extremely encouraging and suggest that the use of an *in-situ* pressure gauge can be a viable path forward in future x-ray diffraction (XRD) measurements on both OMEGA and the NIF.

Development of Simultaneous Diffraction and EXAFS Measurements

Principal Investigator: F. Coppari
Co-investigators: Y. Ping and J. H. Eggert

Being able to measure simultaneous diffraction and an extended x-ray absorption fine-structure (EXAFS) signal in the same shot will be an enormous advance for laser-based materials experiments, providing a simultaneous probe of both the long-range [x-ray diffraction (XRD)] and short-range (EXAFS) order of the material, as well as two complementary probes of the Debye–Waller factor to gain information about the temperature state of the material under investigation. The approach successfully developed in FY16 was to use the PXRDIP diagnostic to measure diffraction and the x-ray source spectrometer to measure EXAFS. The challenge was to find a single suitable backlighter that would generate both a monochromatic (for diffraction) and broadband (for EXAFS) x-ray source. Success was achieved in measuring simultaneous

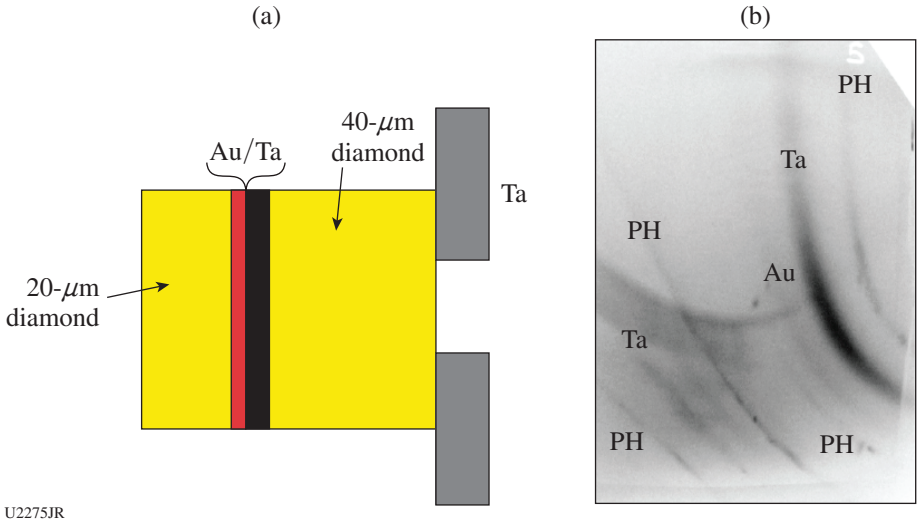

Figure 152.96
(a) Target schematic and (b) example of a diffraction image showing features from Au and Ta.

XRD and EXAFS of Fe by using a dual-foil bremsstrahlung backlighter, where one foil is optimized to generate He_α radiation for diffraction and the other to generate a continuous and broadband x-ray source for EXAFS (see Fig. 152.97).

The goal for the FY17 campaign was to improve the quality of the EXAFS measurement by using a higher-Z foil to increase the bremsstrahlung radiation, thereby generating a brighter x-ray source to allow EXAFS measurements at a higher energy (Zr K edge at 18 keV). Both Au and Ta were tested as x-ray sources for EXAFS and Fe or Cu as an x-ray source for diffraction. The spectrum generated by Au is indeed brighter, but it was not yet possible to see the EXAFS modulation above the Zr K edge. Poor spectral resolution certainly played a role in the deterioration of the EXAFS data: in this experimental setup, the spectral resolution is limited by the x-ray source size, which is enlarged by the expanding plasma generated by direct laser ablation of the foil. Further improvement could be obtained by using a spectrometer with focusing geometry that would be less sensitive to the effects of the source size.

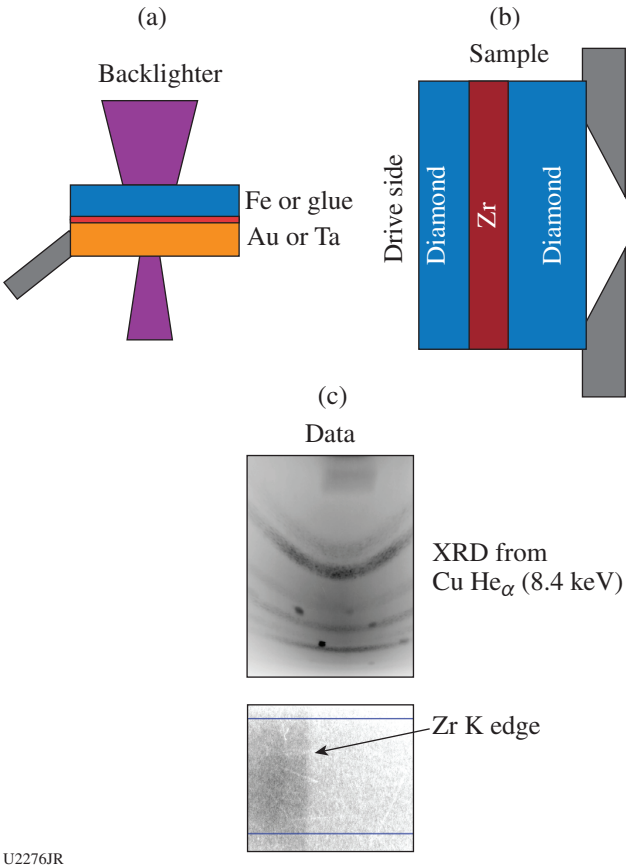

Figure 152.97
Target schematics for the (a) backlighter and (b) physics package, respectively; (c) example of diffraction and EXAFS images.

Texture Diffraction and Recovery of Shock-Compressed Samples for* Ex-Situ *Study

Principal Investigator: A. Krygier

Co-investigators: C. E. Wehrenberg, H.-S. Park, and D. C. Swift

This shot day continued the previous work of Wehrenberg on highly textured Ta that studied the deformation response of Ta to shock waves. The goal of these shots is to study if effects seen on the initial shock are present during a second shock. In particular, twinning, which is not included in the Livermore strength model for Ta, was observed to play a significant role in deformation over a wide range of shock pressures (30 to 150 GPa). X-ray scattering was measured using the PXRDIP platform in combination with VISAR on OMEGA EP.

These shots included a time series of x-ray diffraction measurements of various pressure histories. In the first configuration, the sample was shocked to the twinning regime, released, and then shocked above twinning. Twinning was observed, as shown by the red circle in Fig. 152.98, in the initial shock but not on release or on the second shock. In the second configuration, the sample was shocked to the twin-

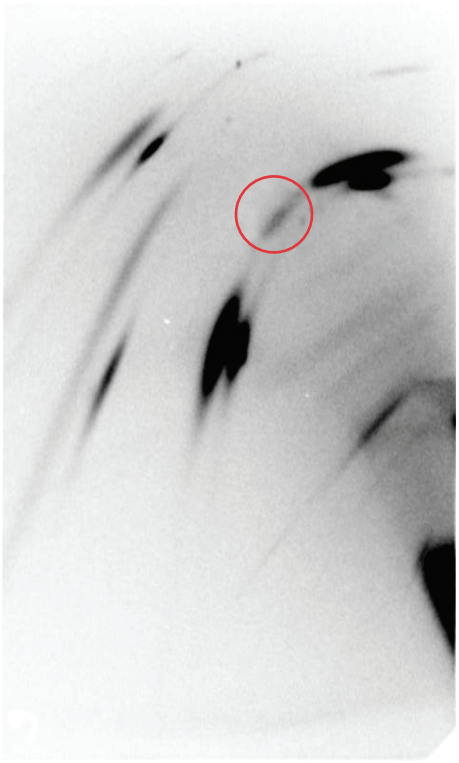

Figure 152.98
Diffraction image for shocked tantalum, showing twinning feature (circled).

ning threshold, released, and then shocked into the twinning regime. Twinning was not observed on either the release or the second shock, suggesting that dislocations generated by a shock wave moderate the deformation response. In addition, a shock-ramp history was performed, using the initial shock in the twinning regime that is approximately analogous to strength experiments in Ta performed on the NIF. In this regime, a new texture was observed that cannot be explained by twinning. Analysis is ongoing.

2. Material Equation of State Using Other Techniques

Development of a Platform for Equation-of-State Measurements Using Flyer Plate Impact

Principal Investigator: F. Coppari
Co-investigators: R. London, P. M. Celliers, M. A. Millot, D. E. Fratanduono, A. Lazicki, and J. H. Eggert

This ongoing campaign is developing a platform to use OMEGA to accelerate flyer plates to a high velocity for absolute equation-of-state (EOS) measurements by symmetric impacts. The concept is to ramp compress a metallic foil through indirect laser ablation across a vacuum gap and observe the flyer impact on a same-material sample, mounted side by side with a transparent LiF window (Fig. 152.99). By measuring the flyer-plate velocity through the transparent window prior to impact, and the resulting shock velocity in the metallic sample using transit time measurements, the principal Hugoniot of the metallic foil can be determined *absolutely* (e.g., without needing a known pressure reference), enabling one to develop an EOS standard.

Specifically, this campaign tested three flyer-plate materials to check performance and hydrodynamic prediction capabilities. Plates of Mo, Cu, and W were chosen because they can be "easily" ramp compressed to a high pressure and do not exhibit structural solid-phase transitions. Building upon the previous FY16 campaign, a successful half-day of eight shots was fielded in FY17, accelerating flyer samples to different velocities. While Cu and W showed anomalous behavior, such as flyer breakup resulting in the loss of VISAR reflectivity before impact, Mo was successfully accelerated to 14 km/s, corresponding to a shock pressure into the Mo sample of ~1 TPa. As Fig. 152.99 shows for the lower-pressure shot, the velocity ramps up smoothly and VISAR data are obtained up to impact. The impact actually shocked the LiF window into a pressure range where it was no longer transparent, impairing the VISAR signal. Future experiments will look at accelerating Mo flyer plates to different pressures to characterize its Hugoniot EOS in a wide pressure range, using quartz as a transparent window.

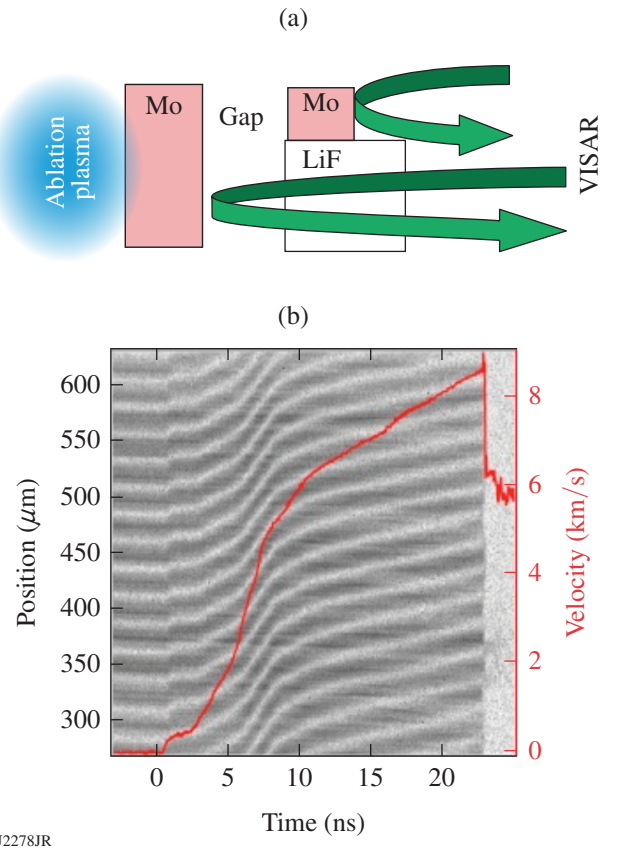

Figure 152.99
(a) Experimental concept and (b) sample VISAR data.

Development of Simultaneous EXAFS and VISAR Measurements

Principal Investigator: Y. Ping
Co-investigators: F. Coppari and J. H. Eggert

This campaign aims to test mirror shielding for simultaneous VISAR measurements in the presence of the implosion backlighter needed for EXAFS measurements. Both the VISAR and EXAFS measurements must pass through the sample, so an x-ray transparent optical mirror is used to redirect the VISAR probe beam onto the sample. This mirror is, however, vulnerable to blanking. For these FY17 shots a tilted mirror design was implemented to move the mirror out of the line of sight of the x-ray transmission path, so that more shielding of the mirror could be applied. This design extended the mirror life time by about 1 ns, but after that, the mirror was still blanked and the VISAR signal lost. On the other hand, good EXAFS data were collected for the Co K edge for the first time, as shown in Fig. 152.100. Separate shots for VISAR without the implosion also produced good VISAR data to characterize the pressure. The similar experimental design on the NIF has

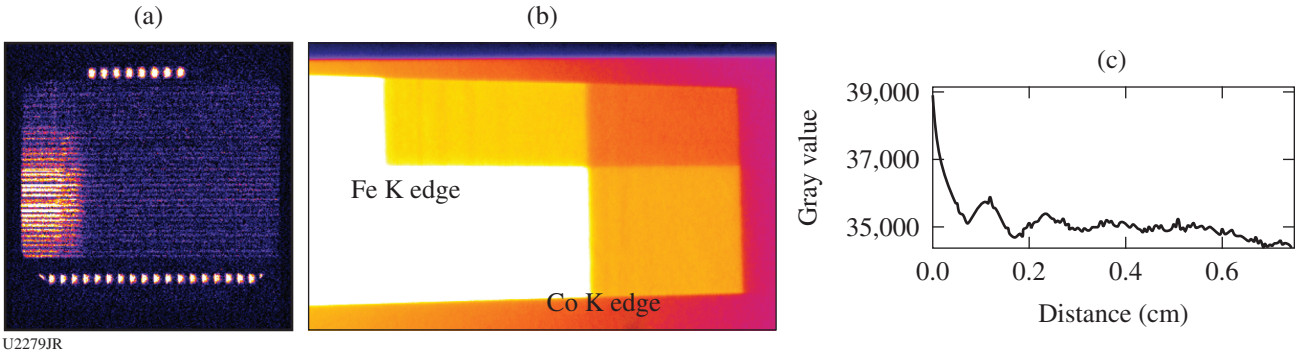

Figure 152.100
(a) Raw image of VISAR, showing blanking of the mirror delayed by ~1 ns. (b) EXAFS spectra at the Fe and Co K edges. (c) The lineout shows the EXAFS modulations at the Co K edge.

the mirror positioned behind the target, which survived and produced a VISAR signal in the presence of the implosion in a recent NIF shot.

Development of a Platform for EXAFS Measurements at the L Absorption Edge of High-Z Materials
Principal Investigator: F. Coppari
Co-investigators: Y. Ping and J. H. Eggert

EXAFS measurements in the 7-keV x-ray region are routinely performed on the OMEGA laser during shock and ramp compression. However, because the brightness of the capsule implosion used as an x-ray source decreases at high energy, measuring the EXAFS of materials with an absorption edge higher than 7 keV is very difficult in a single shot. In addition, as one seeks to study higher-Z materials and observe the L absorption edge, the amplitude of the EXAFS signal decreases as well because the cross section for the absorption at the L edge is lower than at the K edge. These issues make these measurements extremely challenging.

In prior years the TaXAFS Campaigns looked at the Ta L3 edge (~10 keV) and were able to obtain a good signal-to-noise ratio by averaging 15 shots or by using a multicrystal spectrometer.[36] The goal of the FY17 campaign is to look at materials whose L edge is closer to 7 keV, where the number of photons generated by the capsule implosion is higher, to see if a good signal can be obtained in a single shot. The shots studied the Ce L3 edge (5.7 keV), but although a nice contrast at the Ce L edge has been measured, no clear EXAFS modulations could be observed in a single shot (Fig. 152.101), probably also a result of limited spectral resolution. This suggests that in order to successfully measure L-edge EXAFS, a spectrometer with focusing geometry is needed to increase the signal because of the higher collection efficiency and reduce the sensitivity to x-ray source size broadening, therefore improving the quality of the data.

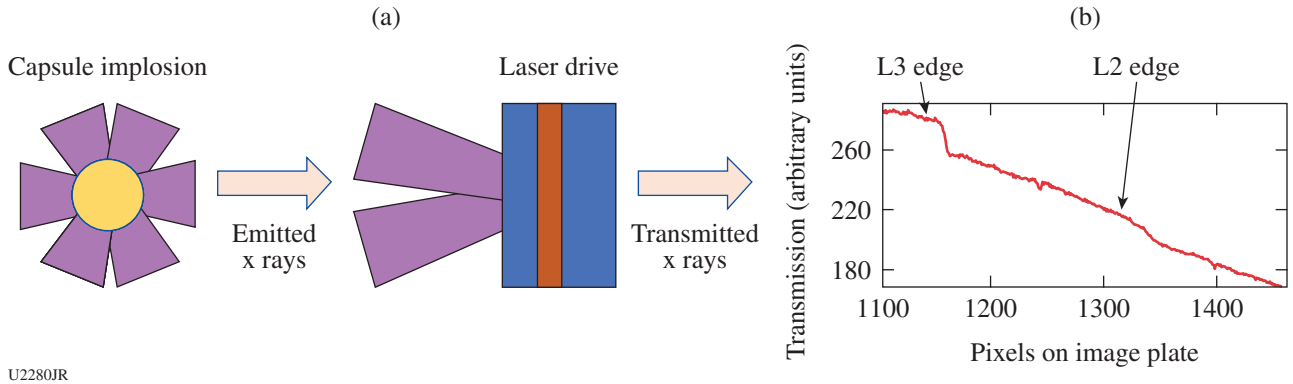

Figure 152.101
(a) Experimental concept and (b) sample EXAFS data.

Development of Spherically Convergent Equation-of-State Measurements

Principal Investigator: A. E. Lazicki
Co-investigators: D. Swift, A. M. Saunders, T. Doeppner, R. Nora, F. Coppari, R. London, P. M. Celliers, J. H. Eggert, G. W. Collins, H. Whitley, J. Castor, and J. Nilsen

This campaign is developing a platform for measuring Hugoniot EOS at pressures much higher than can be achieved using a standard planar drive. This platform is intended to collect data in the pressure regime of 100+ Mbar, where currently very little data exist for any material, for the purpose of constraining EOS models.

The FY17 campaigns first used a hohlraum (indirect drive) to launch converging shock waves into solid spheres of CD (deuterated) and CH (normal) plastic. Along the axis of the hohlraum, vanadium He_α backlit 2-D x-ray images of the imploding sphere were collected with a framing camera. On some shots, x-ray Thomson-scattering measurements were also made using a Zn backlighter and a spectrometer at the hohlraum equator [Figs. 152.102(a) and 152.102(b)]. The radiographs yield density and shock velocity that make it possible to calculate the shock state using the Rankine–Hugoniot equations, and the scattering data yield information about temperature and ionization state.

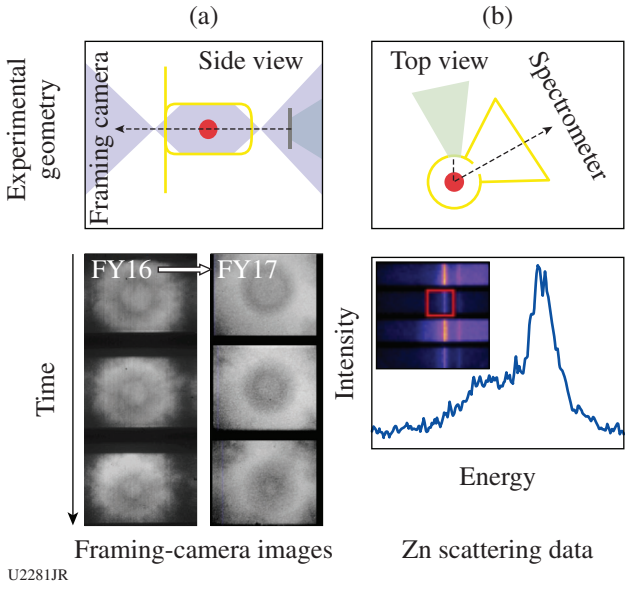

Figure 152.102
(a) Experimental geometry and representative 2-D framing-camera images of the imploding sphere, comparing results from FY16 and FY17 (shot 83557). (b) Geometry and representative Zn x-ray Thomson-scattering data (shot 85304).

The FY17 shots improved on prior measurements by increasing hohlraum gas fill to eliminate suspected hohlraum blowoff features and using faster-gating cameras to improve spatial resolution. Neutron diagnostics were also fielded to detect neutrons from the hot spot. The new design for the x-ray scattering measurement yielded a high-quality Compton feature and an elastic feature potentially artificially elevated because of Zn plasma leakage. These results, together with the FY16 measurements on CH_2, are being summarized for a publication that will describe the principal Hugoniot of plastic from the initial densities of CH, CH_2, and CD.

In addition, a separate half-day of shots continued development of a platform to achieve hundreds-of-Mbar pressures in a spherically converging shock wave, launched by using direct laser ablation of the sphere. This measurement probed deuterated plastic (CD) using radiography, x-ray Thomson scattering, and neutron yield. Data improved in quality compared to FY16 but indicated some drive asymmetry and preheating effects, requiring further design optimization.

Development of a Conically Convergent Platform for Hugoniot Equation-of-State Measurements in the 100-Mbar to 1-Gbar Pressure Regime

Principal Investigator: A. E. Lazicki
Co-investigators: D. Swift, F. Coppari, R. London, D. Erskine, D. E. Fratanduono, P. M. Celliers, J. H. Eggert, G. W. Collins, H. Whitley, J. Castor, and J. Nilsen

This campaign was designed to develop a platform for measuring Hugoniot EOS of arbitrary (including high-Z) materials at pressures much higher than can be achieved using a standard planar drive. This platform is intended to collect data in the pressure regime of 100+ Mbar, where currently very little data exist for any material, for the purpose of constraining EOS models.

To achieve the desired pressure amplification, converging shock waves are launched into a cone inset in a halfraum. For appropriate cone angles, nonlinear reflections of the shock wave result in the formation of a Mach stem: a planar high-pressure shock that propagates along the axis of the cone. This approach was tested in FY16 and produced promising results but suggested the need for preheat shielding. The FY17 half-day campaign attempted to overcome this need with Au preheat shield layers by experimenting with a porous cone material, from which simulations suggested that increased pressure amplification would be possible. Additionally, these shots tested multiple cone angles and fielded targets with quartz

windows and Al steps to attempt to quantify the Mach wave's strength and steadiness. Two results are shown in Fig. 152.103. Transit time calculations indicate that 100+ Mbar shock waves were generated in the CH cones. At peak laser intensities the quartz windows blanked, indicating that the Au preheat shield thicknesses were not sufficient, and the profile of the shock breakout suggested the Mach wave was decaying (unsupported) through the full target thickness. A subset of the shots also attempted to use area-backlit radiography to image the Mach wave formation in the cones themselves, through slits in the halfraums. Geometric issues made it very difficult to interpret the framing-camera images. However, the lessons learned on this shot day were very important in designing a successful test shot on the NIF, completed on 31 August 2017.

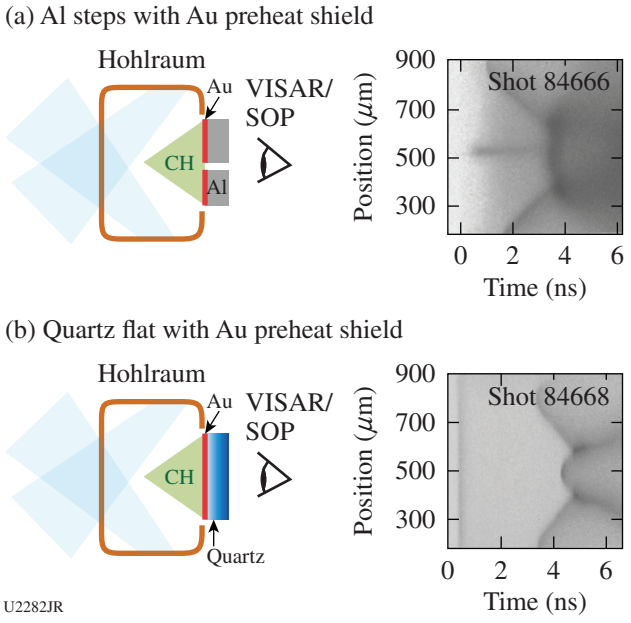

Figure 152.103
Experimental configuration and raw SOP data showing the breakout time from (a) a stepped Al sample with Au preheat shield layers and (b) a thick quartz sample with a Au preheat shield layer.

3. Material Dynamics and Strength

Copper Rayleigh–Taylor (CuRT) Growth Measurements

Principal Investigator: J. M. McNaney
Co-investigators: S. Prisbrey, H.-S. Park, C. M. Huntington, and C. E. Wehrenberg

The CuRT Campaign is part of the material strength effort, which is aimed at assessing the strength of various metals at high pressure and high strain rate. The goal of the CuRT platform is to measure Rayleigh–Taylor (RT) growth of samples that behave "classically," i.e., can be fully modeled using a fluid description. In this series of experiments the intent is to measure RT growth in liquid copper at high pressures. A second goal is to demonstrate the dynamic range of the technique by measuring RT growth in solid copper.

Without the stabilization of strength, classical RT growth is characterized by a growth rate $\gamma = \sqrt{kgA_n}$, where k is the wavelength of the unstable mode, g is the acceleration, and the Atwood number A_n quantifies the magnitude of the density jump at the interface. Acceleration of the sample in the experiment is provided by the stagnation of a releasing shocked plastic "reservoir," which is directly driven by ~2 to 8 kJ of laser energy, depending on the desired material condition. The growth of preimposed ripples is recorded using transmission x-ray radiography of a copper He_α slit source, where the opacity of the sample is calibrated to the ripple amplitude. The preshot metrology and measured ρr of the driven sample together yield the growth factor, which is compared to models of RT growth. Diagnostic features such as a gold knife edge on the sample allow one to measure the modulation transfer function and create an opacity look-up table on each shot, resulting in error bars of approximately ±10%.

The March 2017 campaign produced the first results for liquid copper RT. Analysis of the velocimetry (Fig. 152.104) indicated that the copper RT samples were subjected to a shock of ≈5 Mbar, leading to a complete melt of the sample and subsequent RT growth in the liquid phase. The liquid Cu RT growth curve is presented in Fig. 152.105. A second day of liquid copper shots took place on 13 September 2017. The results of those experiments (also in Fig. 152.105) were consistent with the values obtained in the March data. Simulations of the liquid Cu growth are in progress.

Evaluation of Additively Manufactured Foams for Ramp-Compression Experiments

Principal Investigator: R. F. Smith

The FY17 "AMFoam" Campaigns continued to evaluate the use of 3-D–printed or additively manufactured foams as surrogates to carbonized resorcinol foams (CRF's) in ramp-compression target designs. The 3-D–printed foams may be characterized as follows: The 100 × 100 × 16-μm^3 log pile blocks, composed of individually printed lines, are stitched together to form 1.7-mm-diam layers. Seven 16-μm^3 layers are then stacked on top of one another to arrive at cylindrical AM foams that are 112 μm tall (Ref. 37). These foams are glued onto a 25 μm Br + 120 μm 12% Br/CH assembly

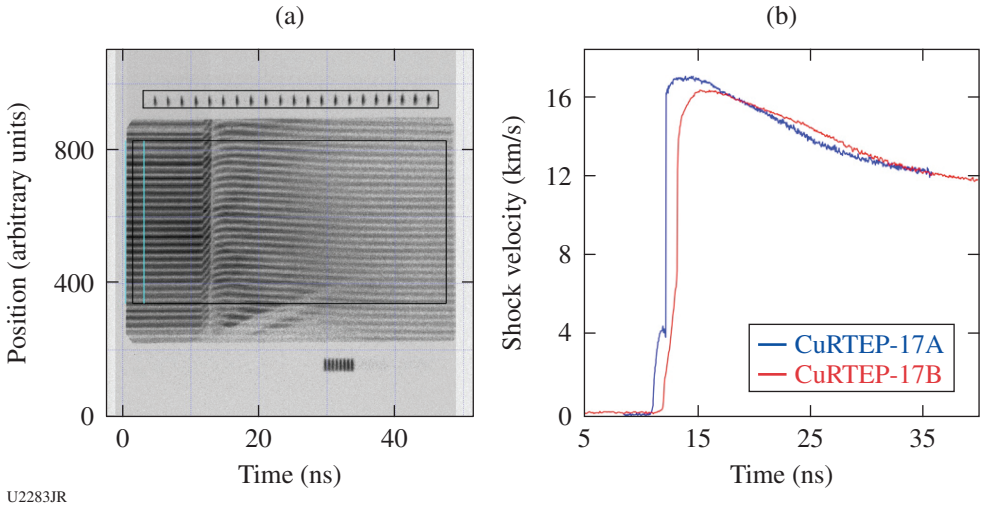

Figure 152.104
(a) The active shock breakout (ASBO) data from shot 26423 (September 2017); (b) analyzed results and comparison to March 2017 results.

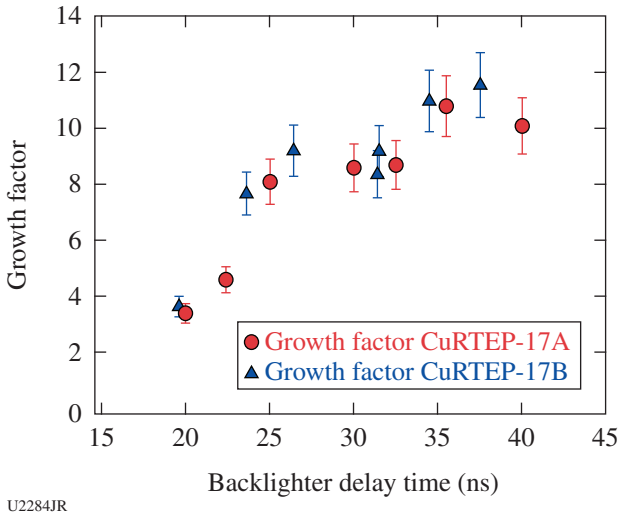

Figure 152.105
Growth factor data for liquid copper from the March and September shot days.

[Fig. 152.106(a)]. Following the ramp-compression design described in Ref. 30, 15 OMEGA beams with 300 J in 2 ns result in a ramp-compression wave being launched into a stepped-Al/LiF sample [Fig. 152.106(a)]. At a controlled time after this compression begins, the OHRV (2-D VISAR probe) takes a 2-D snapshot of the reflectivity and velocity field with a spatial resolution of ~3 μm (Ref. 38). An example of the intensity field recorded on the 2-D VISAR is shown in Fig. 152.106(c).

These campaigns have varied the structure of the 3-D–printed foam with the goal of optimizing the temporal ramp profile. These experiments have been conducted in support of material strength experiments on the NIF.

4. National Security Applications

SolarCellESD: Solar Cell Electrostatic Discharge Experiments

Principal Investigator: K. Widmann
Co-investigators: P. Jenkins (NRL); S. Seiler (DTRA); and P. Poole and B. Blue (LLNL)

The overall goal of the SolarCellESD Campaign is to determine experimentally whether prompt x rays can induce failure modes in solar arrays that are not accounted for by simply testing the individual solar cells alone. The solar-cell array is fielded as part of the x-ray Langmuir probe detector (XLPD) cassettes and exposed to x rays from a laser-driven source. The FY17 campaigns added a partial electromagnetic-interference enclosure of the XLPD front end—"partial" because the enclosure has a large rectangular opening providing an unobstructed view of the x-ray source for the solar-cell array. The bias and diagnostic electronics for the solar cells were also improved such that the bias circuit is fully isolated from any of the target chamber components and the bias voltage can be changed manually between shots. This bias voltage allows one to mimic the voltage difference between two adjacent solar cells from different strings in large arrays, which can range from tens to a few hundred volts. Figure 152.107 shows a schematic and a photo of the new and improved XLPD front end.

The FY17 campaign continued using the x-ray source developed in FY15: a small gold halfraum (600-μm diameter, 600-μm long) with a small pinhole (60-μm or 100-μm diameter) at the "closed" side of the halfraum. The targets were driven with three sets of 1-ns laser pulses to generate x-ray pulses of 3-ns duration. These targets provide two significantly different

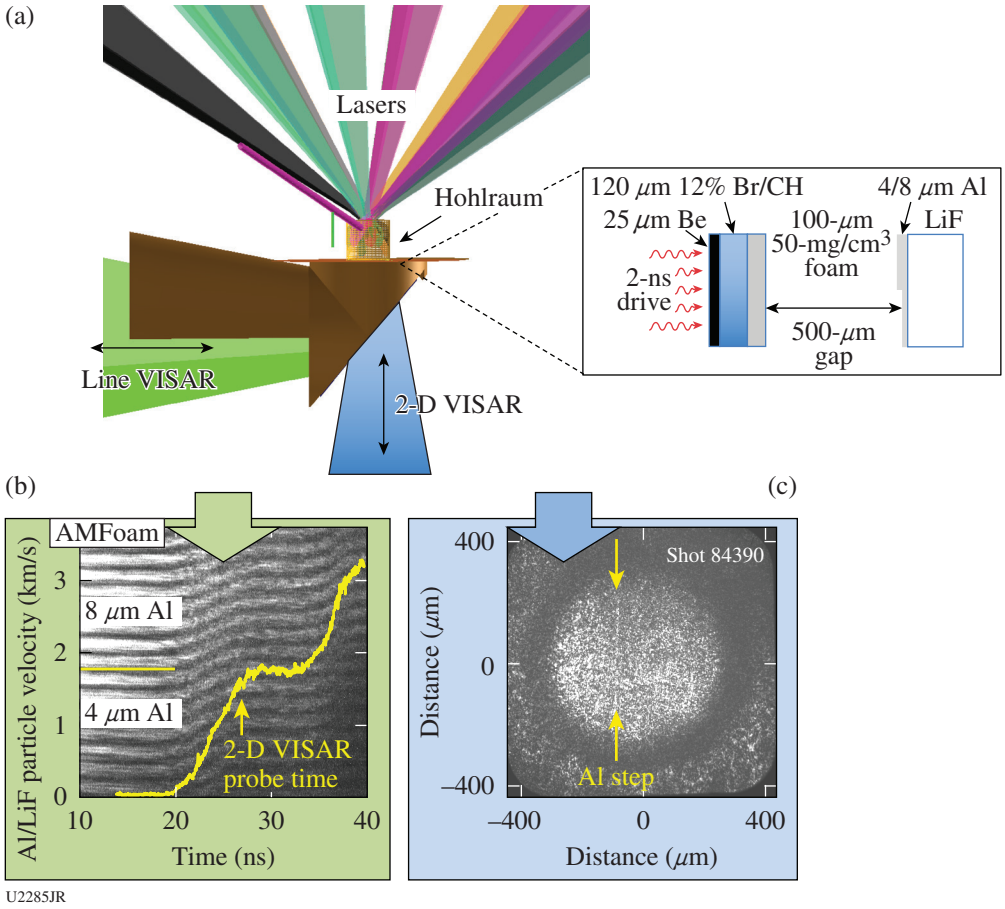

Figure 152.106
(a) Schematic diagram describing the experimental setup for the AMFoam-17A Campaign, which combined the ASBO and OHRV (2-D VISAR) diagnostics on a single shot. The goal of these shots was to characterize the temporal and spatial drive associated with additively manufactured (3-D–printed) foam targets. The line VISAR shows the 1-D velocity measure as a function of time. Two-dimensional VISAR provides the 2-D velocity measurement of 3-D–printed foams at a snapshot in time. (b) The ASBO record shows a characteristic ramp/pressure-hold/ramp compression profile. (c) Sample reflectivity at OHRV probe time. For the AMFoam-17B Campaigns, only the ASBO (VISAR) diagnostic was used. Preliminary 2-D VISAR non-fringes image and velocity analysis shows AMFoam exhibits a spatial structure comparable or perhaps smoother than CRF foam.

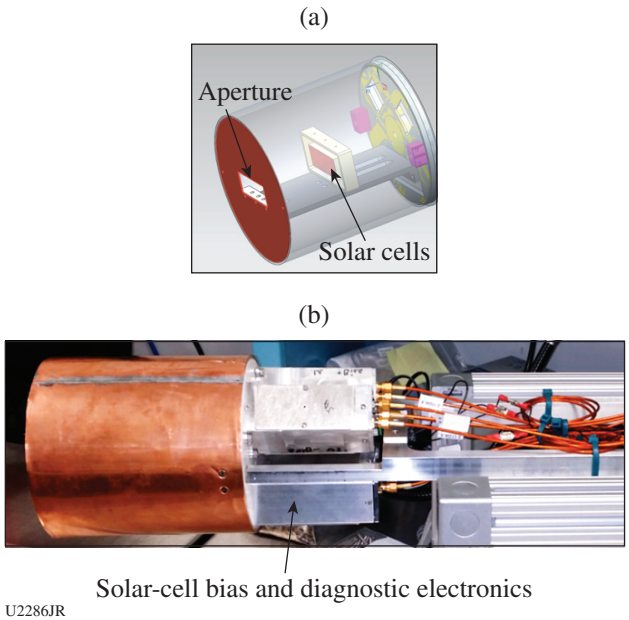

Figure 152.107
(a) Front end of the x-ray Langmuir probe detector (XLPD) with the solar cell (mini) array, i.e., 2 × 1 cells and (b) photo of the XLPD (side-on view) with the new electromagnetic-interference enclosure and the various bias and diagnostic electronics.

x-ray flux (and fluence) levels depending on the target orientation with respect to the solar cell array ("open side" versus "pinhole side"). Despite the large difference in the measured radiant x-ray power, from 300-GW/sr peak flux for the open side down to a few tens of GW/sr for the pinhole side, the spectral intensity distribution should be very similar. Unfortunately, the low signal level on the Dante x-ray diodes for the low-flux case did not allow us to make a good quantitative comparison of the unfolded spectral intensities. Figure 152.108 shows the x-ray flux measured with Dante for two open-side shots.

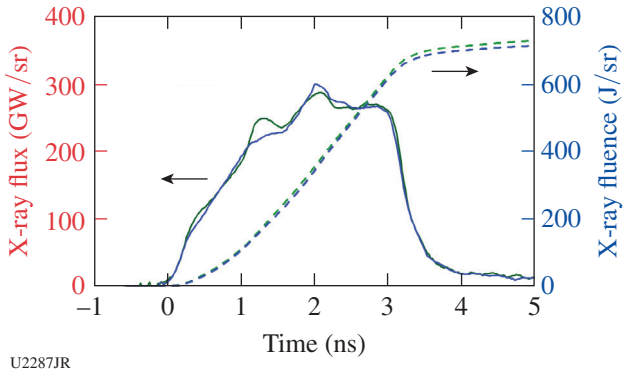

Figure 152.108
Dante measurements of the output (radiant power and x-ray fluence) of the laser-driven x-ray sources for two shots in the "open side" configurations (see text for details) showing a shot-to-shot variation of only 2% in the total x-ray fluence, within the uncertainty of the Dante x-ray flux measurement.

With the improved hardware, it was possible to generate and observe, for the first time, x-ray–induced arcing just between the solar cells without creating discharge between the solar cells and any of the other components in the target chamber. These shots also demonstrated the feasibility of mitigating the x-ray–induced arcing by altering the bias voltage for the solar-cell array. The next goal for the this campaign is a detailed parameter scan to determine the threshold values for the x-ray fluence and associated bias voltage levels, respectively, for x-ray–induced arcing in solar-cell arrays.

Plasma Instability Control to Generate a High-Energy Bremsstrahlung X-Ray Source
Principal Investigator: P. L. Poole
Co-investigators: R. Kirkwood, S. C. Wilks, M. May, K. Widmann, and B. E. Blue

In FY17 a campaign began to develop a high-fluence x-ray source in the 30- to 100-keV range by deliberately stimulating and optimizing plasma instabilities. High-fluence sources at lower energies are currently used for materials effects studies in extreme environments, but stronger sources are needed for >30-keV x rays. This project aims to enhance laser conversion to plasma instabilities such as stimulated Raman scattering (SRS), which accelerate electrons in plasma waves that will convert to high-energy x rays via bremsstrahlung in the high-Z hohlraum wall.

The SRS-Xray-17A half-day centered on optimizing plasma conditions within a hohlraum for high SRS gain by reversing ideas on how to mitigate these effects for fusion conditions (SSD bandwidth off, phase plate changes, etc.). Two types of targets were fielded to test SRS generation: one with 6-mg/cm^3 (0.2 n_c) SiO_2 foam fill, the other with 10 μm of parylene-N (CH) inner lining. The CH-lined hohlraums were illuminated with an 80-ps picket prepulse arriving a variable time before the main 1-ns, 450-J/beam laser drive.

Primary results were promising: the best targets exhibited *10× more x-ray yield in the >50-keV regime than typically seen on direct-drive shots*. The SRS streak data are being compared to the various x-ray diagnostics fielded to obtain a detailed picture of instability gain and directionality and its impact on x-ray fluence. While the CH prepulsed targets exhibited factors-of-6 more direct SRS backscatter than the no-prepulse CH and foam targets, these latter configurations had the best x-ray yield (Fig. 152.109). The increased indirect backscatter on the no-prepulse CH target provides an avenue of further simulation and future experimental study to investigate the directionality of SRS backscatter within the hohlraum and its impact on the ultimate x-ray yield. Target design simulations are underway, using these valuable experimental results to plan the FY18 OMEGA and NIF campaigns. These promising initial results are a valuable stepping stone toward a new x-ray source that will represent a large capability increase for national security applications and related materials under extreme conditions studies, with the additional benefit of broadening the understanding of plasma instability control for fusion and other applications.

5. Plasma Properties

Investigation of Orthogonal Plasma Flows in the Presence of Background Magnetic Fields
Principal Investigator: B. B. Pollock
Co-investigators: T. Johnson, G. F. Swadling, J.S. Ross, and H.-S. Park

The DebrisPlasma-17A shots continued the Magnetized Collisionless Shock–Weapons Effect Campaign from previous

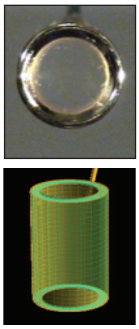

Backscattered-light calorimetry	
Target	Increase factor
Foam filled	1.1×
CH-lined, 1.0-ns prepulse	5×
CH-lined, 1.5-ns prepulse	6.6×
CH-lined, 2.0-ns prepulse	6.1×

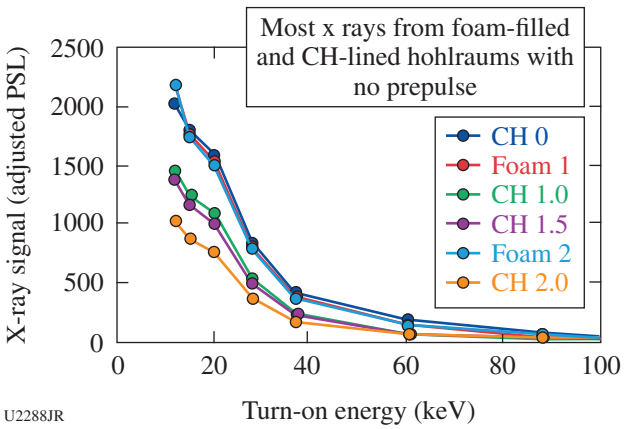

Figure 152.109
Data summary for SRS-Xray-17: highest SRS backscatter from CH-lined hohlraums irradiated with prepulse; highest x-ray yield from no-prepulse CH and foam-filled targets. PSL: photostimulated luminescence.

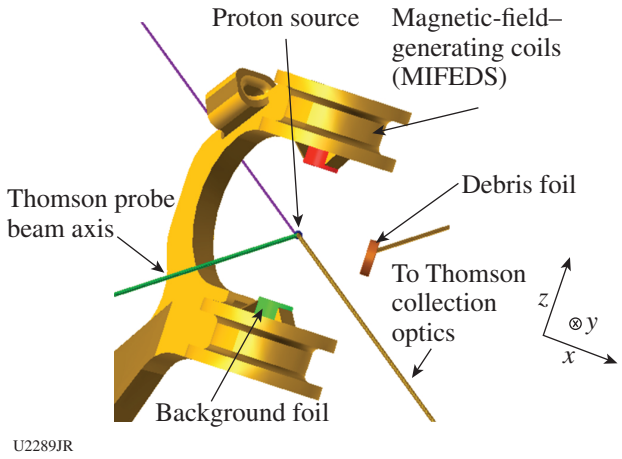

Figure 152.110
Experimental configuration viewed from the proton detector in TIM-1. One or two foils can be mounted to the MIFEDS structure, which is centered at target chamber center (TCC). The Thomson-scattering geometry is *k* matched to the *z* axis of the experiment. The capsule is 1 cm into the plane of the page from TCC and the debris foil is 2 mm from TCC.

years. The goal for this series of experiments is to quantify the interaction of orthogonal plasma flows, with and without a background magnetic field. The field is supplied by LLE's magneto-inertial fusion electrical discharge system (MIFEDS), which delivers 4 to 8 T at the interaction region of the experiments, depending upon the specific geometry of the MIFEDS coils (Fig. 152.110). The orthogonal plasma flows originate from two separate foil targets, one of which is mounted to the MIFEDS structure. The foil material composition, laser drive, spacing, and time of flight to the interaction region can be varied on each shot.

The interaction region of the two flows is simultaneously probed with 2ω Thomson scattering and protons from the implosion of a D^3He-filled capsule. Initial measurements of the electron density and temperature from the Thomson scattering do not indicate a strong dependence on the strength or direction of the background magnetic field. The proton deflectometry data do show structural differences in the measured proton distribution with and without the field, but further modeling and simulations are needed to quantify these differences.

Measurement of Gold Thermal Transport and M-Shell Emission Using a Buried Layer Platform

Principal Investigator: E. V. Marley
Co-investigators: L. C. Jarrott, M. B. Schneider, G. E. Kemp, M. E. Foord, R. F. Heeter, D. A. Liedahl, K. Widmann, C. W. Mauche, G. V. Brown, and J. A. Emig

This campaign was designed to measure the thermal transport through gold layers as well the emitted M-shell gold spectra from a well-characterized and uniform plasma for comparison to atomic kinetic models. The buried layer target geometry used for this experiment is capable of generating plasmas with an electron temperature of ~2 keV at electron densities of 10^{21} electrons per cubic centimeter. These are within the range of conditions found inside gold hohlraums used on experiments on the NIF, providing a stable laboratory setting for radiation transport and atomic kinetic studies of hohlraum plasmas.

Planar, buried layer targets composed of Ti, Mn, and Au were illuminated evenly on both sides (Fig. 152.111) to heat the sample. The sample was buried between two 5-μm-thick layers of Be serving as an inertial tamp to slow the expansion of the sample. Time-resolved 2-D images of the target's x-ray emission, viewed both face-on and side-on, were recorded using time-gated pinhole cameras. The K-shell spectra from the Ti and Mn were used to determine the electron temperature of the plasma. The time-resolved spectra were recorded using a

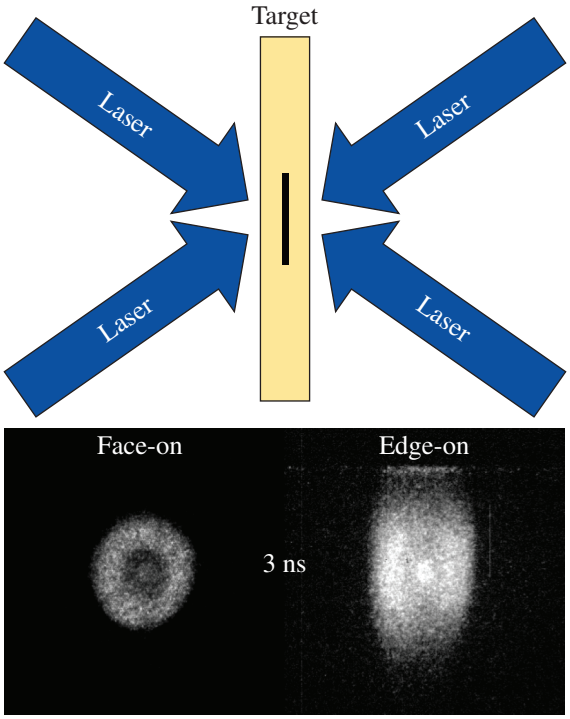

Figure 152.111
Experimental configuration and pinhole images of the emission area at 3 ns of shot 86860.

crystal spectrometer coupled to a framing camera, as well as a crystal spectrometer coupled to an x-ray streak camera. Two additional time-resolved crystal spectrometers were used to record the full range of the Au M-shell emission. All of the framing cameras used, for imaging as well as spectroscopy, were co-timed so the plasma conditions at the time of the measured Au M-shell emission could be established from synchronous K-shell and imaging data.

During the campaign two different sample thicknesses were used to measure the thermal transport through Au. Two different pulse shapes were also used to assess which was most efficient for coupling laser energy into the buried layer target. A complete set of data from all six precisely co-timed diagnostics was recorded for both target types, using both pulse shapes during this August campaign, at temperatures ~2 keV. Data analysis is underway.

6. Hydrodynamics

Experiments on the Rayleigh–Taylor Instability in the Highly Nonlinear Regime

Principal Investigators: C. C. Kuranz (University of Michigan) and C. M. Huntington (LLNL)

Co-investigators: L. Elgin, G. Malamud, S. R. Klein, R. P. Drake, and D. Shvarts (University of Michigan) and T. Handy and M. R. Trantham (LLNL)

These experiments observe the evolution of the single-mode Rayleigh–Taylor instability (RTI) in low- and high-Atwood-number regimes at late scaled times (Fig. 152.112). Models predict two growth phases of the RTI: exponential growth, followed by a nonlinear stage reaching a terminal velocity.[39] For low-Atwood number systems, numerical simulations show an additional growth phase in the late nonlinear stage, characterized by reacceleration.[40] There are, however, claims that this reacceleration may be an artifact of the simulations and may not reflect the evolution of classical RTI. Prior experimental studies of RTI growth have not created the conditions necessary to observe the late nonlinear stage, which requires large aspect ratios of the spike and bubble amplitudes to the perturbation wavelength $\left(1 \le h_{s,b} / \lambda \le 3\right)$ (Ref. 40).

The first two experiments in this new campaign were conducted in FY17. A laser-driven blast wave accelerates an RT-unstable interface in a shock tube. X-ray radiographs along dual orthogonal axes capture the evolution of RTI. Late scaled times are achieved with small-wavelength ($\lambda = 40$-μm) seed perturbations at the interface. PAI (polyamide-imide) plastic (1.4 g/cm^3) is used as the heavy fluid. The lighter fluid consists of CRF, with pre-shock densities of 0.05 g/cm^3 (high Atwood) or 0.4 g/cm^3 (low Atwood). The first shot day demonstrated x-ray–backlit imaging capable of resolving

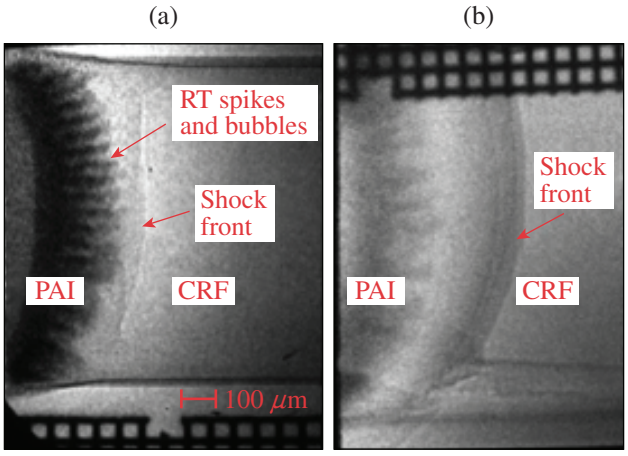

Figure 152.112
(a) RID 83095 (10/06/16) with high-Atwood, λ = 40-μm target at 15 ns and (b) RID 85111 (4/06/2017) with low-Atwood, "flat" interface target at 26 ns. PAI: polyamide-imide; CRF: carbon resorcinol formaldehyde.

the small-wavelength RT spikes and bubbles. But the plastic shock tube could not support the higher internal pressure of the dense, low-Atwood targets. A new target design was developed and fielded for the second shot day. Improvements included Be walls, which can be thicker because of the high x-ray transmission of Be, and a larger tube diameter, which delays the effects of transverse waves. The new design extended the time scale for observations of RTI growth in low-Atwood targets from 30 ns to >40 ns. However, the ablators did not meet specifications, compromising the physics of the experiment. The data are being analyzed to extract as much information as possible, and the team is working with the ablator manufacturer to ensure that the parts for the FY18 experiments meet all specifications.

This work is funded by LLNL under subcontract B614207.

Proton Heating of Copper Foam on OMEGA EP

Principal Investigator: J. Benstead
Co-investigators: E. Gumbrell, S. McAlpin, M. Crook-Rubery, R. Merritt, and W. Garbett (AWE)

This LLNL–AWE campaign studies the heating of a cylindrical puck of copper foam irradiated by a short-pulse–generated proton beam. This shot day was an extension of previous shot days in 2014 and 2016 and featured a refined target and diagnostic design. The two major aims of the experiment were to measure the temperature distribution through the target and to quantify the extent of expansion of the rear surface.

The experimental setup is shown in Fig. 152.113. A gold foil was irradiated with the OMEGA EP sidelighter (SL) beam delivering 200 J over 3 ps. The SL produced a beam of protons and ions that were used to heat a copper-foam puck positioned 0.5 mm away. An aluminum foil was placed between the gold foil and the copper puck to improve heating by filtering out heavier ions and low-energy protons, which nonuniformly heat the target. The subsequent sample expansion was imaged with an x-ray radiography system. This used a nickel area backlighter, irradiated with three long-pulse beams, coupled to an x-ray framing camera (XRFC) that imaged the backlit target. The backlighter (BL) beams were delayed with respect to the SL beam in order to observe the heated and expanded target at different times. The streaked optical pyrometry (SOP) diagnostic was fielded orthogonally to the heating axis with its imaging slit oriented such that the temperature through the central section of the disk could be measured front to rear over the first 5 ns of heating (see Fig. 152.114); an RCF stack measured the proton/ion beam spectrum on each shot (see Fig. 152.115).

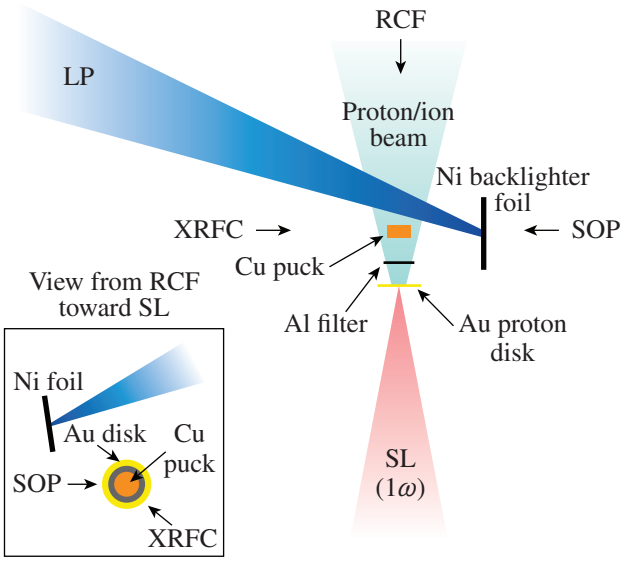

U2292JR

Figure 152.113
Experimental layout for proton-heating shots with combined x-ray radiography, SOP, and RCF. Only one long-pulse beam (of the three used) is shown for simplicity.

In total, seven shots were fired with data acquired on the XRFC, RCF, and SOP diagnostics. Full data analysis is still in progress, but preliminary results indicate that the degree of heating achieved was as desired. Slightly unusual features present on the SOP data have been attributed to the reduced target size relative to previous shot days, causing unexpected interactions with the SL pulse.

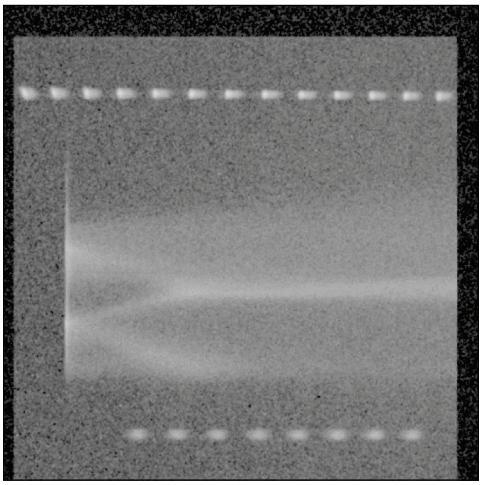

U2293JR

Figure 152.114
SOP data from a proton-heating shot. The proton field is directed from the top downward, and the 1-D spatial image is taken through the center of the puck. The anomalous features observed appear to be caused by the reduced target dimensions causing more-complicated interactions with the beam and proton field relative to previous shot days in this campaign.

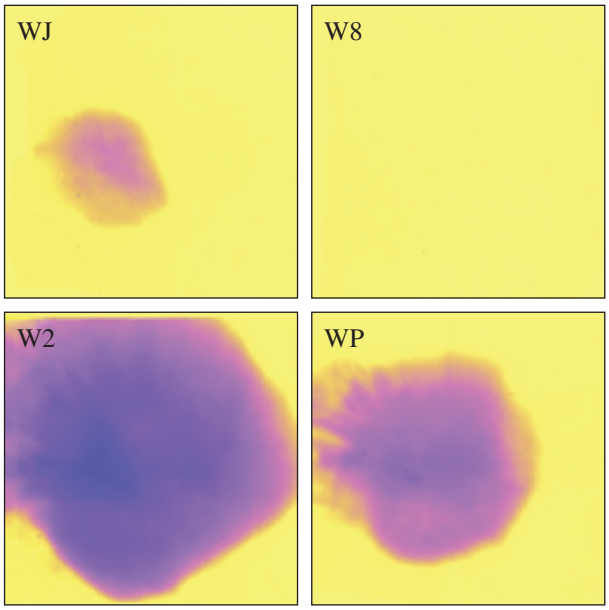

Figure 152.115
RCF data showing the attenuation of the proton and ion fields on one shot in the final four pieces of the film stack. The film pieces move progressively farther away from the target beginning at the bottom left image, then bottom right, then top left, and finally top right.

Development of Radiography-and-VISAR Platform for Hydrodynamics Measurements

Principal Investigators: M. Rubery (AWE) and D. A. Martinez (LLNL)
Co-investigators: G. Glendinning (LLNL); and S. McAlpin, J. Benstead, and W. Garbett (AWE)

As part of the LLNL/AWE Carisbrook Campaign, one and a half shot days of experiments were performed on the OMEGA Laser System during FY17. The platform consists of a halfraum and shock tube package driven by 15 × 500-J beams from the OMEGA H7 axis [Fig. 152.116(a)]. The objectives for these shot days were to diagnose the evolution of a hohlraum-driven interface using simultaneous point-projection x-ray radiography and VISAR, a configuration that was successfully demonstrated during FY16. A secondary objective for FY17 was to demonstrate the use of a reduced-mass backlighter [3-mm Ta disk versus 4-mm Ta square, Fig. 152.116(b)]. If successful, the new configuration should sufficiently reduce the amount of vaporized metal generated during the experiment to allow future campaigns to use the OMEGA EP short-pulse beam with debris shields removed (higher energy).

To generate the 7.8-keV He_α point-projection x-ray source, a 600-μm-sq nickel microdot was driven to 2×10^{15} W/cm^2 using 4 × 400-J, 1-ns backlighter beams [Fig. 152.116(b)]. The x-ray emission is projected through a 20-μm Ta pinhole plate aligned along the shock tube and toward the TIM-6 cranked snout axis of $\theta = 123.1$ and $\phi = 172.76$. Images were recorded on film using a gated XRFC.

(a)

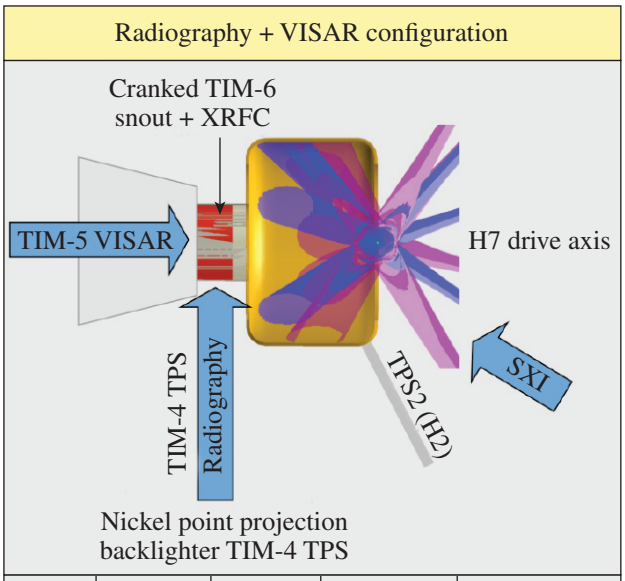

Beams	# CPP's	CPP size	Pulse	Special/DDS
6+9 H7	15	IDI 300	1-ns square	500 J/beam
4× BL	Removed	280 μm	1-ns square	400 J/beam

(b)

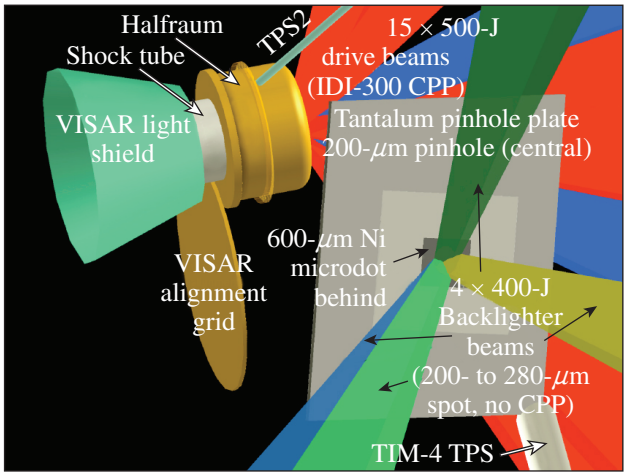

Figure 152.116
(a) Radiography + VISAR configuration overview and (b) VISRAD isometric view of the experiment. TPS: target positioner system.

A quartz window, aluminum flash coating, and light shield cone were added to the rear of the target, allowing us to make VISAR measurements along the TIM-5 H14 axis.

The VISAR diagnostic performed well during all shots from Ca-17A and 17B. Figure 152.117 shows good-quality streak-camera images from both legs of the VISAR diagnostic on shot 86473. The SOP diagnostic, which uses the same optical relay as the VISAR, also produced good quality data on both shot days.

Unfortunately, during the first shot day, no radiography images were recorded. The source of this failure was found to be in the assembly of the backlighter. The mounting location of the nickel microdot was measured >100 μm away from the design position; this deviation is sufficiently large to move the nickel x-ray emission out of the XRFC field of view. In response to this, the backlighter design was modified to reduce sensitivity to assembly and target misalignment. The microdot was increased from 400 μm square to 600 μm square, and the backlighter beam spots increased from 200-μm to 280-μm diameter. The backlighter energy was also increased from 200 J/beam to 400 J/beam to maintain intensity. On the second half-day of shots these modifications were found to be 100% successful.

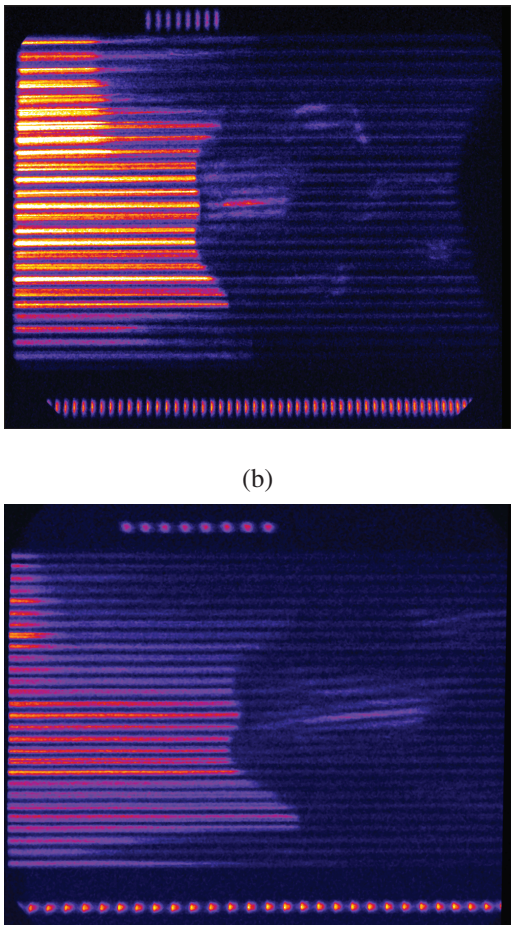

Figure 152.117
VISAR streaked images from OMEGA shot 86473, Ca-17B.

In addition, the new reduced-mass backlighter was successfully fielded on the second day and produced a radiograph with no observable drop in image quality, opening up the possibility of a future joint shot day, without the limitations on pulse energy introduced by parabola debris shields.

Development of Gamma-Ray Sources for MeV Radiography

Principal Investigator: F. Albert
Co-investigators: N. Lemos and J. Shaw (LLE); and D. A. Martinez and V. A. Smalyuk (LLNL)

This series of shots was designed to develop gamma-ray sources intended for a future MeV radiography capability on NIF's Advanced Radiography Capability (ARC) short-pulse laser. Megavolt radiography on the NIF will serve a number of applications, such as double-shell implosions and imaging of dense objects.

The first FY17 campaign alternatively focused the backlighter and sidelighter short pulses (10 ps, 900 J) onto tantalum targets coated with 10 μm of plastic to produce hot electrons and subsequent gamma-ray emission from bremsstrahlung radiation (Fig. 152.118). The electron spectrum was measured with an electron positron proton spectrometer (EPPS) (along the short-pulse laser axis and also at 90°), and the gamma-ray spectrum with HERIE (a high-energy radiography imager) using a tantalum step-wedge filter pack. This diagnostic was used to retrieve an emitted photon spectrum of the form $f(E) = A\exp(E/E_T)$, where E_T is the spectrum temperature, comprised between 0.5 and 1 MeV for this experiment. About 10^{12} to 10^{13} photons/eV/steradian were detected with this process. Targets included both 1-mm-thick, 1-mm-diam, as well as 500-μm-thick, 25-μm-diam, tantalum pucks. The source size was measured by imaging an 800-μm-diam tungsten sphere onto HERIE and was found to be around a few 100 μm for the thick targets. Further shots are required to determine the effect of the target geometry on the source size.

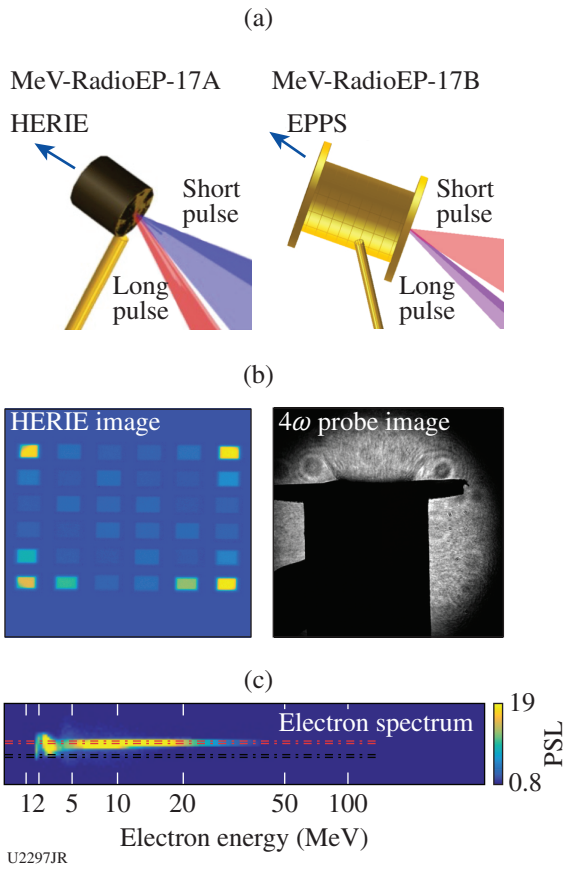

Figure 152.118
(a) Experimental configurations for the two shot days, (b) HERIE diagnostic image for MeV-RadioEP-17A and 4ω probe image, and (c) measured electron spectrum for MeV-RadioEP-17B.

The second campaign (MeV-Radio-EP-17B) aimed to look at an alternative electron production scheme (laser-wakefield acceleration in underdense plasmas) for future development of MeV photon sources on ARC. During this shot day, the 3- to 10-ps OMEGA EP short-pulse beams (alternately sidelighter and backlighter) were focused at intensities ~10^{18} W/cm^2 onto a 3-mm plastic gas tube filled with helium at atmospheric pressure. The gas tube was closed with 1-μm-thick mylar windows, which were blown down using an OMEGA EP long-pulse beam timed 5 to 10 ns before the short pulse. Plasma density at the entrance of the gas tube was monitored with the 4ω probe diagnostic. The main diagnostic, EPPS, measured accelerated electron energies up to 50 MeV.

Analysis of these campaigns is ongoing, and the results of the two shot days will be used to design efficient gamma-ray sources for LLNL programs.

Measurements of Instability Growth and Shell Trajectory Relevant to NIF Double-Shell Designs

Principal Investigator: Y. Ping
Co-investigators: V. A. Smalyuk, P. A. Amendt, R. Tipton, J. Pino, O. L. Landen, F. Graziani

The goal of this campaign is to measure instability growth rate and shell trajectory in planar geometry under conditions relevant to the double-shell design on the NIF. The target is a halfraum with an attached physics package consisting of an ablator, CRF foam, and a Cu inner shell. For the instability growth measurements, ripples with 30-μm and 60-μm periods and 0.5-μm amplitude were imprinted on the Cu inner surface, and face-on gated x-ray radiography was employed to measure the ripple growth over time. For the shell-trajectory measurements, side-on x-ray radiography with a streak camera was employed. The shot day was very successful with excellent data in both configurations, as shown in Fig. 152.119. Data analysis shows reasonable agreement with simulations on the ripple growth, yet the observed preheat of the Cu shell was underpredicted in the modeling. These results are being organized for publications and will also be used for target designs in FY18.

ACKNOWLEDGMENT

This work was performed under the auspices of the U.S. Department of Energy by Lawrence Livermore National Laboratory under contract DE-AC52-07NA27344.

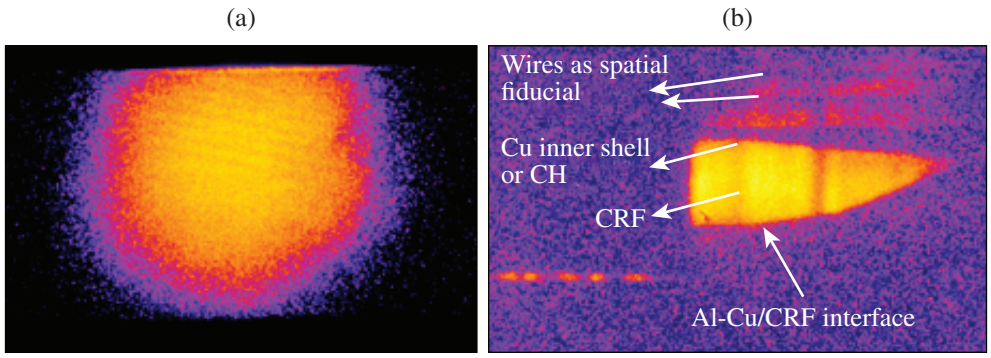

Figure 152.119
(a) A typical x-ray radiograph of ripple growth and (b) streaked x-ray radiograph of the shell trajectory.

FY17 LANL Report on Omega Facility Experiments

In FY17, Los Alamos National Laboratory carried out 17 shot days on the OMEGA and OMEGA EP Laser Systems in the areas of high-energy-density (HED) science and inertial confinement fusion (ICF). In HED our focus areas were on radiation flow, hydrodynamic turbulent mix and burn, warm-dense-matter equations of state, and coupled Kelvin–Helmholtz (KH)/Richtmyer–Meshkov (RM) instability growth. For ICF our campaigns focused on the Priority Research Directions (PRD's) of implosion phase mix and stagnation and burn, specifically as they pertain to laser direct drive (LDD). We also had several shot days focused on transport properties in the kinetic regime. We continue to develop advanced diagnostics such as neutron imaging, gamma reaction history, and gas Cherenkov detectors. The following reports summarize our campaigns, their motivation, and our main results from this year.

BeBoron

Shots were taken to measure the ablation rate of polyethylene to be evaluated for use as an ablator material for imploding capsules. Polyethylene was used at the last minute to replace Be:B flats that did not survive transportation, nor polishing. Polyethylene thin flats positioned at the end of the half-hohlraum and driven by the hohlraum radiation were used. This technique is similar to that used previously.[41,42] The shock breakout data gave us good measurements at 175 and 204 eV, with an ablation rate between 3 to 4 mg/cm^2/ns (Fig. 152.120).

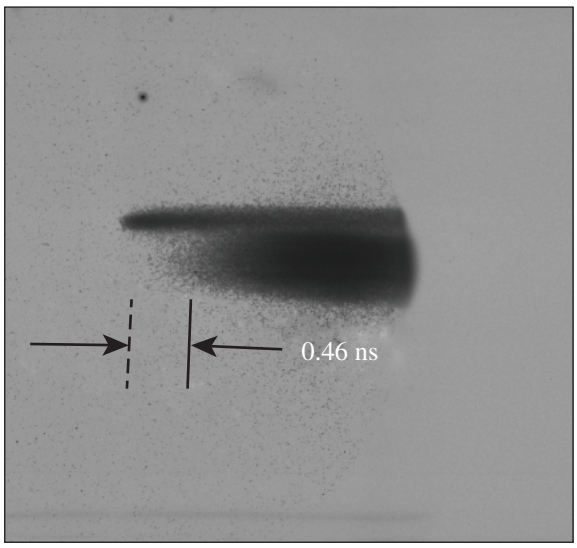

U2197JR

Figure 152.120
Shock breakout data from shot 84428.

Because of the poor reflectivity of the targets, only three shots gave data. Shot 84428 at 100-eV drive gave good VISAR data with a velocity reaching 30 km/s, with the data being consistent with a reflecting shock in the quartz (Figs. 152.121 and 152.122).

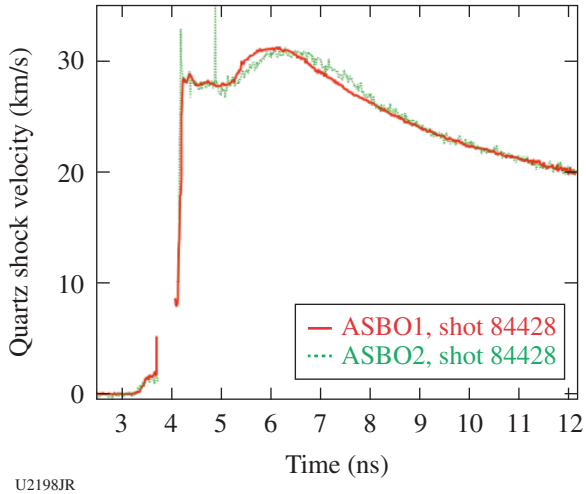

U2198JR

Figure 152.121
Analyzed VISAR data from shot 84428.

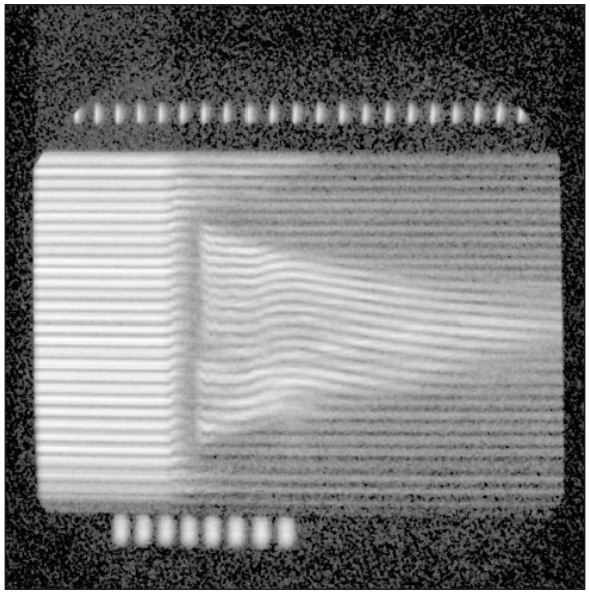

U2199JR

Figure 152.122
VISAR data from shot 84428.

COAX

The goal for COAX in FY17 was to complete platform development to prepare the way for addressing radiation-transport

physics questions in supersonic → subsonic fronts on OMEGA and the NIF. To accomplish this, COAX had three shot days in FY17. This platform uses a halfraum to launch a radiation front down a cylindrical target featuring a doped aerogel foam coaxially contained in an undoped aerogel and a Be sleeve. This target is point-projection backlit by a V foil and pinhole target to radiograph the density spike that occurs when the radiation front cools and hydrodynamic expansion exceeds the rate of radiation flow. A 600-μm CH capsule with 1.5-atm Kr fill is used to backlight the target earlier in time to collect the temperature of the supersonic front from the ionization balance of dopant revealed through K-shell absorption spectroscopy of 1s–2p and 1s–3p Ti or Sc. Dante is used to measure the halfraum temperature through the laser entrance hole (LEH). As the impedance offered by the foam to the radiation front is increased, the slope of the front increases. This provides a window into radiation-transport physics in the supersonic to subsonic regime, which is important for astrophysical objects such as supernovae.

In November 2016, COAX collected useful radiography data of the subsonic front. The spectroscopic backlighter still needed development work to achieve high-resolution Ti and Sc K-shell spectra. We tested a method for evaluating the temperature sensitivity of the platform: putting an 8-μm-thick Cu ring or "top hat" around the lower half of the doped foam. In Fig. 152.123 we observed the difference between two shots in which the doped foam's density was equivalent, but one target contained a top hat and the other did not. A simple examination of the data was shown at the 2016 APS DPP Meeting (Fig. 152.124).

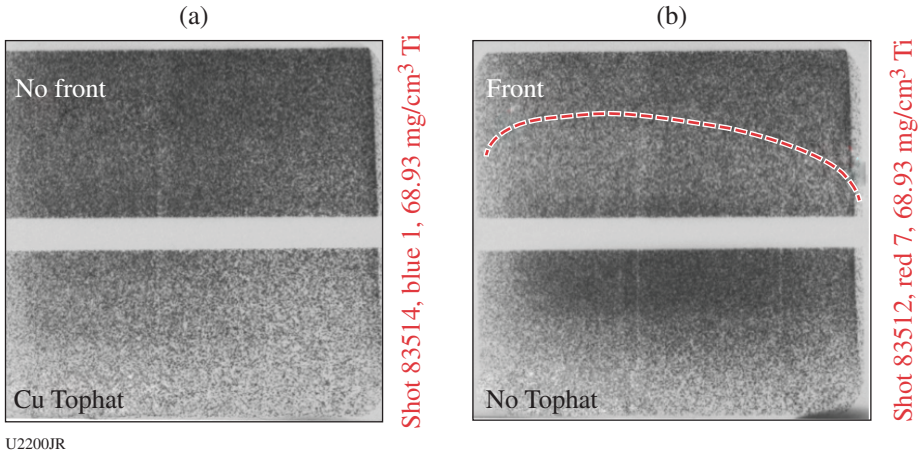

Figure 152.123
Comparison of COAX radiography from targets (a) with and (b) without the copper "top hat."

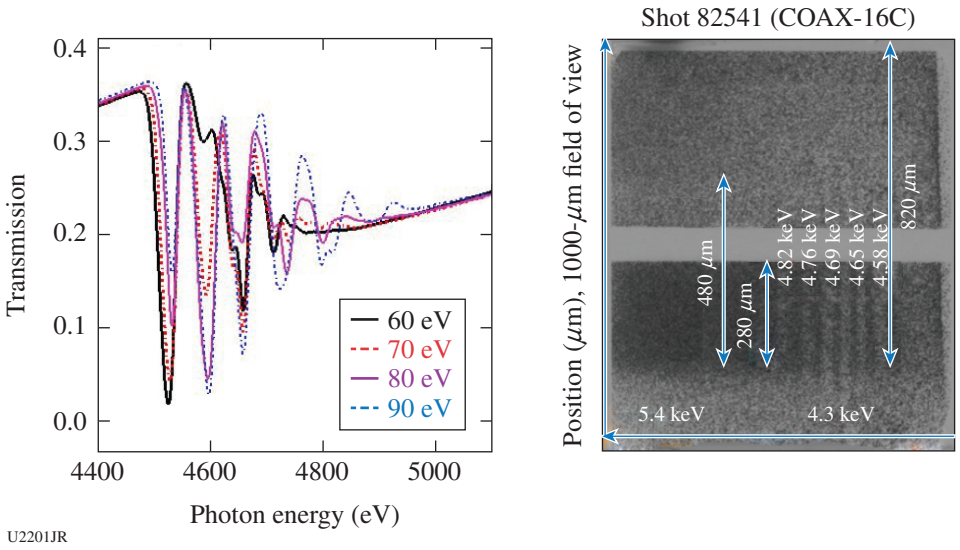

Figure 152.124
Data presented at APS DPP 2016 showing emission from the subsonic density spike superimposed on the spectral data.[43]

We observed emission from the subsonic density spike superimposed on the spectral data for the first time.

In May 2017 we collected high-resolution (~1000 resolving power) Ti and Sc spectroscopic data (Fig. 152.125). We tested a new design for the radiography backlighter, which unfortunately did not meet specification. The quality of the radiography was reduced as a result. We drove some targets with 600-ps and some with 1-ns square laser pulses to evaluate whether increased coasting time would improve the backlighter brightness. While that did occur, the physics target was much cooler than is typical because of the reduced drive energy. We repeated the observation of the subsonic front in the spectroscopic data with this higher-resolution, brighter spectra (produced as a result of improvements to the beam pointing for the capsule backlighter). A comparison between data from May and synthetic spectra produced with OPLIB in *PrismSPECT* was included in a presentation at the 2017 Anomalous Absorption Conference (Fig. 152.125).

In August 2017, we made a platform design change to move the physics target closer to target chamber center (TCC). This was partly to move the hohlraum back into the field of view for Dante and partly to improve backlighter flux through the physics target. We improved our design for the radiography V-foil backlighter and moved that target closer to TCC as well, to take advantage of the maximum drive range for the beams that this design allowed. We collected high-quality radiography and spectroscopy data with the new design (Fig. 152.126). We collected data at a sequence of times to study the transition between the supersonic and the subsonic flow over time. The times shown in Fig. 152.126 are the difference in time between the start of hohlraum drive and the time at which data were actually collected. At this year's APS DPP Meeting we will discuss early analysis results for this data, such as shown in Fig. 152.127. To address radiation-transport physics questions precisely enough to constrain radiation–hydrodynamics models, we need T_e uncertainty <5 eV and spatial uncertainty (from radiography) ~20 μm, which early analysis of our results

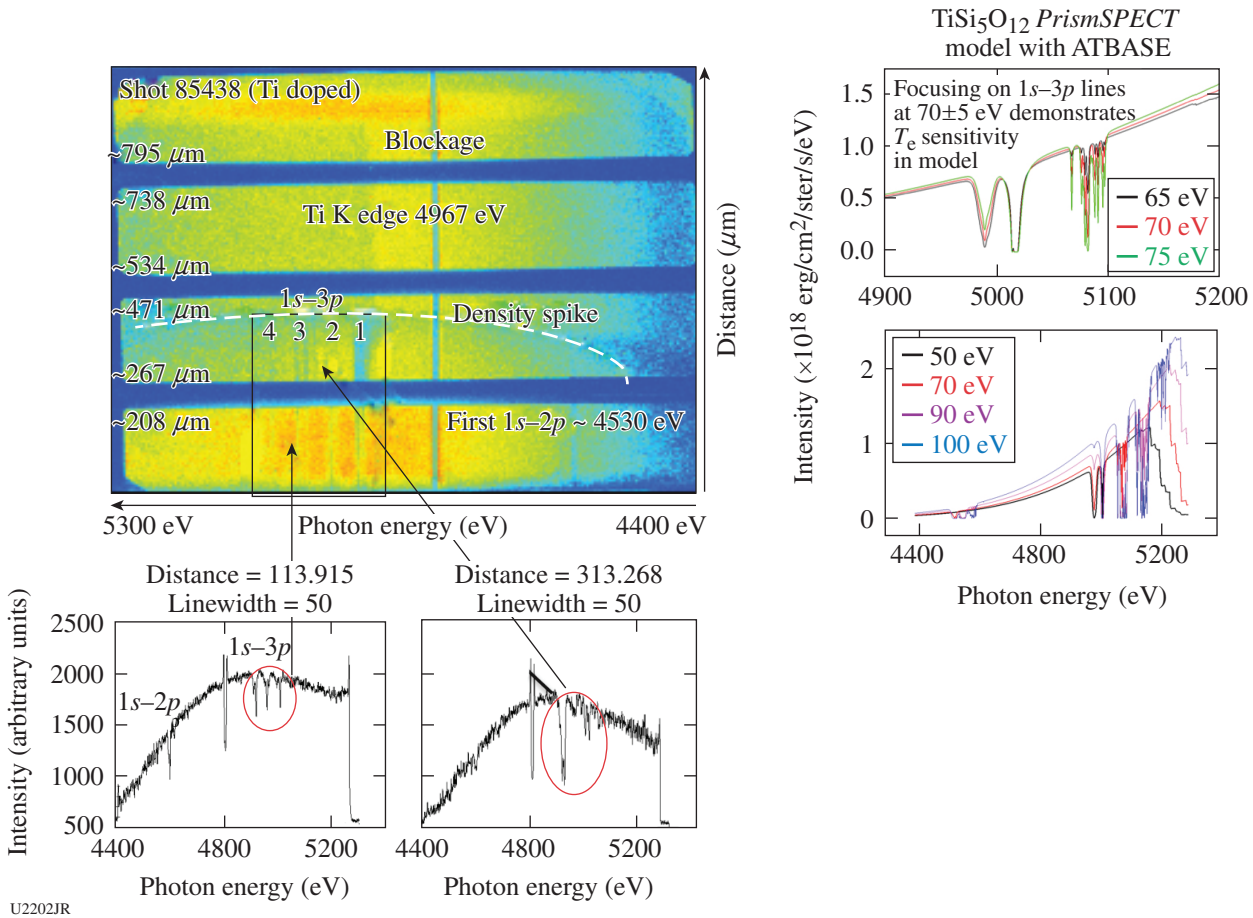

Figure 152.125
High-resolution Ti and Sc data with a comparison to synthetic data created using OPLIB in *PrismSPECT*.

(Fig. 152.127) implies we have achieved. Provided the rest of the analysis of the data from COAX-17B and COAX-17C is as promising, we will be starting the process for applying for NIF shots in 2018.

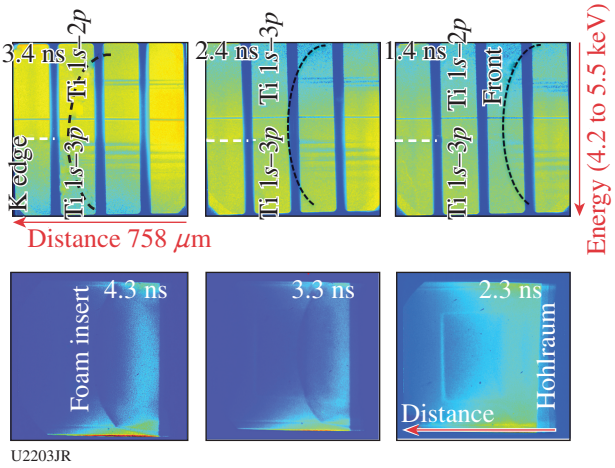

Figure 152.126
Improved data quality obtained using the modified platform developed in COAX-17C.

CylDRT

The first CylDRT/CylStalk shot day was scheduled on 29 August 2017. The main objective for this shot day was to measure the deceleration-phase Rayleigh–Taylor (RT) growth of the sine wave perturbations on the inner side of an aluminum marker layer in cylindrical geometry using face-on radiography. We are reviving the cylindrical problem after more than ten years on OMEGA. The cylinder is 250 μm longer than what was previously used because of the requirement to use SG5 phase plates. The Target Fabrication Group had to re-establish their capabilities including an outside vendor (AlumiPlate) for the marker layer coating. The goal is to measure the deceleration RT growth of the m = 10-mode sine wave inner perturbation on the aluminum marker layer.

Figure 152.128 shows the axial and transverse views of the cylindrical target. The cylinder was 2.5-mm long and had a 986-μm outer diameter. The inner diameter of the cylinder was 860 μm. In the middle and inner side of the cylinder was a 500-μm-long aluminum marker band, and the inner aluminum layer had sine wave perturbations mode 10 with 3-μm amplitude. Figure 152.129 shows the experimental geometry.

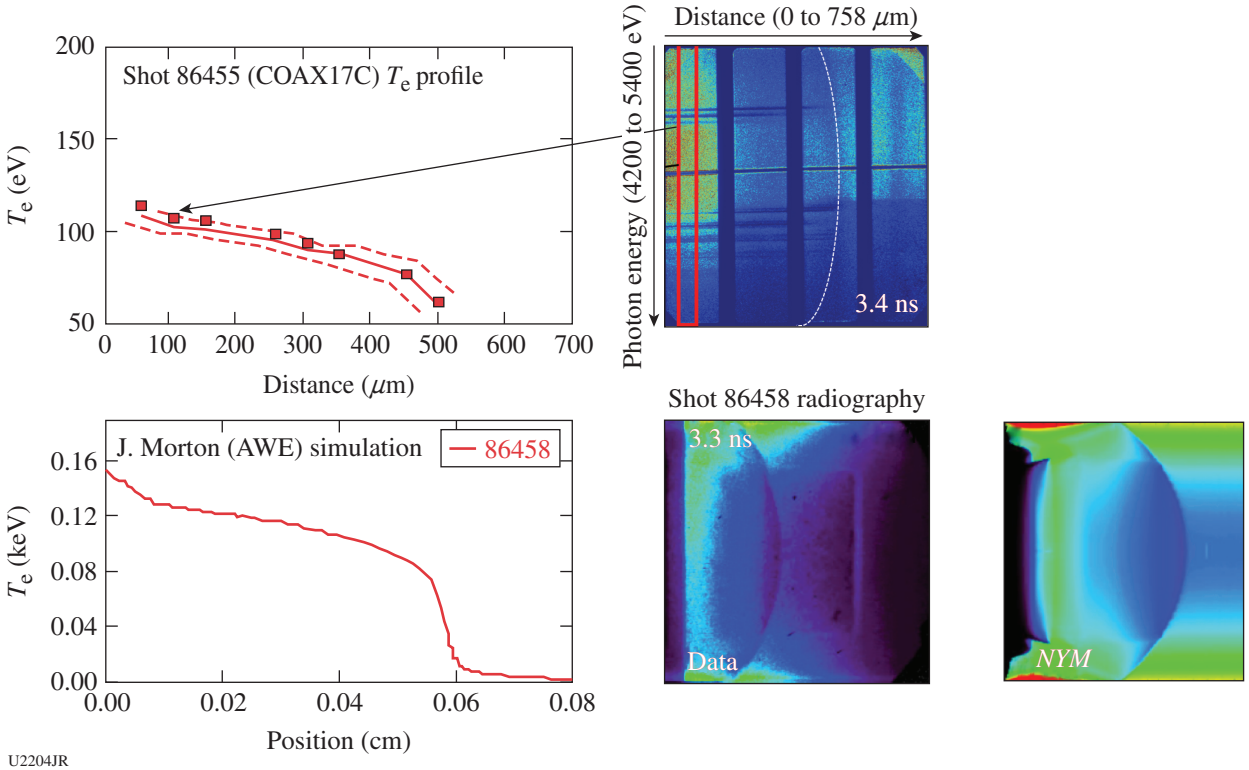

Figure 152.127
Electron temperature profiles obtained from the COAX data compared to simulations.

The cylinder was driven by 40 beams with a 1-ns square pulse. An iron or nickel backlighter was attached to the TIM-4 end of the cylinder. The x-ray framing camera was on TIM-6. We used 12× magnification with a 15-μm pinhole onto a four-strip framing camera. We also used a TIM-2/TIM-3 side imaging of the target to see the uniformity of the implosion.

Figure 152.130 shows the experimental image from a smooth target that had no sine wave perturbation for reference. Figure 152.131 shows the experimental image for a target with mode-10 sine wave. The preliminary analysis of the experimental results shows deceleration phase RT growth agreeing with hydro calculations.

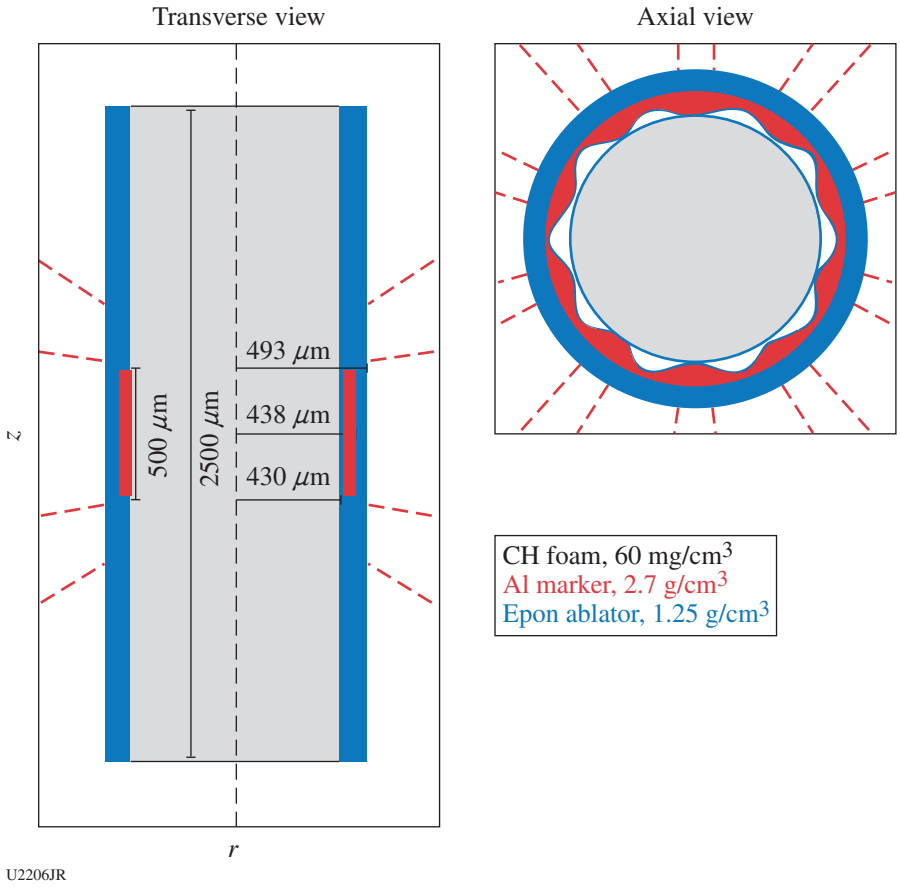

Figure 152.128
(a) Transverse and (b) axial views of the target.

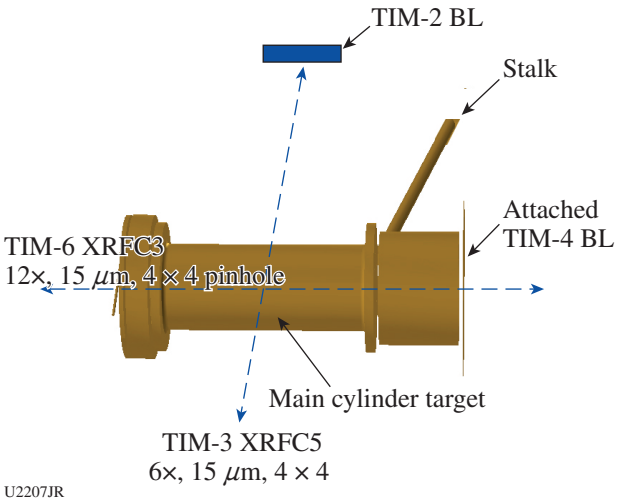

Figure 152.129
Experimental geometry for the CylDRT Campaign.

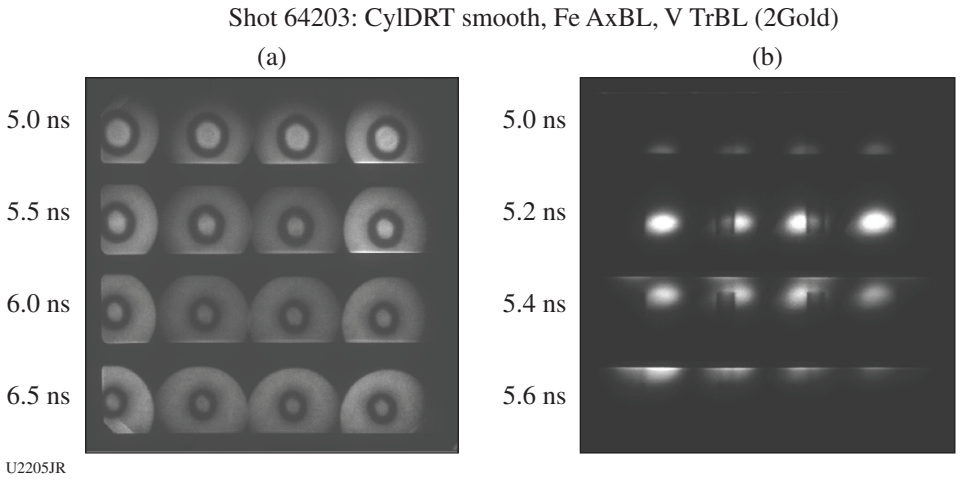

Figure 152.130
(a) Axial and (b) transverse x-ray radiographs of a smooth target.

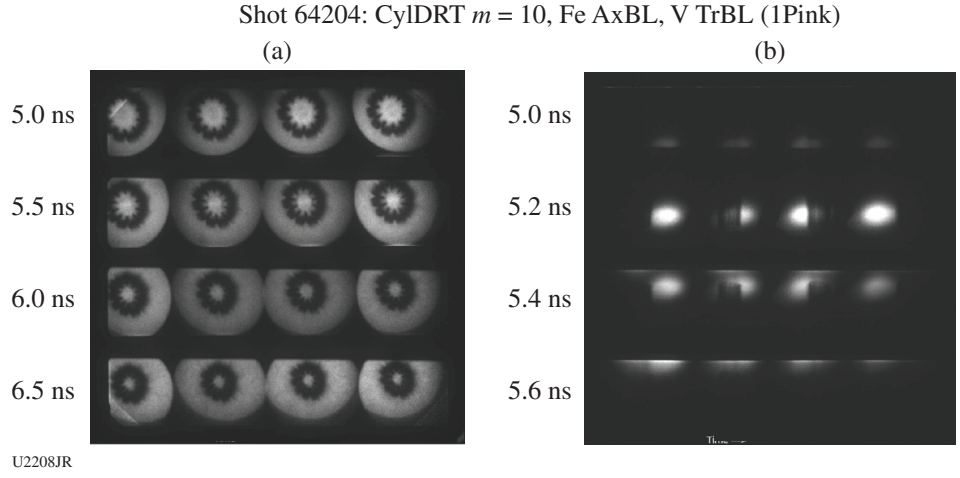

Figure 152.131
(a) Axial and (b) transverse x-ray radiographs of a mode-10 sine wave perturbation target.

DSPlanar

The Los Alamos Double-Shell team completed two planar double-shell (DSPlanar) experiments at the Omega Laser Facility in FY17. This campaign of experiments is part of the larger overall double-shell effort at Los Alamos, which is intended to test double-shell–relevant physics and materials in a planar geometry for ease of simulation and diagnosis. Specifically, these experiments are intended to validate our ability to predict hydro coupling, instability growth, with and without tamper mitigation, and the impact of target-fabrication artifacts such as fill tubes or joints in a double-shell target in the simplified planar geometry.

The first FY17 experiments examined momentum transfer during the ablator "inner shell" collision to benchmark *RAGE* simulations for similar systems. In these experiments, an indirectly driven ablator propagated down a shock tube [Fig. 152.132(a)] to impact a SiO_2 layer serving as an inner-shell surrogate. VISAR measurements [Fig. 152.132(b)] of the shock propagation, for pre- through post-ablator/layer impact, showed good breakout timing and average velocity agreement with pre-shot simulations.

The second FY17 shot day focused on studies of joint perturbation growth in support of NIF target-fabrication efforts.

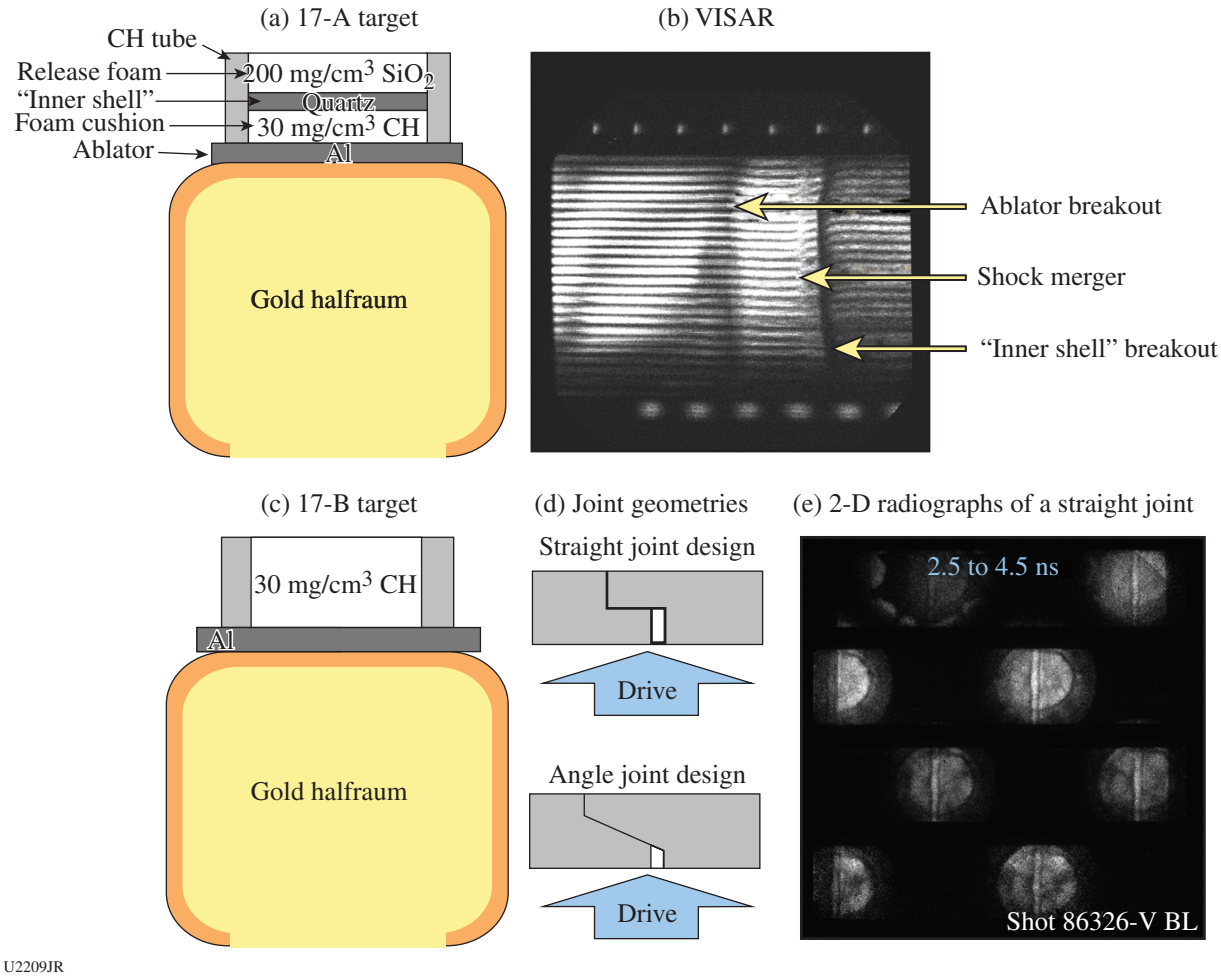

Figure 152.132
(a) Planar double-shell momentum transfer and (b) joint perturbation targets. (c) VISAR measurement of shock propagation, (d) schematic of joint propagation targets, and (e) radiographs of growth in a target with a straight joint.

These experiments again used indirectly driven ablators, but this time the ablator had a joint down the center. We varied the width of the joint gap as well as the geometry of the joint seam [Fig. 152.132(d)] for comparison to *RAGE* simulations. Early analysis suggests that *RAGE* simulations bound the observed joint growth rate and can serve to calculate an upper limit on the joint perturbation growth in a double-shell target.

HKMix

HKMix is a continuing LANL campaign to study mix physics in implosions between the fuel and shell, with the overarching goal of benchmarking models used in simulations of ICF and HED systems. These shots used 9- or 15-μm-thick, 860-μm-diam plastic shells with a thin deuterated (CD) layer in the shell and a HT gas fill. Using the LANL Cherenkov-based gamma ray detectors, both the HT (core) and DT (mix) burn histories can be measured.[44] The timing difference between mix and core burn is a novel constraint on modeling these implosions; good data were acquired, with analysis and interpretation ongoing.

These campaigns also used much thinner deuterated layers (0.15 μm) than past work, which enables higher resolution of the effect mix depth. Past work with 15-μm-thick shells could be explained using turbulence-based mix models, and these were used to predict the mix (DT) yield versus CD layer recession depth for these shots, shown by the green curves in Fig. 152.133. The data, however, show a dramatic 100× decrease in mix yield as the CD layer is recessed by only 0.3 μm. This trend cannot be explained by a turbulence-based model, but good agreement is found with a diffusion-based model (black curve).[45] At a 1-μm recession depth, the mix yield is observed to increase, indicating another "inversion" mix mechanism, potentially caused by a jet from the target support stalk.

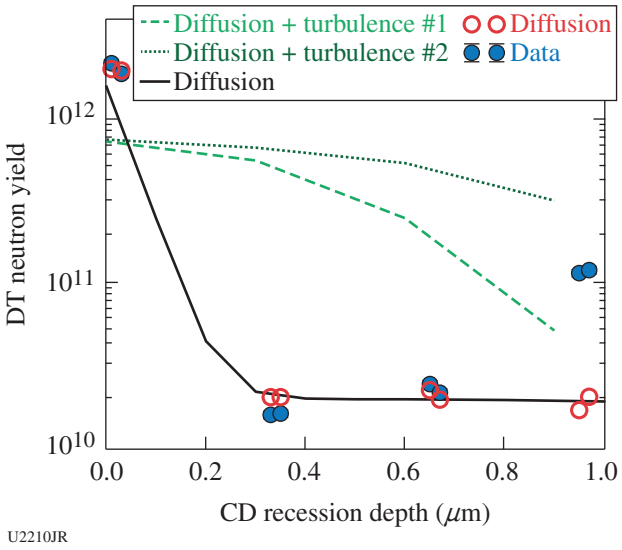

Figure 152.133
Mix (DT) yield versus CD layer recession depth compared to models.

IonSepMMI

In ICF experiments, interspecies ion separation is considered to be a candidate mechanism for yield degradation compared to radiation–hydrodynamic code predictions. This species separation could be driven by multispecies diffusive processes (e.g., thermodiffusion), as suggested by simulations employing recently implemented first-principles–based multi-ion–species transport models. The same physics also appears to drive ablator/gas mix in ongoing experiments focused on studying that problem.

Detailed analyses of x-ray–imaging spectroscopy data obtained from the earlier IonSepMMI-15A Campaign (in 2015) provided the first direct experimental evidence of interspecies ion separation in ICF experiments.[46,47]

To obtain the earlier results, we assumed 1-D spherical symmetry in the analysis procedure. In the recent IonSepMMI-17A Campaign (August 2017), we recorded x-ray–imaging spectroscopy data along three different lines of sight, which will allow us to analyze the data without needing to assume spherical symmetry and to perform 2-D/3-D reconstructions of spatial profiles of ion densities to infer ion species separation in the implosion core. We conducted 12 target shots with a high return of x-ray–imaging spectroscopy data on four target types of varying fill pressure and dopant (Ar) concentration. We also collected time-evolution data of both x-ray and DD-neutron reaction histories in collaboration with MIT, which fielded their PXTD diagnostic for this purpose. We anticipate improved observations of stronger and weaker interspecies ion separation as a function of target type. We are now processing and analyzing the x-ray spectroscopy data (Figs. 152.134 and 152.135). Further processing/analysis is being conducted to infer the spatial profile of argon concentration versus time, which is the smoking gun for whether species separation is occurring.

Results from these campaigns will add to our experimental database for validating first-principles models of multi-ion–species transport and diffusion that have been implemented in LANL ASC (advanced simulation and computing) codes. The latter will allow us to better quantitatively assess the impact of species separation that are initially mixed, as well as the mix of species that are initially separated (e.g., ablator/fuel) in ICF implosion performance.

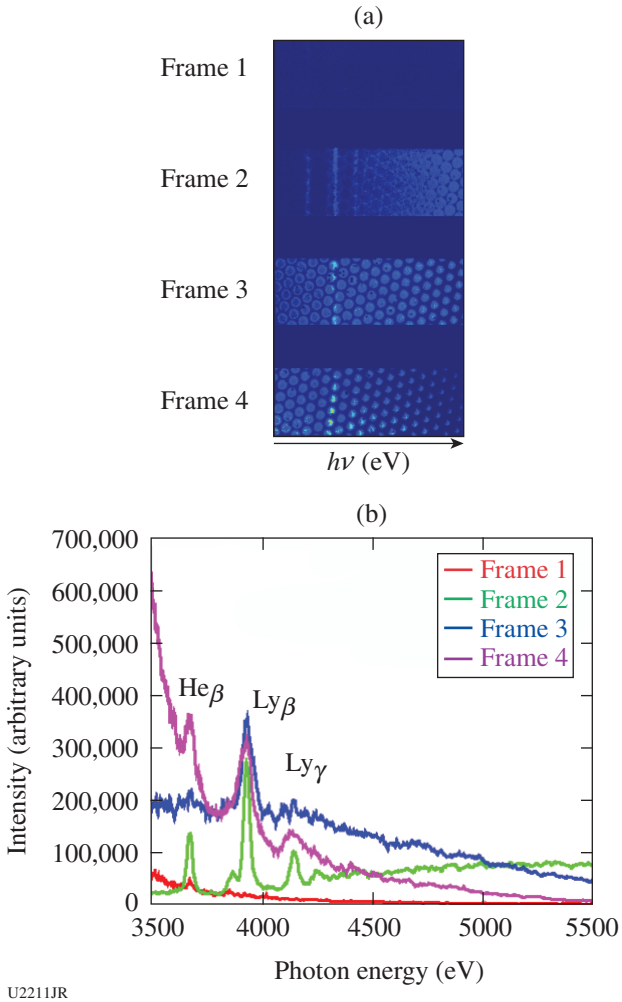

Figure 152.134
(a) Multi-monochromatic x-ray imager (MMI) data from shot 86678 (XRFC1, TIM-2) after processing and (b) space-integrated spectra from four frames of MMI (progressing in time, ~100-ps time interval between subsequent frames).

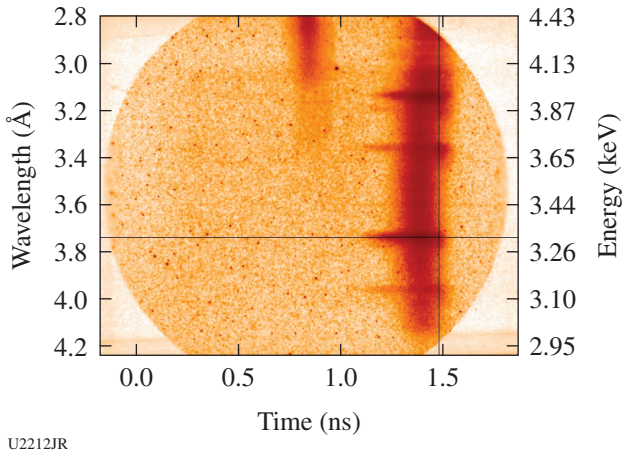

Figure 152.135
Streaked-crystal spectrometer (SSCA) data from shot 86678 (photon energy on vertical and time on horizontal axes, respectively).

Marble VC

The Marble Void Collapse Campaign was developed to address (1) fundamental issues relevant to understanding of Marble implosions on the NIF and (2) simulation capability of macro-pore engineered foams. This year, the Marble team refined a laser-driven shock-tube platform and tested two topics. First, shock propagation through macro-pore engineered foams were investigated to examine if the pore size affects shock speed. Three types of macro-pore engineered foams (<1, 50, and 90 μm in diameter) were used in shock-tube experiments driven by the OMEGA laser. X-ray radiographic data indicate that shock speed through macro-pore engineered foams depends strongly on foam density, less on pore size [Fig. 152.136(a)]. Data were successfully used to validate LANL simulation capability. Second, we designed a single foam-filled void (250 μm in diameter) [Fig. 152.136(b)] and shocked it from two opposing directions, aiming to increase turbulence at the spherical boundary and as a result induce magnetic fields. X-ray radiographic data show that while the first shock compressed a spherical foam-void without much turbulence, the time-delayed second shock seems to increase a turbulent motion. D^3He proton radiographic data (supported by the MIT group) were successfully obtained and are being analyzed.

MShock

The LANL MShock Campaign is studying the feedthrough of the RM instability in a thin layer, analogous to previous gas-curtain experiments. RM is relevant to mix in an ICF capsule where the ablative drive on capsule imperfections gives rise to RM and secondary shocks re-shock the linearly growing RM instability. It is known from fluids that such a re-shock can

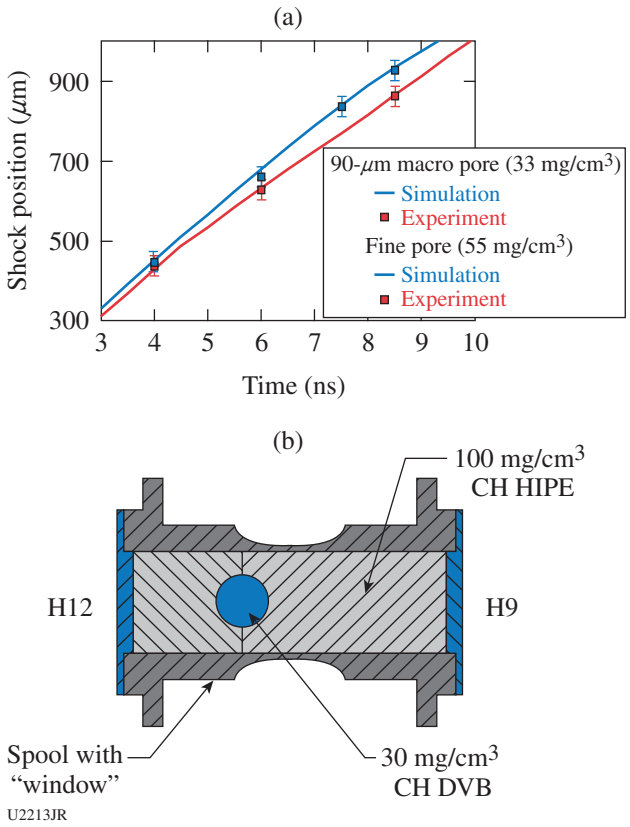

Figure 152.136
(a) Comparison of the simulated and measured shock position in fine-pore and 90-μm macropore foam and (b) the single-void target with the walls reduced in thickness to allow proton radiography of the shocked void. DVB: polystyrene/divinylbenzene.

drive RM to turbulence. The MShock platform utilizes a beryllium shock tube analogous to the previous Shear Campaign. A thin high-density layer ~10× denser than surrounding foam is located a short distance from the first drive ablator. Two opposing laser drives with a 3-ns time delay directly drive ablators on the opposite side of the shock tube. This allows for a growth period between the initial excitation of the RM instability and the re-shock. X-ray radiography is used to capture the evolving layer; mix-width measurements are compared with the LANL Besnard–Harlow–Rauenzahn (BHR) turbulence model.

FY17 was the first year of the MShock Campaign. The first shot day was focused on platform development and proof of concept for the target design. Data were collected to calibrate shock timings with simulations, and a new central doping technique applied to the high-density layer was verified (Fig. 152.137). In addition, the experiment showed no distortions of the mix layer, which had been previously observed in the OMEGA Re-shock Campaign. The second shot day focused on capturing time sequences for three surface perturbations

and collecting photometric data for dopants in the high-density layer. Preheat characterizations on this day showed that preheat effects are strong enough to affect surface profiles. Sufficient data were collected for one of the surface modes and nearly all data were collected for another. The results from both of these days will aid in preparing future experiments for both OMEGA and the NIF.

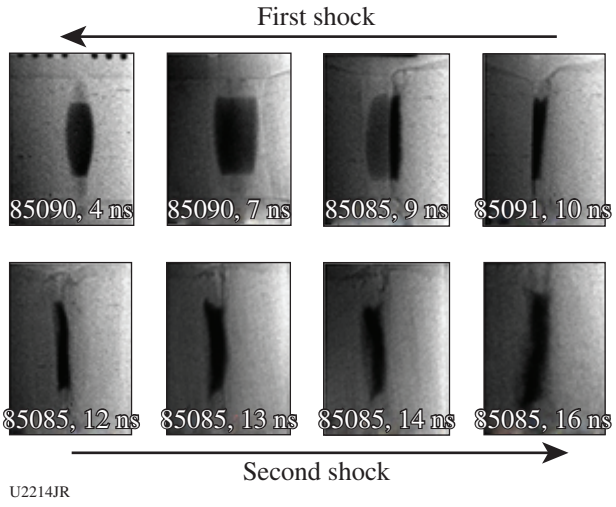

Figure 152.137
Data from a series of shots in the MShock Campaign.

Oblique Shock

The LANL Oblique Shock Campaign on OMEGA EP had two shot days in FY17 with a total of 14 shots. This campaign is designed to study the interplay between RM and KH hydrodynamic instabilities. It was conceived as a collaborative effort between LANL and the University of Michigan. The platform will also allow us to provide experimental input for testing and validation studies for turbulent transitional models like the LANL's modal model,[48] which will provide input for initial conditions for full turbulence models[49] like BHR.[50]

The first day was dedicated to testing (1) a 30-ns extended drive as an alternative to the typical 10-ns drive, and (2) the platform in a regime that more closely mirrors the University of Michigan'a hydro experiments on tilted interfaces (light to heavy). The Oblique Shock Campaign has been looking at shocks driven across an inclined (heavy-to-light) surface into a low-density foam (Fig. 152.138). Instead of three beams driving the target at one time, the three beams were stacked in time with 10 ns each, making a 30-ns train. In this configuration, the intensity driving the shock is reduced by a factor of 3, but the shock is supported for almost the entire experiment.

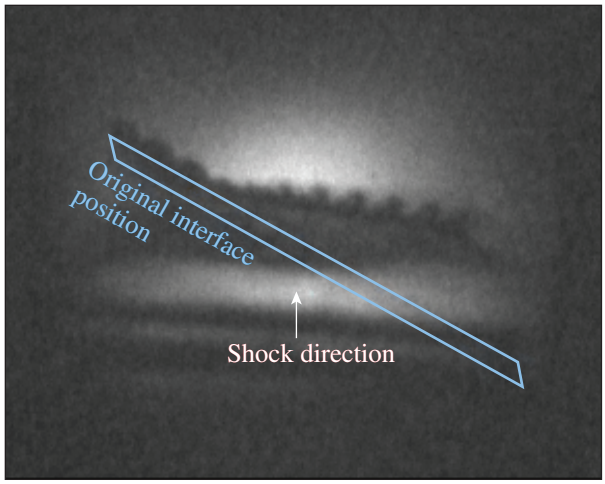

Figure 152.138
A two-mode interface undergoing shock with the original interface becoming flat with RM ripples on the front surface—an inversion of the original surface structure.

The current shots are intended to collect a time series of data that show how a two-mode perturbation on a heavy-to-light interface evolves with a sustained drive. This results in a later arrival time at the interface for the laser turn-off rarefaction, extending the time over which mixing-width growth can be considered to be predominantly caused by RM and KH growth. A two-mode interface was tested (Fig. 152.139) with the longer pulse, yielding a new data set for modeling.

The second shot day was dedicated to testing a new multimode surface to study the effects of mode coupling on the growth of the interface. The 10-ns drive focused three beams

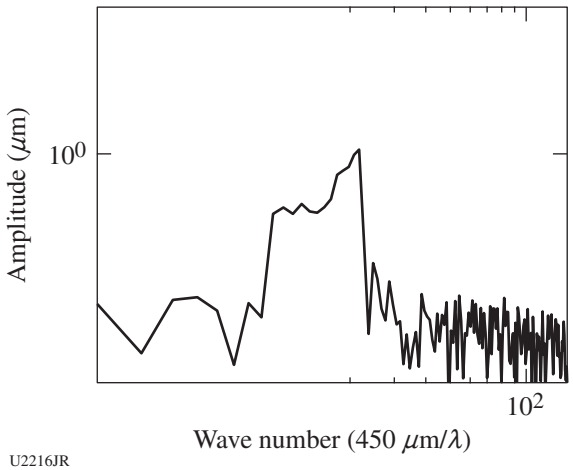

Figure 152.139
The machined interface of the single-band multimode spectrum in wavenumber space that was used as a seed for the RM instability.

on the ablator to drive a strong shock into the tube as in previous experiments; the setup was the same as Fig. 152.138. Figure 152.140 shows the imposed interface for studying mode coupling. The idea is for the mid modes to couple to the low modes, which would allow us to track the mode growth. The shot day showed very promising results; however, it also showed the limitations of our diagnostics and alignment procedures (Fig. 152.141). These are being enhanced for the next shot day to improve our resolution and contrast using a new Mn-He$_\alpha$ quartz asphere for the spherical crystal imager (SCI), which will allow us to use long-pulse (0.5- to 1-ns) beams to illuminate the backlighter targets; this in turn will allow us to produce far more x rays to view the layer and increase our resolution by using film instead of image plates. In the future, we will take advantage of the new SCI magnification (15×) to further increase resolution.

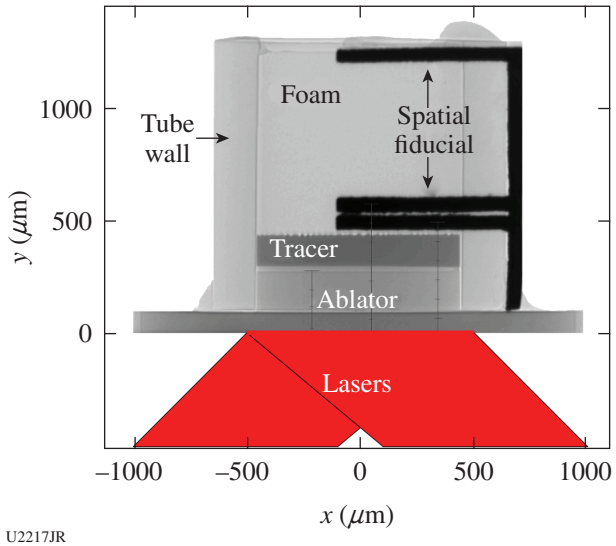

Figure 152.140
The Oblique Shock shock tube for OMEGA EP consists of a CH or Be tube with a CH ablator top hat, where laser energy is absorbed and launches a shock into the tube across the high-density tracer layer into the low-density foam.

WFEOS

The goal of the WFEOS-17A shot day was to study the equation of state (EOS) of wetted-foam material. The LANL ICF Program is conducting liquid layer implosions on the NIF, where the liquid is wicked into a supporting foam shell on the inner surface of the capsule. The implosion dynamics and performance are sensitive to the EOS of the mixed foam/DT material because it sets the implosion adiabat, but the EOS of such mixtures has not been measured. The WFEOS-17A Campaign used the planar cryogenic capability on OMEGA with the active shock breakout (ASBO)/streaked optical pyrometer

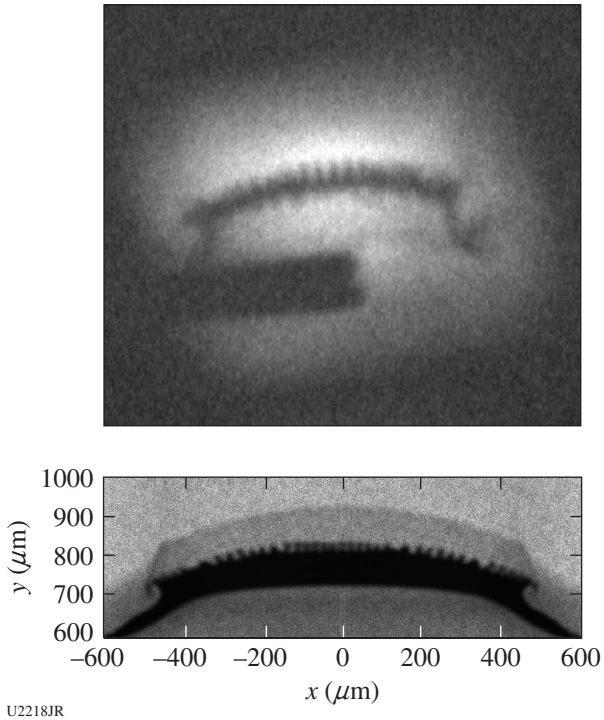

Figure 152.141
Experimental image of the single-band multimode interface on top and underneath the simulated image using *RAGE*.

(SOP) diagnostic to measure the shock propagation through a liquid-D_2 wetted foam. Good data were acquired on several shots. An example interferometry streak from VISAR on shot 85712 is shown in Fig. 152.142. In addition to the shock release

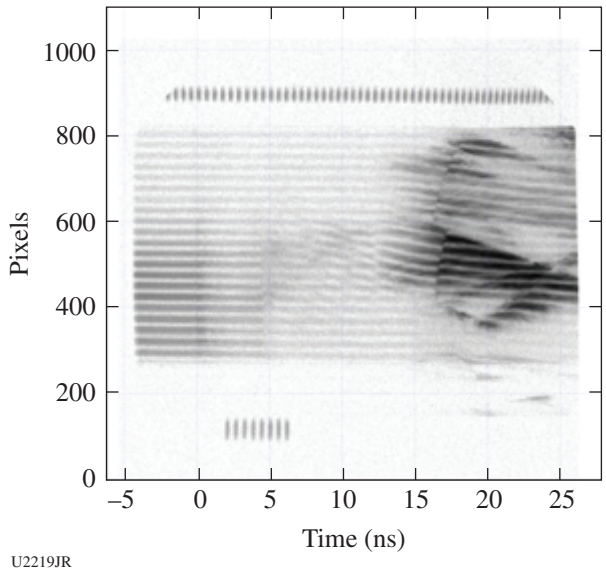

Figure 152.142
ASBO data from WFEOS-17A shot 85712.

from a high-density carbon pusher into the wetted-foam material, we observe a change in shock velocity at the wetted-foam interface with pure D_2, indicating a noticeable difference in the EOS of the two materials.

FY17 SNL Report on Omega Facility Experiments

MagLIFEP and MagLIFSNL

Principal Investigators: A. J. Harvey-Thompson, M. Glinsky, M. Weis, T. Nagayama, and K. Peterson (SNL); M. S. Wei, J. Fooks, E. Giraldez, and C. M. Krauland (General Atomics); E. M. Campbell, J. R. Davies, J. Peebles, R. E. Bahr, D. H. Edgell, C. Stoeckl, D. Turnbull, and V. Yu. Glebov (LLE); and J. A. Emig, R. F. Heeter, and D. Strozzi (LLNL)

The MagLIFEP and MagLIFSNL Campaigns at LLE operated by Sandia National Laboratories conducted a total of four shot days in FY17 (one on OMEGA and three on OMEGA EP) aimed at characterizing the laser heating of underdense plasmas (D_2, Ar) at parameters that are relevant to the magnetized liner inertial fusion (MagLIF) ICF scheme.[51,52] MagLIF combines fuel preheat, magnetization, and pulsed-power implosion to significantly relax the implosion velocity and ρR required for self-heating. Effective fuel preheat requires coupling several kilojoules of laser energy into the 10-mm-long, underdense (typically $n_e/n_c < 0.1$) fusion fuel without introducing significant mix. Barriers to achieving this include the presence of laser–plasma instabilities (LPI's) as laser energy is coupled to the initially cold fuel, and the presence of a thin, polyimide laser entrance hole (LEH) foil that the laser must pass through and that can be a significant perturbation.

Experiments, having different goals, were performed on the OMEGA and OMEGA EP lasers. The objectives of the OMEGA EP experiments were to develop a spectrometer capable of viewing Ne K-shell emission ($h\nu$ = 920 to 1100 eV), and to continue to investigate the effects of pulse shaping and LEH foil thickness on energy coupling. Capturing Ne spectra required developing a new spectrometer based on the spatially (in 1-D) and temporally resolved multipurpose spectrometer (MSPEC) design that used a KAP or RbAP with a maximized Bragg angle giving an observable energy range of 891 to 1773 eV (Ref. 53). In addition, modifications to the targets were required that allowed soft x rays to escape while still accommodating high-pressure (up to 10 atm) gas fills. This was achieved by machining up to five slots in the sides of the 115-μm-thick CH tube target and covering the slots with a 2-μm-thick polyimide foil, as shown in Fig. 152.143(a). Capturing Ne spectrum was challenging but was achieved as shown in Fig. 152.143(b). The instrument should allow one to observe cooling of the plasma after the laser has turned off, potentially facilitating the study an applied magnetic field's effect on the electron thermal conduction and cooling process.

The objective of the OMEGA laser experiments was to compare energy coupling into underdense D_2 plasmas with 2ω

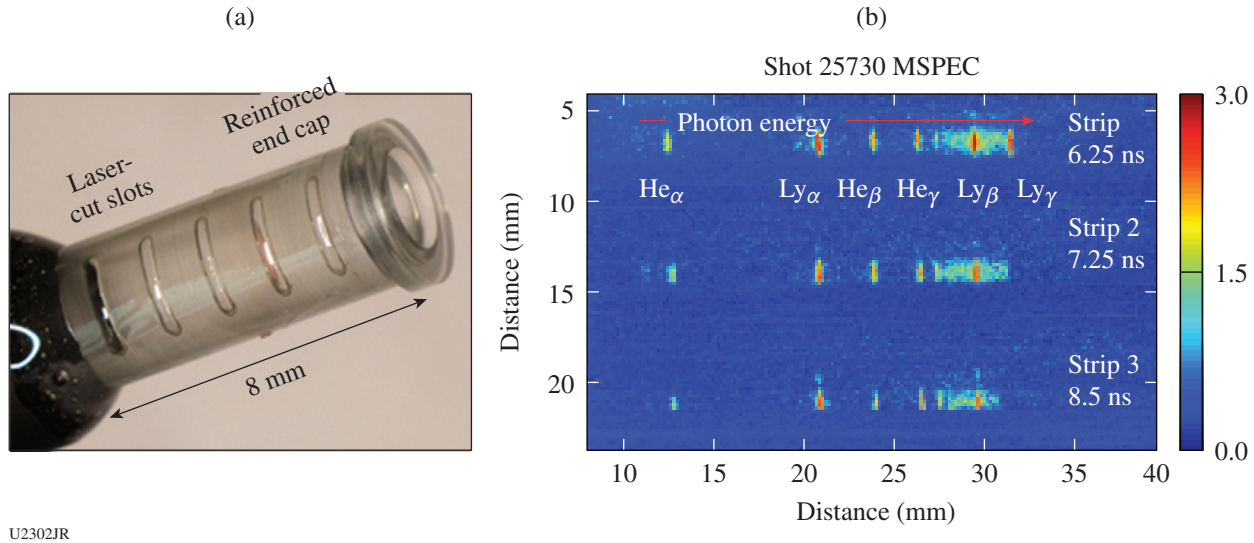

Figure 152.143

(a) Photograph of an OMEGA EP target with five side-on windows covered with a 2-μm polyimide foil capable of holding 10 atm and (b) a spectrum captured with the Ne multipurpose spectroscopy snout (MSPEC) on shot 25730 from MagLIFEP_17B showing the observed multiple Ne K-shell lines.

and 3ω beams, with and without smoothing by spectral dispersion (SSD), and for different beam intensities. This shot series was the first Sandia-led effort to investigate preheat on this laser, and, as such, scaled-down versions of the OMEGA EP targets were required because of the reduced energies per beam available (~450 J max compared to >3 kJ on OMEGA EP). Of particular interest in this series was the effect that changing the laser wavelength, intensity, and smoothing had on-beam propagation and on-stimulated Brillouin scattering (SBS) and stimulated Raman scattering (SRS) levels. The results suggest that for similar intensities and similar values of n_e/n_c, the laser wavelength has a significant effect on the beam propagation, as measured by x-ray framing camera (XRFC) imaging [Fig. 152.144(a)], and on LPI levels, as inferred by hard x-ray signal levels [Fig. 152.144(b)], while SSD has little impact. The results have implications for the future of MagLIF laser preheat, which currently uses a 2ω laser and is susceptible to significant LPI at relatively low intensities. The data suggest that a 3ω laser could make preheat possible at higher intensities for given plasma parameters while minimizing LPI, ensuring that greater energy coupling could be possible over a given propagation distance.

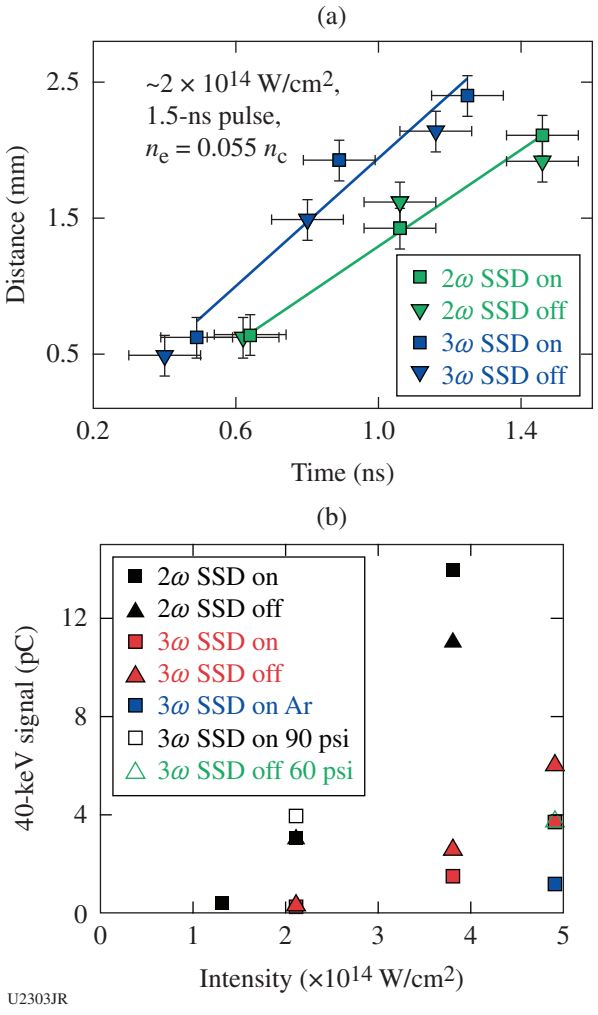

Figure 152.144
(a) Emission depth as a function of time measured from time-gated XRFC images for 2ω and 3ω light with SSD on and off and (b) hard x-ray signal levels as a function of intensity for the various parameters tested in the experiment.

ACKNOWLEDGMENT

Sandia National Laboratories is a multi-mission laboratory managed and operated by National Technology & Engineering Solutions of Sandia, LLC, a wholly owned subsidiary of Honeywell International, Inc., for the U.S. Department of Energy's National Nuclear Security Administration under contract DE-NA0003525.

FY17 NRL Report on Omega Facility Experiments

During FY17, an NRL/LLE collaboration on laser imprint led to three successful shot days on OMEGA EP. The experiments showed that the application of a prepulse that preexpands and lifts off the coating prior to the arrival of the main laser pulse gives an order-of-magnitude reduction of laser imprint, as expected on the basis of the original experiments on the Nike laser and understanding the mechanism of the imprint suppression (Fig. 152.145). Further experiments demonstrated imprint reduction with prepulse times compatible with pulse durations available for implosions on the Omega 60-beam laser. Moreover, we were able to utilize thinner coatings, minimizing the risk of fuel preheat and increasing the chances that they will be compatible with low-adiabat, thin-ablator shell implosions on OMEGA.

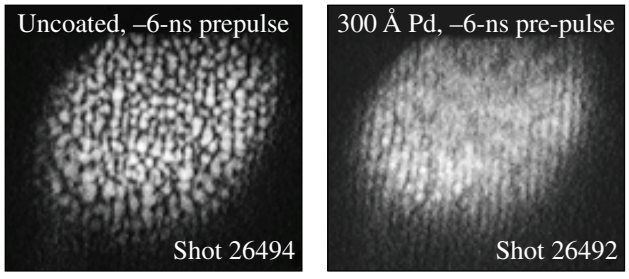

Figure 152.145
Measurements on OMEGA EP showing a reduction in laser imprint with a thin Pd coating. (a) An accelerated uncoated plastic foil broken up by Rayleigh–Taylor instability amplified laser imprint. (b) With a thin palladium coating, the target maintains integrity and the regular ripple structure preimposed on the foils becomes evident.

FY17 CEA Report on Omega Facility Experiments

Experimental Investigation of the Collective Stimulated Raman and Brillouin Scattering of Multiple Laser Beams in Inertial Confinement Fusion Experiments

Principal Investigators: C. Neuville, S. Depierreux, V. Tassin, M.-C. Monteil, P.-E. Masson-Laborde, P. Fremerye, F. Philippe, P. Seytor, D. Teychenné, M. Casanova, A. Debayle, P. Loiseau, and G. Tran (CEA-DAM-DIF); C. Baccou, C. Labaune, and C. Riconda (LULI); D. Pesme, S. Hüller, and A. Heron (Centre de Physique Theorique); V. Tikhonchuk, A. Colaitis, G. Duchateau, and P. Nicolaï (CELIA); N. Borisenko and A. Orekhov (Lebedev Physical Institute); and R. Bahr, J. Katz, C. Stoeckl, and W. Seka (LLE)

In the direct- and indirect-drive approaches to inertial confinement fusion, the megajoule laser energy is delivered through tens of beams grouped by cones—a regular arrangement that intrinsically includes principal directions for the amplification of laser–plasma instabilities (LPI's) by multiple beams. In this way, a collective instability can develop when all the incident laser waves located in a cone couple to a same daughter wave growing along the cone's symmetry axis. These collective effects were theoretically studied in the 1990s (Ref. 54) and evidenced for the two-plasmon decay in direct-drive experiments performed on OMEGA.[55–57] Similar collective multibeam coupling may be expected for the stimulated scattering instabilities, namely stimulated Brillouin scattering (SBS) and stimulated Raman scattering (SRS), in which the incident laser waves resonantly couple with ion acoustic waves (IAW's) or electron plasma waves (EPW's) to amplify scattered light waves. As in the single-beam configuration, the collective scattering instabilities can reduce the coupling efficiency of the beams with the target, accelerate copious amount of hot electrons, and modify the symmetry of the implosion. Additionally, the convective gain for the collective instabilities is increased compared to the single-beam instability, leading to expected higher levels of scattering. Another aspect of collective instabilities concerns its sidescattering geometry that results in the emission of the scattered light in novel directions compared to backscattering.

Multibeam effects in LPI at the megajoule scale were first considered through the cross-beam energy transfer between two beams that was used to adjust the symmetry of irradiation.[58,59] Recent experiments performed in near-vacuum hohlraums have revealed another multibeam effect, namely the electromagnetic seeding[60–62] of the sidescattering for some beams by the backscattering or transmission of additional beams.[63] The issue of collective scattering instabilities has recently become an emerging field with several reported experimental studies. In this context, two experiments have been performed on OMEGA to investigate collective SRS[64] and collective SBS.[65] The SRS of two beams has been evidenced in an inhomogeneous plasma produced in an open planar geometry where the significant amplification of the Raman light at large angles from the density gradient has been observed for the first time. The collective Brillouin amplification of shared IAW's has been observed in indirect-drive experiments using a rugby-ball–shaped hohlraum. In both types of experiments, the flexibility of the Omega Laser Facility and its large battery of diagnostics have played a critical role toward the physical understanding of the collective mechanisms.

The first experiment was performed to investigate the collective SRS produced by two beams sharing a common electromagnetic daughter wave in an inhomogeneous plasma. The targets were 7-mg/cm^3 $C_{12}H_{16}O_8$ foams with a diameter of 2.5 mm and a length of 950 μm aligned along the H3–H18 axis of the OMEGA target chamber. The laser beams were focused by f = 6.7 lenses through elliptical phase plates, producing spot sizes with a 200 × 300-μm diameter [full width at half maximum (FWHM)]. These beams were fired at an energy level of 400 J in a 1-ns square pulse. Twelve beams were used, incident at 60° from the foam axis, making a six-beam cone on each side of the target, as is illustrated for the H18 side in Fig. 152.146(a). After ~0.5 ns, the regions of foam ionized by the different beams of the same cone began to superimpose.

Figure 152.146(b) shows a typical measurement with the near-backscatter imager (NBI) of the time-integrated angular distribution of the light scattered in the Raman wavelength range (450 to 900 nm) around the midplane of Beamlines 45 and 50 with angles between 20° and 60° from the target normal. The SRS signal was maximum in the bisecting plane of beams 45 and 50 at angles between 42° and 54° from the target normal, close to the full-aperture backscatter station of Beamline 25 (FABS25). Figure 152.146(c) shows the time-resolved spectrum of the light scattered in this direction collected in an aperture of ±4° in FABS25 for the same shot. The SRS signal started at $t \sim 0.5$ ns, as soon as the beams started overlapping in the foam plasma. It lasted until the end of the laser pulses with an almost constant wavelength of $\lambda_{SRS} \sim 600$ nm, corresponding to the electron density (~0.17 n_c) in the region of beam overlap.

This observation in vacuum of the SRS scattered light at ~48° from the target normal corresponds to SRS light produced at ~80° from the density gradient in the plasma region of interaction. This optimum angle results from the increase of

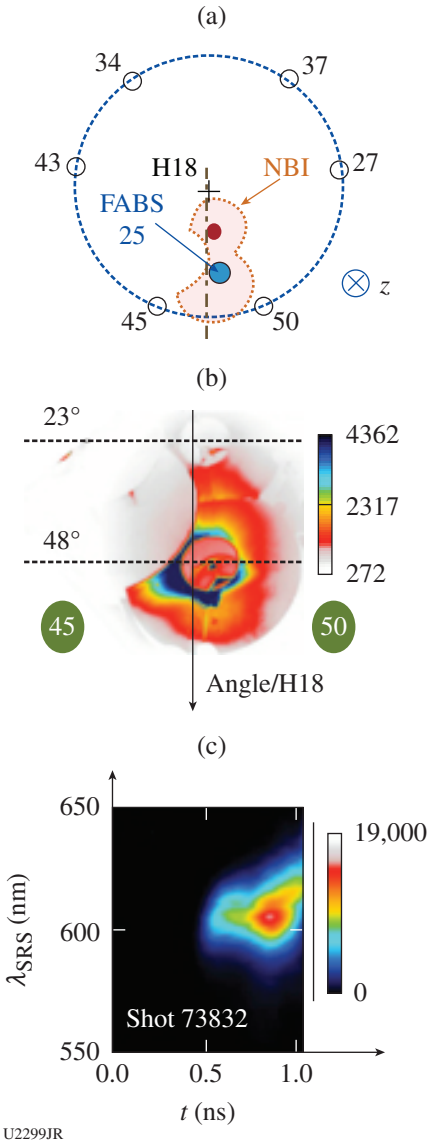

Figure 152.146
(a) Angular distribution of the six beams incident on the H18 side and scheme of the near-backscatter imaging (NBI) diffuser plate. (b) Typical image recorded with the NBI diagnostic for a 7-mg/cm^3 foam. (c) Time-resolved spectrum of the stimulated Raman scattering (SRS) light collected in the direction of FABS25 (full-aperture backscatter station) in the same shot as for (b).

the SRS collective gain partly compensated by the increased collisional absorption of the SRS signal as the light is scattered at larger angles from the density gradient. Absolute energy measurements performed in a calorimeter in this same direction indicated that the SRS losses associated with this signal maximized at ~5% of the power available in one beam. Last, the initial scattering angle ~80° is in good agreement with the hot-electron generation inferred from hard x-ray emission, giving a hot-electron temperature of 20 keV compared to an expected temperature of 25 keV.

The collective nature of the coupling and the amplification at large angles from the density gradient are found to increase the global SRS losses and to produce light scattered in novel directions outside the planes of incidence of the two beams. The mechanism evidenced in this experiment can occur in both direct- and indirect-drive experiments between any pair of beams. Such a collective amplification of a common scattered-light wave has been proposed to explain the large amount of SRS measured in the NIF indirect-drive experiments.[66] It results in an underestimation of the scattered-light losses because this red-shifted Raman light experiences significant refraction and absorption before exiting the plasma and in the acceleration of hot electrons, which can preheat the capsule.

The second experiment was performed to investigate collective Brillouin scattering in indirect-drive experiments. The interaction was studied at the laser entrance hole (LEH) of rugby-ball–shaped hohlraums filled with 1 atm of methane gas. The revolution axis of the hohlraum was aligned along the P5–P8 axis of the OMEGA target chamber. Twenty laser beams were incident on each side of the target distributed along three cones [see Fig. 152.147(a)]: five beams, at 21° from the axis, were pointed at 500 μm from the window outside the hohlraum; similarly, five beams at 42° and ten beams at 59° were pointed at the LEH. The beams were focused by $f = 6.7$ lenses through random-phase plates, producing focal spots with a diameter of 300-μm FWHM. The laser pulse, with a total duration of 2.5 ns, was made of a prepulse of intensity ~8×10^{13} W/cm^2 per beam followed by a main pulse for $t = 1.8$ to $t = 2.3$ ns at an intensity per beam of 5×10^{14} W/cm^2. The plasma conditions were characterized thanks to thermal Thomson-scattering (TS) measurements performed at the LEH and at 300 μm from the LEH outside the hohlraum as illustrated in Fig. 152.147(a).

The scattered light was collected in the backward direction of one beam of the 59° cone (Beamline 30) and one beam of the 42° cone (Beamline 25) and analyzed in time and wavelength by full-aperture backscatter stations (FABS30 and FABS25). Figure 152.147(b) shows a typical spectrum measured in FABS30. For the time interval (1.8 ns to 2.4 ns), when the laser intensity was close to its maximum, two contributions were detected in FABS30. The first signal, starting at $t = 1.8$ ns, was caused by Brillouin backscattering of Beamline 30 developing in the plasma inside the hohlraum. The backscattering was identified in the single-beam linear gain calculations performed by post-processing the hydrodynamics simulations. It simply

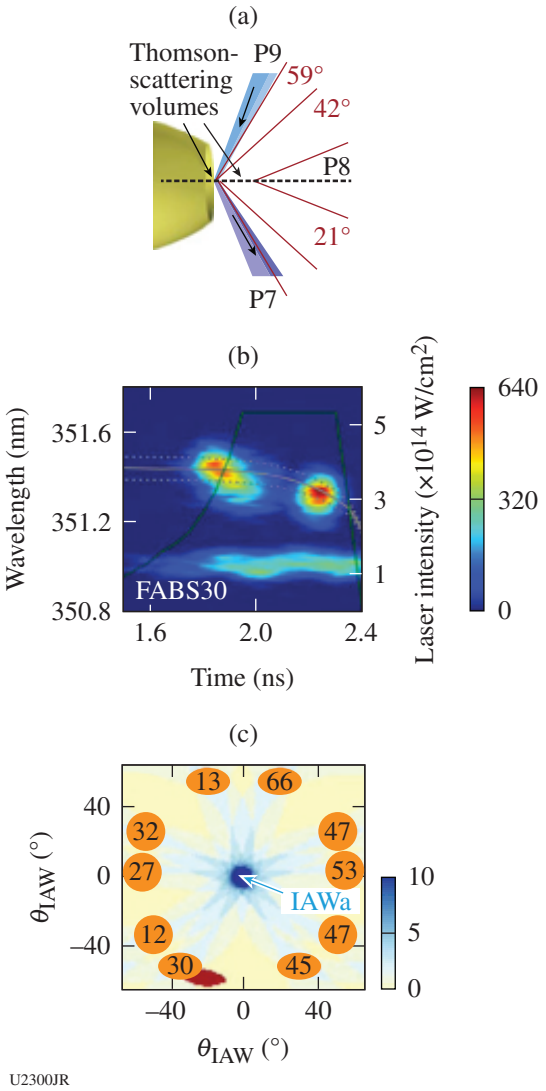

Figure 152.147
(a) Representation of the laser entrance hole (LEH) showing three cones of heater beams and the geometry of the Thomson-scattering (TS) diagnostic. (b) Time-resolved spectrum of the scattered light collected in the backward direction of Beamline 30. The gray lines represent the wavelength range calculated for the light scattered by Beamline 66 in the FABS30 direction off the collective IAW driven along the hohlraum axis by the ten-beam instability. (c) The direction of the IAW's having equal wave vectors are shown with respect to the ten laser beams of the 59° cone. A collective IAW is driven in each of the directions where multiple beams contribute. In the direction indicated as IAWa, the ten beams amplify the corresponding IAW. The region shown in red represents the scattering direction of Beamline 66 off IAWa.

depended on the energy of the beam itself. The origin of the second signal, observed after t = 2.2 ns, was different since we observed that the variations in time and amplitude were dependent on the energy of the other cone of crossing beams. This signal extended over a very narrow spectral range, corresponding exactly to the wavelength expected as a result of the Thomson-scattering measurements for the light scattered by Beamline 66 off the collective IAW's generated by the ten beams at 59° [IAWa in Fig. 152.147(c)]. The observation of a sidescattering signal peaked in wavelength was a strong indication of multibeam effects. In a different experiment, using a different pointing[67] of the ten beams of the 59° cone to improve the uniformity of irradiation on the hohlraum wall, significant spectral broadening of this second signal was observed as expected from the widening of the crossing volume of the ten beams of the 59° cone.

The absolute energy measurements performed in the FABS made it possible to evaluate the energy losses caused by the collective SBS instability of the 59° cone. To do so, we first considered the geometry of the scattering, taking into account the aperture of the beams and the diagnostic. The geometry of the SBS of Beamline 66 in the collective instability that drove the IAW along the hohlraum axis (IAWa) is shown in Fig. 152.147(c), assuming straight-line propagation of the light in front of the crossing-beam region at LEH. Its analysis showed that only a small fraction (<1/15) of the scattered light was collected in the FABS. The signal associated with the collective instability of the ten beams peaked at ~3% of the laser power per beam, but we estimate that the scattering losses may be 10× higher than those directly measured in the FABS. Therefore, collective Brillouin scattering can result in high scattering amplitude and significantly impair the laser–target coupling in indirect-drive experiments.

REFERENCES

1. D. B. Schaeffer, W. Fox, D. Haberberger, G. Fiksel, A. Bhattacharjee, D. H. Barnak, S. X. Hu, and K. Germaschewski, Phys. Rev. Lett. **119**, 025001 (2017).

2. D. B. Schaeffer, W. Fox, D. Haberberger, G. Fiksel, A. Bhattacharjee, D. H. Barnak, S. X. Hu, K. Germaschewski, and R. Follett, "High-Mach Number, Laser-Driven Magnetized Collisionless Shocks," submitted to Phys. Plasmas.

3. G. Fiksel, W. Fox, A. Bhattacharjee, D. H. Barnak, P.-Y. Chang, K. Germaschewski, S. X. Hu, and P. M. Nilson, Phys. Rev. Lett. **113**, 105003 (2014).

4. L. Willingale, P. M. Nilson, A. G. R. Thomas, J. Cobble, R. S. Craxton, A. Maksimchuk, P. A. Norreys, T. C. Sangster, R. H. H. Scott, C. Stoeckl, C. Zulick, and K. Krushelnick, Phys. Rev. Lett. **106**, 105002 (2011).

5. L. Willingale, A. G. R. Thomas, P. M. Nilson, H. Chen, J. Cobble, R. S. Craxton, A. Maksimchuk, P. A. Norreys, T. C. Sangster, R. H. H. Scott, C. Stoeckl, C. Zulick, and K. Krushelnick, New J. Phys. **15**, 025023 (2013).

6. S. Brygoo, M. Millot, P. Loubeyre, A. E. Lazicki, S. Hamel, T. Qi, P. M. Celliers, F. Coppari, J. H. Eggert, D. E. Fratanduono, D. G. Hicks, J. R.

Rygg, R. F. Smith, D. C. Swift, G. W. Collins, and R. Jeanloz, J. Appl. Phys. **118**, 195901 (2015).

7. H. Sio, R. Hua, Y. Ping, C. McGuffey, F. Beg, R. Heeter, C. K. Li, R. D. Petrasso, and G. W. Collins, Rev. Sci. Instrum. **88**, 013503 (2017).

8. M. Gatu Johnson, A. B. Zylstra, A. Bacher, C. R. Brune, D. T. Casey, C. Forrest, H. W. Herrmann, M. Hohenberger, D. B. Sayre, R. M. Bionta, J.-L. Bourgade, J. A. Caggiano, C. Cerjan, R. S. Craxton, D. Dearborn, M. Farrell, J. A Frenje, E. M. Garcia, V. Yu. Glebov, G. Hale, E. P. Hartouni, R. Hatarik, M. Hohensee, D. M. Holunga, M. Hoppe, R. J. Janezic, S. F. Khan, J. D. Kilkenny, Y. H. Kim, J. P. Knauer, T. R. Kohut, B. Lahmann, O. Landoas, C. K. Li, F. J. Marshall, L. Masse, A. McEvoy, P. McKenty, D. P. McNabb, A. Nikroo, T. G. Parham, M. Paris, R. D. Petrasso, J. Pino, P. B. Radha, B. Remington, H. G. Rinderknecht, H. Robey, M. J. Rosenberg, B. Rosse, M. Rubery, T. C. Sangster, J. Sanchez, M. Schmitt, M. Schoff, F. H. Séguin, W. Seka, H. Sio, C. Stoeckl, and R. E. Tipton, Phys. Plasmas **24**, 041407 (2017).

9. C. Stoeckl, R. Epstein, R. Betti, W. Bittle, J. A. Delettrez, C. J. Forrest, V. Yu. Glebov, V. N. Goncharov, D. R. Harding, I. V. Igumenshchev, D. W. Jacobs-Perkins, R. T. Janezic, J. H. Kelly, T. Z. Kosc, R. L. McCrory, D. T. Michel, C. Mileham, P. W. McKenty, F. J. Marshall, S. F. B. Morse, S. P. Regan, P. B. Radha, B. S. Rice, T. C. Sangster, M. J. Shoup III, W. T. Shmayda, C. Sorce, W. Theobald, J. Ulreich, M. D. Wittman, D. D. Meyerhofer, J. A. Frenje, M. Gatu Johnson, and R. D. Petrasso, Phys. Plasmas **24**, 056304 (2017).

10. V. N. Goncharov, S. P. Regan, E. M. Campbell, T. C. Sangster, P. B. Radha, J. F. Myatt, D. H. Froula, R. Betti, T. R. Boehly, J. A. Delettrez, D. H. Edgell, R. Epstein, C. J. Forrest, V. Yu. Glebov, D. R. Harding, S. X. Hu, I. V. Igumenshchev, F. J. Marshall, R. L. McCrory, D. T. Michel, W. Seka, A. Shvydky, C. Stoeckl, W. Theobald, and M. Gatu-Johnson, Plasma Phys. Control. Fusion **59**, 014008 (2017).

11. H. G. Rinderknecht, P. A. Amendt, M. J. Rosenberg, C. L. Li, J. A. Frenje, M. Gatu Johnson, H. Sio, F. H. Séguin, R. D. Petrasso, A. B. Zylstra, G. Kagan, N. M. Hoffman, D. Svyatsky, S. C. Wilks, V. Yu. Glebov, C. Stoeckl, and T. C. Sangster, Nucl. Fusion **57**, 066014 (2017).

12. R. Hua, H. Sio, S. C. Wilks, F. N. Beg, C. McGuffey, M. Bailly-Grandvaux, G. W. Collins, and Y. Ping, Appl. Phys. Lett. **111**, 034102 (2017).

13. C. K. Li, P. Tzeferacos, D. Lamb, G. Gregori, P. A. Norreys, M. J. Rosenberg, R. K. Follett, D. H. Froula, M. Koenig, F. H. Seguin, J. A. Frenje, H. G. Rinderknecht, H. Sio, A. B. Zylstra, R. D. Petrasso, P. A. Amendt, H. S. Park, B. A. Remington, D. D. Ryutov, S. C. Wilks, R. Betti, A. Frank, S. X. Hu, T. C. Sangster, P. Hartigan, R. P. Drake, C. C. Kuranz, S. V. Lebedev, and N. C. Woolsey, Nat. Commun. **7**, 13081 (2016).

14. H. Sio, J. A. Frenje, J. Katz, C. Stoeckl, D. Weiner, M. Bedzyk, V. Glebov, C. Sorce, M. Gatu Johnson, H. G. Rinderknecht, A. B. Zylstra, T. C. Sangster, S. P. Regan, T. Kwan, A. Le, A. N. Simakov, W. T. Taitano, L. Chacòn, B. Keenan, R. Shah, G. Sutcliffe, and R. D. Petrasso, Rev. Sci. Instrum. **87**, 11D701 (2016).

15. N. V. Kabadi, H. Sio, V. Glebov, M. Gatu Johnson, A. MacPhee, J. A. Frenje, C. K. Li, F. Seguin, R. Petrasso, C. Forrest, J. Knauer, and H. G. Rinderknecht, Rev. Sci. Instrum. **87**, 11D817 (2016).

16. G. D. Sutcliffe, L. M. Milanese, D. Orozco, B. Lahmann, M. Gatu Johnson, F. H. Séguin, H. Sio, J. A. Frenje, C. K. Li, R. D. Petrasso, H.-S. Park, J. R. Rygg, D. T. Casey, R. Bionta, D. P. Turnbull, C. M. Huntington, J. S. Ross, A. B. Zylstra, M. J. Rosenberg, and V. Yu. Glebov, Rev. Sci. Instrum. **87**, 11D812 (2016).

17. B. Lahmann *et al*., Rev. Sci. Instrum. **87**, 11D801 (2016).

18. H. Chen *et al*., Phys. Rev. Lett. **102**, 105001 (2009).

19. H. Chen, S. C. Wilks, D. D. Meyerhofer, J. Bonlie, C. D. Chen, S. N. Chen, C. Courtois, L. Elberson, G. Gregori, W. Kruer, O. Landoas, J. Mithen, J. Myatt, C. D. Murphy, P. Nilson, D. Price, M. Schneider, R. Shepherd, C. Stoeckl, M. Tabak, R. Tommasini, and P. Beiersdorfer, Phys. Rev. Lett. **105**, 015003 (2010).

20. H. Chen, G. Fiksel, D. Barnak, P.-Y. Chang, R. F. Heeter, A. Link, and D. D. Meyerhofer, Phys. Plasmas **21**, 040703 (2014).

21. O. V. Gotchev, J. P. Knauer, P. Y. Chang, N. W. Jang, M. J. Shoup III, D. D. Meyerhofer, and R. Betti, Rev. Sci. Instrum. **80**, 043504 (2009).

22. H. Chen *et al*., Phys. Rev. Lett. **114**, 215001 (2015).

23. H. Chen *et al*., Phys. Plasmas **22**, 056705 (2015).

24. H. Chen, D. D. Meyerhofer, S. C. Wilks, R. Cauble, F. Dollar, K. Falk, G. Gregori, A. Hazi, E. I. Moses, C. D. Murphy, J. Myatt, J. Park, J. Seely, R. Shepherd, A. Spitkovsky, C. Stoeckl, C. I. Szabo, R. Tommasini, C. Zulick, and P. Beirsdorfer, High Energy Density Phys. **7**, 225 (2011).

25. M. Millot, N. Dubrovinskaia, A. Černok, S. Blaha, L. Dubrovinsky, D. G. Braun, P. M. Celliers, G. W. Collins, J. H. Eggert, and R. Jeanloz, Science **347**, 418 (2015).

26. J. R. Rygg, J. H. Eggert, A. E. Lazicki, F. Coppari, J. A. Hawreliak, D. G. Hicks, R. F. Smith, C. M. Sorce, T. M. Uphaus, B. Yaakobi, and G. W. Collins, Rev. Sci. Instrum. **83**, 113904 (2012).

27. E. A. Mathez *et al*., Geochim. Cosmochim. Acta **59**, 781 (1995).

28. Z. Konôpková *et al*., Nature **534**, 99 (2016).

29. K. Ohta et al., Nature **534**, 95 (2016).

30. R. F. Smith, S. M. Pollaine, S. J. Moon, K. T. Lorenz, P. M. Celliers, J. H. Eggert, H.-S. Park, and G. W. Collins, Phys. Plasmas **14**, 057105 (2007).

31. S. Zhao *et al*., Proc. Nat. Acad. Sci. **114**, 9791 (2017).

32. S. Zhao *et al*., Acta Mater. **103**, 519 (2016).

33. J. A. Frenje, P. E. Grabowski, C. K. Li, F. H. Séguin, A. B. Zylstra, M. Gatu Johnson, R. D. Petrasso, V. Yu. Glebov, and T. C. Sangster, Phys. Rev. Lett. **115**, 205001 (2015).

34. D. E. Fratanduono, D. H. Munro, P. M. Celliers, and G. W. Collins, J. Appl. Phys. **116**, 033517 (2014).

35. H. G. Rinderknecht *et al*., Bull. Am. Phys. Soc. **61**, BAPS.2016.DPP.GO5.11 (2016).

36. Y. Ping, D. G. Hicks, B. Yaakobi, F. Coppari, J. Eggert, and G. W. Collins, Rev. Sci. Instrum. **84**, 123105 (2013).

37. J. S. Oakdale *et al*., Adv. Funct. Mater. **27**, 1702425 (2017).

38. R. F. Smith, C. A. Bolme, D. J. Erskine, P. M. Celliers, S. Ali, J. H. Eggert, S. L. Brygoo, B. D. Hammel, J. Wang, and G. W. Collins, J. Appl. Phys. **114**, 133504 (2013).

39. D. Layzer, Astrophys. J. **122**, 1 (1955).

40. P. Ramaprabhu *et al*., Phys. Fluids **24**, 074107 (2012).

41. R. E. Olson, D. K. Bradley, G. A. Rochau, G. W. Collins, R. J. Leeper, and L. J. Suter, Rev. Sci. Instrum. **77**, 10E523 (2006).

42. R. E. Olson *et al*., Phys. Plasma **18**, 032706 (2011).

43. H. M. Johns *et al*., Bull. Am. Phys. Soc. **61**, BAPS.2016.DPP.PO8.6 (2016).

44. A. B. Zylstra, H. W. Herrmann, Y. H. Kim, A. M. McEvoy, M. J. Schmitt, G. Hale, C. Forrest, Y. Yu. Glebov, and C. Stoeckl, Rev. Sci. Instrum. **88**, 053504 (2017).

45. A. B. Zylstra, J. A. Frenje, M. Gatu Johnson, G. M. Hale, C. R. Brune, A. Bacher, D. T. Casey, C. K. Li, D. McNabb, M. Paris, R. D. Petrasso, T. C. Sangster, D. B. Sayre, and F. H. Séguin, Phys. Rev. Lett. **119**, 222701 (2017).

46. S. C. Hsu *et al*., EPL **115**, 65001 (2016).

47. T. R. Joshi *et al*., Phys. Plasmas **24**, 056305 (2017).

48. B. Rollin and M. J. Andrews, J. Turbul. **14**, 77 (2013).

49. J. D. Schwarzkopf *et al*., Flow Turbulence Combust. **96**, 1 (2016).

50. D. Besnard *et al*., Los Alamos National Laboratory, Los Alamos, NM, Report LA-12303-MS (1992); K. Stalsberg-Zarling and R. Gore, Los Alamos National Laboratory, Los Alamos, NM, Report LA-UR-11-04773 (2011).

51. S. A. Slutz, M. C. Herrmann, R. A. Vesey, A. B. Sefkow, D. B. Sinars, D. C. Rovang, K. J. Peterson, and M. E. Cuneo, Phys. Plasmas **17**, 056303 (2010).

52. M. R. Gomez, S. A. Slutz, A. B. Sefkow, D. B. Sinars, K. D. Hahn, S. B. Hansen, E. C. Harding, P. F. Knapp, P. F. Schmit, C. A. Jennings, T. J. Awe, M. Geissel, D. C. Rovang, G. A. Chandler, G. W. Cooper, M. E. Cuneo, A. J. Harvey-Thompson, M. C. Herrmann, M. H. Hess, O. Johns, D. C. Lamppa, M. R. Martin, R. D. McBride, K. J. Peterson, J. L. Porter, G. K. Robertson, G. A. Rochau, C. L. Ruiz, M. E. Savage, I. C. Smith, W. A. Stygar, and R. A. Vesey, Phys. Rev. Lett. **113**, 155003 (2014).

53. R. F. Heeter *et al*., Rev. Sci. Instrum. **75**, 3762 (2004).

54. D. F. DuBois, B. Bezzerides, and H. A. Rose, Phys. Fluids B **4**, 241 (1992).

55. C. Stoeckl, R. E. Bahr, B. Yaakobi, W. Seka, S. P. Regan, R. S. Craxton, J. A. Delettrez, R. W. Short, J. Myatt, A. V. Maximov, and H. Baldis, Phys. Rev. Lett. **90**, 235002 (2003).

56. D. T. Michel, A. V. Maximov, R. W. Short, S. X. Hu, J. F. Myatt, W. Seka, A. A. Solodov, B. Yaakobi, and D. H. Froula, Phys. Rev. Lett. **109**, 155007 (2012).

57. R. K. Follett, D. H. Edgell, R. J. Henchen, S. X. Hu, J. Katz, D. T. Michel, J. F. Myatt, J. Shaw, and D. H. Froula, Phys. Rev. E **91**, 031104(R) (2015).

58. R. K. Kirkwood, B. B. Afeyan, W. L. Kruer, B. J. MacGowan, J. D. Moody, D. S. Montgomery, D. M. Pennington, T. L. Weiland, and S. C. Wilks, Phys. Rev. Lett. **76**, 2065 (1996).

59. P. Michel *et al*., Phys. Rev. Lett. **102**, 025004 (2009).

60. J. C. Fernández *et al*., Phys. Rev. Lett. **81**, 2252 (1998).

61. H. A. Baldis *et al*., Phys. Rev. Lett. **77**, 2957 (1996).

62. W. Seka, H. A. Baldis, J. Fuchs, S. P. Regan, D. D. Meyerhofer, C. Stoeckl, B. Yaakobi, R. S. Craxton, and R. W. Short, Phys. Rev. Lett. **89**, 175002 (2002).

63. D. Turnbull, P. Michel, J. E. Ralph, L. Divol, J. S. Ross, L. F. Berzak Hopkins, A. L. Kritcher, D. E. Hinkel, and J. D. Moody, Phys. Rev. Lett. **114**, 125001 (2015).

64. S. Depierreux, C. Neuville, C. Baccou, V. Tassin, M. Casanova, P.-E. Masson-Laborde, N. Borisenko, A. Orekhov, A. Colaitis, A. Debayle, G. Duchateau, A. Heron, S. Huller, P. Loiseau, P. Nicolaï, D. Pesme, C. Riconda, G. Tran, R. Bahr, J. Katz, C. Stoeckl, W. Seka, V. Tikhonchuk, and C. Labaune, Phys. Rev. Lett. **117**, 235002 (2016).

65. C. Neuville, V. Tassin, D. Pesme, M. C. Monteil, P. E. Masson-Laborde, C. Baccou, P. Fremerye, F. Philippe, P. Seytor, D. Teychenné, W. Seka, J. Katz, R. Bahr, and S. Depierreux, Phys. Rev. Lett. **116**, 235002 (2016).

66. D. E. Hinkel *et al*., Phys. Plasmas **18**, 056312 (2011).

67. P. E. Masson-Laborde, M. C. Monteil, V. Tassin, F. Philippe, P. Gauthier, A. Casner, S. Depierreux, C. Neuville, B. Villette, S. Laffite, P. Seytor, P. Fremerye, W. Seka, D. Teychenné, A. Debayle, D. Marion, P. Loiseau, and M. Casanova, Phys. Plasmas **23**, 022703 (2016).

Publications and Conference Presentations

Publications

S. G. Demos, C. W. Carr, and D. A. Cross, "Mechanisms of Surface Contamination in Fused Silica by Means of Laser-Induced Electrostatic Effects," Opt. Lett. **42**, 2643 (2017).

S. X. Hu, "Continuum Lowering and Fermi-Surface Rising in Strongly Coupled and Degenerate Plasmas," Phys. Rev. Lett. **119**, 065001 (2017).

F. J. Marshall, R. E. Bahr, V. N. Goncharov, V. Yu. Glebov, B. Peng, S. P. Regan, T. C. Sangster, and C. Stoeckl, "A Framed, 16-Image Kirkpatrick–Baez X-Ray Microscope," Rev. Sci. Instrum. **88**, 093702 (2017).

J. M. Ngoko Djiokap, A. V. Meremianin, N. L. Manakov, S. X. Hu, L. B. Madsen, and A. F. Starace, "Kinematical Vortices in Double Photoionization of Helium by Attosecond Pulses," Phys. Rev. A **96**, 013405 (2017).

T. Petersen, J. D. Zuegel, and J. Bromage, "Thermal Effects in an Ultrafast BiB_3O_6 Optical Parametric Oscillator at High Average Powers," Appl. Opt. **56**, 6923 (2017).

D. B. Schaeffer, W. Fox, D. Haberberger, G. Fiksel, A. Bhattacharjee, D. H. Barnak, S. X. Hu, and K. Germaschewski, "Generation and Evolution of High-Mach-Number Laser-Driven Magnetized Collisionless Shocks in the Laboratory," Phys. Rev. Lett. **119**, 025001 (2017).

J. Serafini, A. Hossain, R. B. James, M. Guziewicz, R. Kruszka, W. Słysz, D. Kochanowska, J. Z. Domagala, A. Mycielski, and R. Sobolewski, "Photoconductive and Electro-Optic Effects in (Cd,Mg)Te Single Crystals Measured in an Experiment-on-Chip Configuration," Appl. Phys. Lett. **111**, 011108 (2017).

Forthcoming Publications

Y. Akbas, G. R. Savich, A. Jukna, T. Plecenik, P. Ďurina, A. Plecenik, G. W. Wicks, and R. Sobolewski, "Low-Temperature Performance of Semiconducting Asymmetric Nano-Channel Diodes," to be published in the Journal of Physics: Conference Series.

P. Angland, D. Haberberger, S. T. Ivancic, and D. H. Froula, "Angular Filter Refractometry Analysis Using Simulated Annealing," to be published in the Review of Scientific Instruments.

A. Bose, R. Betti, D. Shvarts, and K. M. Woo, "The Physics of Long- and Intermediate-Wavelength Asymmetries of the Hot Spot: Compression Hydrodynamics and Energetics," to be published in Physics of Plasmas.

L. Calderín, V. V. Karasiev, and S. B. Trickey, "Kubo–Greenwood Electrical Conductivity Formulation and Implementation for Projector Augmented Wave Datasets," to be published in Computer Physics Communications.

G. Chen, R. Shrestha, A. Amori, Z. Staniszewski, A. Jukna, A. Koroliov, C. Richter, M. El Fray, T. Krauss, and R. Sobolewski, "Terahertz Time-Domain Spectroscopy Characterization of Carbon Nanostructures Embedded in Polymer," to be published in the Journal of Physics: Conference Series.

B. P. Chock, D. R. Harding, and T. B. Jones, "Using Digital Microfluidics to Dispense, Combine, and Transport Low-Surface-Energy Fluids," to be published in Fusion Science and Technology.

C. Dorrer, A. Consentino, R. Cuffney, I. A. Begishev, E. M. Hill, and J. Bromage, "Spectrally Tunable, Temporally Shaped Parametric Front End to Seed High-Energy Nd:Glass Laser Systems," to be published in Optics Express.

R. K. Follett, D. H. Edgell, D. H. Froula, V. N. Goncharov, I. V. Igumenshchev, J. G. Shaw, and J. F. Myatt, "Full-Wave and Ray-Based Modeling of Cross-Beam Energy Transfer Between

Laser Beams with Distributed Phase Plates and Polarization Smoothing," to be published in Physics of Plasmas.

R. K. Follett, J. F. Myatt, R. J. Henchen, J. G. Shaw, D. T. Michel, A. A. Solodov, D. H. Edgell, J. Katz, C. Stoeckl, B. Yaakobi, and D. H. Froula, "Simulations and Measurements of Hot-Electron Generation Driven by the Multibeam Two-Plasmon–Decay Instability," to be published in Physics of Plasmas.

T. A. Germer, K. A. Sharma, T. G. Brown, and J. B. Oliver, "Polarized Optical Scattering by Inhomogeneities and Surface Roughness in an Anisotropic Thin Film," to be published in the Journal of the Optical Society of America A.

S. X. Hu, L. A. Collins, J. P. Colgan, V. N. Goncharov, and D. P. Kilcrease, "Optical Properties of Highly Compressed Polystyrene: An *Ab Initio* Study," to be published in Physical Review B.

A. Jukna, J. Gradauskas, A. Sužiedelis, A. Maneikis, K. Šliužienė, and R. Sobolewski, "Investigation of the I–V Characteristics as Asymmetry in Semiconducting Y–Ba–Cu–O Diodes," to be published in Micro and Nano Letters.

R. K. Kirkwood, D. P. Turnbull, T. Chapman, S. C. Wilks, M. D. Rosen, R. A. London, L. A. Pickworth, W. H. Dunlop, J. D. Moody, D. J. Strozzi, P. A. Michel, L. Divol, O. L. Landen, B. J. MacGowan, B. M. Van Wonterghem, K. B. Fournier, and B. E. Blue, "Plasma-Based Combiner for Very High Fluence and Energy," to be published in Nature Physics.

S. A. Muller, D. N. Kaczala, H. M. Abu-Shawareb, E. L. Alfonso, L. C. Carlson, M. Mauldin, P. Fitzsimmons, D. Lamb, P. Tzeferacos, L. Chen, G. Gregori, A. Rigby, A. Bott, T. G. White, D. Froula, and J. Katz, "Evolution of the Design and Fabrication of Astrophysics Targets for Turbulent Dynamo (TDYNO) Experiments on OMEGA," to be published in Fusion Science and Technology.

B. W. Plansinis, W. R. Donaldson, and G. P. Agrawal, "Single-Pulse Interference Caused by Temporal Reflection at Moving Refractive-Index Boundaries," to be published in the Journal of the Optical Society of America B.

D. N. Polsin, D. E. Fratanduono, J. R. Rygg, A. Lazicki, R. F. Smith, J. H. Eggert, M. C. Gregor, B. H. Henderson, J. A. Delettrez, R. G. Kraus, P. M. Celliers, F. Coppari, D. C. Swift, C. A. McCoy, C. T. Seagle, J.-P. Davis, S. J. Burns, G. W. Collins, and T. R. Boehly, "Measurement of Body-Centered-Cubic Aluminum at 475 GPa," to be published in Physical Review Letters.

S. P. Regan, V. N. Goncharov, T. C. Sangster, E. M. Campbell, R. Betti, T. Bernat, A. Bose, T. R. Boehly, M. J. Bonino, D. Cao, R. Chapman, T. J. B. Collins, R. S. Craxton, A. K. Davis, J. A. Delettrez, D. H. Edgell, R. Epstein, M. Farrell, C. J. Forrest, J. A. Frenje, D. H. Froula, M. Gatu Johnson, C. Gibson, V. Yu. Glebov, A. Greenwood, D. R. Harding, M. Hohenberger, S. X. Hu, H. Huang, J. Hund, I. V. Igumenshchev, D. W. Jacobs-Perkins, R. T. Janezic, M. Karasik, R. L. Keck, J. H. Kelly, T. J. Kessler, J. P. Knauer, T. Z. Kosc, S. J. Loucks, J. A. Marozas, F. J. Marshall, R. L. McCrory, P. W. McKenty, D. D. Meyerhofer, D. T. Michel, J. F. Myatt, S. P. Obenschain, R. D. Petrasso, N. Petta, P. B. Radha, M. J. Mosenberg, A. J. Schmitt, M. J. Schmitt, M. Schoff, W. Seka, W. T. Shmayda, M. J. Shoup III, A. Shvydky, A. A. Solodov, C. Stoeckl, W. Sweet, C. Taylor, R. Taylor, W. Theobald, J. Ulreich, M. D. Wittman, K. M. Woo, and J. D. Zuegel, "The National Direct-Drive Program: OMEGA to the National Ignition Facility," to be published in Fusion Science and Technology.

D. B. Schaeffer, W. Fox, D. Haberberger, G. Fiksel, A. Bhattacharjee, D. H. Barnak, S. X. Hu, K. Germaschewski, and R. K. Follett, "High-Mach Number, Laser-Driven Magnetized Collisionless Shocks," to be published in Physics of Plasmas.

J. Serafini, S. B. Trivedi, D. Kochanowska, M. Witkowska-Baran, A. Mycielski, M. Guziewicz, R. Kruszka, W. Słysz, and R. Sobolewski, "Characterization of (Cd,Mg)Te and (Cd,Mn)Te Single Crystals in the THz Frequency Range Using Integrated Photoconductive and Electro-Optics Effects," to be published in the Journal of Physics: Conference Series.

W. L. Shang, R. Betti, S. X. Hu, K. Woo, L. Hao, C. Ren, A. R. Christopherson, A. Bose, and W. Theobald, "Electron Shock Ignition of Inertial Fusion Targets," to be published in Physical Review Letters.

W. Theobald, A. Bose, R. Yan, R. Betti, M. Lafon, D. Mangino, A. R. Christopherson, C. Stoeckl, W. Seka, W. Shang, D. T. Michel, C. Ren, R. C. Nora, A. Casner, J. Peebles, F. N. Beg, X. Ribeyre, E. Llor Aisa, A. Colaïtis, V. Tikhonchuk, and M. S. Wei, "Enhanced Hot-Electron Production and Strong-Shock Generation in Hydrogen-Rich Ablators for Shock Ignition," to be published in Physics of Plasmas.

D. Turnbull, S. Bucht, A. S. Davies, D. Haberberger, T. J. Kessler, J. L. Shaw, and D. H. Froula, "Raman Amplification with a Flying Focus," to be published in Physical Review Letters.

M. D. Wittman, M. J. Bonino, C. Fella, D. R. Harding, and J. Sanchez, "Effect of Tritium-Induced Damage on Plastic Targets from High-Density DT Permeation," to be published in Fusion Science and Technology.

M. Zaghoo and I. F. Silvera, "Conductivity and Dissociation in Liquid Metallic Hydrogen and Implication for Planetary Interiors," to be published in the Proceedings of the National Academy of Science.

A. B. Zylstra, J. A. Frenje, M. Gatu Johnson, G. M. Hale, C. R. Brune A. Bacher, D. T. Casey, C. K. Li, D. McNabb, M. Paris, R. D. Petrasso, T. C. Sangster, D. B. Sayre, and F. H. Séguin, "Proton Spectra from ^{3}He + T and ^{3}He + ^{3}He Fusion at Low Center-of-Mass Energy, with Potential Implications for Solar Fusion Cross Sections," to be published in Physical Review Letters.

Conference Presentations

E. M. Schiesser, S.- W. Bahk, and J. P. Rolland, "Three Unobscured Reflective Relays for High-Power, Broadband Laser Beam Transport," presented at the International Optical Design Conference, Denver, CO, 9–13 July 2017.

The following presentations were made at the 20th Conference on Shock Compression of Condensed Matter, St. Louis, MO, 9–14 July 2017:

B. Henderson, D. N. Polsin, T. R. Boehly, M. C. Gregor, S. X. Hu, G. W. Collins, J. R. Rygg, D. E. Fratanduono, and P. M. Celliers, "Hugoniot Measurements of Silicon Shock Compressed to 25 Mbar."

D. N. Polsin, T. R. Boehly, J. A. Delettrez, G. W. Collins, J. R. Rygg, M. C. Gregor, B. Henderson, C. A. McCoy, D. E. Fratanduono, R. F. Smith, R. G. Kraus, J. H. Eggert, F. Coppari, A. Jenei, D. C. Swift, and P. M. Celliers, "The First Observation of the bcc Phase in Aluminum Compressed to 559 GPa."

D. N. Polsin, T. R. Boehly, J. A. Delettrez, G. W. Collins, J. R. Rygg, M. C. Gregor, C. A. McCoy, B. J. Henderson, D. E. Fratandouno, R. Smith, R. Kraus, J. H. Eggert, F. Coppari, A. Jenei, D. C. Swift, and P. M. Celliers, "X-Ray Diffraction Experiments on Ramp-Compressed Aluminum at the National Ignition Facility and on OMEGA."

The following presentations were made at the 20th International Conference on Electron Dynamics in Semiconductors, Optoelectronics, and Nanostructures, Buffalo, NY, 17–21 July 2017:

Y. Akbas, G. R. Savich, A. Jukna, T. Plecenik, P. Ďurina, A. Plecenik, G. W. Wicks, and R. Sobolewski, "Low-Temperature Performance of Semiconducting Asymmetric Nano-Channel Diodes."

G. Chen, R. Shrestha, A. Amori, Z. Staniszewski, A. Jukna, A. Koroliov, C. Richter, M. El Fray, T. Krauss, and R. Sobolewski, "Terahertz Time-Domain Spectroscopy Characterization of Carbon Nanostructures Embedded in Polymer."

J. Serafini, S. B. Trivedi, D. Kochanowska, M. Witkowska-Baran, A. Mycielski, M. Guziewicz, R. Kruszka, W. Słysz, and R. Sobolewski, "Characterization of (Cd,Mg)Te and (Cd,Mn)Te Single Crystals in the THz Frequency Range Using Integrated Photoconductive and Electro-Optics Effects."

N. D. Viza, M. H. Romanofsky, and D. R. Harding, "Droplet-Based Microfluidic Approach for Producing Inertial Confinement Fusion Polymer Shells," presented at the 2nd Microfluidics Congress, Philadelphia, PA, 25–26 July 2016.

The following presentations were made at High Energy Density Science Summer School, La Jolla, CA, 30 July–11 August 2017:

D. A. Chin, P. M. Nilson, G. W. Collins, and J. R. Rygg, "Interpreting EXAFS Spectra: Toward Ramp-Compression Studies of Iron Oxide."

G. W. Collins, "Physics of Matter at Extreme Pressure."

Y. H. Ding, "A First-Principles Equation-of-State Table of Beryllium for High-Energy-Density Plasma Simulations."

V. Gopalaswamy, H. Zhang, R. Betti, R. Yan, and H. Aluie, "Finite-Amplitude Modes in the Ablative Rayleigh–Taylor Instability."

A. Hansen, "OMEGA Supersonic Gas-Jet Target System Characterization."

A. Kar, P. B. Radha, T. R. Boehly, D. H. Edgell, S. X. Hu, A. Shvydky, V. N. Goncharov, and S. P. Regan, "X-Ray Radiography of Laser-Driven Shocks for Inertial Confinement Fusion."

O. Mannion, and G. Grim, "Simulating Neutron Time of Flight Data."

A. L. Milder, and D. H. Froula, "Measuring Non-Maxwellian Distribution Functions Using Expanded Thomson Scattering."

S. Miller, J. Knauer, P. B. Radha, and V. N. Goncharov, "Studying Deceleration-Phase Rayleigh–Taylor Growth by Varying D:T Ratios in Gas-Filled Plastic Implosions."

M. Stoeckl and A. A. Solodov, "Dependence of Readout Fade Rate on X-Ray Energy for $BaFBr_{0.85}I_{0.15}$:Eu Image Plates."

M. Zaghoo, R. J. Husband, and I. F. Silvera, "Striking Isotope Effect in Hydrogen Dissociation Under Pressure."

The following presentations were made at Liquid Crystals XXI, San Diego, CA, 6–10 August 2017:

K. L. Marshall, D. Saulnier, T. Z. Kosc, O. Didovets, and S. H. Chen, "Optically Robust Photoalignment Materials for Liquid Crystal Device Applications in the Near-UV Region."

K. L. Marshall, U. Kurumbail, A. Hosein, and M. Hanchett, "Computational Chemistry Modeling and Design of Photoswitchable Alignment Materials for Optically Addressable Liquid Crystal Devices. II. Transition-State Modeling in Azobenzene and Spiropyran Oligomers."

J. Kendrick, R. Boni, and C. Sorce, "An Optically Passive Method that Rate Doubles 2-GHz Timing Fiducials," presented at SPIE Optical Engineering and Applications, San Diego, CA, 6–10 August 2017.

S. Bucht, D. Haberberger, J. Bromage, and D. H. Froula, "Transforming the Idler to Seed Raman Amplification," presented at the OSA Foundation Siegman International School on Lasers, Leon, Mexico, 6–11 August 2017.

J. L. Shaw, N. Lemos, L. D. Amorim, N. Vafaei-Najafabadi, K. A. Marsh, F. S. Tsung, W. B. Mori, C. Joshi, and D. H. Froula, "Direct Laser Acceleration of Electrons in a Laser Wakefield Accelerator with Ionization Injection," presented at the Laser Plasma Accelerator Workshop, Jeju Island, South Korea, 27 August–1 September, 2017.

The following presentations were made at the 2nd Asia-Pacific Symposium on Tritium Science, Livermore Valley, CA, 5–8 September 2017:

W. T. Shmayda, M. Sharpe, C. Fagan, and W. U. Schröder, "Adsorbed Water Influence on Tritium Migration into and out of 316 Stainless Steel."

W. T. Shmayda, M Sharpe, C. Fagan, and M. D. Wittman, "Tritium Operations at the University of Rochester's Laboratory for Laser Energetics."

The following presentations were made at the 10th International Conference on Inertial Fusion Sciences and Applications, Saint Malo, France, 11–15 September 2017:

R. Betti, J. P. Knauer, V. Gopalaswamy, D. Patel, K.-M. Woo, W. Shang, A. Bose, K. S. Anderson, T. J. B. Collins, V. Yu. Glebov, A. V. Maximov, C. Stoeckl, F. J. Marshall, E. M. Campbell, and S. P. Regan, "The One-Dimensional Cryogenic Implosion Campaign on the OMEGA Laser System."

D. H. Froula, D Turnbull, J. Bromage, E. M. Campbell, T. Chapman, A. Consentino, L. Divol, C. Dorrer, D. H. Edgell, R. K. Follett, A. Hansen, E. M. Hill, J. Katz, T. J. Kessler, B. E. Kruschwitz, J. Kwiatkowski, P. Michel, J. F. Myatt, J. C. Puth, T. C. Sangster, A. B. Sefkow, J. G. Shaw, M. J. Shoup III, and D. J. Strozzi, "Cross-Beam Energy Transfer Platform on OMEGA."

V. N. Goncharov, S. P. Regan, E. M. Campbell, T. C. Sangster, R. Betti, T. R. Boehly, M. J. Bonino, D. Cao, A. K. Davis, D. H. Edgell, R. Epstein, C. J. Forrest, D. H. Froula, V. Yu. Glebov, D. R. Harding, S. X. Hu, I. V. Igumenshchev, R. T. Janezic, J. H. Kelly, F. J. Marshall, R. L. McCrory, D. T. Michel, J. F. Myatt, P. B. Radha, W. Seka, A. Shvydky, C. Stoeckl, and M. Gatu Johnson, "Understanding the Performance Limitations of Direct-Drive Implosions on OMEGA."

S. X. Hu, L. A. Collins, T. R. Boehly, G. W. Collins, P. B. Radha, E. M. Campbell, J. D. Kress, and V. N. Goncharov, "A Review of High-Energy-Density-Physics Studies for Inertial Confinement Fusion Applications."

P. B. Radha, J. A. Marozas, M. J. Rosenberg, D. Turnbull, T. R. Boehly, E. M. Campbell, T. J. B. Collins, D. H. Edgell, V. N. Goncharov, R. L. McCrory, D. T. Michel, S. P. Regan, T. C. Sangster, W. Seka, A. A. Solodov, A. Shvydky, B. J. MacGowan, J. DiNicola, M. Hohenberger, J. M Moody, and M. Karasik, "Direct-Drive Experiments at the National Ignition Facility."

S. P. Regan, V. N. Goncharov, T. C. Sangster, E. M. Campbell, K. S. Anderson, R. Betti, T. R. Boehly, R. Boni, M. J. Bonino, D. Canning, D. Cao, T. J. B. Collins, R. S. Craxton, A. K. Davis, J. A. Delettrez, W. R. Donaldson, D. H. Edgell, R. Epstein, C. J. Forrest, D. H. Froula, V. Yu. Glebov, D. R. Harding, S. X. Hu, H. Huang, I. V. Igumenshchev, R. T. Janezic, D. W. Jacobs-Perkins, J. Katz, R. L. Keck, J. H. Kelly, T. J. Kessler, B. E. Kruschwitz, J. P. Knauer, T. Z. Kosc, S. J. Loucks, J. A. Marozas, F. J. Marshall, A. V. Maximov, R. L. McCrory, P. W. McKenty, D. T. Michel, S. F. B. Morse, J. F. Myatt, P. M. Nilson, J. C. Puth, P. B. Radha, M. J. Rosenberg, W. Seka, R. Shah, W. T. Shmayda, R. W. Short, A. Shvydky, M. J. Shoup III, S. Skupsky, A. A. Solodov, C. Sorce, S. Stagnitto, C. Stoeckl, W. Theobald, D. Turnbull, J. Ulreich, M. D. Wittman, V. Gopalaswamy, J. D. Zuegel, J. A. Frenje, M. Gatu Johnson, R. D. Petrasso, H. Sio, B. Lahmann, P. Bell, S. Bhandarkar, D. K. Bradley, D. A. Callahan, A. Carpenter, D. T. Casey, J. Celeste, M. Dayton, S. N. Dixit, C. S. Goyon, M. Hohenberger, O. A. Hurricane, S. Le Pape, L. Masse, P. Michel, J. D. Moody, S. R. Nagel, A. Nikroo, R. Nora, L. Pickworth, J. E. Ralph, H. G. Rinderknecht, R. P. J. Town, R. J. Wallace, P. Wegner, M. Farrell, P. Fitzsimmons, C. Gibson, A. Greenwood, L. Carlson, T. Hilsabeck, H. Huang, J. D. Kilkenny, R. W. Luo, N. Rice, M. Schoff, W. Sweet, A. Tambazidis, T. Bernat, N. Petta, J. Hund, S. P. Obenschain, J. W. Bates, M. Karasik, A. J. Schmitt, J. Weaver, M. J. Schmitt, S. Hsu, G. Rochau, L. Claus, Q. Looker, J. Porter, G. Robertson, M. Sanchez, J. Hares, and T. Dymoke-Bradshaw, "The National Direct-Drive Inertial Confinement Fusion Program."

T. C. Sangster, J. D. Kilkenny, G. A. Rochau, and S. H. Batha, "The National Diagnostics Strategy in the US."

The following presentations were made at the 49th Annual Symposium on Optical Materials for High Power Lasers, Boulder, CO, 24–27 September 2017:

S. M. Gracewski, S. Boylan, J. C. Lambropoulos, J. B. Oliver, T. J. Kessler, and S. G. Demos, "Simulation of Internal Stress Waves Leading to Laser-Induced Damage in Multilayer Dielectric Gratings."

K. R. P. Kafka, S. Papernov, M. A. DeMarco, C. Hall, K. L. Marshall, B. Hoffman, and S. G. Demos, "Damage Performance Under 351-nm, Nanosecond Pulses of Magnetorheological Finishing-Polished Fused-Silica Samples Using Different Polishing Compounds and Postprocessing Methods."

T. Z. Kosc, K. L. Marshall, A. A. Kozlov, S. Papernov, and S. G. Demos, "Damage Resistance of Nematic Liquid Crystal Materials for Femtosecond to Nanosecond Pulse Lengths at 1053 nm."

A. A. Kozlov, S. Papernov, S. G. Demos, J. B. Oliver, A. L. Rigatti, B. Hoffman, and J. C. Lambropoulos, "Picosecond Pulse-Damage Mechanism of Hafnia-Silica High Reflectors Investigated by High-Resolution Microscopy."

S. Papernov, M. D. Brunsman, J. B. Oliver, B. Hoffman, A. A. Kozlov, S. G. Demos, A. Shvydky, F. Cavalcante, L. Yang, C. S. Menoni, B. Roshanzadeh, S. T. P. Boyd, L. A. Emmert, and W. Rudolph, "Characterization of Hafnium Oxide Thin Films with Varying Oxygen Content."

J. L. Shaw, N. Lemos, L. D. Amorim, N. Vafaei-Najafabadi, K. A. Marsh, F. S. Tsung, W. B. Mori, C. Joshi, and D. H. Froula, "Direct Laser Acceleration of Electrons in a Laser Wakefield Accelerator with Ionization Injection," presented at

the 3rd European Advanced Accelerator Concepts Workshop, Biodola, Italy, 24–30 September 2017.

The following presentations were made at the 11th International Laser Operations Workshop, Rochester, NY, 26–28 September 2017:

M. Barczys, D. Canning, A. Consentino, C. Dorrer, M. J. Guardalben, E. M. Hill, S. Householder, B. E. Kruschwitz, J. Kwiatkowski, J. O'Sullivan, and L. J. Waxer, "Activation Strategy for a Tunable UV Beamline on OMEGA and OMEGA EP."

E. M. Hill, C. Dorrer, G. Balonek, R. Cuffney, J. H. Kelly, T. Z. Kosc, and M. Spilatro, "Advances in Pulse-Shaping Technology on OMEGA and OMEGA EP."

B. E. Kruschwitz, M. Barczys, A. Consentino, C. Dorrer, M. J. Guardalben, E. M. Hill, J. Kwiatkowski, D. Nelson, J. C. Puth, D. Turnbull, and L. J. Waxer, "Development of a Tunable UV Capability for Cross-Beam Energy Transfer Mitigation Studies in the OMEGA Target Chamber."

J. Kwiatkowski, M. Barczys, D. Canning, B. Ehrich, A. Kalb, B. E. Kruschwitz, N. Mahmutovic, and S. Stagnitto, "*In-Situ* Transmission Measurements of Optical Components Using a Ratiometer Technique."

G. Pien, W. J. Armstrong, and M. Krieger, "Use of CAD Data for Real-Time Target-Position Guidance and Geometry Validation."

J. Puth, S. F. B. Morse, M. Barczys, D. Canning, J. Kelly, B. E. Kruschwitz, S. Sampat, and S. Stagnitto, "The Omega Laser Facility: Status and Performance."

S. Sampat, J. H. Kelly, T. Z. Kosc, A. L. Rigatti, J. Kwiatkowski, W. R. Donaldson, M. H. Romanofsky, L. J. Waxer, R. Dean, and R. Moshier, "100-Gbar Power-Balance Activities on OMEGA."

L. J. Waxer, C. Dorrer, E. M. Hill, A. Kalb, and W. A. Bittle, "Development and Implementation of a Single-Shot Diagnostic for Characterizing 0.5- to 250-ps Pulses on OMEGA EP."

L. J. Waxer, M. Heimbueger, J. H. Kelly, S. F. B. Morse, D. Nelson, D. Weiner, and G. Weselak, "On-Shot Focal-Spot Characterization in the OMEGA Target Chamber."

L. E. Bukowski, "Shaping of Transverse Beam Profiles Through Optical Gain Media," presented at IONS Rochester 2017, Rochester, NY, 29 September–1 October 2017.


1850
MELIORA
UNIVERSITY of
ROCHESTER